MIXING AND REACTION
IN THE SUBSONIC 2-D TURBULENT FREE SHEAR LAYER

Thesis by

Clifford Eugene Frieler

In Partial Fulfillment of the Requirements

for the Degree of

Doctor of Philosophy

California Institute of Technology

Pasadena, California

1992

(Defended May 26, 1989)

Acknowledgements

Because of the seperation this last decade and a half of academic life has caused, I would like to thank my family for their patience, encouragement and support. Special appreciation goes to my wife, Mary Rodgers. Because of the close proximity she bore the brunt of my mood in addition to contributing many hours of help in preparing this document. With any luck, life will now become "normal" and she might remember why she married me. My Love Always.

Finally, I would like to thank my advisor, Paul Dimotakis. His influence on the scope and progress of this work cannot be overstated.

Financial support by the California Institute of Technology is gratefully acknowledged. This research was sponsored by AFOSR Grant Number AFOSR-83-0219.

Abstract

Several aspects of mixing and reaction in a turbulent two-dimensional shear layer have been studied. Experiments have been performed with reacting H_2 , F_2 and NO in inert diluent gases. Sensing the heat release by these reactions, several aspects of the mixing process can be examined without the usual resolution limitations. For example, in contrast with direct measurements of composition, the amount of mixed fluid can be *conservatively* estimated with the results of the "flip" experiments. These have been performed over a range of density ratios, Reynolds numbers and heat release.

The effects of initial conditions are of primary importance when comparisons to other studies are undertaken. Aspects as fundamental as growth rate of the turbulent region, or as obscure as the mixed fluid flux ratio depend strongly on the boundary conditions of this flow. These effects are examined in conjunction with those of Reynolds number and density ratio. For most cases studied here, tripping of the high speed boundary layer led to growth rate decreases. An exception was found for the case of high density ratio where the opposite effect was observed. This anomalous result occurred at conditions under which a new mode of instability has been shown to exist. Parallels exist between this unusual result and those of Batt in the uniform density case.

An extensive study of the effects of density ratio on the mixing and reaction in the 2-D shear layer has been performed. Results indicate that several aspects of the mixing process are remarkably similar. Profiles of mixed fluid change little as the density ratio varies by a factor of 30. The integral amount of mixed fluid varies less than 6% for all density ratios examined. This insensitivity contrasts with that of the profiles of mixed fluid composition. While having very similar

shapes the profiles are offset by an amount which depends very strongly upon the density ratio. The entrainment into the mixing layer has also been examined. Power spectral densities of the temperature time series were calculated and found to collapse upon normalization with the adiabatic flame temperature and large structure passage frequency. Least squares fits of the probability density functions were also examined.

The initial work of Mungal and Frieler (1988) on the effects of chemical kinetics on the formation of product in the 2-D mixing layer have been greatly expanded. Measurements have been extended to include a wider range of NO concentrations and have been performed for two other stoichiometries. Results indicate that the simple model envisioned in Mungal and Frieler may only be suited for cases with extreme stoichiometry (very high or very low). Further investigations have turned up a serious discrepancy reflecting both on the experimental technique and on theory and modeling of this reacting flow. Experiments run under otherwise identical conditions demonstrate that more product is formed when F_2 is the rich reactant than when H_2 is the rich reactant. This dependence upon molecular character is counter intuitive and stems from a coupling of the effects of differing diffusivity and chemical kinetics. Numerical calculations based on simplified flow models are reported which demonstrate this coupling. These results indicate that even subtle diffusion effects can measurably effect reacting flows and imply that assumptions common among current modeling efforts must be re-examined.

The effects of Reynolds number on mixing and reaction in the 2-D turbulent mixing layer have been examined. Evidence of the remnants of the initial roll up and mixing transition are seen for Reynolds numbers as large as 30,000. Indications of a resonance with the acoustic mode of the apparatus exist which affect results

for Reynolds numbers up to 60,000. Natural transition of the high and low speed boundary layer on the splitter plate complicate comparisons of the high Reynolds number data with the remainder. In spite of all of these qualifications, the amount of mixed fluid is nearly constant. Over the range of Reynolds numbers 10,000 to 200,000, it varies by less than 12%. No evidence of an asymptotic decline in the amount of mixed fluid is observed.

Table of Contents

Acknowledgements iii

Abstract iv

Table of Contents vii

List of Figures x

List of Tables xvi

Nomenclature xvii

Introduction 1

Chapter 1. Experimental Facility and Technique 4

- Flow Apparatus 4
- Pressure Gradient 7
- Schleiren Photography 8
- Dynamic Pressure 9
- Temperature 10
- Calibration Procedures 13

Chapter 2. Initial Conditions 14

- Growth Rates Dependence on Velocity Ratio 15
- Growth Rates Dependence on Reynolds Number 16
- Acoustic Resonance 18
- Growth Rates Dependence on Density Ratio 21
- Summary 24

Chapter 3. Heat Release 27

- Background 28
- Experiments 30
- Mixing Layer Growth 30
- Mixed Fluid Distributions 32
- Autocorrelation and Spectra 38
- Summary 45

Chapter 4. The Effects of Freestream Density Ratio 46

- Product Probability Distributions 54
- Product Distributions 60
- Entrainment Rates and Ratios 69
- Autocorrelations and Spectra 75
- Probability Density Function of Composition 81
- Summary 83

Chapter 5. Chemistry, Differing Diffusivity and Damköhler Number 88

- H_2 / F_2 / NO 88
- NO / F_2 110
- Effects of Tertiary Diffusion 113
- Summary 114

Chapter 6. The Effects of Reynolds Number 116

- Mixed Fluid Profiles 120
- Entrainment 130
- Spectra and Autocorrelations 134
- Probability Density Functions 140
- Summary 143

Conclusions 147

Appendix A. Temperature Measurements and Probe Response . 151

- Temperature 151
- Temperature Measurement Compensation 153
- Noise Measurements 156

Appendix B. Analysis 170

- Local 170
- Dilitation Considerations 177
- Integral Quantities 179
- Flux Integrals 182

Appendix C. PDF of Composition 186

- Mean Temperature Technique 187
- Technique Based on Measured PDF of Temperature 188

Appendix D. Laminar Strained Diffusion Flame 193

- Results for Hypergolic Reactions 201
- Discussion and Results for Finite Activation Energy 207

Appendix E. Homogeneously Mixed Reactor 212

- CHEMKIN Solutions 220

References: 225

List of Figures

Chapter 1. Experimental Facility and Technique

1.1 Layout of GALCIT Reacting Shear-Flow Lab. 5

1.2 Side View of the Facility. 8

1.3 Schlieren Photograph of $U_2 = .386\,U_1$, $\rho_2 = \rho_1$ Mixing Layer. . . 10

1.4 Schematic of the Mixing Layer. 11

1.5 Cold Wire Probe and it's Circuit. 12

Chapter 2. Initial Conditions

2.1 Accumulation of Data for Mixing layer Growth ($\rho_2 = \rho_1$). . . . 15

2.2 Mixing Layer Growth Rate versus Reynolds Number. 17

2.3 Power Spectral Density For Several Reynolds Number. 19

2.4 Mixing Layer Growth Rate versus Density Ratio. 20

Chapter 3. The Effects of Heat Release

3.1 Mixing Layer Growth versus Dilatation. 31

3.2 Mixed High-Speed Fluid and Mean Number Density Profiles. . . 32

3.3 Mixed Low-Speed Fluid and Mean Number Density Profiles. . . . 33

3.4 Mixed-Fluid and Mean Number Density Profiles. 34

3.5 Mixed-Fluid Volume Fraction and Mixed-Fluid Fraction. 36

3.6 Power Spectral Density (PSD) of Temperature Fluctuations. . . . 37

3.7 Normalized PSD for Each Flip. 39

3.8 Autocorrelation of Instantaneous Temperature Integral. 42

3.9 Large Structure Spacing Normalized by Layer Width. 43

Chapter 4. The Effects of Freestream Density Ratio

4.1 Mixing Layer Growth Rates versus Density Ratio. 52

4.2 Normalized Temperature Profiles for $\phi = 1$. 54

4.3 Probability of Mixed High-Speed Fluid Profiles. 56

4.4 Probability of Mixed Low-Speed Fluid Profiles. 57

4.5 Probability of Mixed-Fluid Profile for Each Density Ratio. . . . 58

4.6 Product Probability Thickness for Each Stoichiometry. 59

4.7 Product Distributions for $\phi = 1$. 60

4.8 Profiles of Mixed High-Speed Fluid. 61

4.9 Profiles of Mixed Low-Speed Fluid. 62

4.10 Product Thickness for Each Stoichiometry. 63

4.11 Mixed High-Speed and Low-Speed Fluid Thickness and Probability Thickness. 64

4.12 Mixed-Fluid and Mean Number Density Profiles for Each Density Ratio. 65

4.13 Several Measures of Mixing Layer Width. 66

4.14 Mixed-Fluid Mole Fractions for Each Density Ratio. 67

4.15 Mixed-Fluid Composition Profiles. 68

4.16 Mean Mixed-Fluid Composition for Each Density Ratio. 69

4.17 Estimates for Mixing Layer Volume Entrainment Rates. 70

4.18 Estimates for Total Volume and Mass Entrainment Rates. 71

4.19 Entrainment Ratio Estimates for Each Density Ratio. 72

4.20 Fluctuation Correlations versus Density Ratio. 76

4.21 Power Spectral Density for Each Density Ratio. 77

4.22 Autocorrelation of Instantaneous Temperature Integral for Each Density Ratio. 78

4.23 Mixing Layer Length Scales Inferred from Autocorrelations. . . . 79

4.24 Autocorrelation Length Scales Normalized by Mixing Layer Width. 80

4.25 Probability Density Function of Composition for $s = 1$. 82

4.26 Contour Plot of PDF for $s = 1$. 83

4.27 Probability Density Function of Composition for $s = 4$. 84

4.28 Contour Plot of PDF for $s = 4$. 85

4.29 Probability Density Function of Composition for $s = 1/7$. 86

4.30 Contour Plot of PDF for $s = 1/7$. 87

Chapter 5. Chemistry, Differing Diffusivity and Damköhler Number

5.1 Product Probability Thickness for $s = 1, r = .386$ versus Stoichiometric Composition. 90

5.2 Normalized Temperature Profiles for F_2 Rich and H_2 Rich $\phi = 7, 1/7$. 91

5.3 H_2 Rich Diffusion Profiles. 94

5.4 F_2 Rich Diffusion Profiles. 95

5.5 Product in the LSDF at Fast Chemistry Limit for Several Diffusivity Ratios. 96

5.6 Product Probability Thickness in H_2 / F_2 / NO Reacting Layer NO Concentration. 98

5.7 Calculated Chemical Times for Overall Reaction System in Homogeneous Reactor. 99

5.8 LSDF Solution versus Time for Several Cases. 104

5.9 LSDF Solution at a Specific Time versus NO Concentration. . . 107

5.10 Temperature-Composition Relationship for NO / F_2 System $\phi = 1/8, 1, 8$. 112

5.11 Tertiary Diffusion Solution and Estimated Probe Response for Konrad's Equal Density Experiments. 113

Chapter 6. The Effects of Reynolds Number

6.1 Growth Rate of Mixing Layer versus Reynolds Number. 119

6.2 Mixed High-Speed Profiles for Each Reynolds Number. 121

6.3 Mixed Low-Speed Profiles for Each Reynolds Number. 122

6.4 Mixed High and Low-Speed Fluid Thicknesses and Probability Thicknesses. 124

6.5 Mixed-Fluid Profiles and Mean Number Density Profiles for Each Reynolds Number. 125

6.6 Mixed High-Speed, Low-Speed and Total Mixed Fluid Mole Fractions. 126

6.7 Mixed-Fluid Composition Profiles for Each Reynolds Number. . . 128

6.8 Mean Mixed-Fluid Composition versus Reynolds Number. 129

6.9 Entrainment of High-Speed Fluid versus Reynolds Number. . . . 130

6.10 Entrainment of Low-Speed Fluid versus Reynolds Number. . . . 131

6.11 Total Volume Entrainment Rate versus Reynolds Number. . . . 132

6.12 Volume Entrainment Ratios versus Reynolds Number. 133

6.13 Power Spectral Density for Each Reynolds Number. 134

6.14 Normalized Power Spectral Density for Each Reynolds Number. . 135

6.15 Autocorrelation of Instaneous Integral Temperature Rise. 137

6.16 Mean Structure Spacing versus Reynolds Number. 138

6.17 Mean Structure Spacing Normalized by Mixing Layer Width. . . 139

6.18 Probability Density Composition for Reynolds Number= 15,000. . 141

6.19 Contour Plot of PDF for Reynolds Number= 15,000. 142

6.20 Probability Density of Composition for Reynolds Number= 36,000. 143

6.21 Contour Plot of PDF for Reynolds Number= 36,000. 144

6.22 Probability Density of Composition for Reynolds Number= 62,000. 145

6.23 Contour Plot of PDF for Reynolds Number= 62,000. 146

Appendix A. Temperature Measurement and Probe Response

A.1 Experimental Results for the case $\rho_2/\rho_1 = 2$. 151

A.2 Temperature Fluctuation Spectra. 157

A.3 Compensated Temperature Fluctuation Spectra. 158

Appendix B. Analysis

B.1 Conceptual PDF of Composition. 171

B.2 Transform between Temperature and Composition for $\phi = 1/2$. . 172

B.3 Mixed-Fluid Function for $\xi_o = 1/9$. 176

Appendix D. Laminar Strained Diffusion Flame

D.1 Streamlines for 2D Irrotational Strain. 195

D.2 Product for Finite Kinetic Rate Laminar Strained Diffusion Flame (LSDF). 203

D.3 Product in LSDF with Damköhler Number Based on Stoichiometric Composition. 204

D.4 Slow Chemistry Dependence of Product in LSDF. 205

D.5 Fast Chemistry Dependence of Product in LSDF. 206

D.6 Demonstration of Patched Asymptotic Approximation. 207

D.7 Product for Finite Kinetic Rate LSDF for Several Ignition Temperatures. 208

D.8 Collapse for Damköhler Number Based on Cold Conditions. . . . 209

D.9 Collapse for Damköhler Number Based on Adiabatic Flame Conditions. 210

Appendix E. Homogeneous Reactor

E.1 Temperature Rise in Homogeneous Reactor for H_2 / NO / F_2 System ($\phi = 1/8, \Delta T_h \cong 82K$) 222

E.2 Temperature Rise in Homogeneous Reactor for H_2 / NO / F_2 System ($\phi = 1, \Delta T_h \cong 82K$) 223

E.3 Temperature Rise in Homogeneous Reactor for H_2 / NO / F_2 System ($\phi = 7, \Delta T_h \cong 56K$) 224

List of Tables

Chapter 1. Experimental Facility and Technique

1.1 Contraction Section Specifications 6

Chapter 3. The Effects of Heat Release

3.1 Compositions for Heat Release Experiments 29

Chapter 4. The Effects of Freestream Density Ratio

4.1 Compositions for Density Ratio Experiments 51

Chapter 5. Chemistry, Diffusion and Damköhler Number

5.1 Rate Constants and Heat Release for Reactions in the H_2 / F_2 / NO System 101

Chapter 6. The Effects of Reynolds Number

6.1 Velocities for Reynolds Number Experiments 117

Appendix A. Temperature Measurement and Probe Response

A. Detailed Experimental Parameters and Results 159

Nomenclature

D_i In Appendix G., the ratio of the diffusivity of the i^{th} species to the reference diffusivity

$\mathcal{D}_{ij}$ Binary diffusion coefficient of the i^{th} species into the j^{th} species

e Total entrainment rate

- e_i entrainment rate from the i^{th} stream
- e_s mass entrainment rate
  - e_δ Determined from mixing layer geometry
  - e Determined from mean fluxes
  - e_m Determined from mixed fluid mean fluxes

E Entrainment ratio

- E_v volume entrainment ratio
- $E_{v\delta}$ Determined from mixing layer geometry
- E_v Determined from mean fluxes
- E_{vm} Determined from mixed fluid mean fluxes

$E_{\bar{\xi}_m}$ Mean mixed fluid composition ratio

$\vec{J}_i$ Diffusive flux of the i^{th} species

n Number density

- n_p Number density of chemical product
- n_∞ Number density of free stream
- n_i Number density of the i^{th} species
- n_{ik} Number density of the i^{th} species in the k^{th} stream

P_T Probability density function of temperature rise

$P(\xi)$ Probability density function of composition

$\mathcal{R}_{ij}$ Production rate of the i^{th} species due to the j^{th} reaction

T_0 Absolute ambient temperature

ΔT_{ave} Average temperature rise measurement

ΔT Temperature rise due to chemical reaction

ΔT_f Adiabatic flame temperature rise

$\Delta T(\xi)$ Temperature rise foe a specific composition

$\vec{u}$ 3-D velocity vector $\vec{u} = (u, v, w)$

u x-component of velocity

V Volume

$\alpha_i, \beta_i, \gamma$ Dummy Variables

δ Mixing layer width

∇ Gradient, $\nabla = \left(\frac{d}{dx}, \frac{d}{dy}, \frac{d}{dz}\right)$

ϵ Dummy variable - $\epsilon \ll 1$

ε Irrotional strain rate

η Laminar strained flame similarity space coordinate

ϕ Stoiciometic mixture ratio

ρ Fluid density

τ Characteristic time (i.e., τ_δ) also in Appendix D, similarity time coordinate

$\theta(\xi_\phi)$ Normalized mean temperature rise

θ_m Probability of mixed fluid

$\theta_1(\xi_\phi)$ Reduced mean temperature rise; probability of mixed high-speed fluid

$\theta_2(\xi_\phi)$ Reduced mean temperature rise; probability of mixed low-speed fluid

$\Theta(\xi, \xi_0)$ Mixed fluid function (Dimotakis)

ξ Composition or high-speed fluid mixture fraction

ξ_ϕ Stoictiometic Composition

$\bar{\xi}$ Mean composition

ξ_m Composition of mixed fluid

Introduction

The two-dimensional turbulent shear layer has been the subject of investigation for many years, particularly the gas-phase layer with uniform freestream densities. This flow represents one of the simplest in which turbulent mixing occurs between two separate streams. Relatively simple boundary conditions and strong similarity properties combine to make this one of the more attractive flows to experimentalists, theorists and modelers.

Brown and Roshko (1971, 1974) performed a series of experiments in subsonic non-homogeneous layers in which they discovered the large-scale structure which spans the mixing region. They concluded that the dynamics of the mixing layer was governed by the evolution and interaction of these large structures, which prompted a renewed interest in analytic modelling from this fresh perspective. They also concluded that the large reductions in spreading rate found in compressible layers could not be attributed to density ratio effects, contrary to proposals entertained at the time. Based on directly measured concentration fields in shear layers at two freestream density ratios, Konrad (1976) concluded that the composition of the mixed fluid was strongly affected by the density ratio of the freestreams but that it did not vary within the mixing region as expected based on conventional gradient transport modeling. J. L. Brown (1978) investigated the inhomogeneous layer at two velocity and density ratios and concluded that the mixing layer was primarily sensitive to the velocity ratio and initial conditions. Breidenthal (1981) investigated a chemical reaction occuring in a liquid shear layer. He presented evidence that the amount of product formed was much less than that found in the gas-phase shear layer by Konrad. Breidenthal noted that

in all techniques which attempt to directly measure the composition field, any failure to resolve fully all the features of the flow field leads to an over-estimate for the amount of mixed fluid. He also noted that when the product of a chemical reaction is used to indicate mixing, the stringent requirements for resolution of the flow were avoided. Wallace (1981) investigated the product formed due to mixing and reaction for both density ratios studied by Konrad. By measuring the temperature rise for several values of the freestream reactant concentration, he found the mean composition of the mixed fluid to be in good agreement with Konrad for the uniform density case, but was unable to use the technique for the non-uniform density case.

There is another study which helped lay the ground work for the present investigation. Koochesfahani and Dimotakis (1986) measured the amount of reaction product in a liquid shear layer at flow conditions comparable to the uniform density case of Konrad and the difference between gas and liquid phase mixing was confirmed. Using the technique of laser induced fluorescence and measuring the result of chemical reactions, they argued that this difference indicated the importance of the Schmidt number ($\nu/\mathcal{D}$) as a parameter. This dependence countered fundamental assumptions in classical analyses of high Reynolds number flow, where the molecular transport coefficients are several orders of magnitude smaller than the effective turbulent transport coefficients. Of particular interest to this work, they also demonstrated how several quantities could be determined from reacting flow measurements as if directly measured with the requisite resolution. Specifically, they demonstrated that by using the molecular nature of chemical reactions and measuring only the mean value of the product concentration, an estimate for the amount of mixing can be derived which is conservative.

In 1982 a new facility was completed which permits the investigation of reacting, gas-phase shear flows. In this facility, several topics related to gas- phase mixing and reaction were investigated, *i.e.,* the low heat release study (Mungal and Dimotakis 1984), the study of heat release effects (Hermanson 1985, Hermanson *et al.* 1989), the study of Reynolds number effects (Mungal *et al.* 1985) and the investigation of Damköhler number effects (Mungal and Frieler 1988). In the same gas-phase facility used by Mungal and Hermanson, several aspects of mixing and reaction in a turbulent two-dimensional shear layer have been studied using experiments which react mixtures of H_2 , F_2 and NO in inert diluent gases. The present study has extended the range of topics to include the effects of freestream density ratio and has gone into considerable more depth on the subjects of the effects of Reynolds number and finite kinetics.

Chapter 1. Experimental Facility and Technique

Flow Apparatus

The apparatus used in these experiments was a blow-down facility designed by B. J. Cantwell, G. L. Brown, M. G. Mungal and P. E. Dimotakis and built by Dr. Godfrey Mungal and Mr. Earl Dahl. Details of the design considerations and construction can be found in Mungal (1983). The apparatus is similar to that designed by Wallace (1981) in Australia, but with a Reynolds number capability similar to that of the Brown-Roshko (1974) gas facility. Figure 1.1 shows the layout of the laboratory. The facility operates at atmospheric pressure in the test section and is capable of velocities of 80 m/sec for 3 sec with a 7.5 $cm \times$ 20 cm exit area.

By using a partial pressure technique, desired concentrations of F_2 and inert gases on one side and H_2 and inert gases on the other may be produced in a fixed mixing volume. The accuracy of this method has been estimated to be 3%. In practice, the largest uncertainty arose from this source or from uncertainty in the freestream ambient temperature ($\sim .5\,K$). Reproducibility is generally within this (3%) tolerance or better, and it is felt that this is a conservative estimate for the absolute accuracy of the temperature measurements. The charges of reactants and diluents are loaded into gas tight FEP Teflon bags within the reactant vessels ($0.6\,m^3$). At run time, the exterior of the bag is connected via a butterfly valve and a check valve to a large surge tank ($13\,m^3$) containing pressurized nitrogen. The surge tank provides the volume source necessary to collapse the Teflon bag and displace the reactant charge during a run, while maintaining a nearly constant

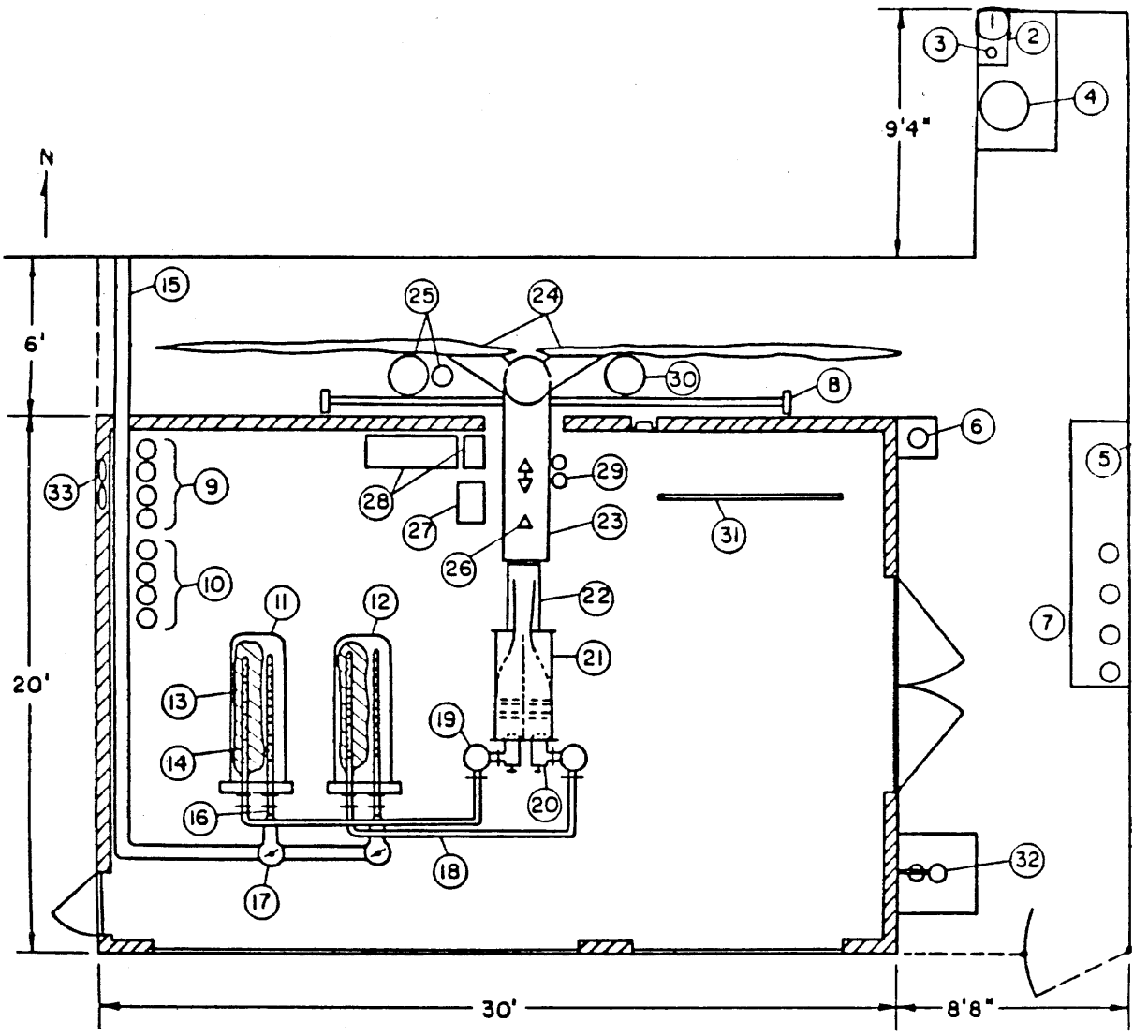

1. F_2 Cylinder
2. 1/8" Steel Barrier
3. HF Absorber
4. Charcoal Burn Barrel
5. H_2 Cylinder
6. NO Cylinder
7. N_2 Surge Tank
8. F_2 Mixing Vessel
9. Inert Gas Manifold H_2 Side
10. Inert Gas Manifold F_2 Side
11. F_2 Reactant Tank
12. H_2 Reactant Tank
13. Upstream Teflon Bag
14. Perforated Tube
15. 6" Line to Surge Tank
16. 3" Check Valve
17. 6" Butterfly Valve
18. 3" 304L SS Inlet Line
19. 3" Main Opening Valve
20. Sonic Metering Valve
21. Contraction Box
22. Test Section
23. Downstream Washing Duct
24. Teflon Exhaust Catch Bags
25. $NaOH$ Supply Tanks
26. $NaOH$ Showerheads
27. $NaOH$ High Pressure Pump
28. Vacuum Pumps
29. Exhaust Gas Scrubber
30. Exhaust Liquid Catch Tank
31. Control Panel
32. Safety Shower
33. 18" Ventilation Fan

Not Shown: Natural Ventilation System

Figure 1.1 Layout of GALCIT Reacting Shear Flow Lab.

upstream stagnation pressure. Downstream of the reactant tanks are fast-acting globe valves ($\sim$ 500 $msec$), which serve as the main opening valves and provide the means of starting and stopping the flow. Each gas stream is metered by a moveable stainless steel piston that controls the open area of a sonic throat. The throat consists of a set of 128 3 mm holes drilled in a spiral about an outer cylinder. Micrometers adjust the position of the piston and therefore the number of holes that are open or blocked. These holes remain choked during an experiment, which limits variations in the flow rates to the amount that the pressure in the surge tank changes during a run ($3-5\%$).

Each stream then enters a noise suppression section, which consists of a length of 20cm diameter stainless steel pipe containing aluminum perforated plate and a 2.5cm thick section of densely packed aluminum screen. Curved and flat stainless steel perforated plates are used to expand the flow from circular to rectangular sections at the settling chamber entrance. These elements are followed within the settling chamber, by screens of 40 and 80 mesh monel having 50% open area to provide flow uniformity. The interior of the contraction section is 30 cm high by 75 cm long by 20 cm wide. Three different contractions were used in the present experiments. Characteristics of each are shown in Table 1.1.

Table 1.1 : Contraction Section Specifications

Contraction

Exit	**Ratio**	$\mathbf{R_1}$	$\mathbf{R_2}$	x_{eff}	$\theta\,(cm)$	Re_θ
(cm)		(cm)	(cm)	(cm)	$(U = 22\ m/sec,\ N_2)$	
5.	6:1	80	40	4.6	.018	260
7.5	4:1	90	42	5.5	.019	285
10.	3:1	100	43	6.4	.021	305

Boundary layer parameters (x_{eff}, θ *and* Re_θ) were calculated using Thwaites method and conventional assumptions. The inlet boundary layer momentum thickness (θ) and Reynolds number (Re_θ) were calculated at the specified conditions. Calculation of inlet boundary layers for other flows may be made using

$$\theta = \sqrt{\frac{\nu\, x_{eff}}{U}}. \tag{1.1}$$

These contractions and flow management features produced good flow quality with a turbulence level measured for the $7.5\,cm$ contraction to be less than 1/3% RMS at $95\,m/sec$ in N_2, and about twice this value at $22\,m/sec$ (Mungal 1983, Mungal and Dimotakis 1984). Figure 1.2 shows a side view of the facility. Flow enters the test section from the contractions and the reactant streams meet at the splitter tip (included angle of $3.8°$). The total length of the test section is $75\,cm$. The length in which the flow can be studied is $50\,cm$, and all temperature measurements in this work were taken at a downstream position $x = 46.6\,cm$.

Pressure Gradient

The static pressure was measured at two points ($x = 5$ and $46\,cm$) on each sidewall and measured across a Barocel differential pressure sensor head (Datametrics, model 573). The signals were recorded on a strip chart during the run. These pressures were used to ensure that the freestream velocities were constant over the length of the test section. The upper and lower guide walls were hinged at the same downstream position as the end of the splitter plate. The walls could be converged or diverged to accommodate the growth, positive or negative, of the shear layers displacement thickness. It was straightforward to select the proper wall orientation for zero pressure gradient after a few initial runs at each condition. The required wall divergence differed with each density ratio, and varied

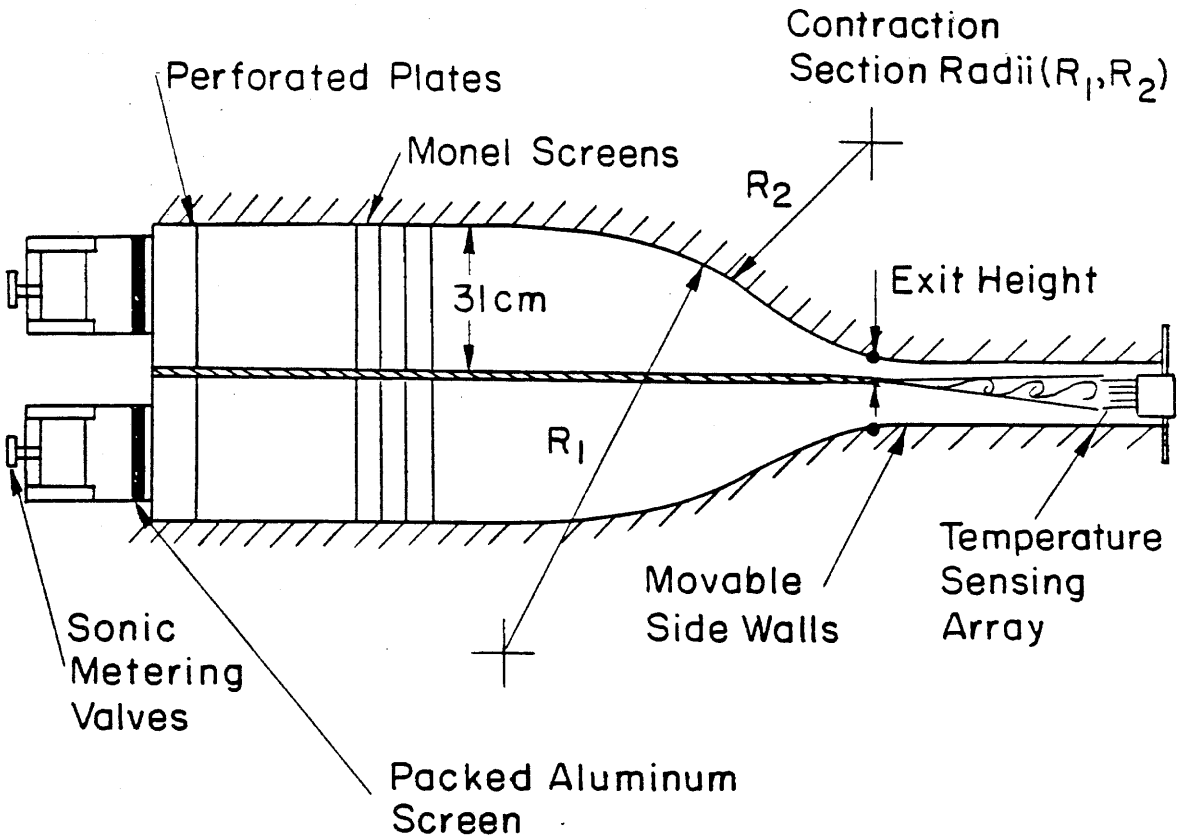

Figure 1.2 Side view of facility.

somewhat less with the amount of heat release and the flow velocity. Based on the measured static pressure gradient, the low-speed velocity varies by less than 1.5% along the length of the test section. For experiments with predominantly He on the low speed side this was more difficult to control, but variations were maintained below 5%. The reader may refer to Hermanson and Dimotakis (1989) for further details and discussion.

Schlieren Photography

A schlieren system designed and constructed by Hermanson (1985) was employed. Using a standard Z-fold configuration, the system collimates the

emission from a spark source ($4\,\mu sec$ duration) and passes it through the test section. In the equal density cases, the mixing region is made visible by the heat release due to reaction. Dilatation of the gas produces a non-uniform index of refraction field that distorts the beam. In the unequal density cases, this field is superimposed on the index differences of the diluent gases. The distorted beam is focused on a filter mask and then passed through an expanding telescope. The image was recorded by a synchronized, motor driven $35\,mm$ camera at the receiving end of the optics. An example of the results appears in Figure 1.3. Figure 1.4 is a schematic of the flow corresponding to the photo in Figure 1.3. Noted in the schematic are the splitter tip and the associated coordinate system used throughout the present work along with conceptual profiles of measured quantities at a downstream location.

Dynamic Pressure

The mean dynamic pressure was measured by a rake of 15 pitot probes located across the layer. The probes were made from $1.7\,mm$ diameter stainless steel tubing and were placed $7.5\,mm$ apart. The total pressures were referenced to the test section static pressure in a miniature manometer bank containing a fluorocarbon oil as the sensing liquid (Hooker Chemical, FS-5). The manometer bank consisted of 17 precision bore quartz tubes ($3\,mm$ ID) connected at their base to a common reservoir. The two outer tubes were connected to the test section static ports at $x = 36\,cm$ on each sidewall, while the fifteen inner tubes were connected to the pitot rake. Thus, any difference in height of the liquid between the outer and inner tubes corresponds to the mean dynamic head. The bank was photographed during a run by a motor driven camera. After the required settling time ($\sim 3\,sec$), several frames were selected from the series of photographs. Measurements of the fluid levels appearing in these photos were made on a HP9874

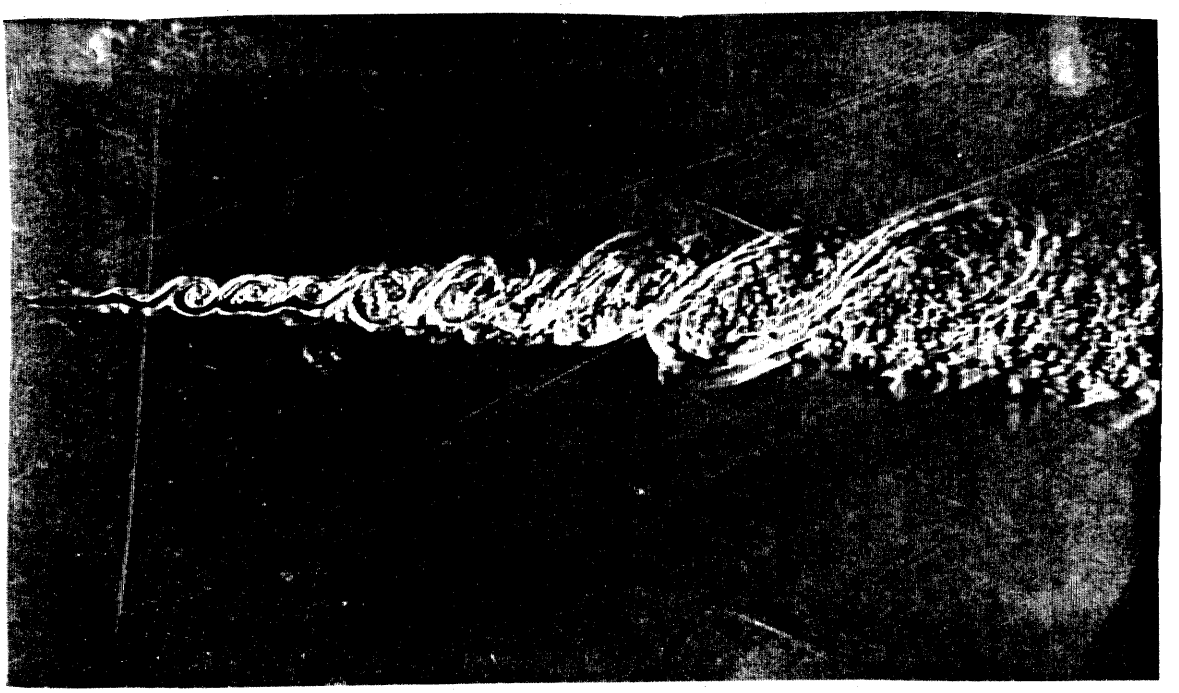

Figure 1.3 Schlieren photograph of $U_2 = .386\,U_1$, $\rho_2 = \rho_1$ layer.

digitizer and averaged. These were converted to a velocity profile using a measured mean density profile and neglecting correlations.

Temperature

The temperature was measured by a rake of 8 resistance thermometers. A temperature rake has been used previously by Fiedler (1974) and Rajagopalan and Antonia (1980) to investigate a mixing layer in which one stream is slightly heated. Results using this technique in the current facility have been previously reported by, *e.g.*, Mungal and Dimotakis (1984), Hermanson and Dimotakis (1989) and Frieler and Dimotakis (1988). Figure 1.5 shows a sketch of a typical sensor. The

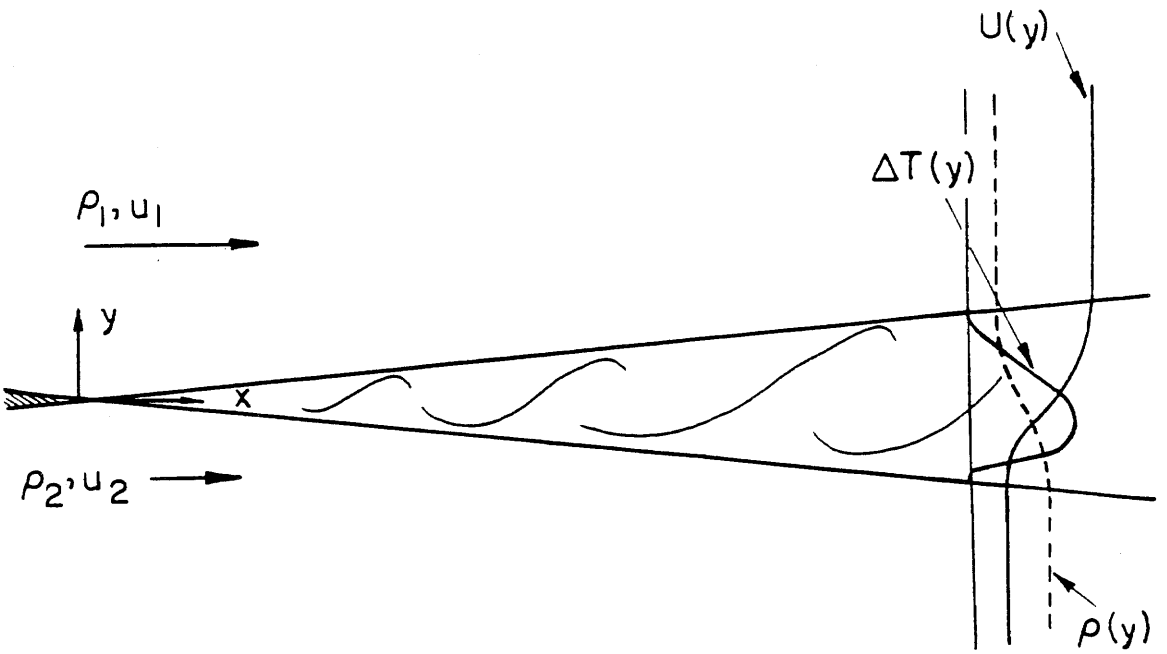

Figure 1.4 Schematic of the mixing layer.

construction consists of a fine wire sensing element (Pt/10%Rh) suspended across a pair of .3 mm inconel wires. These support wires are contained within a dual bore ceramic tube (Al_2O_3) surrounded by a 316 stainless steel outer sheath. The sensing element was welded to the supporting prongs, rather than soldered, to provide long term fluorine compatibility. The $2.5\,\mu m$ wires used in these experiments provided a theoretical response of roughly $3\,kHz$, for the nominal conditions of N_2 at $15\,m/sec$, with the measured response somewhat slower. Each wire is $1 - 1.5\,mm$ in length, for an aspect ratio of 500 and a typical resistance of $50\,\Omega$. The driving and amplification circuit provided $0.1\,mA$ constant current to each

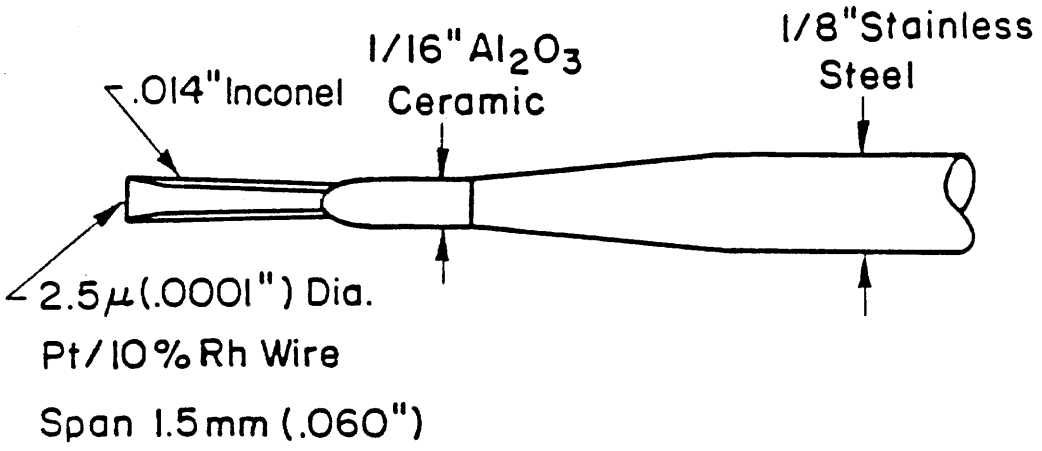

Figure 1.5 Cold wire probe.

wire. Changes in the voltage required to drive this current correspond to changes in wire resistance. Temperature may be obtained using this resistance to measure heating of the sensing element by the flow. Details of the probe response and compensation may be found in Appendix A.

The signal from each wire was amplified by a variable gain stage followed by a third-order lowpass Butterworth filter with the knee ($-3\,dB$ point) set at $16\,kHz$. All data was acquired with the portable HYDRA computer systems. Designed and assembled at GALCIT by P. E. Dimotakis and D. B. Lang, the systems were based on Digital Equipment Corporation LSI 11/23 or 11/73 CPUs. Data was

digitized with a Data Translation DT3362 12 bit, 32 channel A/D converter that has a maximum aggregate data rate of $250\,kHz$. The cold wires were sampled at between 8.5 and $30\,kHz$ each. The total number of data points taken in an experiment varied with the AD rate and the memory capabilities. For each experiment reported here, between 98,304 and 1,015,808 measurements were made. Data was processed on a μVax 3200 computer, another of the Hydra systems.

Calibration Procedures

The cold wire probes were calibrated before a run using a simple procedure. Two jets at different temperatures were directed at each probe and the output of the A/D converter recorded. Each jet contained a thermocouple junction embedded in its centerline, close to its exit plane, to provide an independent measure of the jet temperature. This was repeated four times each for the hot and cool jet. Over the narrow range of absolute temperatures encountered in these experiments, the output may be assumed linear with temperature. Therefore, the measurements were least squares fit and a calibration constant needed to convert A/D counts to temperature rise was determined.

Chapter 2. Initial Conditions

The effects of the initial conditions upon the $2D$ mixing layer have been examined by many investigators. This interest stemmed from the first conflicting measurements of spreading rate of the turbulent region, which were reported by the second investigator to make such a measurement. Liepmann and Laufer (1947) were among the first to make detailed measurements in a two-dimensional shear flow. Working in a half-jet issuing smoothly into quiescent fluid ($U_2/U_1 = 0$), they established the self-similarity of the turbulent flow and measured its growth rate. Wygnanski and Fiedler (1970) also studied the half-jet, but found the growth rate significantly greater. Speculation arose that some difference in the experimental apparatus might be the cause. Wygnanski's use of a trip wire in the inlet flow's boundary layer to initiate turbulent flow, a technique not used by Liepmann and Laufer, drew attention. Batt (1975) measured the growth rates for both tripped and untripped cases, finding $\sim 25\%$ increase in growth rate when tripped. Oster *et al.* (1976) reported similar experiments and confirmed this effect, although he found it to be smaller. However, Oster and others (*e.g.,* Browand and Latigo 1979, Weisbrot *et al.* 1982) have reported that for mixing layers at other velocity ratios, the effect of tripping was to decrease layer growth.

The dependences of the mixing layer upon initial and environmental conditions is a complex subject and will remain an active research area. These effects, in many cases, cannot be seperated from other parametric studies and complicate the analysis of the experimental data. However, this chapter is not an independent investigation of the subject. Observations of the effects upon the mixing layer made during experimental study of other topics will be discussed. For

additional information on this topic, the reader is referred to the works of Hill and Page (1969), Ho and Huerre (1984), Maslowe and Thompson (1971), Menon *et al.* (1984), Miau and Karlsson (1986), Michalke (1965), Oh and Bushnell (1976), Oster and Wygnanski (1982), Wygnanski and Petersen (1985), as well as other works referenced throughout this chapter.

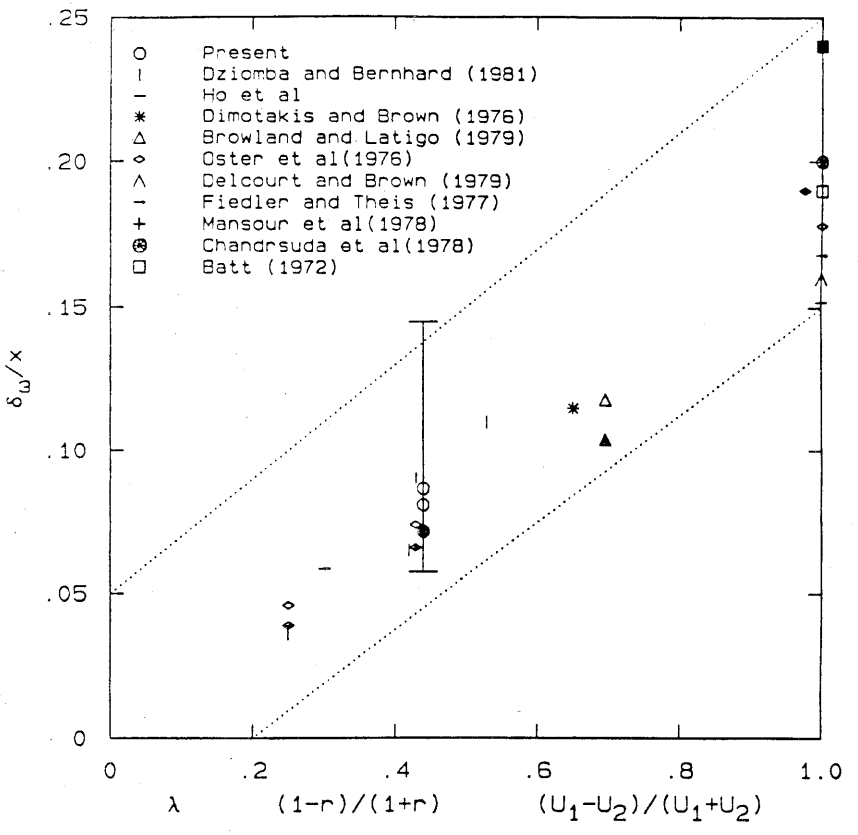

Figure 2.1 Accumulation of data for δ/x at $\rho_2 = \rho_1$.

Growth Rates Dependence on Velocity Ratio

An updated accumulation of data for the growth of the equal density shear layer as a function of the velocity ratio is shown in Figure 2.1. The area between the dotted lines represents the area occupied by data as gathered by Brown and

Roshko (1974) and previous works. Additions to this figure are indicated by the symbols and represent data published over the subsequent decade. The data shows that characterization of the mixing layer, seen here by the vorticity thickness (δ_ω), contains considerable uncertainty despite years of study. This is not an indictment of the various researchers. The wide range of values indicates the complexity of turbulence and is perhaps an indictment of the naive belief that the 2D mixing layer is a simple flow. Several works included in this figure, have data for both tripped or turbulent inlet boundary layers (indicated by filled symbols) and for laminar initial separation. The vertical bar represents the range of growth rates measured for the uniform density ($\rho_2/\rho_1 = 1$) shear layer in the present work. The circles were measured at the nominal Reynolds number ($Re_\delta \approx 6 \times 10^4$) with the remainder of the range occurring in experiments at other Reynolds numbers.

Growth Rates Dependence on Reynolds Number

In the present facility, at a fixed velocity ratio, the growth rate of the uniform density mixing layer depends strongly on the velocity. Shown in Figure 2.2 are the results from reacting flow experiments covering two decades of Reynolds number over which the growth rate decreased by 60%. The shaded symbols represent experiments for which an inlet boundary layer was tripped. The Reynolds number has been based on the local layer width (δ) at the measuring station $x = 46.6\ cm$, and is defined as $Re_\delta = \Delta U\, \delta/\nu$ where ΔU is the freestream velocity difference. The large range of growth rates in the current work, plotted in Figure 2.1 and 2.2, is disturbing. Scatter in the published data for uniform density is smaller at this velocity ratio than at either extreme. This is also in direct contrast with the results of Brown and Roshko (1974). Over a range of Reynolds numbers covering a factor of 4, no change in shear-layer growth was measured. Yet the values at

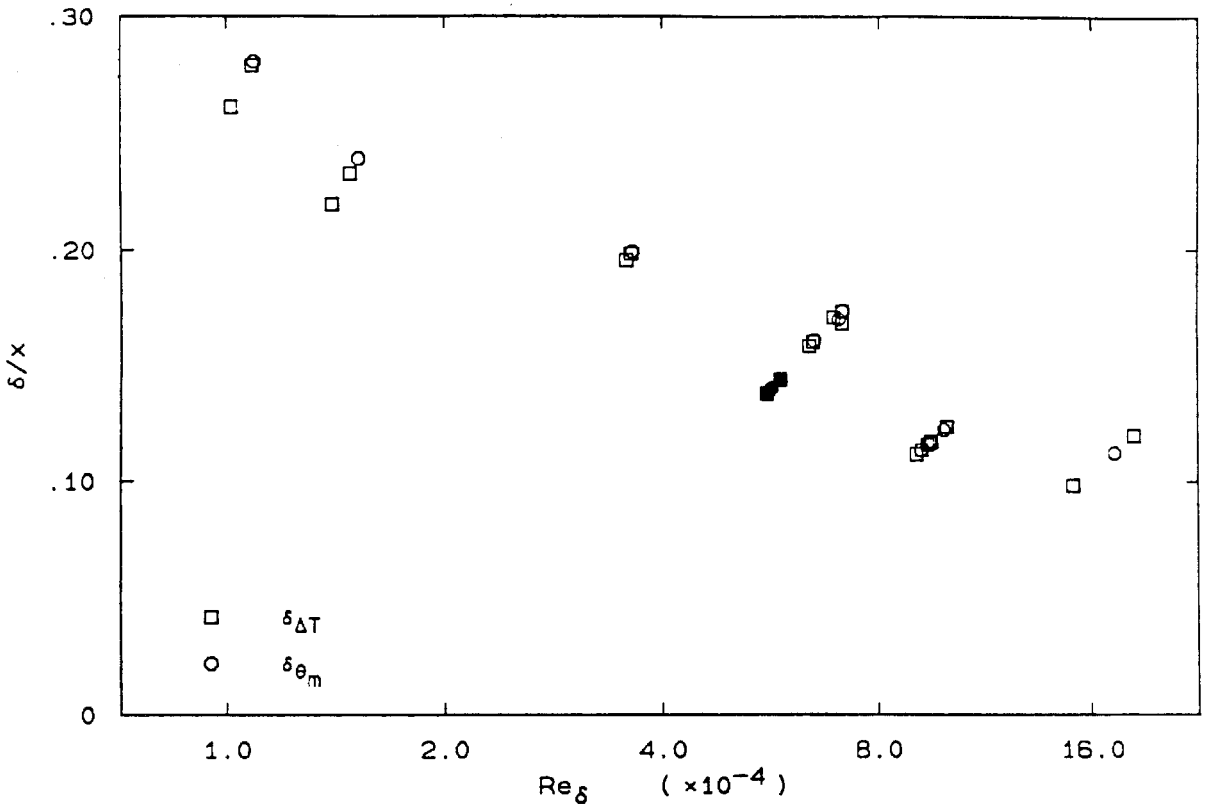

Figure 2.2 Mixing layer growth rate versus Reynolds number.

the nominal Reynolds numbers in the present work are in satisfactory agreement with previous results.

Despite the presentation of the data in Figure 2.2, it must be pointed out that a dependence upon the Reynolds number based on the layer width is not indicated. As noted by Dimotakis (1989), if the layer growth were to depend upon the local Reynolds number the edges of the mixing region would appear to curve. As shown in Figure 1.3 and documented in Mungal *et al.* (1984), the growth at each Reynolds number is linear with downstream distance. This suggests that if the proper correlation of this effect is with a Reynolds number , the relevant length scale must not be the local layer width.

Several authors (*e.g.*, Breidenthal 1979, Dziomba and Fiedler 1985) suggest that the momentum thickness at the trailing edge of the splitter tip is an important parameter in determining the character of the mixing layer downstream. The experiments reported by Brown and Roshko had a maximum inlet boundary layer Reynolds number of $Re_\theta \approx 30$, while for the nominal case in the present experimental apparatus, $Re_\theta \approx 300$. This order of magnitude difference number might explain the present works sensitivity, and Brown and Roshko's insensitivity to the Reynolds number. The mixing layers displayed in Figure 2.2 with $Re_\delta > 7 \times 10^4$ experience natural transition of the inlet boundary layers. The same mechanism which causes the tripped nominal case to grow more slowly may account for the 30% change in the growth rate measured for high Reynolds numbers, however, it will not account for the much greater growth observed at lower Reynolds numbers.

Acoustic Resonance

A phenomena has been reported which could account for abnormally high growth rates. The mixing-layer growth can be substantially altered if the layer is forced at particular frequencies. The forcing amplitude needed is small, and as observed by Roberts (1984), Ho and Huerre (1984) and others, increases in growth as large as a factor of two may result.

Figure 2.3 shows evidence for the existence of forcing in the current experiments. Plotted are the power spectral density of the temperature measurements for the same cases as in Figure 6.15. To accentuate differences in the spectra for the lower frequencies, these curves have been plotted with a linear vertical axis. Peaks agree with the measured value of the first longitudinal acoustic mode of the apparatus, with the fundamental near $12Hz$ in N_2. The height of these peaks appears to first decrease, then later increase as the velocity is increased.

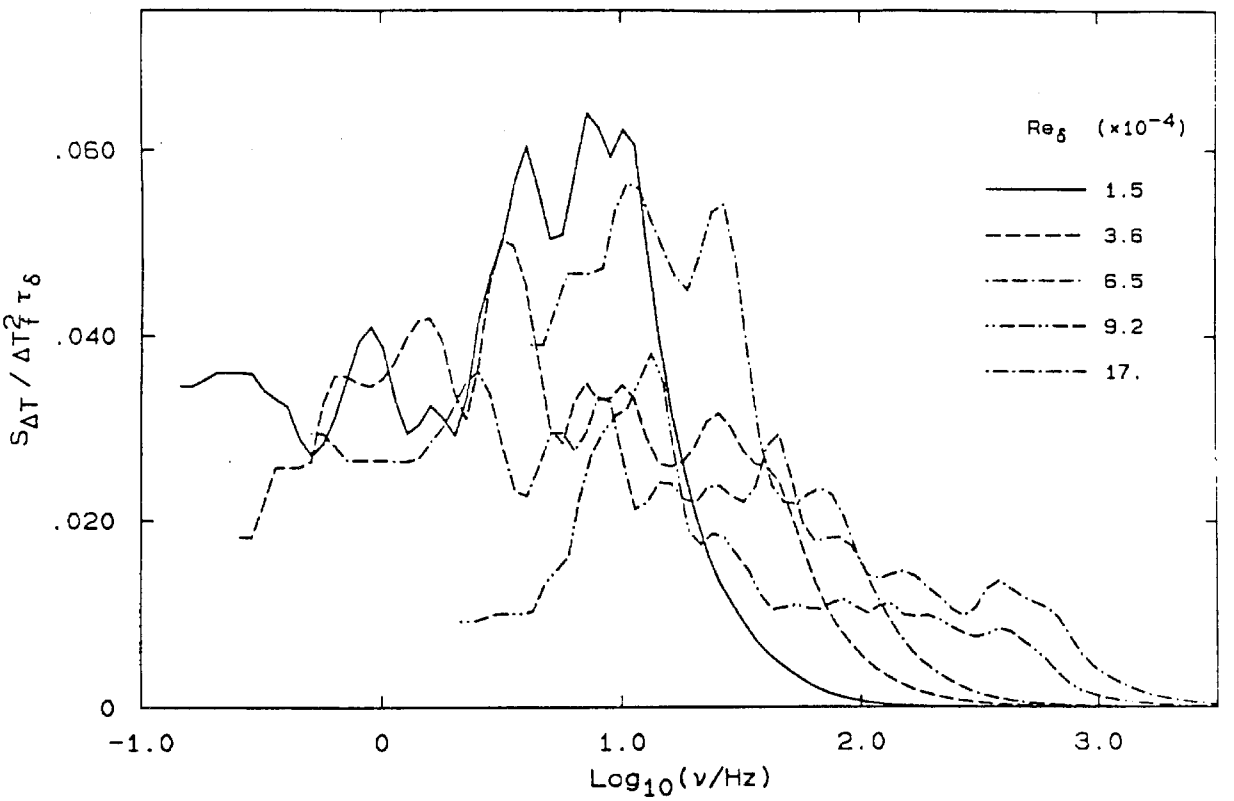

Figure 2.3 Power spectral density (PSD) for several Reynolds numbers.

This may be explained as follows. The large-structure passage frequency at the measuring station coincides with the duct resonance at a velocity corresponding to $Re_\delta \sim 10^4$. The shear layer is most sensitive to sub-harmonics of this passage frequency, therefore, the peak in "susceptibility" occurs for $Re_\delta \sim 2 \times 10^4$. As the velocity is raised, this resonance location moves downstream and out of the duct. Harmonics of the duct mode come into resonance, but have much lower initial amplitudes and are attenuated more by the apparatus. Therefore, the layer response is observed to decrease as the velocity is increased.

Two reasons exist for the reappearance of these peaks as the velocity is further increased. The amplitude of the acoustic modes in this facility are primarily determined by the initial forcing and the time over which the mode is attenuated

before data is taken. The initial amplitude is determined by the opening time of the fast acting valves ($\sim .5sec$) and the flow through the sonic metering valves. Since the flow increases directly in proportion to the velocity, the highest Reynolds number cases experienced the largest initial amplitude of acoustic disturbance. At the higher velocities, run times are shorter ($\sim 2sec$) which means less damping occurs. Note that although the peak in the PSD reappears, for these velocities the large-structure passage frequency is an order of magnitude higher than the duct mode and no increase in growth is observed.

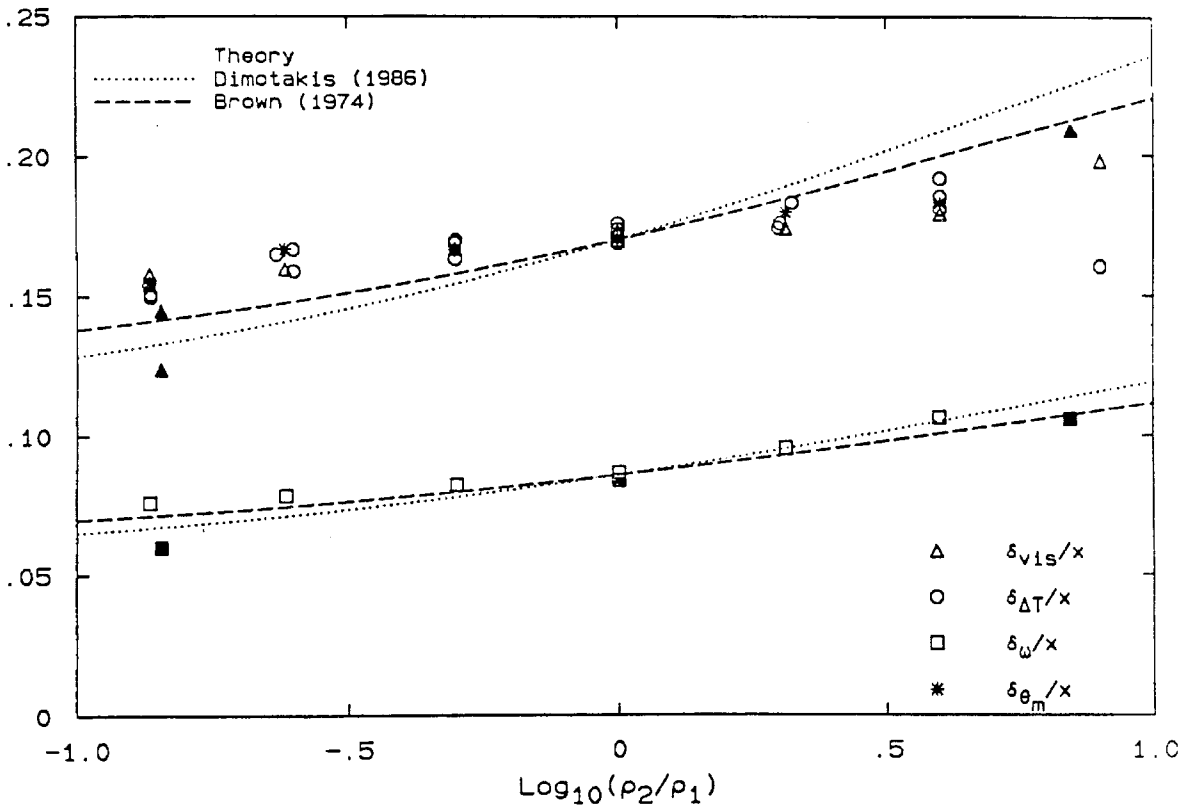

Figure 2.4 Mixing layer growth rate versus density ratio.

Growth Rates Dependence on Density Ratio

Figure 2.4 shows the measured growth rate for the present work as a function of density ratio. Several estimates using schlieren photos, dynamic pressure measurements and reacting flow temperature distributions are plotted and are in good agreement. The ratio of temperature and visual thicknesses to the velocity based estimate is nearly constant at $\delta_\omega/\delta_{vis} = 1/2$. Also shown as filled symbols are the results of measurements by Brown (1974), Brown and Roshko (1974), and Konrad (1976). Agreement between present and past work for the uniform density case is good. Note, however, the differences between present and past results at extreme density ratios. At low density ratios the present work has a growth rate 25% greater than Konrad. Ignoring the $\rho_2/\rho_1 = 8$ case, results in the current work follow a smooth dependence as the density ratio is varied. This suggests that the shear-layer growth's dependence on density ratio may be sensitive to some facility dependent parameter. Also in shown Figure 2.4 are theoretical predictions published by Dimotakis (1986), and Brown (1974). When plotted against a tenfold increase in the available data, the growth of the shear layer is clearly governed as much by the differences between facilities as by the density ratio. This conclusion is velocity ratio dependent, however. J. L. Brown (1978) observed that shear-layer growth was insensitive to the density ratio at $U_2/U_1 = .3$, but very sensitive at $U_2/U_1 = .6$. These findings indicate that experiments at several velocity ratios over a range of density ratios must be performed if either theory is to be verified.

The experiment at $\rho_2/\rho_1 = 8$ is unique, being the sole condition where the dynamic head in the low-speed stream exceeded that in the high-speed stream ($\rho_2 U_2^2/\rho_1 U_1^2 = 1.16$). Estimates for the visual and temperature profile widths differ markedly for this case. This has has been observed by others. Brown (1974) reported a measurable difference between the visual thickness and the

width of the density profiles for $\rho_2/\rho_1 = 7$. Note, that the present work's visual thickness matches Brown's. Wallace (1981) found differences between velocity and temperature profile widths for experiments at large density ratio. As mentioned previously, J. L. Brown (1978) also reported that the growth of a heterogeneous layer was significantly greater than the corresponding homogeneous layer. This was at a velocity ratio of $U_2/U_1 = .6$ and a density ratio of $\rho_2/\rho_1 = 4$, again yielding a larger dynamic head in the low-speed stream ($\rho_2 U_2^2/\rho_1 U_1^2 = 1.44$). He attributed this result to the greater momentum flux in the low-speed stream, therefore the greater deficit in the low-speed inlet boundary layer, arguing that the initial instability formation had been altered.

Our early experiments on the effects of tripping the inlet boundary layers in non-homogeneous mixing layers also produced contradictory results. For fixed velocities ($U_2/U_1 = .386$ and $U_1 = 44\, m/sec$) and several density ratios ($\rho_2/\rho_1 = 1/10,\ 1/3,\ 1, 3$), tripping either the high-speed or low-speed inlet boundary layer decreased the growth rate by 20%. However, when the ratio of the freestream densities was large ($\rho_2/\rho_1 = 10$), it was found that tripping either boundary layer *enhanced* the growth by $\approx 20\%$. The recurrence of this anomaly prompted a series of experiments and an analysis.

Initial conditions for experimental shear layers differ from the ideal conditions used in many modeling efforts. Specifically, a wake component within the velocity profile forms when the boundary layers from the two streams merge at the splitter tip. The importance of the wake in the near field flow has been reported by Miau and Karlsson (1986). In mixing layer experiments at Reynolds numbers of 4000-6000 and high velocity ratios ($U_2/U_1 > .5$), they describe a wake-like instability which enhances the development of the turbulent region by extracting additional energy from the mean flow.

Detailed in Koochesfahani and Frieler (1987), the combined wake and shear velocity profile gives rise to two modes of instability, rather than to the single Kelvin-Helmholz instability found in simpler hyperbolic tangent velocity profiles. These two families of solutions to the linearized inviscid stability problem are termed the "shear layer" mode and the "wake" mode based on the appearance of calculated streaklines. Note that this nomenclature does not imply that the wake mode is identical to the instability which would occur for the case of equal freestream velocities, and in particular, does not imply that the wake's far field growth characteristics are expected. Rather, the similarity with a wake is the formation of structures having vorticity of alternating sign. In Koochesfahani and Frieler the wake mode is shown to be recessive for most shear layers with low velocity ratio ($U_2/U_1 = .386$). However, when the density ratio is high enough and the interface between the two fluids is sufficiently distinct, conditions were found where the wake mode has a higher amplification rate. Schlieren photographs displaying fluid interfaces that closely resembled the calculated streaklines for each mode, confirmed their existance.

Using these concepts, a method of organizing the disparate observations of this chapter can be offered. The non-linear dynamics responsible for the growth of the shear layer may be envisioned as the simultaneous growth of several modes. These independent entities interact non-linearly in the turbulent mixing layer, and their growth is a form of competitive interference, one mode's growth inhibiting the others.

In the "normal" layer, the shear layer mode is dominant. Tripping the inlet boundary layers increases the wake component of the velocity profile. In cases where the initial Reynolds number of this wake is high enough, the momentum deficit will persist long enough so that a wake mode can amplify, perhaps

sufficiently to interfere with the growth of the normal or shear-layer mode. For flows where the dynamic pressure in the low-speed stream is greater than that in the high-speed stream ($\rho_2 U_2^2 \geq \rho_1 U_1^2$), the roles of the two modes are reversed. Tripping the inlet boundary layers again increases the wake, however, in this case the wake mode was already dominant, and the result is enhanced growth of the layer. The change in the large-scale structure suggested by the presence of an active wake mode, might also explain the change in corellation between visual and temperature thicknesses for large density ratios.

Observations by Batt (1975) and Oster *et al.* (1976), that the tripped $\lambda = 1$ layer grows faster, can also be reconciled. In this flow, no wake is possible. Tripping the boundary layer merely displaces the apparent position of the splitter tip, and also introduces turbulent motion into the layer. Since non-linear competition between a wake and shear-layer mode cannot occur, this additional motion is transformed into increased growth of the sole instability.

Summary

For the purposes of the remainder of this thesis, several conclusions must be drawn from this chapter. The growth of the mixing layer is not a function solely of the few variables under this experimenter's control. As a review, consider the results in Figure 2.2 again. Effects of forcing of the flow by the acoustic mode of the apparatus are seen for Reynolds numbers at or below 3×10^4. Natural transition of the high-speed boundary layer at the inlet occurs for Reynolds numbers greater than 7×10^4. Natural transition of the low-speed boundary layer at the inlet occurs for Reynolds numbers greater than 1.3×10^5. Therefore, all the results for the Reynolds number experiments are affected by some identifiable feature of the initial conditions. More importantly, effects caused by variation of some parameter under study are difficult to isolated from the effects of initial conditions. It can

be seen that if anything is to be learned about the mixing and reaction processes within the shear layer, some method of discounting the effects of initial conditions must be found. Results presented in subsequent chapters will be normalized by the width of the mixing region, in the hope that the primary effect of initial and environmental conditions upon the mixing layer is in the growth rate.

Many observations seem to be properly accounted for by the conjecture of competitive interference of multiple modes of instability. Still, it seems strange that an initial condition could have an effect on the shear layer that persists for so long. In the present experiments $x/\theta \sim 2500$, which implies that the layer has grown until $\delta/\theta \sim 400$. These effects are therefore observed where the layer has grown by orders of magnitude from the initial separation thickness. It is intuitively very compelling to insist on a unique "asymptotic" flow that will exist if one goes *far enough* downstream, however, the longevity of these effects calls this into question. While the philisophical aspects of this debate may be difficult to address experimentaly, is is clear that growth is affected over practical experimental scales, and therefore over scales of engineering interest.

The primary utility of the discussion above is the motivation it provides for several areas of research. For example, questions about the relationship between the solutions of linearized instability theory and the large-scale motions in the turbulent flow have been discussed for years and yet, to some extent, are unresolved. If such a connection is to be made, questions such as how a family of instabilities might interact to produce a single large-scale structure, must be addressed. Also of interest would be an analytical or numerical investigation of the non-linear interaction between two modes, under conditions where they have comparable amplification rates. In conjunction with this analysis, continued experimental work would be valuable, particularly on the persistence of the wake

mode into the far field. These are among the most interesting questions raised in the course of this work.

Chapter 3. The Effects of Heat Release

Several investigations in the past have dealt with heat release as a central topic. Wallace (1981) performed a series of experiments in subsonic mixing layers using pitot static pressure measurements and the Brown-Rebello (1972) concentration probe. Using the reaction of NO with O_3, he measured the temperature rise for several values of the freestream reactant concentrations. Despite the significant volume expansion incurred by the mixed fluid as the heat release increased, he found that the mixing region did not enlarge. Instead he found that the amount of fluid entrained and mixed in the shear layer decreased with increasing heat release, to such an extent that no expansion of the layer was observed. Hermanson and Dimotakis (1989) performed extensive experiments using measurements of the temperature field, spark and high-speed movie schlieren photography, and stagnation pressure. Their work covered a range of adiabatic flame temperatures $186 < \Delta T_f < 940K$ (a factor of four higher than Wallace) and confirmed the reduction of entrainment. Over this much larger range, they found that heat release caused a slight reduction in the growth of the turbulent mixing region. Using measurements of the mean density and velocity, they argued that the reduction in entrainment corresponded to a reduction in the turbulent shear stress and linked this effect to a decrease in the mean large structure spacing.

The data presented here cover the range of adiabatic flame temperatures $22 < \Delta T_f < 166K$. This range is equivalent to that of Wallace, and therefore much smaller than that of Hermanson and Dimotakis and other previous work on this topic (*i.e.*, Ganji and Sawyer 1980, Keller and Daily 1983, Pitz and Daily 1983, etc.). For this reason, results and discussion in this chapter will be brief,

consisting primarily of those necessary to quantify the effects that heat release has on the remainder of the work in this thesis. Also, a selection of results concerning the fluctuations of temperature within the mixing region will be discussed.

Background

The present work is concerned with mixing and reaction in gas-phase flows at low pressure and low heat release. A primary dynamic effect of heat release in this regime is the volume expansion or dilatation it induces in the fluid. The dilatation will be defined as the mean reduction of the number density within the layer, *i.e.*,

$$1 - \frac{\tilde{\delta}}{\delta} = \int_{-\infty}^{\infty} 1 - \frac{\overline{n}(y)}{n_\infty}\, dy \tag{3.1}$$

where δ is the layer width, and $\tilde{\delta}$ represents the mole thickness of the fluid in the layer. If the freestream densities are equal, this is equivalent to the expression used by Hermanson and Dimotakis for the mean reduction in density,

$$1 - \frac{\tilde{\delta}}{\delta} \rightarrow \frac{\overline{\Delta\rho}}{\rho_\infty} = \int_{-\infty}^{\infty} \frac{\rho_\infty - \overline{\rho}(y)}{\rho_\infty}\, dy \tag{3.2}$$

where the density in the freestreams is ρ_∞. The need for the generalization arises when density differences exist in the freestream, such as the work in Chapter 4. Dilatation is not the only effect of heat release, however, as molecular transport processes are temperature dependent. At the highest heat release in the present work, the Reynolds number based on the homogeneously mixed and reacted conditions drops by nearly a factor of two (from 65,000 to 37,000) through the temperature dependence of the kinematic viscosity. This has observable effects on the flow, as both Wallace and Hermanson noted a decrease in the amount of small-scale structure within the turbulent region as heat release increased.

At the same time, the diffusivity of each species increases as the heat release increases. This increase can be as large as 50% comparing cold flow to the homogeneously mixed conditions, and more than a factor of two at stoichiometric conditions. Since the present work measures the amount of mixing by measuring the result of chemical reactions, and chemical reactions occur only where reactants have interdiffused, this could clearly affect the amount of mixing. A separate experimental examination of these effects was not attempted in the present work. While the dilatation will be used to quantify the effects, it should be kept in mind that any of the three physical effects mentioned above might be responsible for a given observation.

Table 3.1 : Compositions for Heat Release Experiments

$\Delta T_f(K)$	Stream	Composition (%molar)*		
		H_2	F_2	NO
22.6	A	0.125		0.011
	B		2.0	
44.6	A	0.25		0.011
	B		4.0	
83.6	A	0.50		0.011
	B		4.0	
166	A	1.0		0.011
	B		8.0	

* Balance of composition in each stream is N_2.

Experiments

Experiments involving chemical reaction between mixtures of H_2 , NO and N_2 in one stream and F_2 and N_2 in the other stream have been performed. Table 3.1 contains the detailed composition of each stream. Measurements of temperature rise in these reacting flows have been made to examine the effect of heat release on several aspects of the mixed fluid state within the turbulent region. Experiment pairs were conducted, keeping the concentrations of the reactants fixed and interchanging the velocities in the two freestreams. For each experiment, the velocities were 22 m/sec in the high-speed stream and 8.5 m/sec in the low-speed stream. The contraction sections used for these experiments had an exit height of 7.5 cm on each side. Therefore, although the velocities were interchanged, the inlet boundary layers, acoustic background and distance of the mixing region from the guide walls were unchanged. Because of the extreme stoichiometry "flip" experiments (described in Koochesfahani *et al.* 1985 and in Appendix B), several quantities may be estimated which previous work was not able to address. Note that the experiments were not carried out at a uniform stoichiometry. To ensure that the chemical kinetics of the reacting flow were sufficiently fast, at the lowest values of the heat release it was necessary to run a large excess of F_2. Owing to safety considerations, however, very high concentrations of F_2 are undesirable. Therefore at higher flame temperatures, the stoichiometric mixture ratio was reduced. Although the mean dilatation in these experiments did not exceed 13% (*i.e.*, $\tilde{\delta} \sim .87\delta$), several quantities showed some evidence of change.

Mixing Layer Growth

Figure 3.1 shows the results of various techniques for determining the extent of the mixing region, plotted versus the mean dilatation of the flow. Note that all the quantities in this figure show a gradual decline with increasing dilatation. The

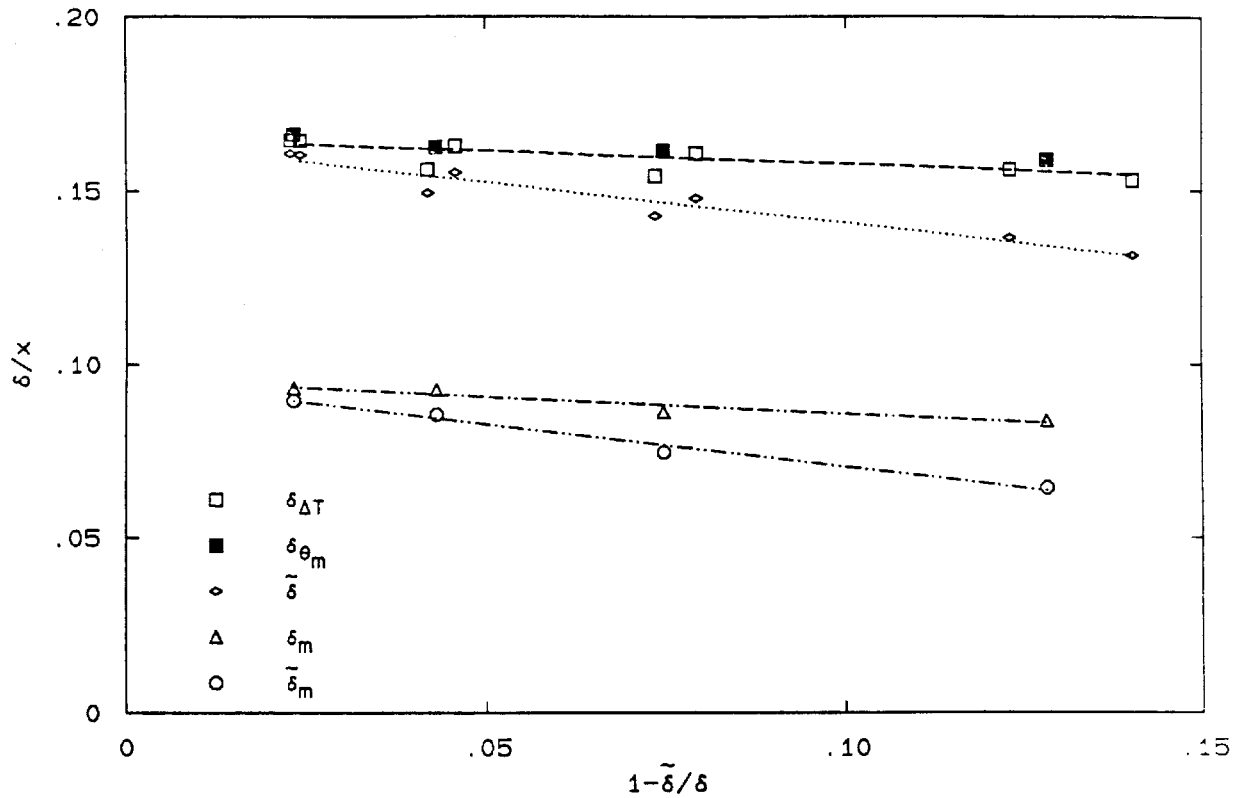

Figure 3.1 Mixing-layer growth versus dilatation.

edges of the temperature profile and of the mixed-fluid probability profile have been used to estimate the layer growth with the results labeled $\delta_{\Delta T}$ and δ_{θ_m}, respectively. Both decrease by $\sim 7\%$ over this range of dilatation, agreeing with the results of Hermanson and Dimotakis. The mixed-fluid probability thickness, in accord with the layer width, decreases 15%. Measures of the amount of fluid are more strongly effected. The mole thickness ($\tilde{\delta}$) decreases by 21%, indicating a decrease in the amount of fluid entrained by the layer. The mole thickness and the temperature distribution widths have a zero heat-release intercept of $\delta/x = .166$. The mixed-fluid thickness ($\tilde{\delta}_m$) decreases by 40%, a significant reduction in the

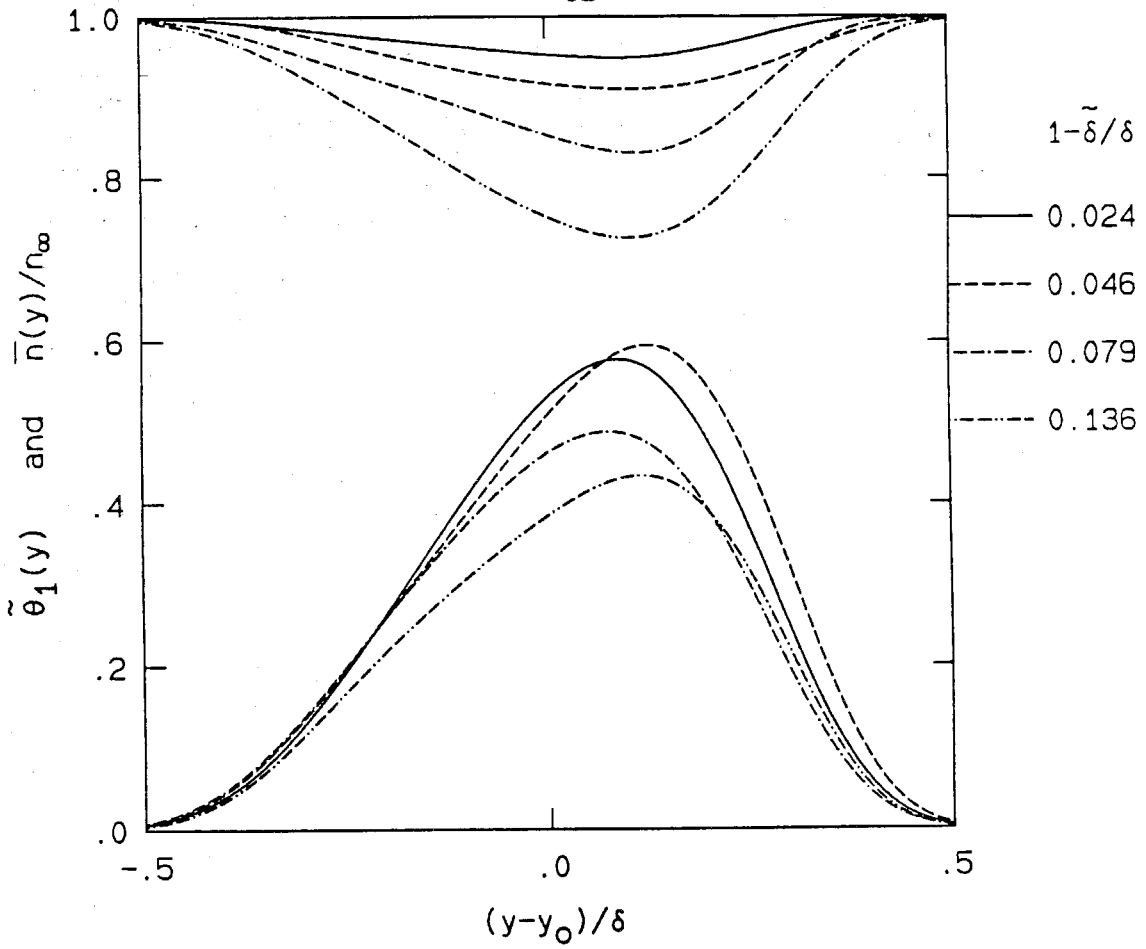

Figure 3.2 Mixed high-speed fluid and mean number density profiles.

amount of mixed fluid within the flow. The amount of mixed fluid and the volume fraction it occupies, have a zero heat-release value of $\delta/x = .097$.

Mixed Fluid Distributions

Figures 3.2 and 3.3 show, respectively, the mixed high-speed and low-speed fluid profiles for each of these flips. Also shown are the mean number density profiles for each experiment. As explained in Appendix B, these quantities can be estimated from the temperature time series measured by the thermistor probes. These estimates are fit (discussed in Appendix A) with a functional representation to obtain the curves shown here. As discussed in Chapter 2, the effects of initial

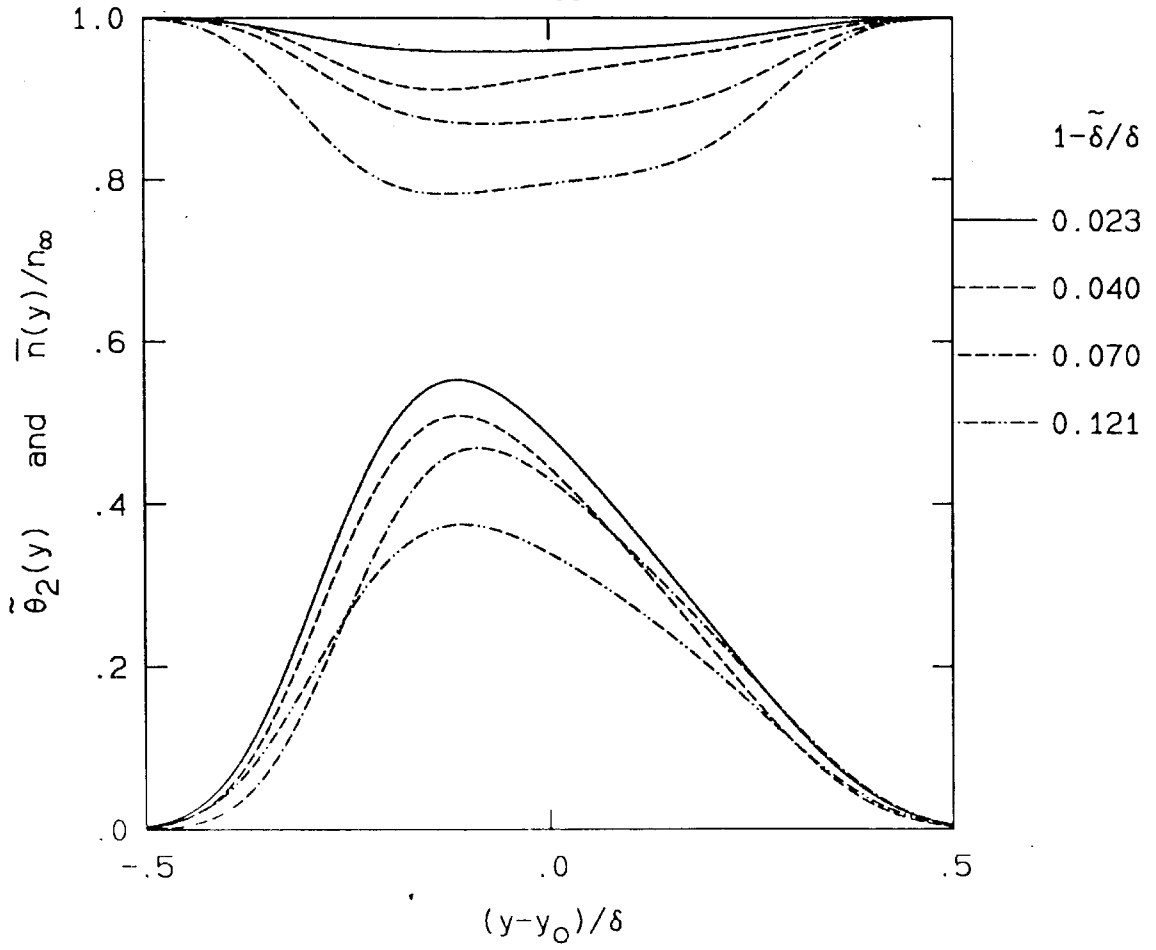

Figure 3.3 Mixed low-speed fluid and mean number density profiles.

conditions on the shear layer make comparison of data between facilities difficult. This investigation of mixing and reaction is primarily concerned with symmetry changes or peak heights which can best be displayed when variations in the shear-layer growth are removed by shifting and scaling the profiles. The width of the shear layer determined from the mixed-fluid probability profile serves here as a reference length scale, and will be labeled simply δ from this point on. No change in the symmetry of the distributions is observed, however the peak of the mixed-fluid profiles decreases with increasing heat release, consistent with the integral value plotted in Figure 3.1. Hermanson and Dimotakis (1989) concluded that when normalized by the mixing layer width, the profiles of normalized temperature rise,

did not change significantly. These two findings are not contradictory, as the former pertains to the number density of reaction product within the flow, while the later relates to the volume fraction occupied by that product. The section "Dilitation Considerations" in Appendix B discusses these issues in greater detail.

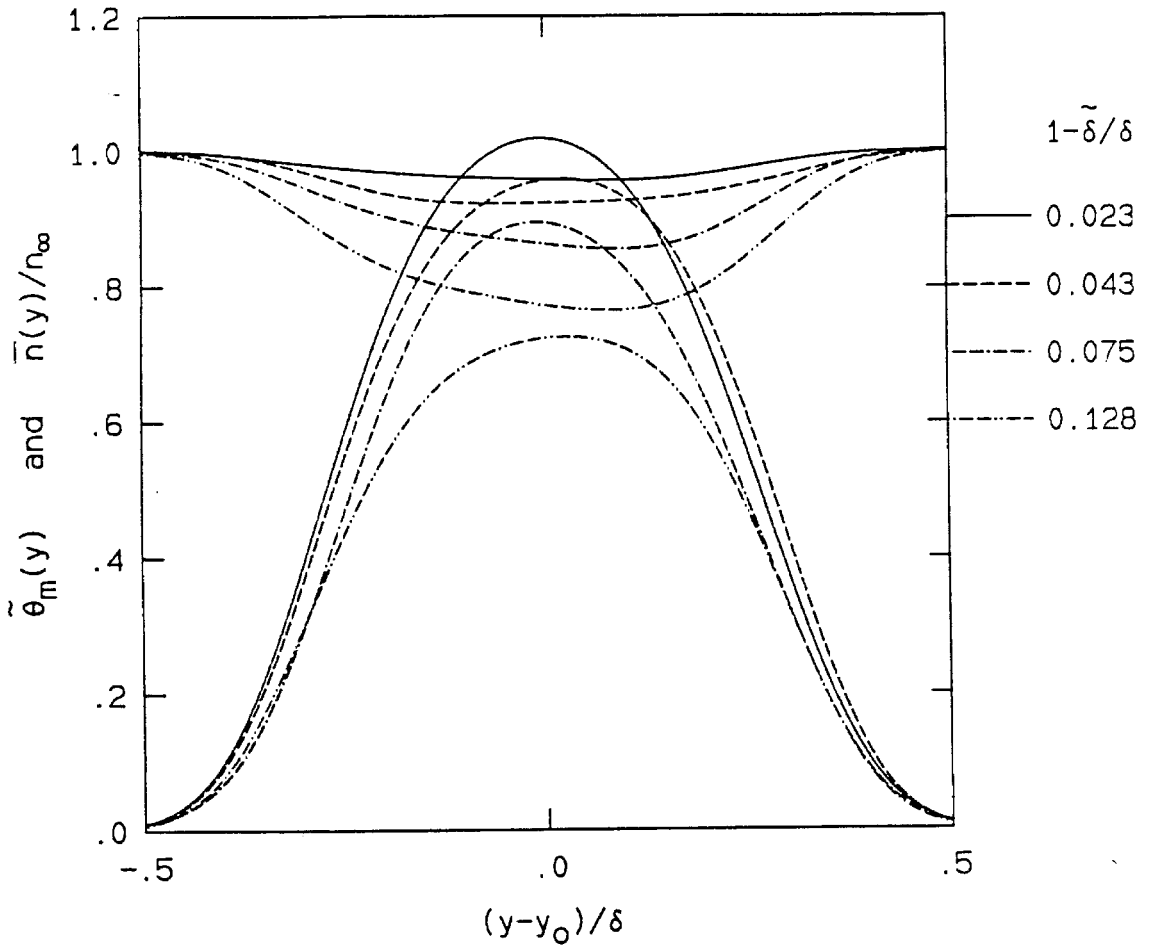

Figure 3.4 Mixed-fluid and mean number density profiles.

Figure 3.4 shows the result of adding the mixed-fluid profiles from the flip experiments. As with the individual mixed fluid profiles, these show no change in symmetry and a decrease in height as heat release increases. Note, however, the relationship between the peak value of the mixed fluid and the corresponding value of mean number density. For the three cases with the smallest dilatation,

the amount of mixed fluid exceeds the amount of fluid present, both mixed and unmixed.

The inference of mixing from measurements of temperature might account for this unphysical result if it appeared with increasing heat release. The analysis section (Appendix B) makes the assumption that the diagnostic (here temperature rise due to reaction) does not effect the distribution or amount of mixed fluid. This may not be true when the amount of heat release is large. Because the heat release is dependent on the stoichiometric mixture ratio, the effect on the distribution of mixed fluid would differ between the flip experiments. This implies that although δ_{p_i} measures the amount of mixed fluid, it is at a specific stoichiometric mixture ratio and dilatation (*i.e.*, $\delta_{p_i} \rightarrow \delta_{p_i}(\phi, \tilde{\delta}/\delta)$). Because the amount mixed from each freestream may depend on the stoichiometry, combining the results for δ_{p_1} and δ_{p_2} to estimate the total amount of mixed fluid is incorrect.

A possible mechanism for this dependence is the baroclinic production of vorticity, which could be argued to preferentially move hot fluid toward the middle of the mixing layer (see *e.g.*, Wallace 1981, McMurtry *et al.* 1985, Ghoniem *et al.* 1988, Hermanson and Dimotakis 1989). This would result in the profiles of mixed fluid from each stream (Figures 3.2 and 3.3) being shifted toward the center. When used to estimate total mixed fluid, the sum of these profiles could exceed the local number density, which is an absolute physical limit. However, this effect should be proportional to the dilatation and should therefore disappear as the heat release is decreased. Figure 3.4 clearly indicates that the opposite occurs.

It appears, as discussed in Chapter 5, that additional reactions are taking place that make proper normalization of temperature rise difficult. It is estimated that the error introduced in this analysis by the additional reactions, for example the overestimate of the amount of mixed fluid, is less than 10%. This is a smaller

effect than that of heat release and should depend little on the heat release itself. Therefore, absolute measures are only slightly affected, while trends and relative changes may be taken as quantitative. Discussion of these additional reactions is continued in Chapter 5.

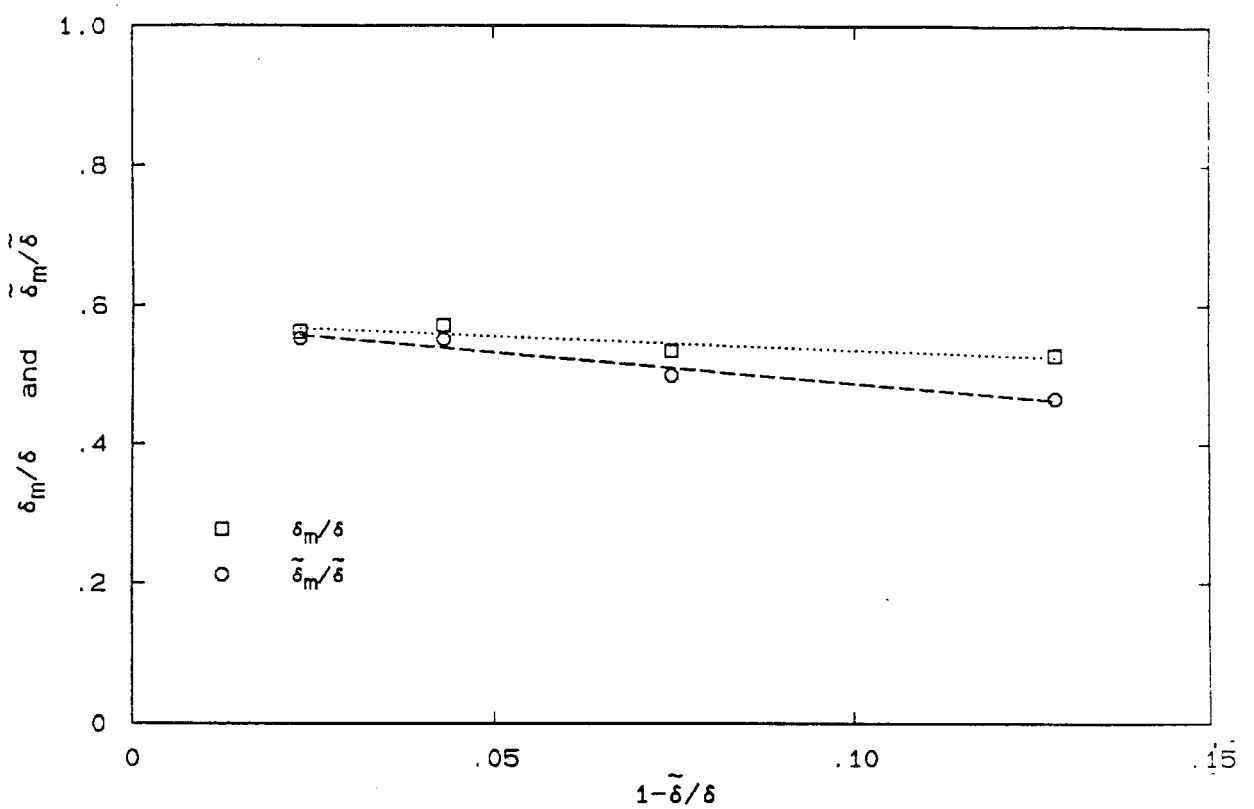

Figure 3.5 Mixed-fluid volume fraction and mixed-fluid mole fraction.

Figure 3.5 shows the mixed-fluid volume fraction (δ_m/δ) and mixed-fluid mole fraction ($\tilde{\delta}_m/\tilde{\delta}$) versus dilatation. This data shows that the amount of mixing occurring in the layer depends, albeit mildly, on the heat release in these experiments. The volume fraction occupied by mixed fluid decreases 10% and the mole fraction by 22% with a mean dilatation of only 15%. These two quantities share a zero heat-release intercept of .58. This data suggests that there is no critical

amount of heat release below which mixing is unaffected. The effects are seen for low flame temperatures ($\Delta T_f \sim 22K$) and appear linear with dilatation in this low heat-release range. However, these results support estimation of heat-release effects present in the remainder of this work. For the density ratio experiments of Chapter 4, whose dilatations were in the range .08-.10, estimates for the volume fraction of mixed fluid would be 5-8% low and estimates for the mixed-fluid mole fractions would be 10-15% low. For the Reynolds number experiments of Chapter 6, the dilatation was less than .05 and therefore all effects of heat release would be below 10%.

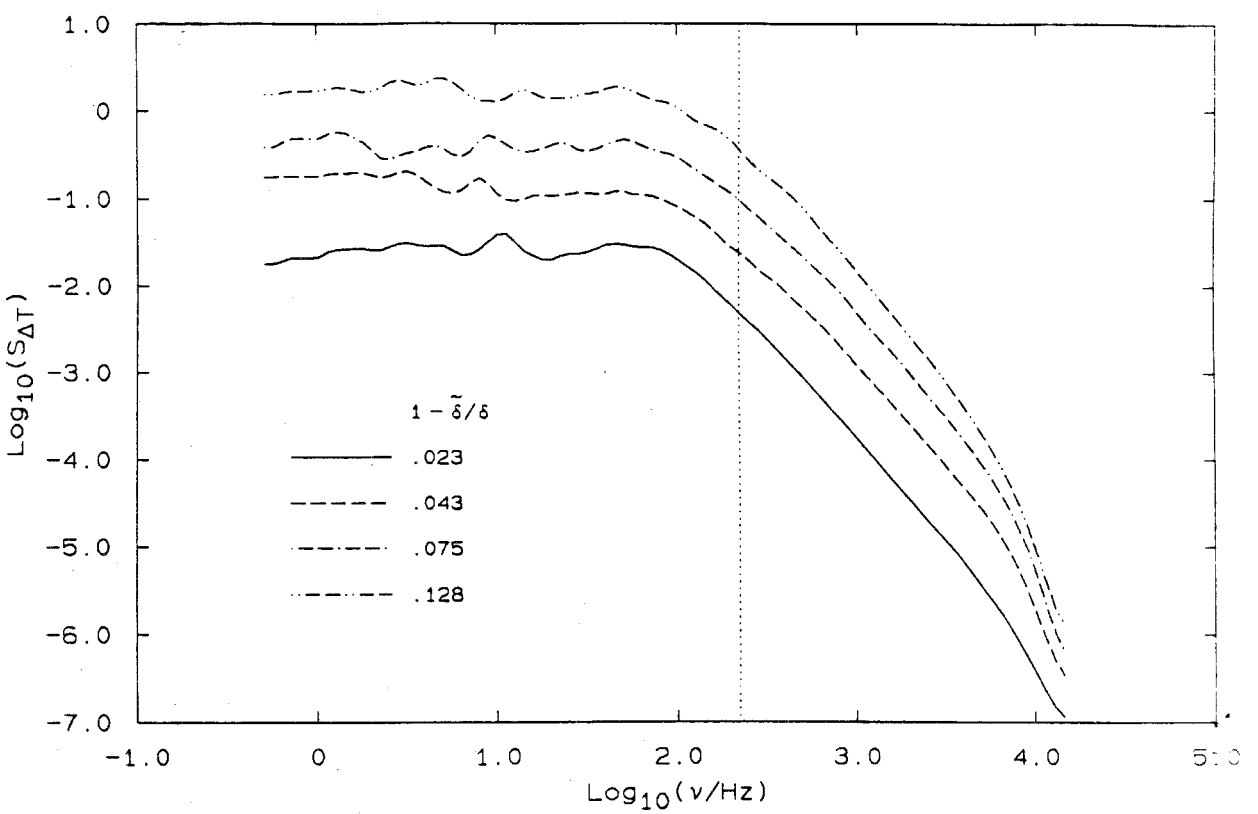

Figure 3.6 Power spectral density (PSD) of temperature fluctuations.

Autocorrelation and Spectra

To investigate the nature of the temperature fluctuations and perhaps their relation to the mixing phenomena discussed above, the power spectral densities (PSDs) of the temperature time-series were calculated. The program used to perform this analysis was developed by D.R. Dowling and details may be found in Dowling (1988) and Dowling and Dimotakis (1988). Individual probe temperature spectra depend on position in the layer, having a slightly greater high-frequency content on the high-speed side of the mixing region. If the spectra are integrated across the layer in an attempt to characterize the average spectra of the mixing region, Figure 3.6 results. In this plot, the probe response is near $\nu = 3kHz$, however, frequencies above this have been compensated for as described in Appendix A. It is important to note that no large frequency peaks appear in these spectra. The fundamental mode of the apparatus ($\sim 12Hz$ with N_2) is discernible in some spectra, but is small, indicating little acoustic forcing of this flow by the surrounding apparatus.

The large variation in absolute magnitude stems from the magnitude of the signal, determined by the adiabatic flame temperature. If the curves are normalized by the adiabatic flame temperature (ΔT_f) and the large-scale structure time,

$$\tau_\delta = \frac{\delta}{U_c} \tag{3.3}$$

good collapse is achieved. In this expression, the velocity U_c is the convection velocity of the large structures as given by Brown (1974) or Dimotakis (1986),

$$U_c = \frac{U_1 + s^{1/2}U_2}{1 + s^{1/2}} \tag{3.4}$$

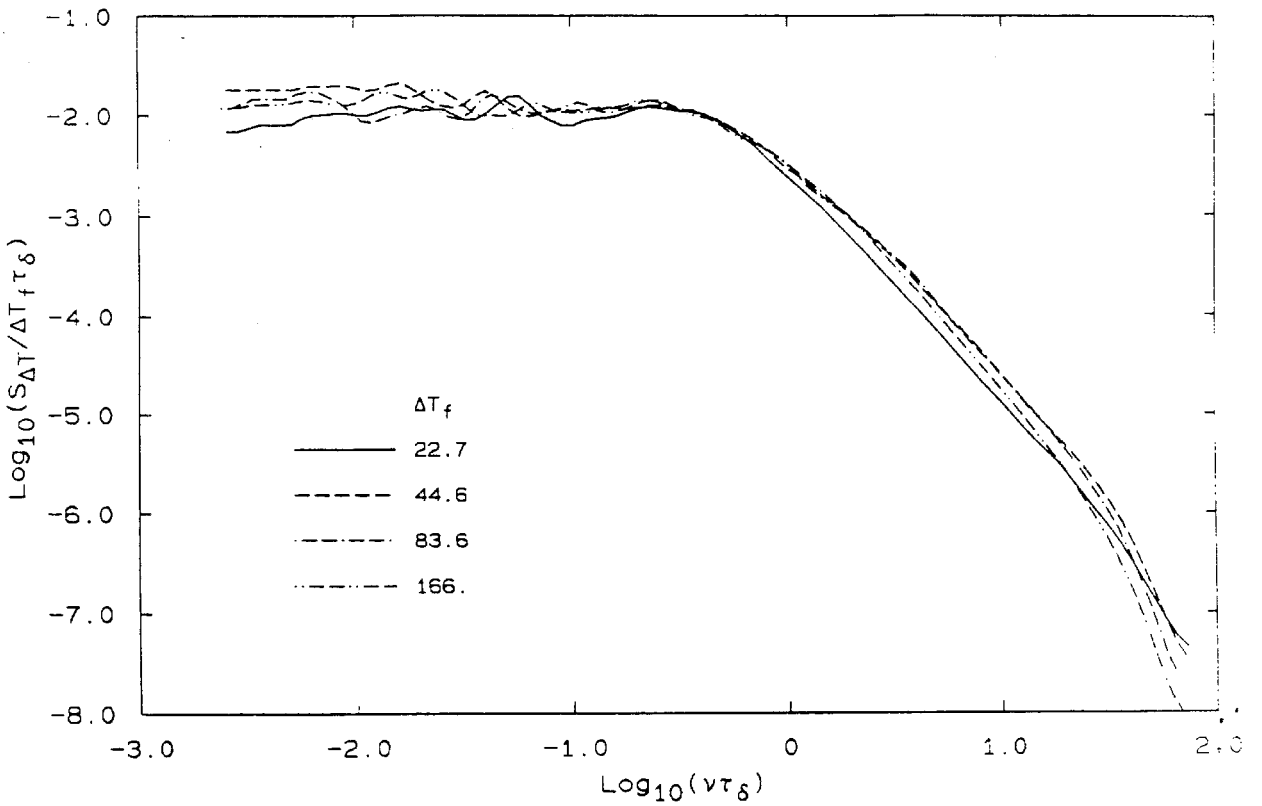

Figure 3.7 Normalized PSD for each flip.

where s is the density ratio in the freestreams ($s = \rho_2/\rho_1$).

Figure 3.7 shows the normalized PSD for each level of heat release. The spectra are uniform at low frequencies up to a break at roughly half τ_δ. This break is related to the spacing of the large-scale structure, implying that the inter-vortex distance $\ell \sim 2\delta$. Another interesting feature of the curves is the straight slope decay beyond this break, nearly two decades with a slope of ν^{-2}. Batt (1977) observed this power-law dependence for both the velocity and temperature fluctuation spectra in a reacting flow half-jet with Reynolds number based on the outer flow scales similar to the present work. Remarking that the turbulent Reynolds number based on the Liepmann-Laufer (1947) microscale and fluctuating data was low (~ 40), he concluded that the Kolmogorov power law for the inertial

subrange ($\nu^{-5/3}$) could not be expected. However, in the current work this power law persists to the highest Reynolds number investigated (see Chapter 6). It is possible that the global strain imposed by the velocity difference in the freestreams violates necessary conditions for the establishment of isotropic turbulence.

One might expect some evidence of the large-scale structure in these spectra and the absence of a peak corresponding to the large-scale structure frequency might be disturbing at first glance. However, the large-scale structure in the $2D$ mixing layer is an enigma. It eluded observation for decades, yet is now a conceptual driving force and plays a central role in much of the analysis and modeling efforts of turbulent shear flow. It is now observed by most investigators of the flow, primarily in photographs that freeze the structure and display the characteristic rollers. A notable example is the shear layer at the exit of a jet and the differences between this flow and the present plane shear apparatus provide a clue. Because the region approximating two-dimensional flow is the near field of the exit, measurements made in these mixing layers are at low values of x/θ, which adds to the coherence of the structures. In addition, a phase reference is provided by the fundamental jet mode downstream of the shear layer and phase-averaged measurements in this flow have been successful in capturing the large structure. While the jet exit flow provides this phase reference naturally, the design of the present two dimensional mixing apparatus intentionally minimized the phenomena that might provide one, such as acoustic disturbance. Conventional techniques of time-series analysis will not show the structure's presence unless it is phase coherent. If the phase is not fixed (*e.g.,* stochastically distributed), the large-scale structure *per se* may exist, while the peak in the PSD that corresponds to its time scale may vanish. This is demonstrated by the clear presence of large-scale structure in Figure 1.3, and its absence in the spectra.

For these reasons a different technique for examining the large structure was attempted that is unique to reacting flows. Since the result of mixing and reaction is the temperature rise sensed in these experiments, and that temperature rise is thought to reside primarily within the large structure, some technique based on the temperature measurements appeared promising. The first attempt was the autocorrelation of individual probe's time-series. This proved to be disappointing, with the scatter in the results larger than any trends. Following the technique successfully used by Dimotakis and Brown (1976) on velocity measurements, cross correlations of temperature measurements from two probes on opposite edges of the mixing region were calculated. The results displayed a few points of interest, such as evidence that the structure leans slightly forward on the high-speed side. However, the large-structure spacing could not be reliably determined. A different approach that makes use of a spatial integral was contrived. Defining the instantaneous temperature integral as

$$\mathcal{T}(t) \;=\; \int_{-\infty}^{\infty} \Delta T(y,t) - \overline{\Delta T}(y)\, dy \tag{3.5}$$

the standard autocorrelation of this instantaneous integral,

$$R_{ii}(\mathcal{T},\tau) \;=\; \frac{\displaystyle\int_{-\infty}^{\infty} \mathcal{T}(t)\,\mathcal{T}(t+\tau)\, dt}{\displaystyle\int_{-\infty}^{\infty} \mathcal{T}^2(t)\, dt} \tag{3.6}$$

is calculated. This measure is compelling, since conceptually, $\mathcal{T}$ should be high when a large structure is passing and low between structures.

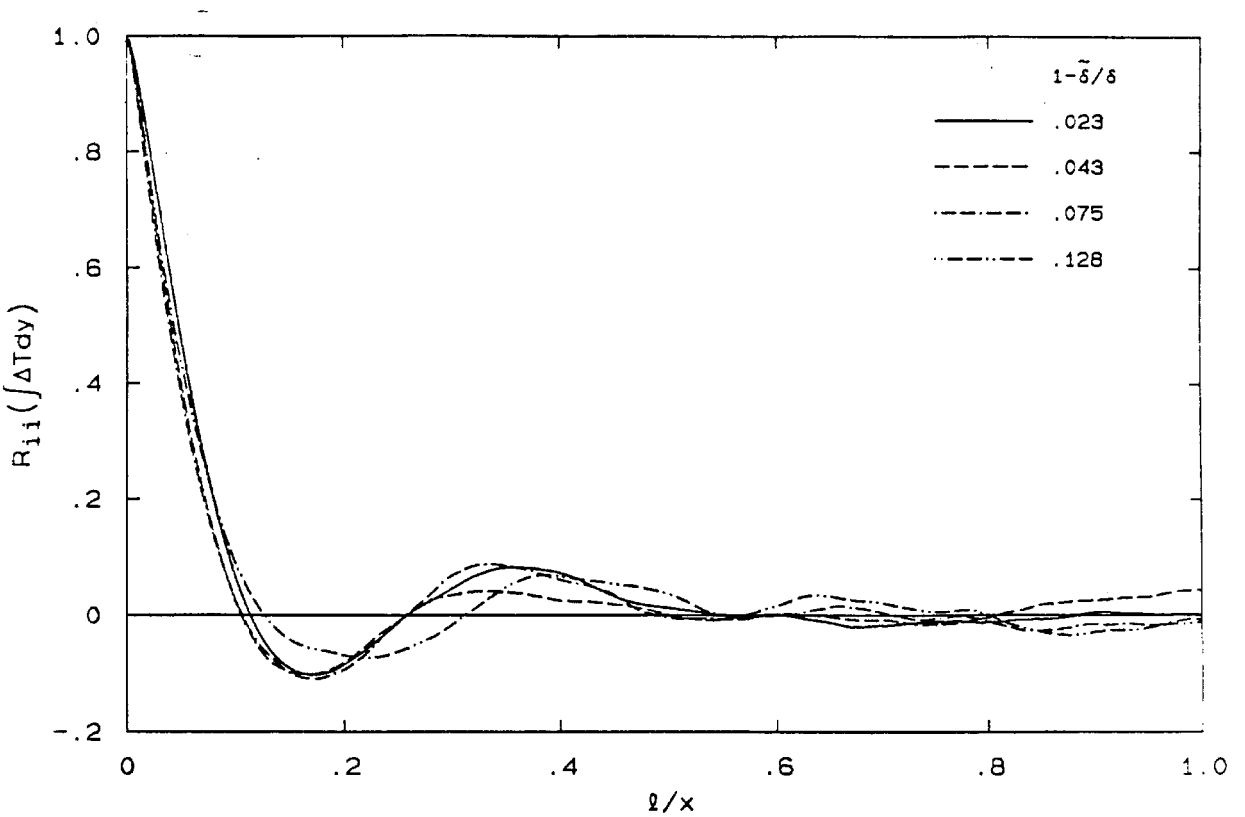

Figure 3.8 Autocorrelation of temperature integral (Re_δ =62,000).

This autocorrelation is shown in Figure 3.8 for each density ratios. The horizontal axis has been transformed to a spatial variable, ℓ , using the Taylor hypothesis,

$$\ell \sim U_c \tau \tag{3.7}$$

and normalized by the downstream position of the measuring station, x. Even in this measure of correlation, the long term memory or phase correlation of the shear layer is poor. The magnitude of both the first minimum and the second maximum is 11% or less for each value of heat release. Over scales comparable with the test

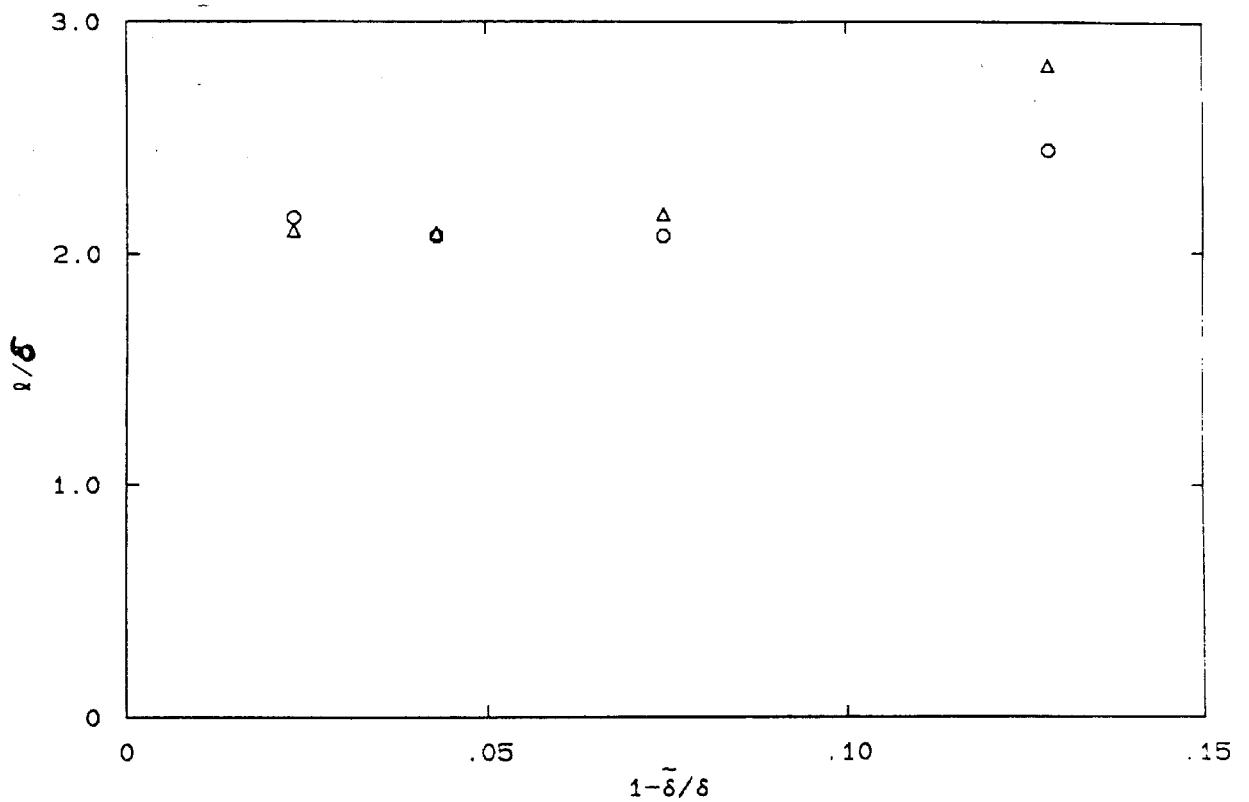

Figure 3.9 Large-structure spacing normalized by layer width.

section length, the correlation has dropped to less than 5% and decays rapidly after that.

The position of extrema in the autocorrelation can be used to measure the large-structure spacing. Plotted in Figure 3.9 is twice the distance to the first minimum (triangles), and the position of the second maximum (circles) normalized by the local layer width. The distance between these two estimates is a measure of the uncertainty in the technique. The value $\ell \sim 2\delta$ agrees well with the break in the PSD discussed above. If the data from Hermanson and Dimotakis (1989) in this facility is extrapolated to low heat release, the result is comparable. However, this value is somewhat greater than measured at higher heat releases, and considerably higher than measured by other previous work. For comparison with the values

plotted in Figure 3.10, Brown and Roshko (1974), Winant and Browand (1974), and Bernal (1981) all found that ℓ/δ was in the range $1.4 - 1.8$.

The apparent difference between results in this facility may be due to technique. Results from the work mention above were derived from flow visualization. Structure spacings measured from pictures are inherently conditionally sampled. Only when the structures are clearly visible, can a determination of their spacing be made. This systematically excludes the fraction of the time the structures are undergoing tearing, pairing or other ammalgomation processes. Determination of the spacing by the present technique makes use of the entire time-series, including the portions of time during which the large structure may not distinctly exist. Dimotakis and Brown (1976) and Koochesfahani *et al.* (1979) measured correlations in velocity fluctuations to estimate structure spacing for mixing layers with lower velocity ratios. Their results indicate $\ell \sim 2\delta$, which is comparable with the lowest three dilatation cases.

However, Hermanson and Dimotakis found that the large-structure spacing decreases as heat release increases while the highest value of the heat release in the present work shows an increase. A change in this quantity indicates either a change in the nature of the large-scale structure, or that the velocity at which it is convecting has changed. Because the pressure gradients were much less than the dynamic head in the low-speed stream, it is unlikely that the velocity of the large-structure is changing. Therefore, some change in the large-scale structure spacing is indicated. It may be that a transition occurs at or about 10% dilatation, and that below this value the large-structure spacing is a constant as indicated in Figure 3.9. Alternatively, this may an additional artifact of the technique differences. Note that no change in the large structure is indicated for values of dilatation lower than 0.1. Therfore, the change in layer structure indicated by the

data in Figure 3.9 does not affect the experiments reported in Chapters 4, 5 and 6.

Summary

Confirmation of the trends observed by Wallace (1981) and Hermanson and Dimotakis (1989) has been found over the modest range of heat release of $22 < \Delta T_f < 166K$. Declines in growth rate (δ/x) and entrainment are observed along with decreases in the probability of mixed fluid (δ_m). These all decrease by roughly 10%. The amount of mixed fluid decreases faster than the growth rate. Using estimates for the mixed-fluid mole thickness for the layer, the

amount of mixed fluid ($\tilde{\delta}_m$) decreases by 40%. The effects of heat release on results appearing in other chapters have been estimated, and they appear minor.

Spectra of the temperature fluctuations have been calculated and found to collapse nicely when normalized by the large-structure convection time and the adiabatic flame temperature. The spectra appear uniform at low frequencies and breaks at the large-structure passage frequency to a -2 slope. Heat release appears to have little effect on the large structure for values of the dilatation less that 0.1. Autocorrelation length scales indicate an inter-structure spacing slightly larger than twice the local layer width, which matches the knee frequency found in the PSD. Hints of change in the large structure exists at the highest heat release investigated were found for $1 - \tilde{\delta} > 10\%$, however, the evidence is not conclusive.

Chapter 4. The Effects of Freestream Density Ratio

The effects of freestream density ratio on the mixing and combustion in a high Reynolds number, subsonic, gas-phase, non-buoyant, two-dimensional turbulent mixing layer, have been investigated. Measurements of temperature rise in a reacting flow have been made which enable us to examine the effect of freestream density ratio on several aspects of the mixed fluid state within the turbulent region. In experiments with very high and very low stoichiometric mixture ratios ("flip" experiments), the heat release from an exothermic reaction serves as a quantitative label for molecularly mixed fluid originating in the lean reactant freestream. Properly normalized, the sum of the mean temperatures from the two flip experiments represents the probability of molecularly mixed fluid at any composition. The number density profile of the mixed fluid and the total number density can also be inferred from temperature measurements. Although the density ratio in these experiments was varied by a factor of thirty, profiles of these quantities show little variation, with integrals varying by less than 10%. This insensitivity differs from that of the composition of mixed fluid, which is very sensitive to the density ratio. While the profiles of composition exhibit some similarity of shape, the average composition of mixed fluid in the layer varies from 1 : 2 to 2 : 1 as the density ratio increases. The entrainment rates and ratios are calculated by several techniques. Agreement between techniques is good, however, the dependence of these quantities upon the density ratio does not match theory. In view of the compelling physical basis of the theory, the discrepancy suggests that the structure of the flow may change as the density ratio is varied.

Although it has been a subject of study in the past, there are several reasons why the present work focuses on the effects of freestream density ratio on the shear layer. As noted by Brown and Roshko (1974), this knowledge is a necessary precursor to the study of compressibility effects. The renewed interest in supersonic mixing and combustion, combined with the experimental difficulties of producing density matched supersonic shear flows has given a new impetus to the search for an understanding of the effects of the density ratio in these flows. However, this is not to imply that the only interest rests in the connection to compressible flows. In many important engineering applications the shear-layer geometry is used to mix reactants or to ignite premixed streams which release large amounts of heat. Optimization of combustion systems used in propulsion and energy "production" roles requires knowledge of the physical mechanisms involved. Again, a study of turbulent combustion with large heat release and therefore large density differences, is aided by, if not founded upon an understanding of density ratio effects.

Several investigations in the past have dealt directly with the subject of the present work. Brown and Roshko (1971, 1974) performed a series of experiments in subsonic non-homogeneous layers using pitot static pressure measurements and an aspirating probe (Brown and Rebollo 1972). Affirming the large-scale structure's presence and persistence, they suggested that the entrainment and mixing within the layer is governed by the dynamics of these structures. Contrary to proposals at the time, they also found that the large reductions in spreading rate found in compressible layers could not be attributed to density ratio effects. Based on the same technique for directly measuring concentration fields, Konrad (1976) investigated shear layers at two freestream density ratios and concluded that the composition of the mixed fluid was strongly affected by the density ratio of

the freestreams but that for each case it did not vary within the mixing region as expected based on conventional gradient transport modeling. Using both a concentration probe and a 2-component LDV system, J. L. Brown investigated mixing in the shear layer at two different velocity and density ratios. Noting that the mixing layer was very sensitive to initial conditions, he concluded that it was largely insensitive to density ratio. Wallace (1981) investigated the product formed due to mixing and reaction for both density ratios studied by Konrad. Using the reaction of NO with O_3 , he measured the temperature rise for several values of the freestream reactant concentrations. Significant discrepancies between his measurements and inferred profiles from Konrad were found when scaling the mixing layer with the measured vorticity thickness. Normalizing with the temperature profile width, he was able to reconcile his results with Konrad and found the composition of the mixed fluid to be in agreement with Konrad for the uniform density case.

Experiments involving chemical reaction between mixtures of hydrogen and inert gases in the high-speed stream and fluorine and inert gases in the low-speed stream have been performed. The apparatus allows the use of precise mixtures of gases which have significant density differences while keeping most other relevant quantities constant. The practical range of diluent gases allowed experiments to be carried out for the range of freestream density ratios $1/8 < \rho_2/\rho_1 < 8$, with the heat capacity of the mixtures carefully matched. Experiments were performed with the heat release maintained below the threshold suggested by Wallace (1981) and confirmed by Hermanson *et al.* (1985), (and Chapter 3) beyond which density changes resulting from heat release begin to affect the fluid mechanics of the turbulent shear layer. While the specific heats were matched in the two streams for a given experiment, no attempt was made to keep the adiabatic flame temperature

constant as the density ratio was varied. In hindsight, it might have been desirable to do so. However, noting that the actual effects of the small heat release used in these experiments depends not only on the flame temperature, but on the amount and composition of the mixed fluid as well, it would have been difficult to have adjusted the flame temperature *a priori*.

Based on an estimation technique described in Mungal and Frieler (1988) and refined in Dimotakis and Hall (1987), kinetic rates for these experiments were all more than a factor of two higher than rates at which product formation becomes mixing limited. Further experiments have uncovered that, for the uniform density case, significant dependence of the product formation on finite kinetic rates remains. Evidence of the effects of additional reaction has been found which depend on the particular stoichiometry. Since this effect hinges on the relative diffusivities of H_2 and NO, there is a strong possibility that this dependence will vary systematically with the density ratio in these experiments. This matter is covered in more detail in Chapter 5 and Appendix D. The analysis in this chapter will proceed under several assumptions which are not, therefore, rigorously correct. It is believed that the trends and qualitative aspects of the results are not in question, while the reader is cautioned that quantitative results must be used carefully. In particular, it appears that experiments performed with excess F_2 measurably overpredict the amount of mixed fluid, while those which are H_2 rich underpredict it. To first order, these two effects may counteract each other when the total amount of mixed fluid is estimated, but for estimates of ratios these errors will be additive. Note that the same physical processes that necessitate these qualifications are present in most reacting turbulent flows, and would be of even greater importance in hydrocarbon combustion. Also note that the raw data is not in question, only the inferences about mixing which are drawn from

them. If the modelor proposes to predict the mixing and reaction in the shear layer, with these specific concentrations of reactants in the freestreams, these are the temperature profiles which must be reproduced.

Measurements of temperature rise were made using a rake of eight resistance wire thermometers ($2.5\,\mu m$ dia.), as described in Chapter 1. Schlieren photographs of the mixing layer were taken to determine visual growth rates, and stagnation pressure measurements were made in order to estimate the velocity profile. The data presented here cover the range of density ratios $.136 < \rho_2/\rho_1 < 4$, which corresponds to a factor of 30 for that parameter. Table 4.1 contains the detailed composition of each stream for all flip experiment pairs for which results are presented here.

Table 4.1 : Composition for Density Ratio Experiments

			Composition (%)					
ρ_1/ρ_2	ϕ		H_2	F_2	N_2	Ar	He	NO
.136	1/8	HSS	4.		.9	95.		.1
		LSS		.5	4.5		95.	
	8	HSS	.5		3.5	96.		.01
		LSS		4.			96.	
.25	1/8	HSS	4.		17.	79.		.1
		LSS		.5	20.5		79.	
	8	HSS	.5		20.1	79.4		.01
		LSS		4.	16.6		79.4	
.5	1/8	HSS	4.		47.4	48.6		.1
		LSS		.5	50.9		48.6	
	8	HSS	.5		51.3	48.2		.01
		LSS		4.	47.8		48.2	
1.	1/8	HSS	4.		93.	3.		.1
		LSS		.5	96.5		3.	
	8	HSS	.5		98.	1.5		.01
		LSS		4.	94.5		1.5	
2.	1/8	HSS	4.		52.9		43.1	.1
		LSS		.5	56.4	43.1		
	8	HSS	.5		53.9		45.6	.01
		LSS		4.	50.4	45.6		
4.	1/8	HSS	4.		22.1		73.9	.1
		LSS		.5	25.6	73.9		
	8	HSS	.5		22.6		76.9	.01
		LSS		4.	19.1	76.9		

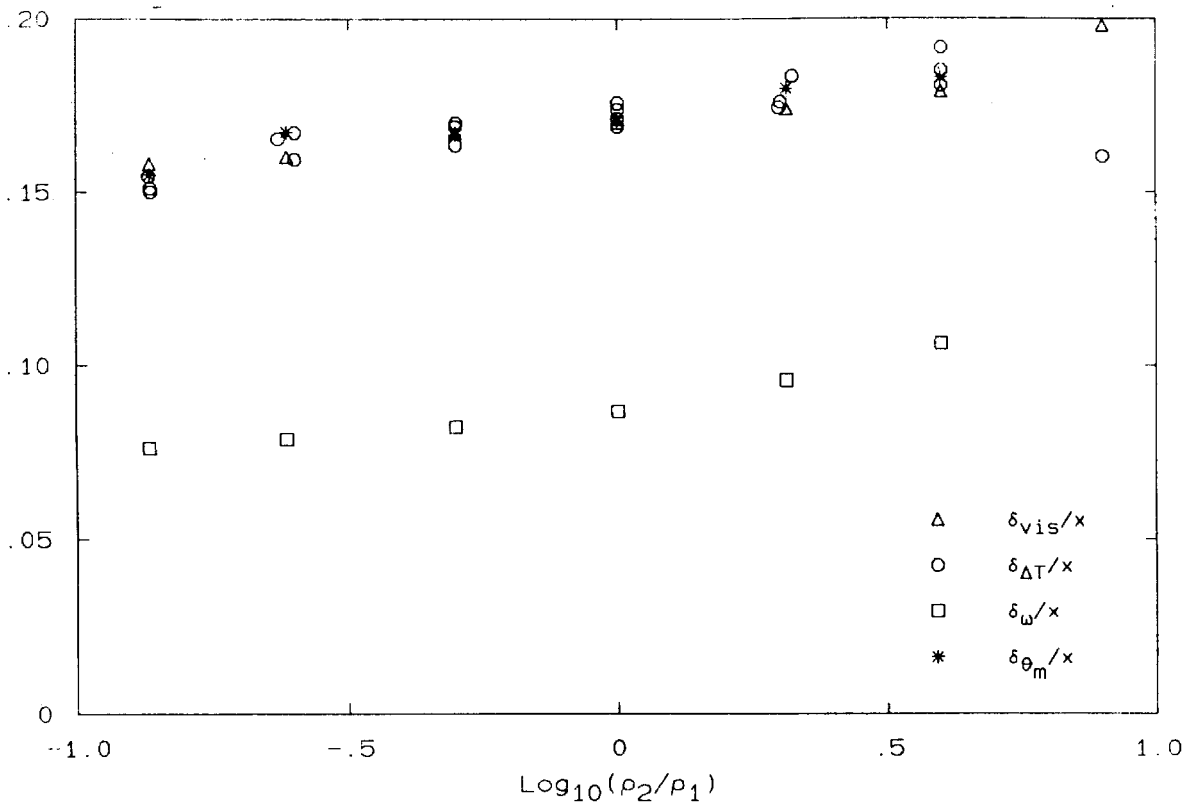

Figure 4.1 Mixing layer growth rates versus density ratio.

Figure 4.1 shows the results of various techniques for determining the extent of the mixing region, plotted versus the logarithm of the freestream density ratio. All of these estimates show a very small dependence, with the layer width changing less than 25% even though the density ratio has varied by a factor of 60. The visual thickness, δ_{vis} , is determined by fitting a straightedge to schlieren photographs. This is the same technique used by Brown and Roshko (1974) and Konrad (1976). In the equal density cases, the mixing region is made visible by the index of refraction difference induced by the slight heat release due to reaction. In the unequal density cases, this is superimposed on the index differences of the diluent gases. The edges of the temperature profile have also been used and the results are labeled $\delta_{\Delta T}$. This estimate was used by Mungal and Dimotakis (1985) and

found to correspond well with the visual thickness. As commented on in Chapter 2, the highest density ratio case ($\rho_2/\rho_1 = 8$) was an exception. Unfortunately, this is the experiment which could most directly be compared to the $\rho_2/\rho_1 = 7$ case of Konrad. Detailed in Koochesfahani and Frieler (1987), a new mode of instability is suspected to become important for large values of the density ratio. Although results for $\rho_2/\rho_1 = 4$ show only a hint of the effects, results for higher density ratios were sufficiently different that comparison with "normal" shear layers would be outside the scope of the present work. In several instances, data for this experiment will be included, but the reader is cautioned that the results must be interpreted carefully. Also shown in Figure 4.1 are the vorticity thicknesses for these experiments. Measurements of the stagnation pressure were used along with composition profiles obtained from the flip experiments in order to derive an estimate for the velocity profile. These in turn were used to estimate the mean fluxes and here, the vorticity thickness δ_ω . The factor of two between visual and vorticity thicknesses agrees with Konrad and the wealth of data for the equal density case. However, the ratio $\delta_\omega/\delta_{vis}$ does appear to depend mildly on the density ratio. Finally, the edges of the mixed-fluid profile were used to estimate the layer width. Labeled here δ_{θ_m} , this width is the distance between the 1% points of the distribution of mixed fluid determined from the flip. As can be seen, the agreement with the other methods is acceptable and the uncertainty in specifying the layer width can be conservatively estimated from the scatter in this plot to be $\sim 5\%$.

Throughout this chapter, the thickness determined from the mixed-fluid profile (δ_{θ_m}) will serve as a reference length scale whenever available, and will be labeled simply δ from this point on.

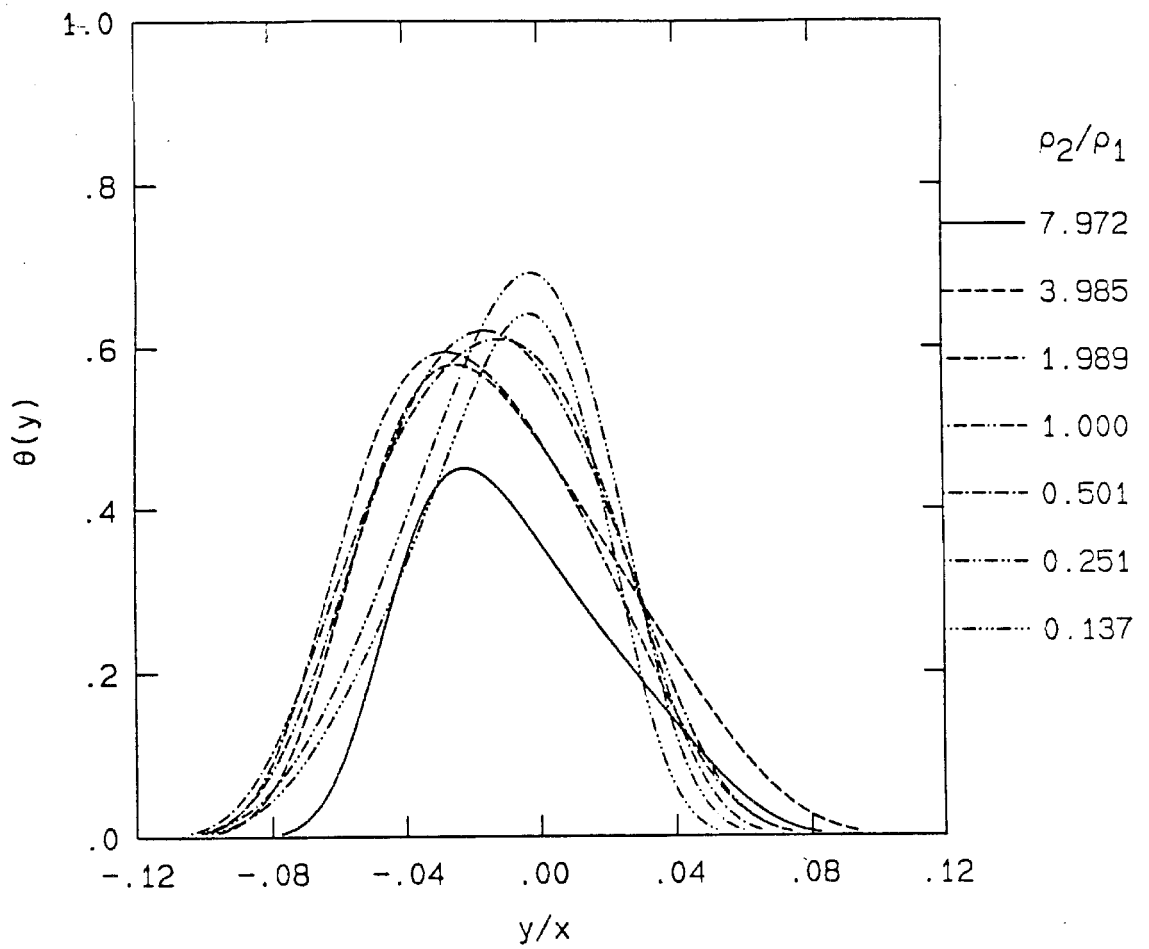

Figure 4.2 Normalized temperature profiles for $\phi = 1$.

Product Probability Distributions

Figure 4.2 shows the normalized temperature profiles, $\theta(y)$, defined by Equation $B.3$ for each density ratio at a stoichiometric mixture ratio of $\phi = 1$. The horizontal axis is the transverse dimension in the layer normalized by the downstream position of the measuring station x. There are several features of interest in this and the subsequent three figures which may be observed. First, the temperature rise distribution is found to move towards the high-density stream as the density ratio increases. Second, the profile symmetry, which is skewed toward

the high-speed side at low density ratios, shifts toward the low-speed side as the density ratio increases. A shift in the horizontal axis about, for example, the dividing streamline would make this symmetry change more apparent. Such a shift would at the same time obscure the movement in absolute position of the mixing region and therefore was not performed for this and the subsequent two figures. Finally, note the dependence of the peak of these profiles upon the density ratio. Neglecting the $\rho_2/\rho_1 = 8$ case, the peak temperature decreases slightly as density ratio increases until about $\rho_2/\rho_1 = 1/2$, where it becomes nearly constant.

Figures 4.3 and 4.4 show, respectively, the probability profiles of mixed high-speed and low-speed fluids. While the shifts in profile locations are the same as in Figure 4.2, note the differences in the symmetry and peak value trends. The probability of mixed high-speed fluid profiles start substantially skewed toward the high-speed side and become more symmetric as the density ratio increases. Also the peak probability increases dramatically as the density ratio increases. These trends are uniformly reversed for the probability of mixed low-speed fluid. The probability of mixed low-speed fluid profiles start more or less symmetric, and become more skewed toward the low-speed side, and the peak probability decreases as the density ratio increases. These profiles suggest a limiting process in which the profiles of mixed low-density fluid become completely symmetric and the probability of mixed high-density fluid decreases to zero as the density ratio tends toward the extremes.

Figure 4.5 shows the result of adding the reduced temperatures from the flip experiments for the six density ratios. Plotted are profiles of the mixed-fluid probability, $\theta_m(y)$, versus position within the mixing region normalized by the downstream position x. These profiles represent the local probability of

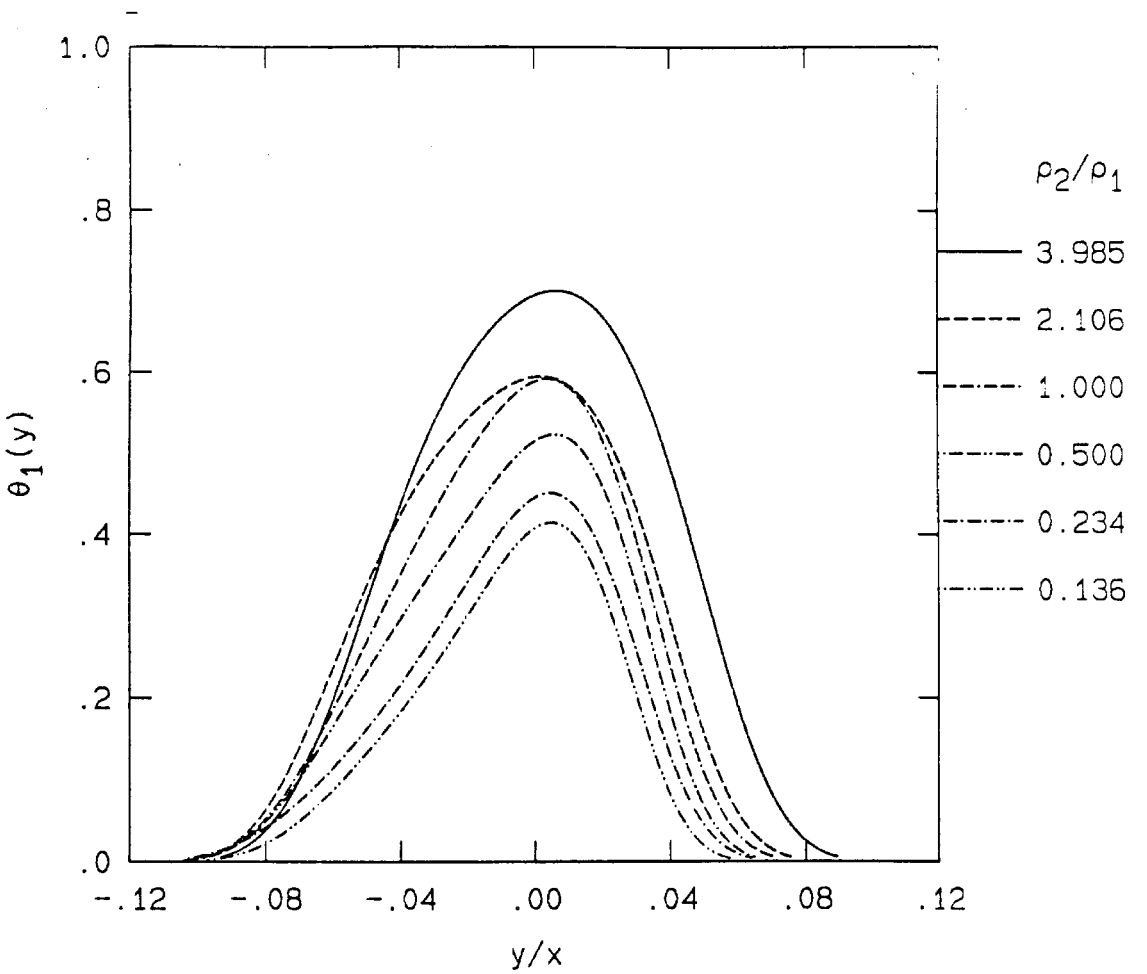

Figure 4.3 Mixed high-speed fluid probability profiles.

mixed fluid at any composition, and are in agreement with Konrad's intermittency profiles once the growth rate differences are discounted. This includes the uniform density case in each study and a comparison of the present $\rho_2/\rho_1 = 4$ case with Konrad's $\rho_2/\rho_1 = 7$ case. Since his definition of intermittency was the fraction of the time that he observed mixed fluid, this should not be too surprising. This detail of nomenclature aside, we find that for all density ratios the probability of finding unmixed fluid in the center of the layer is low, in agreement with his measurements. This is contrary to the liquid shear layer result (Koochesfahani

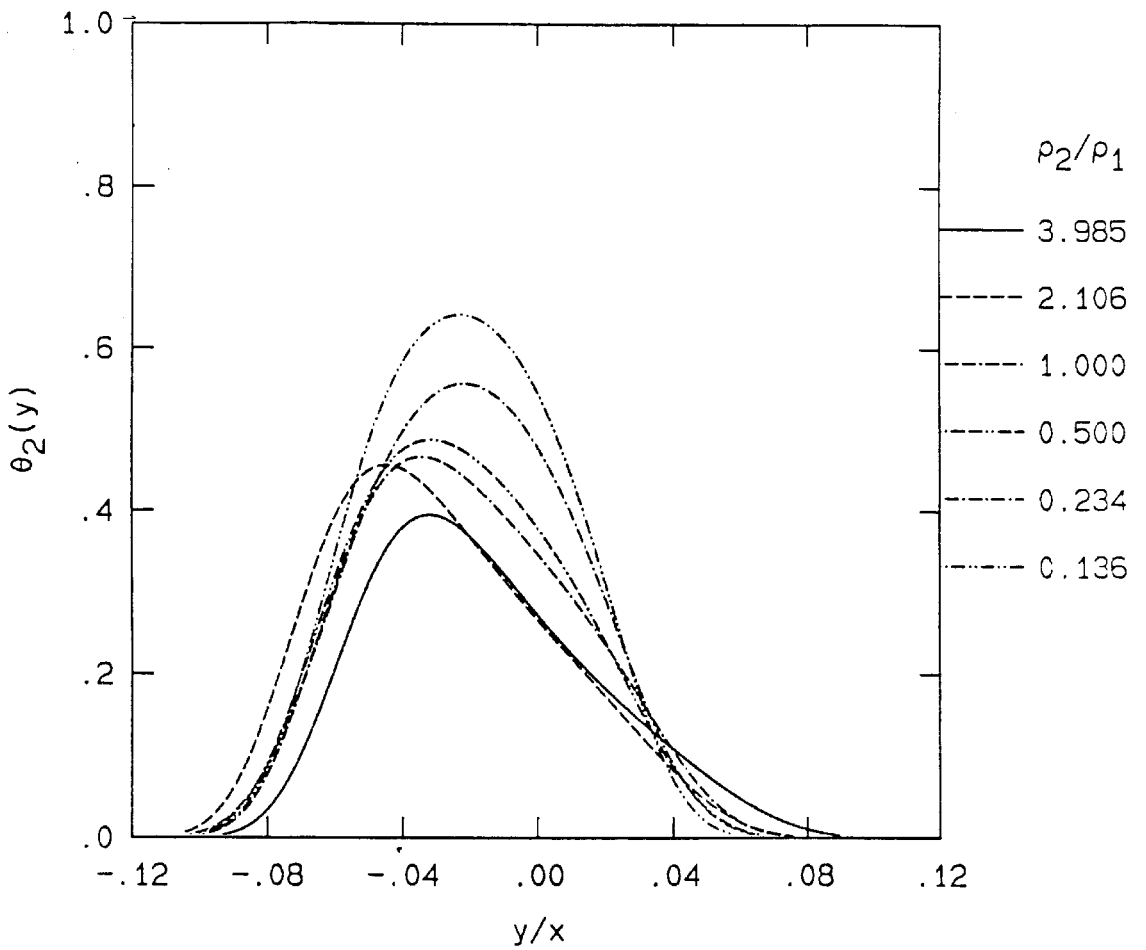

Figure 4.4 Mixed low-speed fluid probability profiles.

and Dimotakis 1984) where the maximum value of this probability was found to be 0.45 . This difference has long been recognized as experimental confirmation of a molecular transport coefficient playing a central role in mixing, even at high Reynolds numbers. Note that the present work removes a key qualification on this conclusion. Konrad's technique of estimating this profile by directly measuring concentration provided an upper bound on the actual profile. Debates about the resolution of his technique suggested to some that the increased mixing he measured in gas=phase flows might in some part be due to measurement errors.

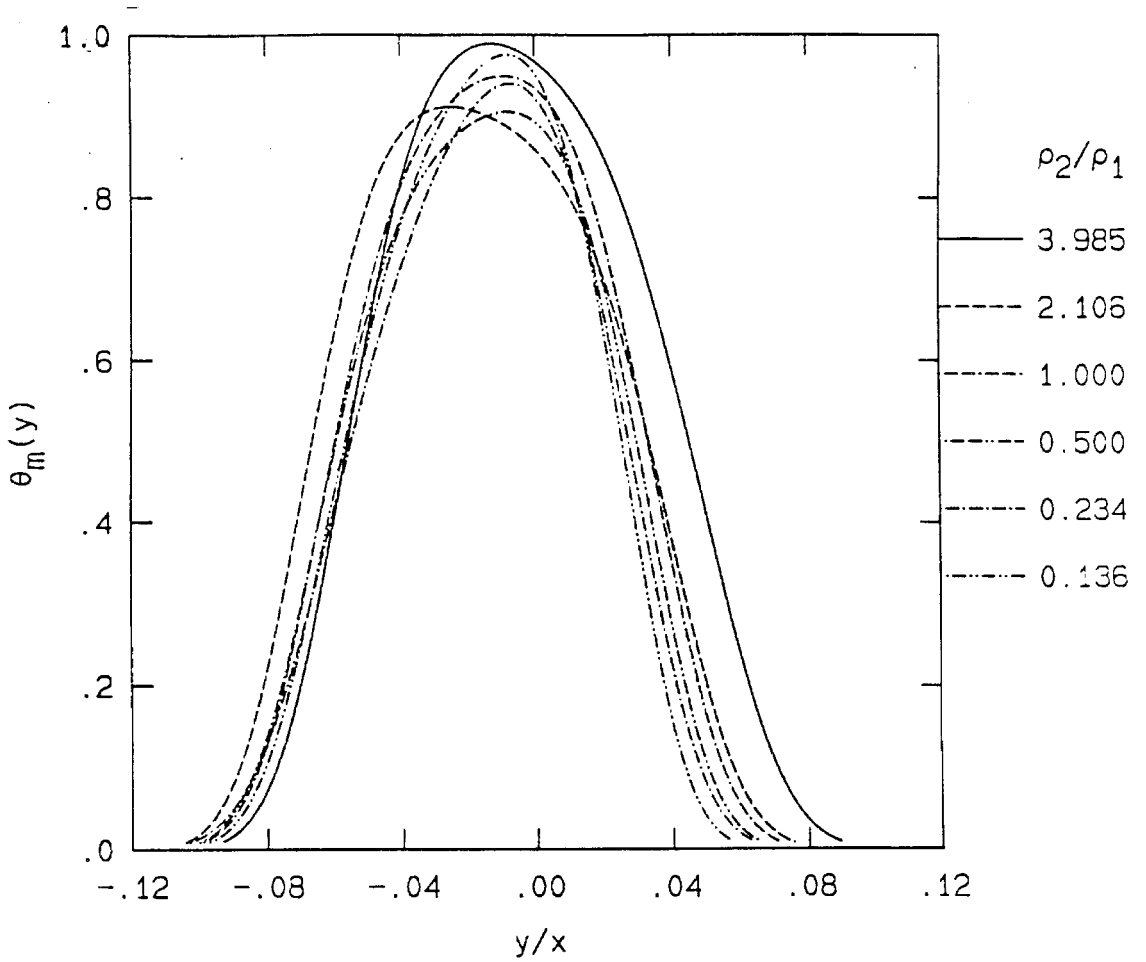

Figure 4.5 Mixed-fluid probability profile for each density ratio.

The present work, which measures the product of a chemical reaction at a finite stoichiometry, provides a lower bound for this same quantity. Since these two are in agreement, each represents an accurate estimate and the difference between mixing in high and unity Schmidt number regimes is reaffirmed.

Figure 4.6 shows the product probability thickness for each of the stoichiometries used in this investigation. Shown in integral form are the same trends observed in the profiles. As the density ratio increases, δ_p increases for high ϕ, (high-speed stream lean), and decreases for low ϕ, (low-speed stream lean). Over

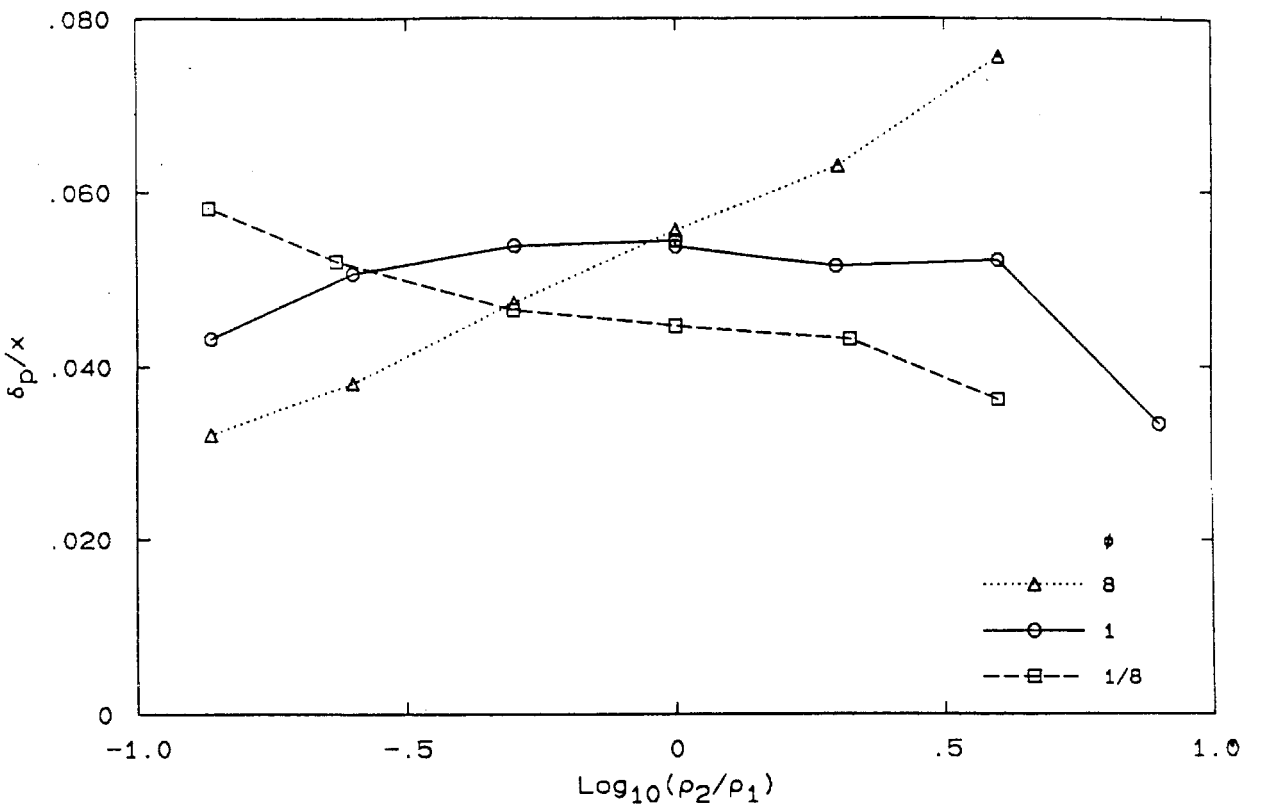

Figure 4.6 Product probability thickness for each stoichiometry.

this range of density ratios, δ_p for $\phi = 1$ does not vary as strongly. This trend (and results of later analysis) suggests that in each limit of the density ratio δ_p for $\phi = 1$ will decrease until it asymptotes to a constant times the decreasing stoichiometry case. If for a moment, the product probability thickness is viewed as a function of density ratio and stoichiometry then specifically,

$$\lim_{s\to\infty} \delta_p(s, \xi_\phi = 1/2) = \alpha_2 \delta_{p_2}(s) \qquad \text{and} \qquad \lim_{s\to 0} \delta_p(s, \xi_\phi = 1/2) = \alpha_1 \delta_{p_2}(s) \tag{4.1}$$

where α_1 and α_2 are constants.

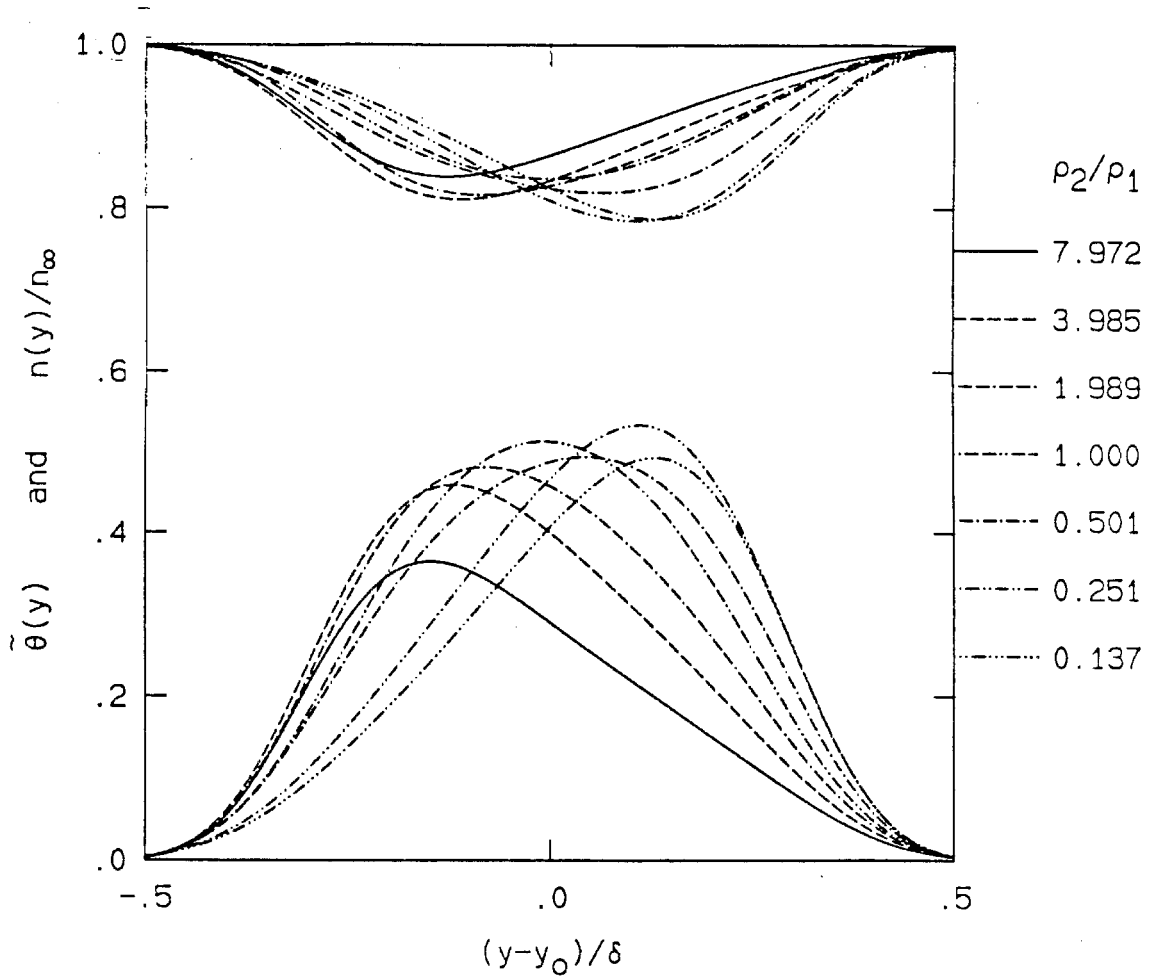

Figure 4.7 Product distributions for $\phi = 1$.

Product Distributions

The mean number density of product and mean molecular number density were also determined for each experiment. Figure 4.7 shows the profile of product, $\tilde{\theta}(y)$, for each density ratio at a stoichiometric mixture ratio of $\phi = 1$. Here the horizontal axis is again the transverse dimension in the layer, but it has now been shifted to align the edges of the mixed-fluid distribution. Also the normalization has been changed to the width δ , of the mixed-fluid distribution. While the symmetry changes seen in the $\theta(y)$ are still evident, with the profiles leaning

toward the high-density fluid, variation of the peak value of $\tilde{\theta}(y)$ is smaller. Also shown in this and the subsequent three figures are the distributions of mean number density, $\overline{n}(y)$. Because of the isobaric conditions and ideal gas behavior, these profiles tend toward 1.0 outside the layer, and decrease inside the layer owing to dilatation from heat released by reaction. The same symmetry shifts seen in $\tilde{\theta}(y)$ may be seen in $\overline{n}(y)$, although to a differing extent.

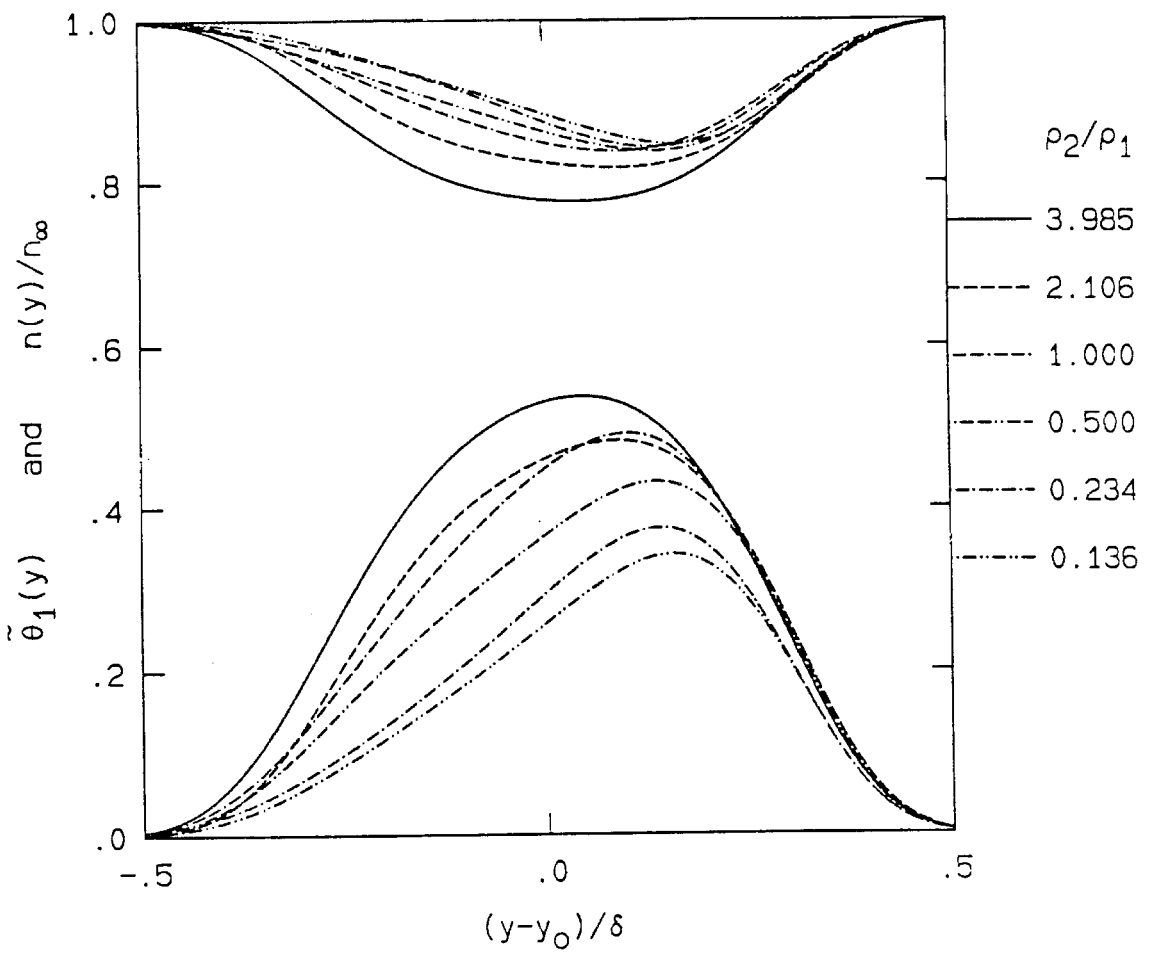

Figure 4.8 Profiles of mixed high-speed fluid.

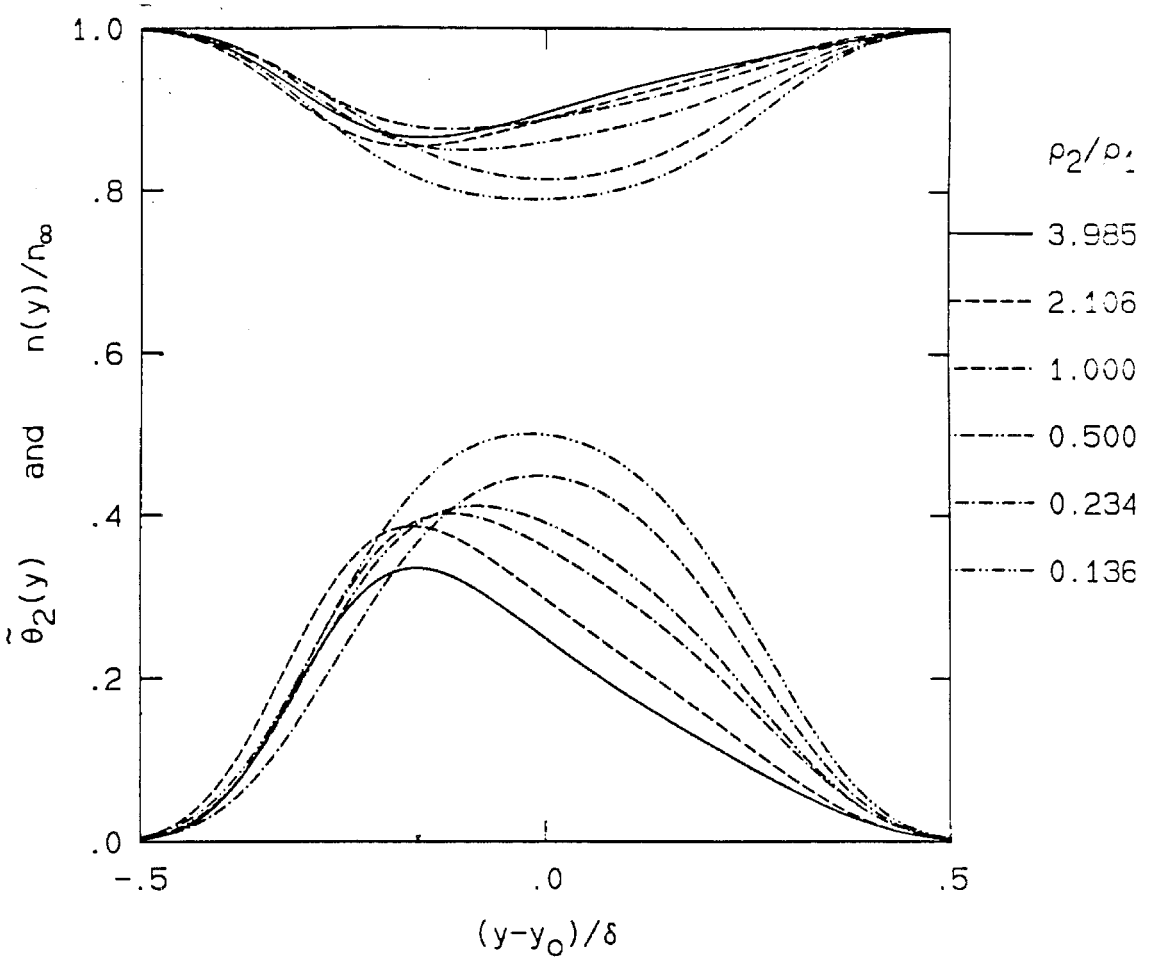

Figure 4.9 Profiles of mixed low-speed fluid.

Figures 4.8 and 4.9 show respectively, the profiles of mixed high-speed fluid and the profiles of mixed low-speed fluid for each of the density ratios. The same trends in peak value and symmetry found for the mixed-fluid probability profiles can again be found in these curves. Note the reduction in peak values. Remember that, in the limit of zero heat release, plots of $\tilde{\theta}_i(y)$ and $\theta_i(y)$ would be identical and the number density $\overline{n}(y)$ would equal 1.0 identically.

Figure 4.10 shows the product thickness obtained for each of the stoichiometries, as a function of the density ratio. Plotted primarily for completeness, no

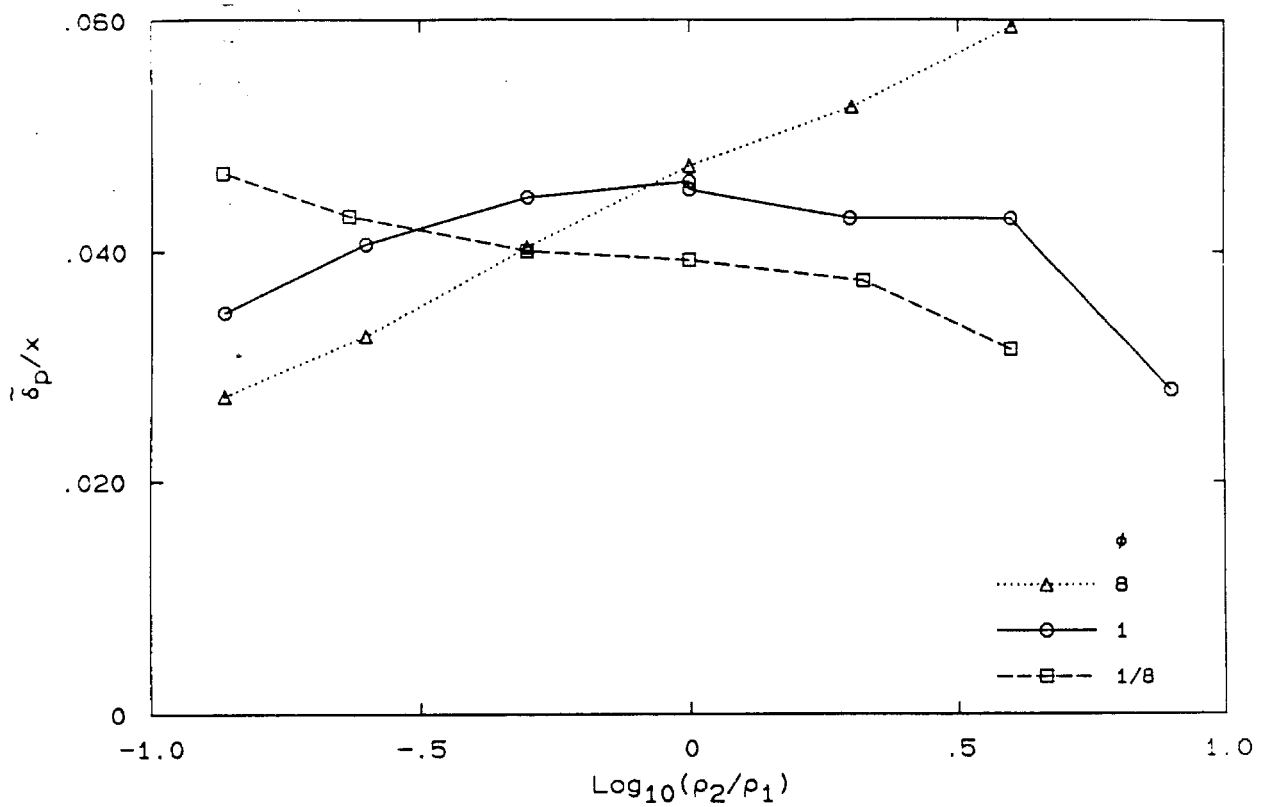

Figure 4.10 Product thickness for each stoichiometry.

striking differences exist between these and the product probability thicknesses in Figure 4.6. Note that the distinction between these two plots lies mainly in the question of interest. If the volume occupied by product is of interest, then the product probability thicknesses are the relevant measure. If on the other hand, the amount of product formed by the mixing and reaction is of concern, then the product thicknesses in Figure 4.10 are pertinent.

Figure 4.11 shows both the mixed high and low-speed fluid thicknesses and probability thicknesses normalized by the mixing layer width. Normalized in this fashion, the mixed-fluid probability thicknesses, δ_{p_1} and δ_{p_2}, can be thought of as the volume fraction occupied by the mixed high-speed and low-speed fluid, respectively. The dependence displayed over this range of density ratios suggest

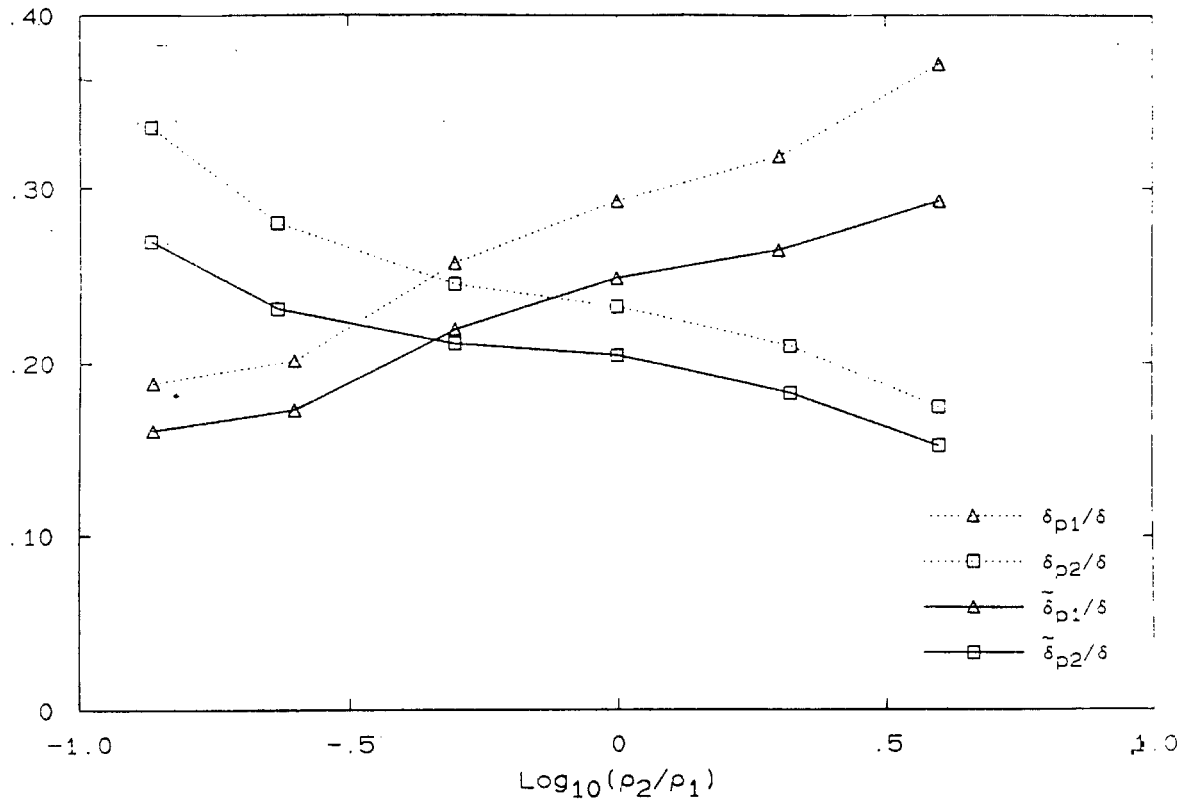

Figure 4.11 Mixed high-speed and low-speed fluid thickness and probability thickness.

that a straight line might be fit. Note that the physical limits for each of these normalized quantities are $0 \leq \delta_{p_i}/\delta \leq \delta_m/\delta$. Nevertheless, the trends are again evident, with the amount of mixed low-density fluid increasing and the amount of mixed high-density fluid decreasing as the density ratio tends toward either extreme.

Figure 4.12 shows the result of adding the mixed-fluid profiles for the flip, along with the mean number density for the pair of experiments. As was the case with the probability profiles, it can be seen that the amount of unmixed fluid in the center third of the layer is very low. Estimated here by the distance between

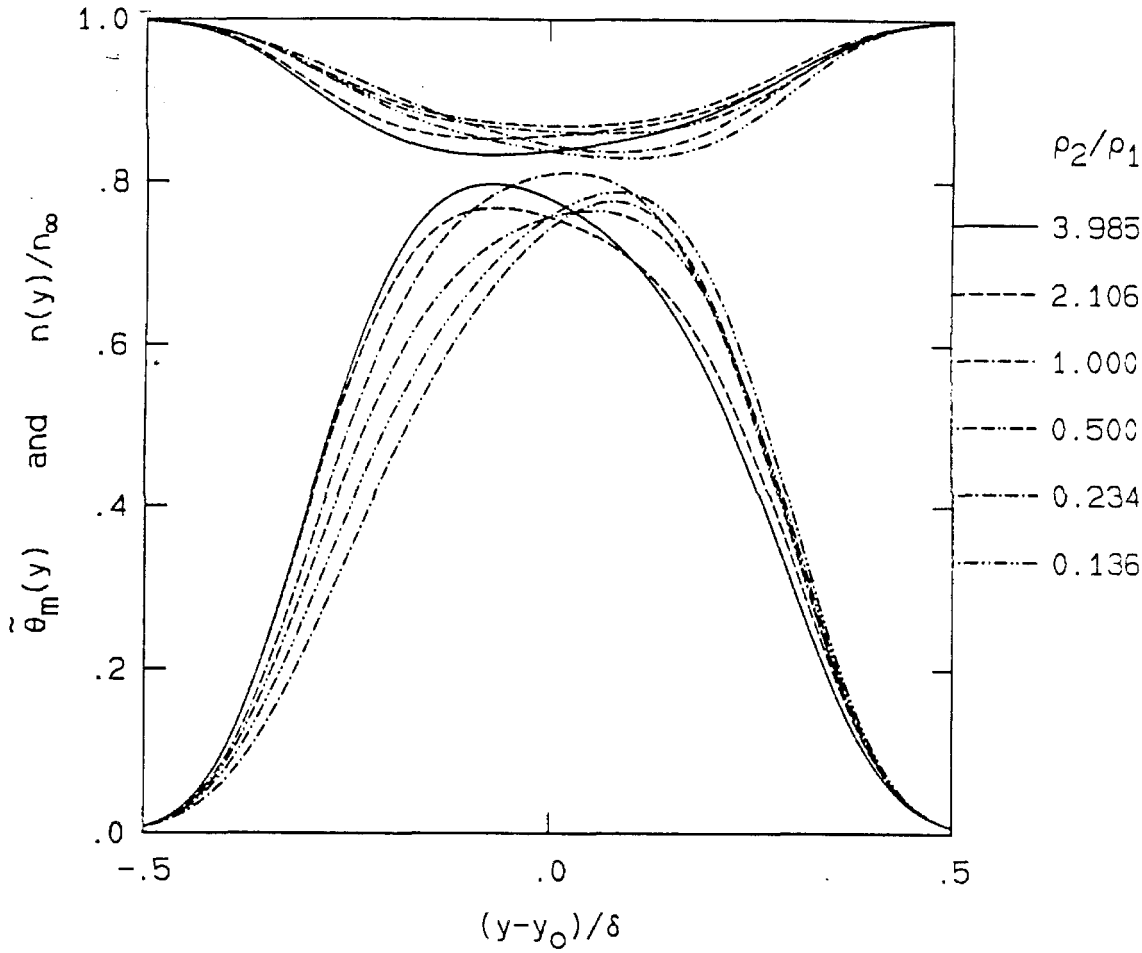

Figure 4.12 Mixed-fluid and mean number density profiles.

$\tilde{\theta}_m(y)$ and $\overline{n}(y)$ for a given density ratio, it is $\sim 10\%$ for all of the data. Note the striking similarity of these profiles.

Three integral quantities, δ_m , $\tilde{\delta}_m$ and $\tilde{\delta}$ are plotted in Figure 4.13 versus the freestream density ratio. As discussed in Chapter 3, the quantity $\tilde{\delta}$, as used in Equation 3.1 can be used to properly gauge the effects of heat release. In each case, $1 - \tilde{\delta}/\delta$ is below 0.1, indicating that the mean number density in the layer has been reduced by less than 10%. The quantity δ_m/δ represents the sum of the high and low-speed mixed-fluid volume fractions, and therefore represents the

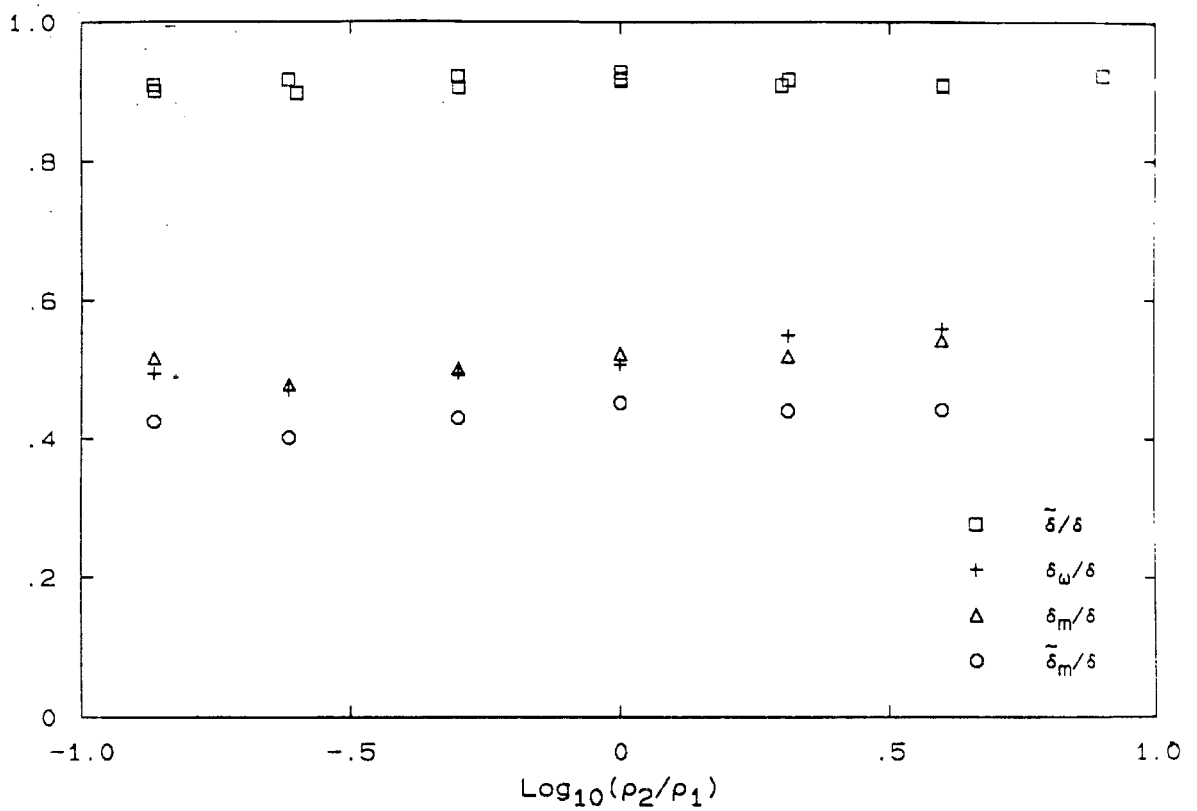

Figure 4.13 Several measures of mixing layer width.

volume fraction occupied by mixed fluid at any composition. It is interesting that this volume fraction very closely matches the vorticity thickness determined from the stagnation pressure measurements. Note the insensitivity of these quantities to the factor of thirty change in density ratio.

Figure 4.14 replots several quantities. Normalized by the mole thickness, $\tilde{\delta}$, these may be interpreted as mole fractions. Hence $\tilde{\delta}_{p_1}/\tilde{\delta}$ and $\tilde{\delta}_{p_2}/\tilde{\delta}$ are respectively, the mixed high-speed fluid and mixed low-speed fluid mole fractions. Also plotted is the mixed-fluid thickness $\tilde{\delta}_m$. Normalized by the mole thickness, $\tilde{\delta}_m/\tilde{\delta}$ represents the mole fraction of mixed fluid at any composition within the layer. The lack of variation with density ratio shown by this quantity is particularly noteworthy, varying by less than 6% with the average value $\tilde{\delta}_m/\tilde{\delta} = 0.47$.

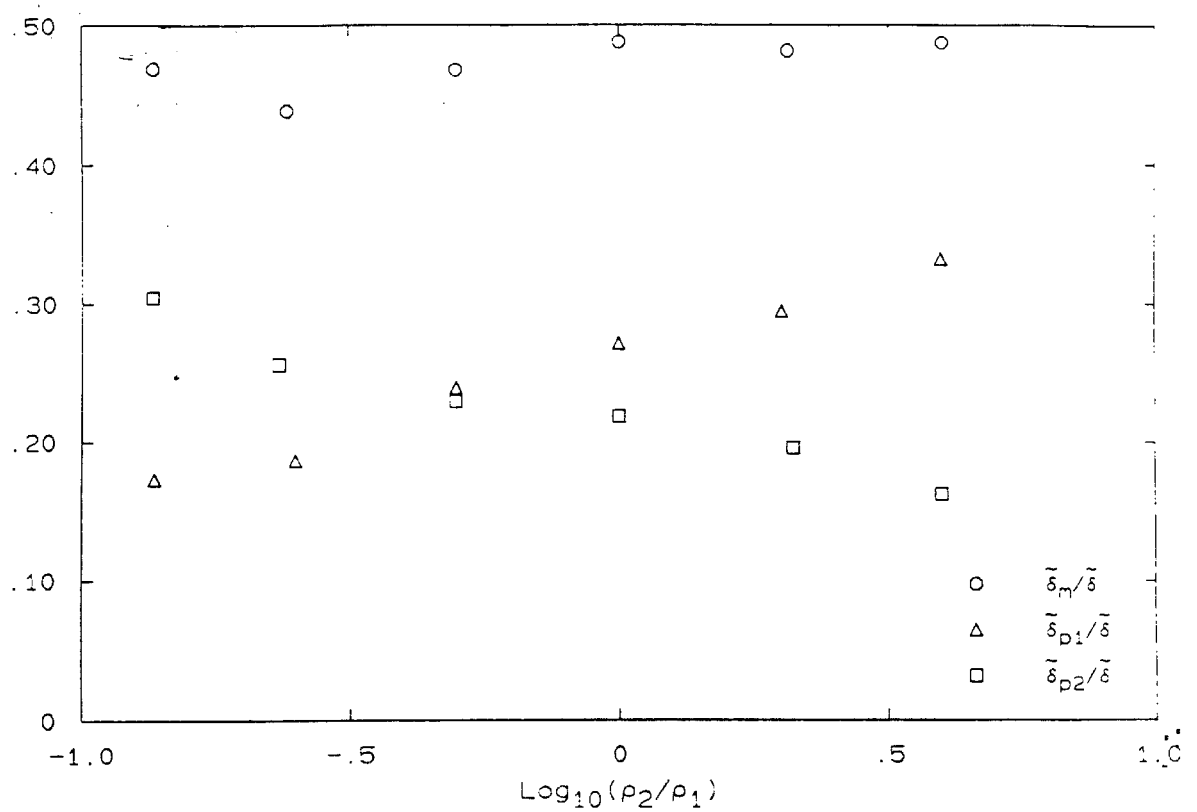

Figure 4.14 Mixed-fluid mole fractions for each density ratio.

Using the approximations detailed in the Appendix B, the mixed-fluid composition profile, $\xi_m(y)$, was also estimated. Shown in Figure 4.15 are the profiles for each of the density ratios investigated. These curves are consistent with those measured by Konrad and also with Wallace when scaled with the temperature profile width, in the fashion he suggested. As noted by Konrad, the composition of the mixed fluid does not extend to the two limits, $\xi = 0$ and 1 . Nevertheless, the variation is not small, with important implications for models which approximate the mixing in the layer as independent of the transverse coordinate. With the exception of an offset or average composition which is dependent upon density ratio, the composition curves are very similar. The major exception to this is the profile for $\rho_2/\rho_1 = 2$. For this case, the composition of

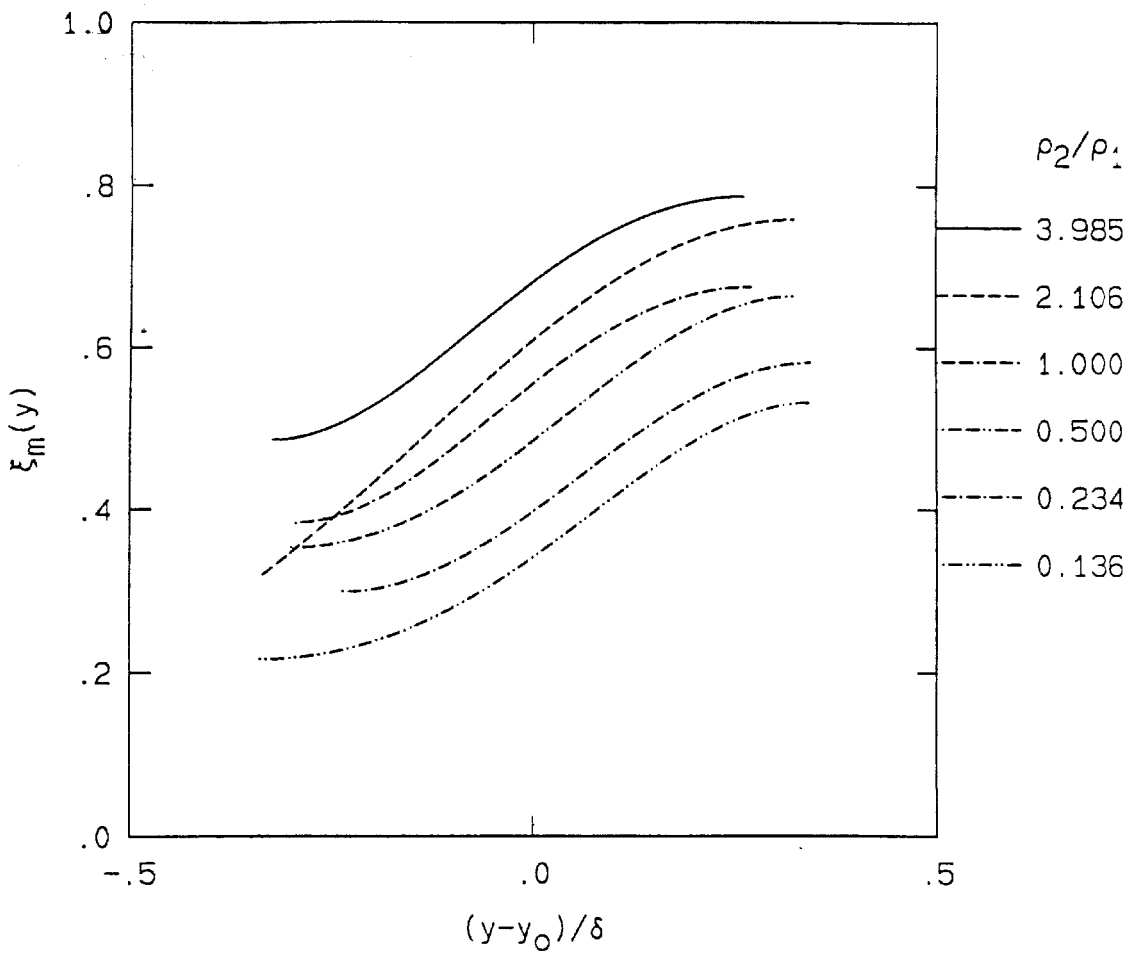

Figure 4.15 Mixed-fluid composition profiles.

the mixed fluid seems to vary over a wider range, particularly on the low-speed side of the mixing layer. This difference actually matches the form of the curve measured by Konrad for $\rho_2/\rho_1 = 7$ more closely than the present results for $\rho_2/\rho_1 = 4$. However, the reason for this difference is unknown.

Figure 4.16 is the average composition for the mixed fluid in the layer, defined by Equation $B.26$. This quantity shows strong dependence upon the density ratio. The trend is in accordance with the measurements of Konrad, indicating that

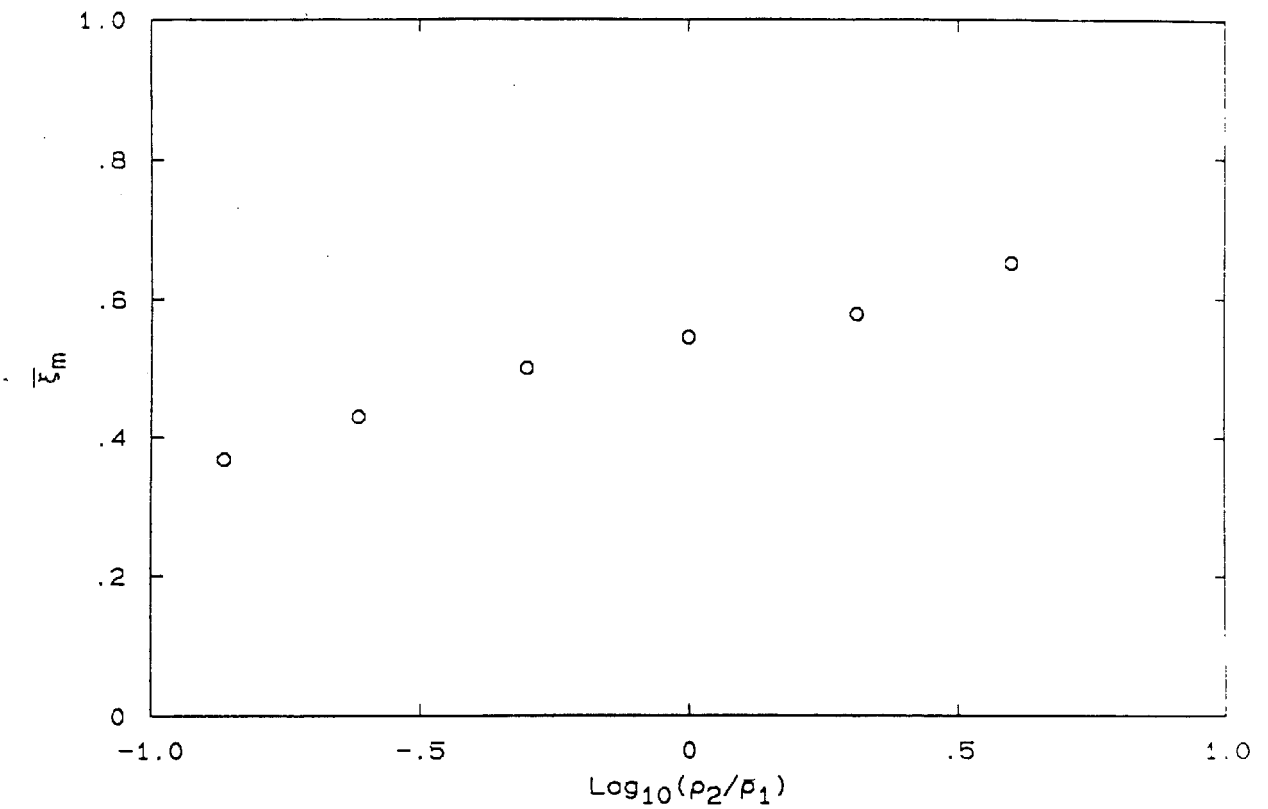

Figure 4.16 Mean mixed-fluid composition for each density ratio.

substantially more of the low-density fluid is found in a mixed state than fluid from the high-density stream.

Entrainment Rates and Ratios

The volume entrainment rate from each stream, e_{v_i}, was estimated by several techniques. Recently, Dimotakis (1986) has related the volume entrainment ratio of the shear layer to the geometry of the mean boundaries of the layer and the orientation of the free stream streamlines. Shown normalized by the high-speed velocity and the layer width, e_δ in Figure 4.17 represents the entrainment estimated by this method. As discussed in Appendix B (defined in Equation $B.27$), e_δ represents the cumulative entrainment from the splitter tip to the measuring

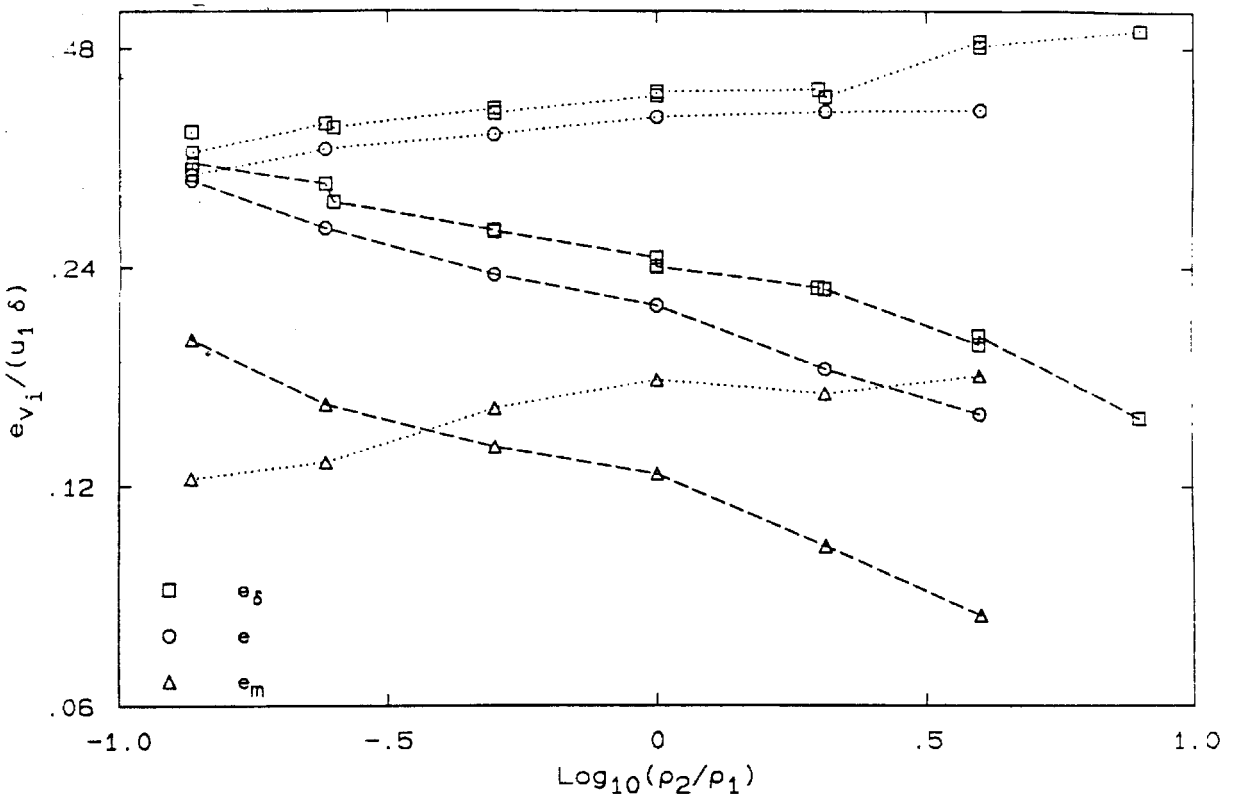

Figure 4.17 Estimates for mixing-layer volume entrainment rates.

station, x , and therefore estimates the total fluxes at x . Using the velocity profiles derived from the stagnation pressure measurements, the mean flux of fluid from each stream can also be calculated from the composition profiles determined from the flip experiment. Defined in Equation $B.31$, these are indicated in the figure by e . The flux of mixed fluid from each stream, e_m , was calculated using the velocity profile estimates along with the mixed-fluid profiles, $\tilde{\theta}_i(y)$ according to Equation $B.33$. The estimates for the entrainment rate from the high-speed stream (e_{v_i}) are shown in Figure 4.17 connected by dotted lines. All of these estimates are nearly independent of the density ratio, at most having a dependence of $s^{\frac{1}{8}}$, where s is the freestream density ratio ρ_2/ρ_1. The estimates for entrainment from the low-speed stream (e_{v_2}) are shown connected by dashed

lines. Again the three quantities have nearly identical dependence upon density ratio and vary roughly as $s^{-\frac{1}{4}}$. The mass entrainment from each stream can be obtained by a simple multiplication of the quantities in this plot. If normalized by the high-speed stream density, ρ_1 , the mass fluxes from the high-speed side are equal to the volume fluxes as plotted, and vary roughly as $s^{\frac{1}{8}}$. The mass fluxes from the low-speed side are then simply the volume fluxes from that stream, multiplied by the density ratio. These would therefore vary as $s^{\frac{3}{4}}$.

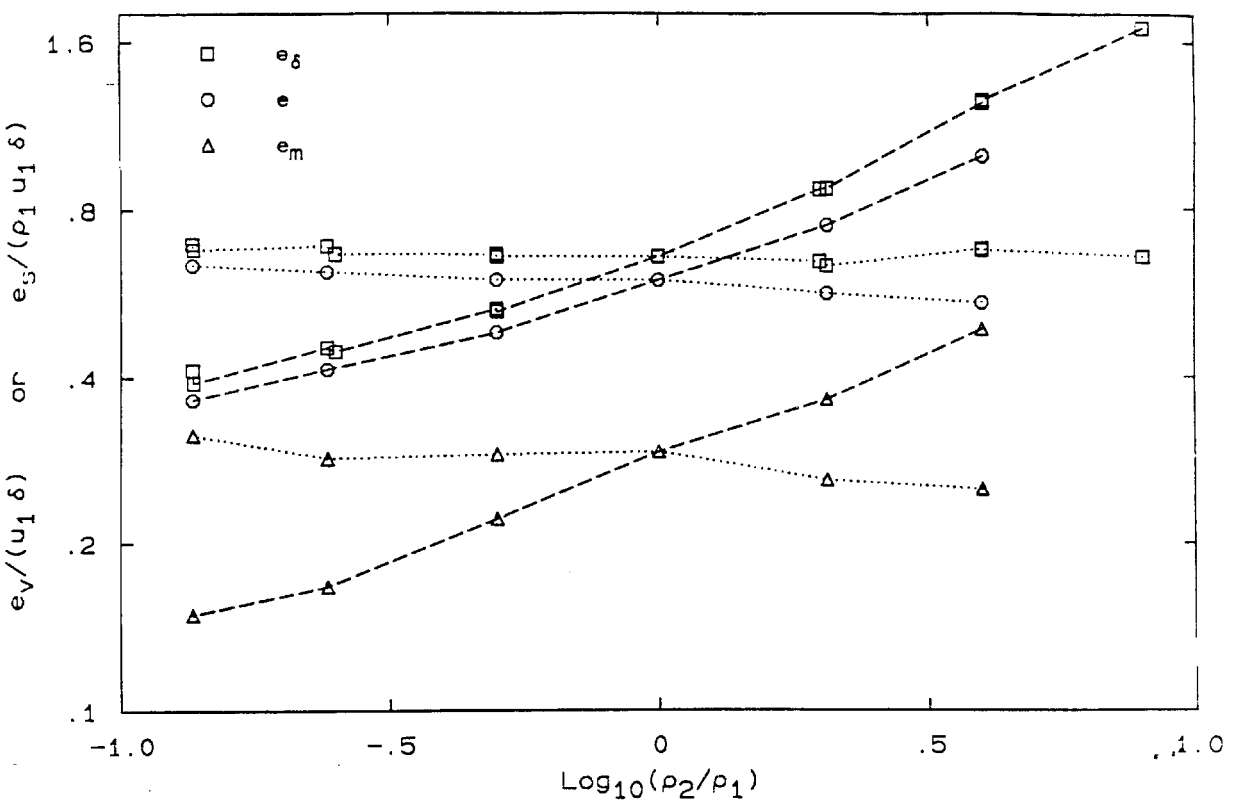

Figure 4.18 Estimates for total volume and mass entrainment rates.

The total fluxes for the layer are shown in Figure 4.18. The dotted lines connect points representing the total volume entrainment estimates, e_v. It can be seen that both the total volume entrainment rate, and the mixed-fluid volume

entrainment rate are nearly independent of the density ratio over the range investigated. The dashed lines connect the estimates for the mass entrainment rate, denoted e_s . Again, both estimates for the total and the mixed-fluid mass entrainment have the same dependence. The mass entrainment strongly depends on the density ratio, something very close to $s^{\frac{3}{8}}$. Interestingly, using the geometric estimate, a fit of the three highest density-ratio points yields that $e_s \sim s^{\frac{1}{2}}$, while the three lowest density ratio points yield that $e_s \sim s^{\frac{1}{4}}$.

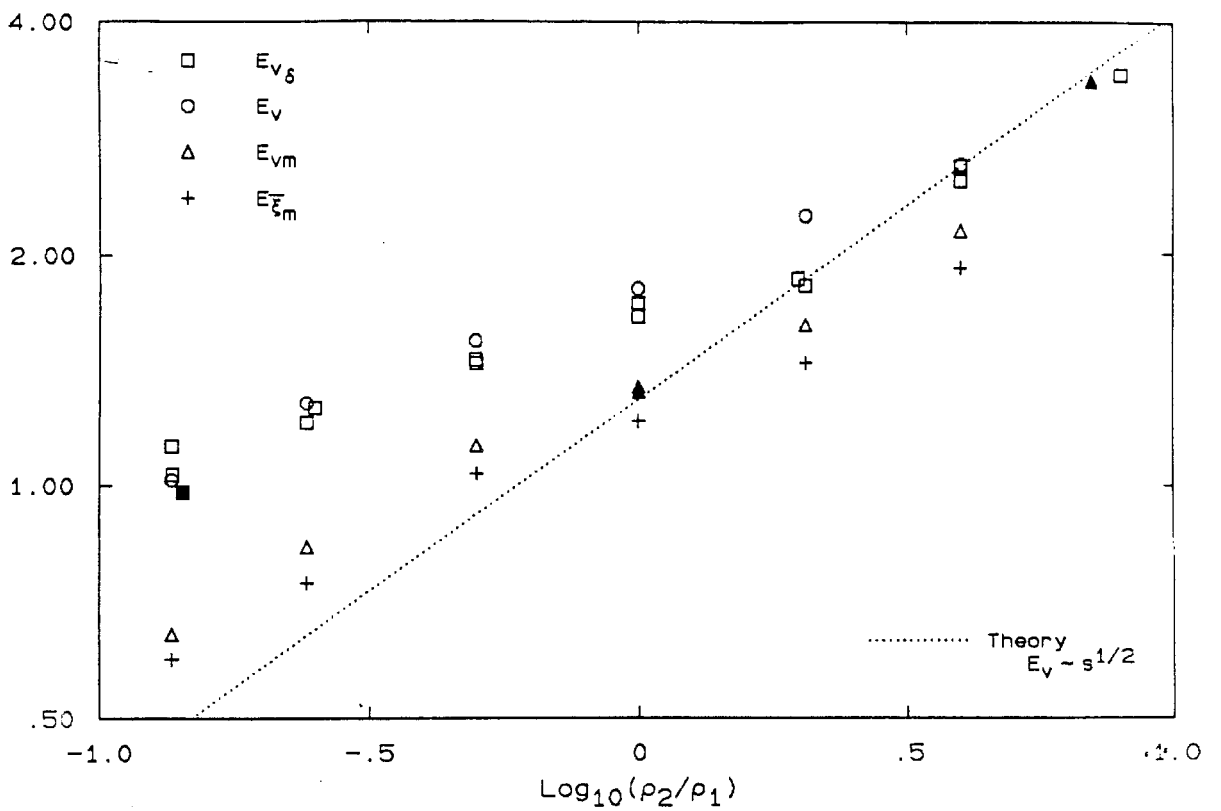

Figure 4.19 Entrainment ratio estimates for each density ratio.

The ratios of entrainment estimated by each technique are plotted in Figure 4.19. These quantities are defined as the flux from the high-speed side divided by the flux from the low-speed side (see, for example, Equation $B.37$). Good

agreement between the visual and mean flux estimates is seen to be the case, except for $s = 2$. The filled symbols in this figure indicate the measurements reported by Brown and Roshko (1974), Brown (1974) and Konrad (1976). Also plotted is a dotted line corresponding to theoretical predictions for this dependence. Brown (1974) has proposed a theory for the entrainment into the mixing layer based on consideration of the large structure dynamics. For a velocity ratio $r = U_2/U_1$ and a density ratio $s = \rho_2/\rho_1$, he proposed an estimate of the entrainment ratio into the mixing layer given by

$$E \sim \frac{U_1 - U_c}{U_c - U_2} \sim s^{1/2} \tag{4.2}$$

Dimotakis (1986) has proposed an extension of this simple relation intended to account for the asymmetry introduced by spatial growth.

$$E \sim s^{1/2}\left(1 + .68\left(\frac{1-r}{1+r}\right)\right) \tag{4.3}$$

Although the two differ by a multiplicative constant (at fixed velocity ratio), it is clear that both Brown and Dimotakis predict the simple dependence $E_v \sim s^{\frac{1}{2}}$. This dependence is shown in Figure 4.19 with the constant corresponding to the relation by Dimotakis. In comparison, the dependence of the visual entrainment ratio data is more nearly $E_v \sim s^{\frac{1}{4}}$. However, if the data for the highest three density ratios is fit, the dependence is $E_v \sim s^{\frac{1}{2}}$. Also the mixed-fluid quantities appear to undergo a transition at $s = 1$. For $s < 1$, $E_{vm} \sim s^{\frac{1}{2}}$ and is slightly above theory, and for $s > 1$, $E_{vm} \sim s^{\frac{1}{2}}$ and is slightly below theory. Unfortunately, it is not clear which estimate, if any, the theory should correspond to.

There is a substantial difference between entrainment ratio and the mixed-fluid flux ratio. As shown in Figure 4.19, this difference is larger at the low density

ratios and it may disappear for very high density ratios. There is evidence in the flow visualization that the fluids do not mix at the same ratio as they are entrained into the mean boundaries of the layer. Schlieren pictures indicate that regions of unmixed fluid within the mixing region increase in size on the light fluid side as density ratio decreases. This change can also be observed in the time traces of temperature for the outer probes in the low-density stream. As the density of the low-speed stream decreases, the occurrences of high temperature fluid become less frequent. Physically, this could be the result of velocity perturbations in the dense gas flinging mixed fluid relatively far into the low-density slow moving stream, which offers little resistance. These occurrences are rare, however they serve to "artificially" widen the layer toward the light fluid stream. While this hand-waving may serve to explain the divergence of the two quantities to some extent, it boils down to the same difficulty indicated above. How much fluid enters the layer, how much enters the structure and what part of that fluid becomes mixed are separate questions. Some work towards clearly defining these quantities, and understanding how each relates to models of the mixing process, remains.

The composition ratio is plotted with crosses in this figure and denoted $E_{\tilde{\xi}_m}$. Although it follows the same dependence as the other quantities in this plot, it must be emphasized that this quantity is distinct from the entrainment ratio of the mixed fluid, E_{vm}, and in fact, does not represent a flux ratio at all. At a given density ratio, the measured difference between E_{vm} and $E_{\tilde{\xi}_m}$ is related to the spatial correlation of the mean velocity and mean mixed-fluid composition profiles. If the distribution of mixed fluid from each stream is treated as a probability distribution, then the mean velocity for the mixed fluid from each freestream can be defined as

$$\overline{u}_{1m} = \frac{\int \tilde{\theta}_1(y)\,\overline{u}(y)\,dy}{\int \tilde{\theta}_1(y)\,dy} \quad \text{and} \quad \overline{u}_{2m} = \frac{\int \tilde{\theta}_2(y)\,\overline{u}(y)\,dy}{\int \tilde{\theta}_2(y)\,dy} \tag{4.4}$$

The ratio of these two quantities can be formed and using the defining relations (Equations $B.36$ and $B.37$), can be related to the composition ratio and mixed-fluid flux ratio,

$$\frac{\overline{u}_{1m}}{\overline{u}_{2m}} = \frac{E_{vm}}{E_{\overline{\xi}_m}} \tag{4.5}$$

Equation 4.5 demonstrates that the difference between E_{vm} and $E_{\overline{\xi}_m}$ indicates that the mean velocity of the mixed fluid from the high-speed stream is higher than the mean velocity of the mixed low-speed fluid. For all the density ratios investigated, the ratio is $\overline{u}_{1m}/\overline{u}_{2m} = 1.10$. This ratio is probably dependent upon the velocity ratio, and is 1.0 for high Schmidt number flows where mixed-fluid profiles are symmetric. Its significance is unknown, but its insensitivity to density ratio is interesting.

As was the case for the entrainment from each stream, mass entrainment ratios may be obtained from this data by dividing by the density ratio. This would result in the mixed-fluid mass entrainment ratio, E_{sm}, decreasing slightly faster than $s^{-\frac{1}{2}}$ and the overall mass entrainment ratio, E_s, decreasing as $s^{-\frac{3}{4}}$ for the data presented here.

The difference between the entrainment estimates based on geometry and those based on mean fluxes can be used to estimate the fluctuation correlations in the layer. These estimates are shown in Figure 4.20. Because of the distance from the measurements, through several stages of approximation and calculation, these data should be viewed as rough estimates of the indicated quantities.

Autocorrelations and Spectra

In order to investigate the nature of the large scale structure in determining the mixing phenomena discussed above, the power spectral densities of the temperature time-series was calculated. Individual probes displayed the same

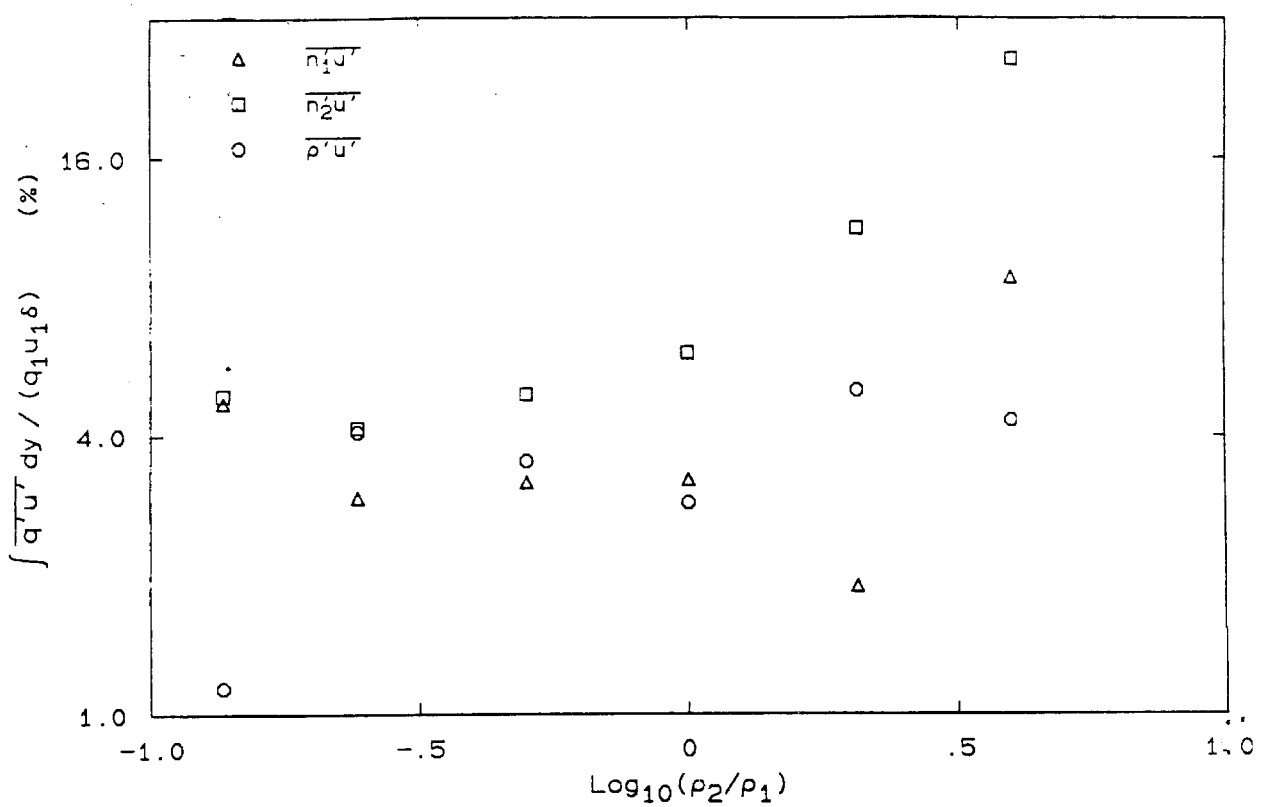

Figure 4.20 Fluctuation correlations versus density ratio.

transverse coordinate dependence found by Konrad with greater high frequency content on the high-density side of the mixing region. More interestingly, if the spectra are averaged for the entire layer, normalized by the adiabatic flame temperature (ΔT_f) and the large scale structure passage time,

$$\tau_\delta = \frac{\delta}{U_c} \tag{4.6}$$

dramatic collapse is achieved. In this expression, the velocity U_c is the convection velocity of the large structures as given by Brown (1974) or Dimotakis (1986);

$$U_c = \frac{U_1 + s^{1/2}\, U_2}{1 + s^{1/2}} \tag{4.7}$$

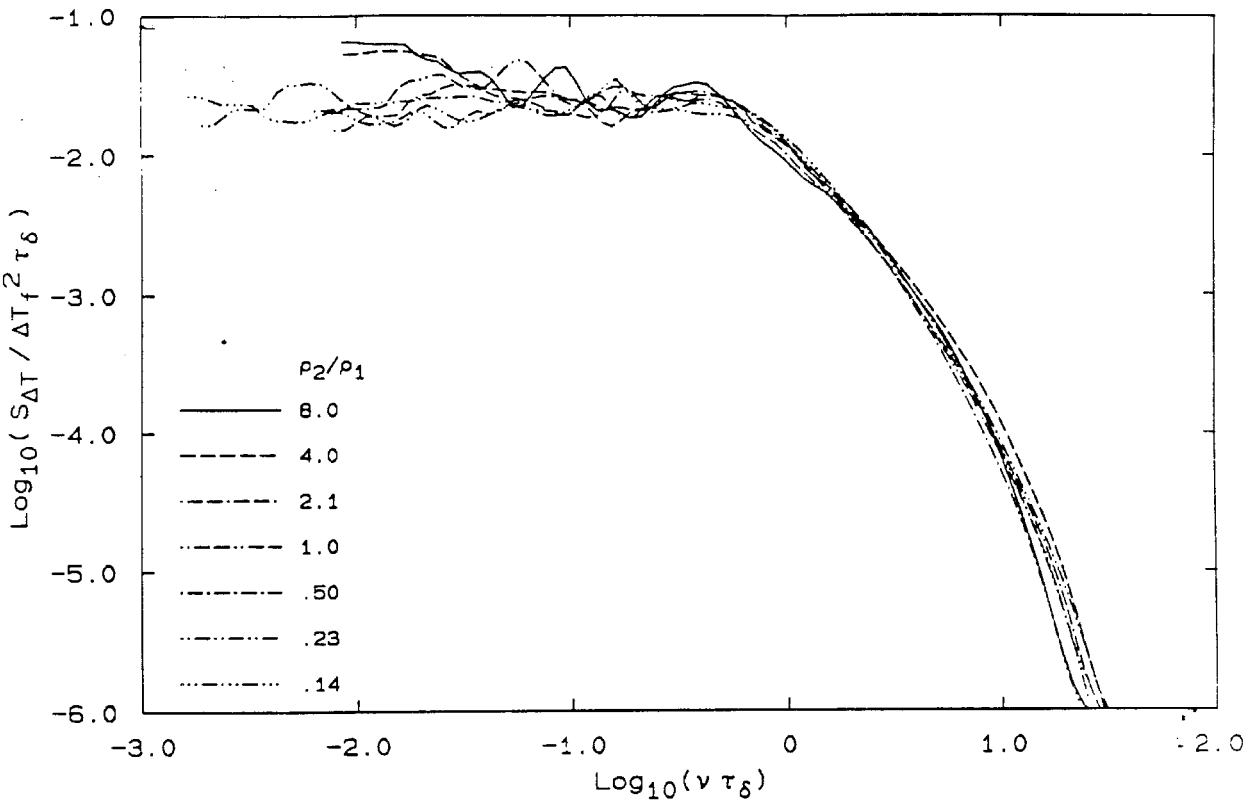

Figure 4.21 Power spectral density for each density ratio.

Figure 4.21 shows the normalized power spectral density (PSD) for each of the density ratios. Despite a factor of 30 change in density ratio, these are remarkably similar. This suggests that although the mixing process (loosely connected to high frequency, and therefore small scale, fluctuations in the concentration) may shift from one side of the mixing layer to the other as the density ratio is varied, the overall mixing process remains unaffected. This is borne out by the invariance of the integral amounts of mixed fluid, Figure 4.14.

This autocorrelation, calculated as described in Chapter 3, is shown in Figure 4.22 for each of the density ratios. The horizontal axis has been transformed to a spatial variable, ℓ , using the Taylor hypothesis,

$$\ell \sim U_c \tau \tag{4.8}$$

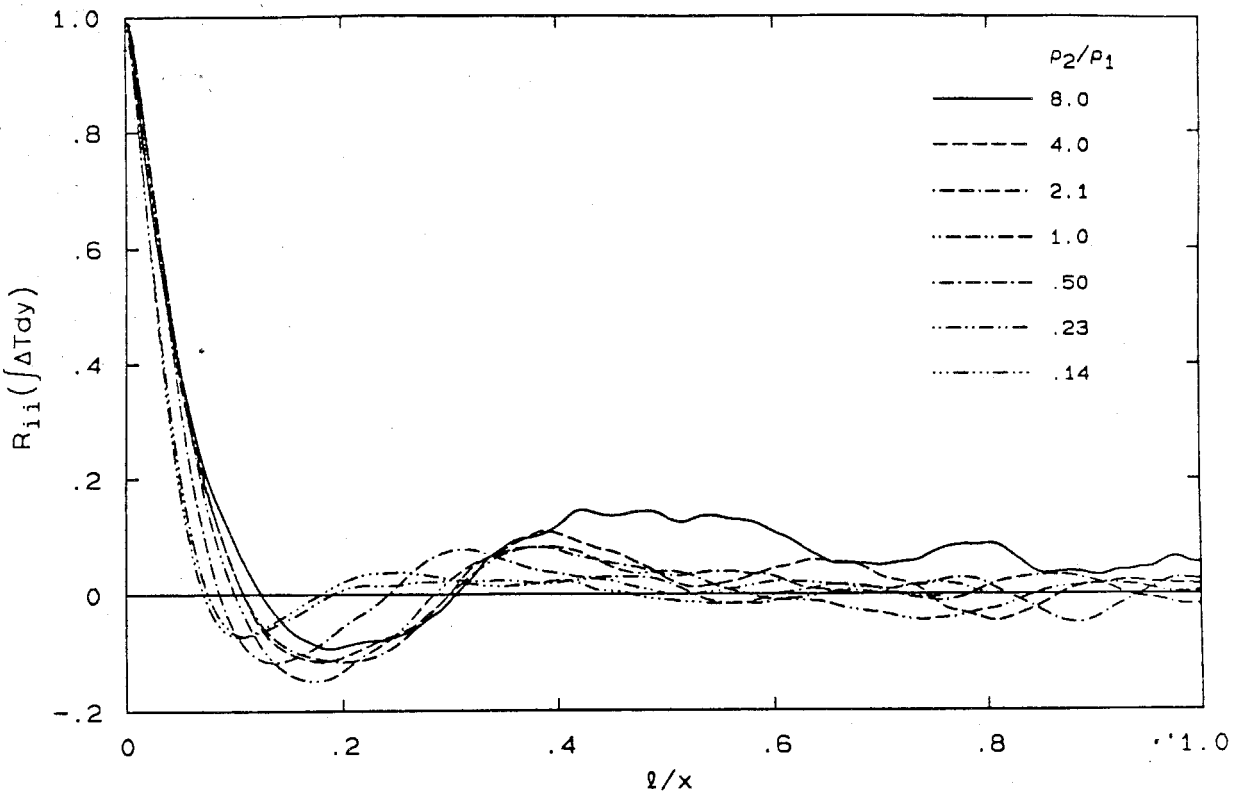

Figure 4.22 Autocorrelation of temperature integral.

and normalized by the downstream position of the measuring station, x. As was the case for the correlations presented in Chapter 3, the long term memory or phase correlation of the shear layer is seen to be poor. The magnitude of both the first minimum and the second maximum is 15% or less for each of the density ratios. Over scales comparable with the test section length, the correlation has dropped to less than 6% and it decays rapidly after that.

The position of the minima and maxima in the autocorrelation can again be used to indicate the structure length scale. Plotted in Figure 4.23 are these positions, ℓ/x , for each of the density ratios. Indicated by the circles are twice the distance to the first minimum. The triangles are the positions of the second maximum for each. The change in this quantity indicates one of two quantities

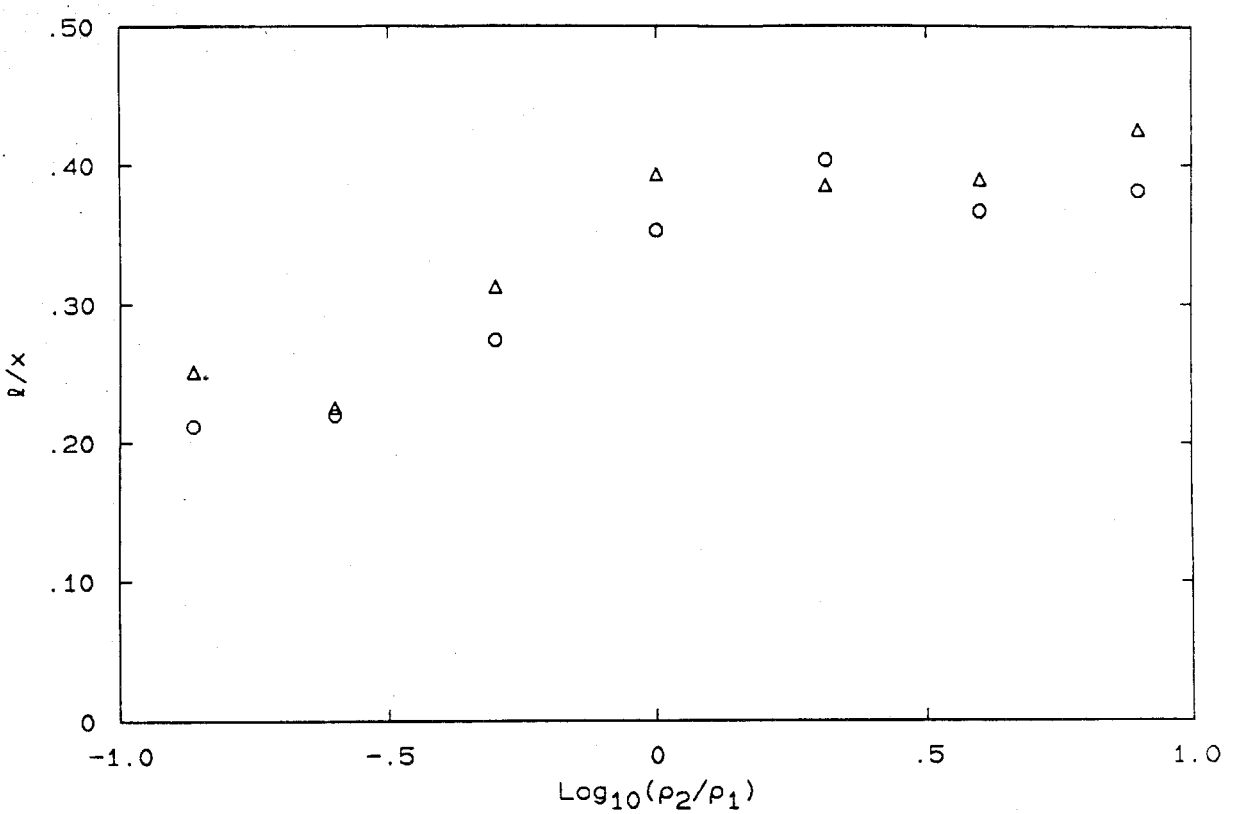

Figure 4.23 Mixing layer length scales inferred from autocorrelations.

are changing within the layer. Either there is a distinct change in the nature of the large scale structure or the velocity at which it is convecting is changing in a fashion not predicted by Brown. However, if we were to assume that the large scale structure remains unchanged, and therefore attribute all the change in ℓ/x to a change in the convection velocity, it would indicate that the structures are moving faster than the high-speed stream velocity in the low density ratio case, or conversely slower than the low-speed stream in the high density ratio cases. Because the pressure gradients were kept to a small percentage of the dynamic head in the low-density fluid freestream, this is not possible. Therefore, some change in the large scale structure is indicated.

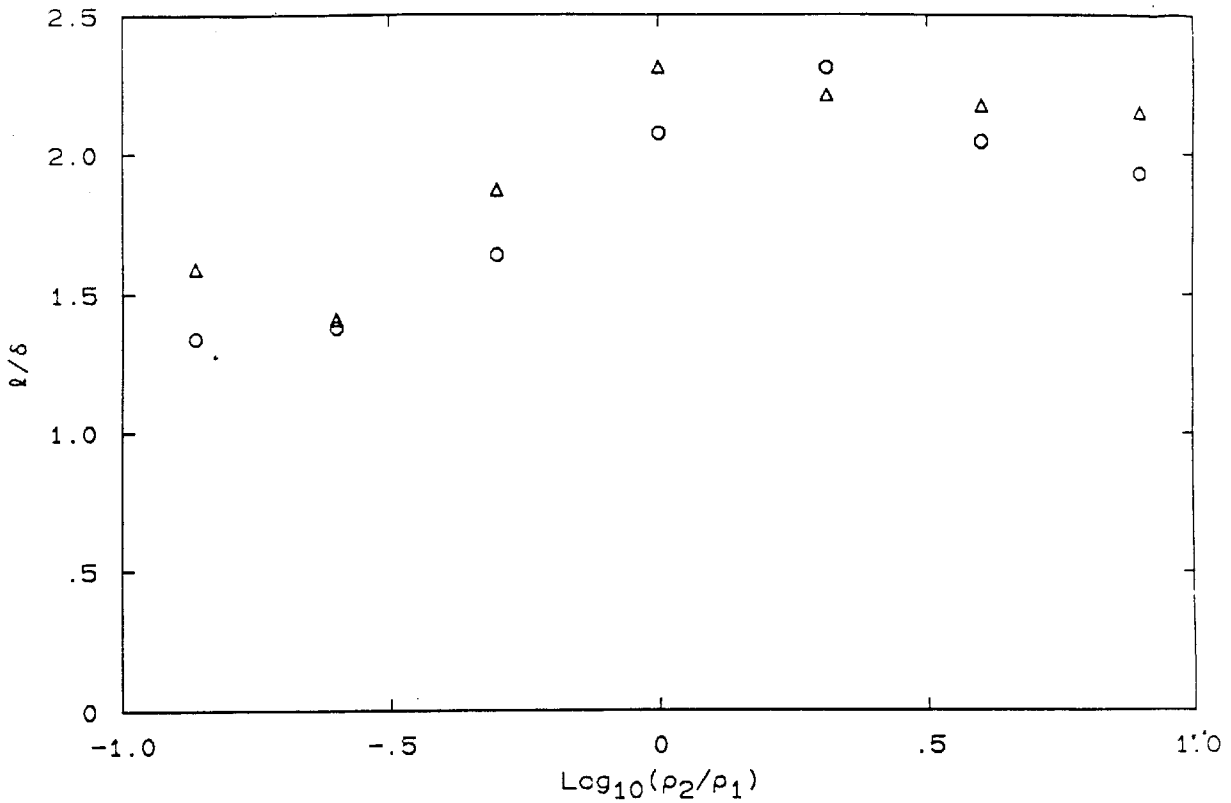

Figure 4.24 Autocorrelation length scales normalized by mixing-layer width.

Figure 4.24 shows the large structure spacing normalized by the local mixing layer width δ. Measurements by other researchers (*e.g.*, Brown and Roshko 1974, Koochesfahani, *et al.* 1979 and Bernal 1981) indicate a large structure spacing at uniform density in the range 1.4 to 1.8. This matches well with the three lowest density ratio cases, but is below the present results for uniform and high density ratio. The change in structure spacing coincides with the mixed-fluid flux ratio estimates crossing from above the theoretical predictions for entrainment ratio, to below. The theory proposed by Dimotakis (1986), mentioned previously, actually relates the entrainment ratio to the density ratio and to the large structure spacing, *i.e.*,

$$E = s^{1/2}\left(1+\frac{\ell}{x}\right) \tag{4.9}$$

Unfortunately, the experiments indicate that the large structure spacing is smaller at low density ratios, when the entrainment ratio is larger than predicted, and the converse for large density ratios. This is exactly the opposite to the dependence implied by Equation 4.9.

Probability Density Function of Composition

Shown in the last six figures in this chapter are the probability density functions (PDF's) of composition for the density ratios $\rho_2/\rho_1 = \frac{1}{7}$, 1, 4 . These are determined from the time-temperature rise data using the analysis detailed in Appendix C. The vertical axis is the probability density, $P(\xi; y)$, which depends on both the composition and the position within the mixing layer. Delta function singularities at the edges of this plot, representing the existence of pure fluid from the corresponding free-stream, have been plotted with the height scaled by the integral. These data are also plotted as a contour plot for each of the density ratios. In these plots two other calculations have been made. The dashed line in each is the mean composition ($\bar{\xi}$), calculated from the PDF and the point denoted by the asterisk on both the plot and the accompanying bar graph is the peak probability location and value. The scale at the right hand side of the figure is linear and shows that the contours in the plot have been exponentially spaced. The least squares fitting technique converged to these solutions with the residual in each case being on the order of 1%.

As noted by Konrad, all the results plotted up to this point which relate to the concentration field (ie. mean composition, mean temperature profiles, etc.) are contained within these figures. Several features are apparent from these plots. Note that the least square fit converged with the delta functions representing pure high-speed fluid growing as you exit the mixing layer toward that side, and the converse for the low-speed side. However, these delta function singularities

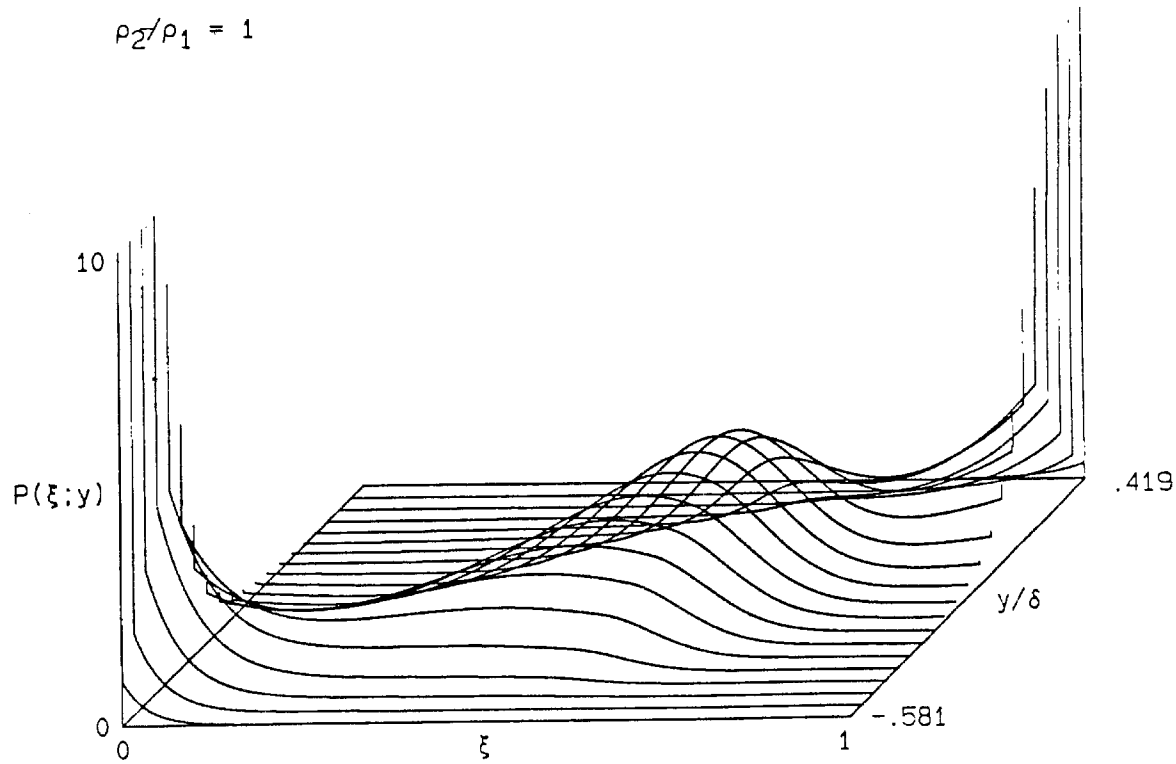

Figure 4.25 PDF of composition for $\rho_2 = \rho_1$.

representing unmixed fluid do not extend into the center of the layer for any of the three density ratios shown.

In agreement with Konrad, the present results display a "lump" of probability at a preferred composition. This composition shifts toward the low-density fluid as the density ratio varies toward either extreme. At the same time, the y-position of the peak of probability also shifts towards the light fluid. Also in good agreement with the measurements of Konrad, the mean composition is slightly flattened near the peak probability composition.

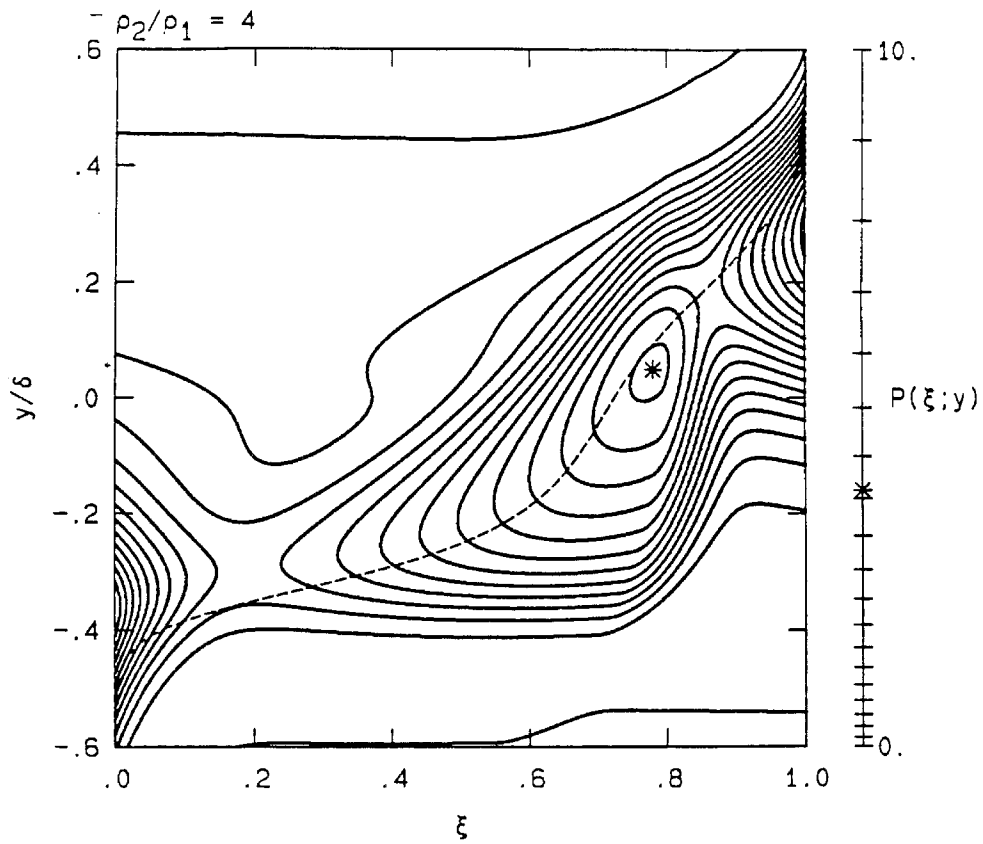

Figure 4.26 Contour plot of PDF for $\rho_2 = \rho_1$.

Summary

Based on the similarity of the profiles in Figure 4.12, it can be concluded that the distribution of mixed fluid within the two-dimensional shear layer is relatively insensitive to freestream density differences. This is reinforced by the invariance of the integral amounts, δ_m/δ and $\tilde{\delta}_m/\tilde{\delta}$ (Figure 4.13 and 4.14), which differ by only 10% for all density ratios investigated. Volume and mass entrainment rates from the high-speed stream and also total volume entrainment rates, do not vary significantly. The average power spectral density of the temperature fluctuations in the layer, when scaled with flame temperature (ΔT_f) and large structure convective time (τ_δ), is very similar for all density ratios and all

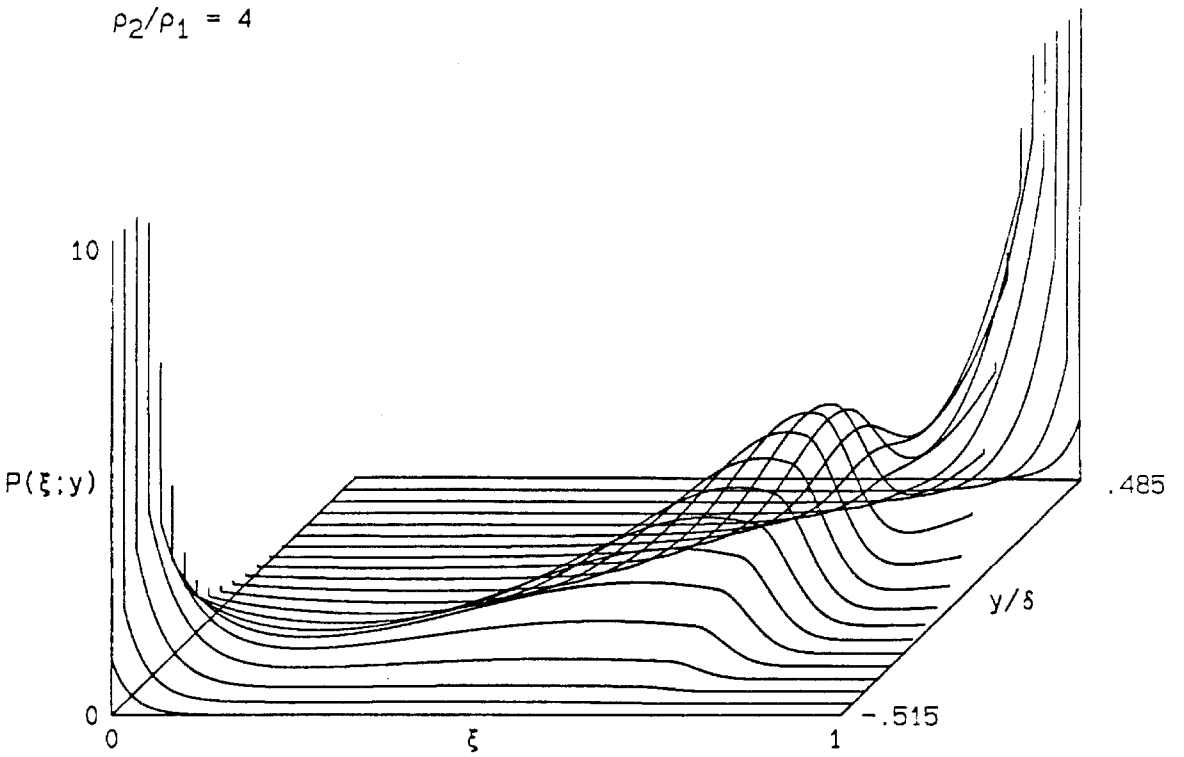

Figure 4.27 PDF of composition for $\rho_2/\rho_1 = 4$.

frequencies. This is not the case for the distributions of mixed fluid from each stream independently, or the composition of mixed fluid, which vary substantially with density ratio. Although the profiles of mixed-fluid composition are very similar, differing primarily by an offset value or constant, this offset or average composition of mixed fluid in the layer varies from nearly 1:2 to over 2:1 as density ratio increases, favoring the low-density fluid. The volume and mass entrainment rates of the low-speed fluid also depend strongly upon the density ratio. The entrainment ratios are shown to vary, but the dependence does not quite follow theory. There is evidence in the entrainment ratio data, the autocorrelation length data and temperature field measurements which indicates that the structure within the turbulent mixing layer is not invariant with respect to density ratio.

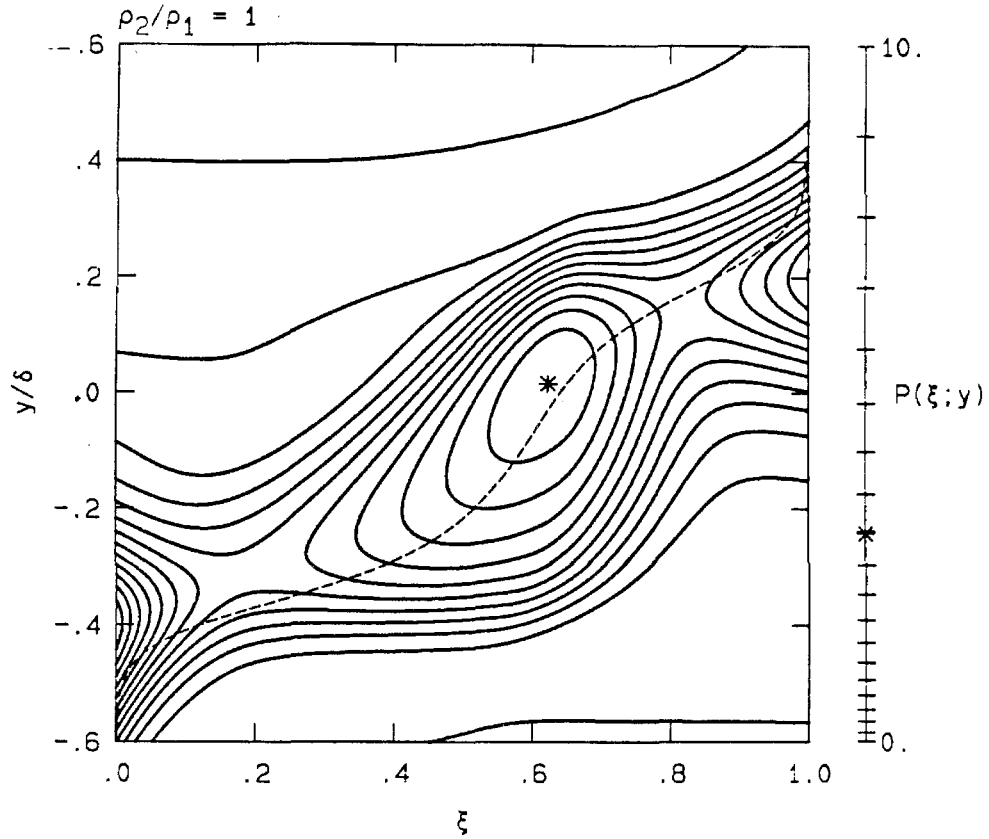

Figure 4.28 Contour plot of PDF for $\rho_2/\rho_1 = 4$.

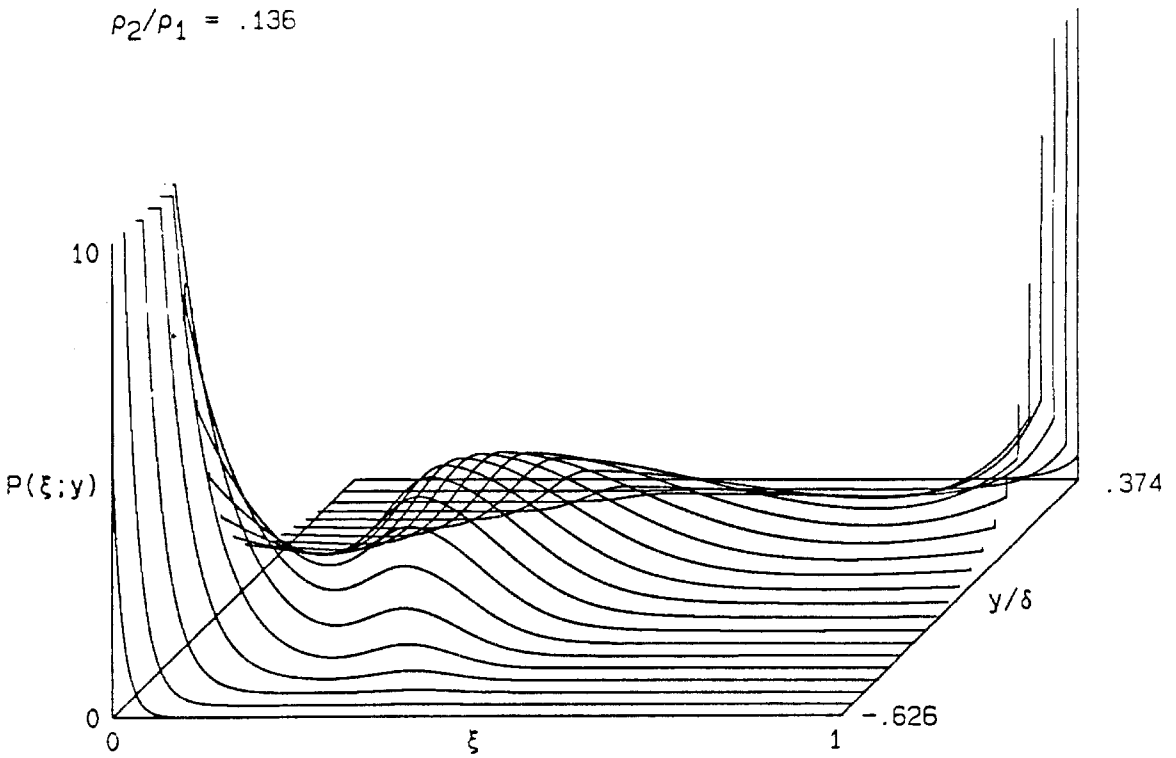

Figure 4.29 PDF of composition for $\rho_2/\rho_1 = 1/7$.

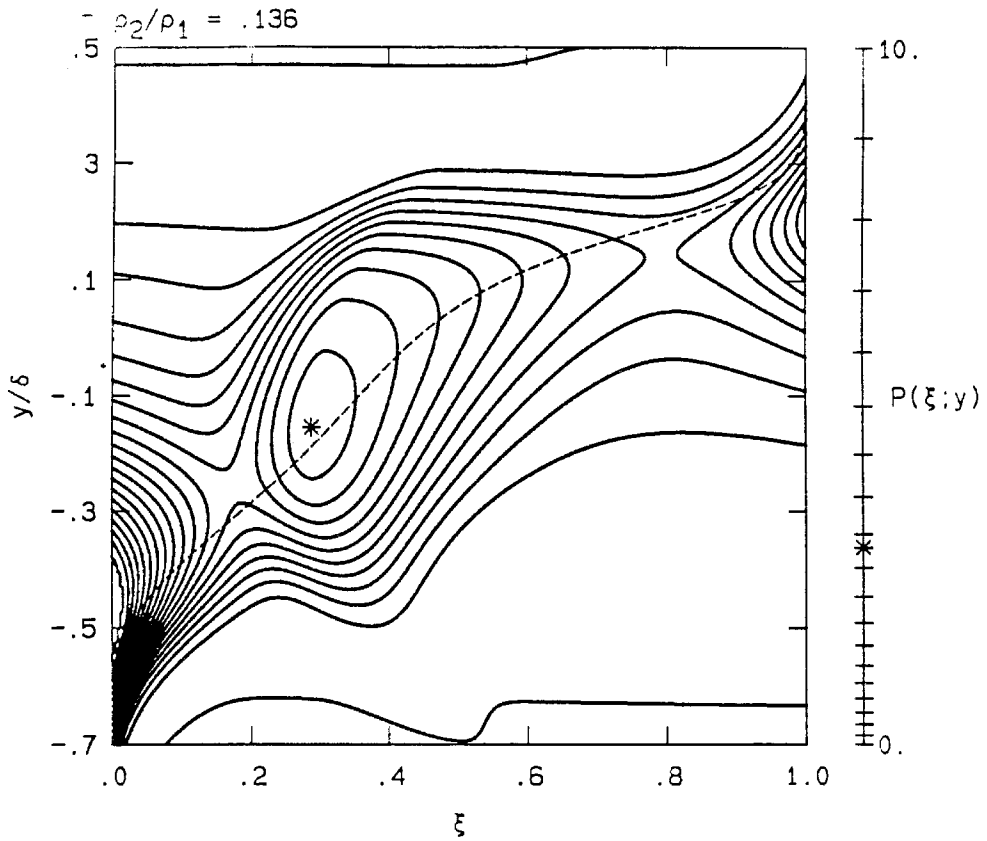

Figure 4.30 Contour plot of PDF for $\rho_2/\rho_1 = 1/7$.

Chapter 5. Chemistry, Diffusion and Damköhler Number

The chemical reactions used in these experiments are of two sets, those in which H_2 reacted with F_2 and NO served only as an initiator, and those in which NO was the primary reactant with F_2 . Both reaction sets are fast, highly exothermic homogeneous gas-phase reactions.

The first case (H_2 / F_2) has been discussed by many researchers (Mungal 1983, Cohen and Bott 1981, etc). It was thought that this reaction set was well understood and could therefore be used as a diagnostic tool and not as the object of investigation itself. However, further research has proved that this was somewhat optimistic.

$\underline{H_2 / F_2 / NO}$

As discussed by Mungal (1983) the overall reaction for the HF system is

$$H_2 + F_2 \rightarrow 2\,HF. \tag{5.1}$$

The probable reaction mechanism consists of a pair of second order reactions,

$$\begin{aligned} H_2 + F &\rightarrow HF + H \\ H + F_2 &\rightarrow HF + F. \end{aligned} \tag{5.2}$$

Both these reactions are very fast and once initiated proceed in an obviously cyclic manner, or more precisely, these two constitute a chain reaction with a branching coefficient of 1.0. However, the equilibrium concentration of dissociated H_2 and F_2 at room temperature is so low that these reactants can be premixed with negligible reaction taking place. Therefore, in the experiments where H_2 and

F_2 are the primary reactants, a small amount of NO must be premixed into the H_2 stream. When the combined mixture of H_2 and NO then comes into contact with F_2 , another second order reaction occurs which is completely hypergolic at ambient temperatures,

$$NO + F_2 \rightarrow ONF + F. \tag{5.3}$$

This reaction releases free molecular fluorine, which can then enter the cyclic reaction set 5.2.

This simple description of the reaction dynamics appeared sufficient. A set of experiments were performed in which the probability density function (PDF) of composition was to be determined from an investigation of the effects of stoichiometry upon the temperature profile of an equal density mixing layer. Using the HF system, an improved version of Wallace's technique for inverting the temperature measurements (discussed in Appendix C) was to be implemented and Konrad's measurement of the PDF for the equal density mixing layer were to be duplicated.

Figure 5.1 shows the product probability thicknesses which resulted from these experiments. Also shown are the results from Mungal (1983). Velocities for these experiments were 22 m/sec with a contraction exit height of $5\,cm$ on the high-speed side and 8.5 m/sec with a $7.5\,cm$ exit on the low-speed side. Note the discrepancies for the high ϕ cases. At a specific stoichiometry ($\phi = 7$), this difference was confirmed by several identical experiments. The sole difference between the present work and that of Mungal was the streams in which H_2 and F_2 were carried. Mungal performed experiments for $\phi < 1$ with the high-speed stream carrying H_2 , then switched the contraction sections and velocities to perform experiments for $\phi > 1$ with F_2 in the high-speed stream. In all cases, the rich reactant was H_2 . The present work used a different approach. Hermanson

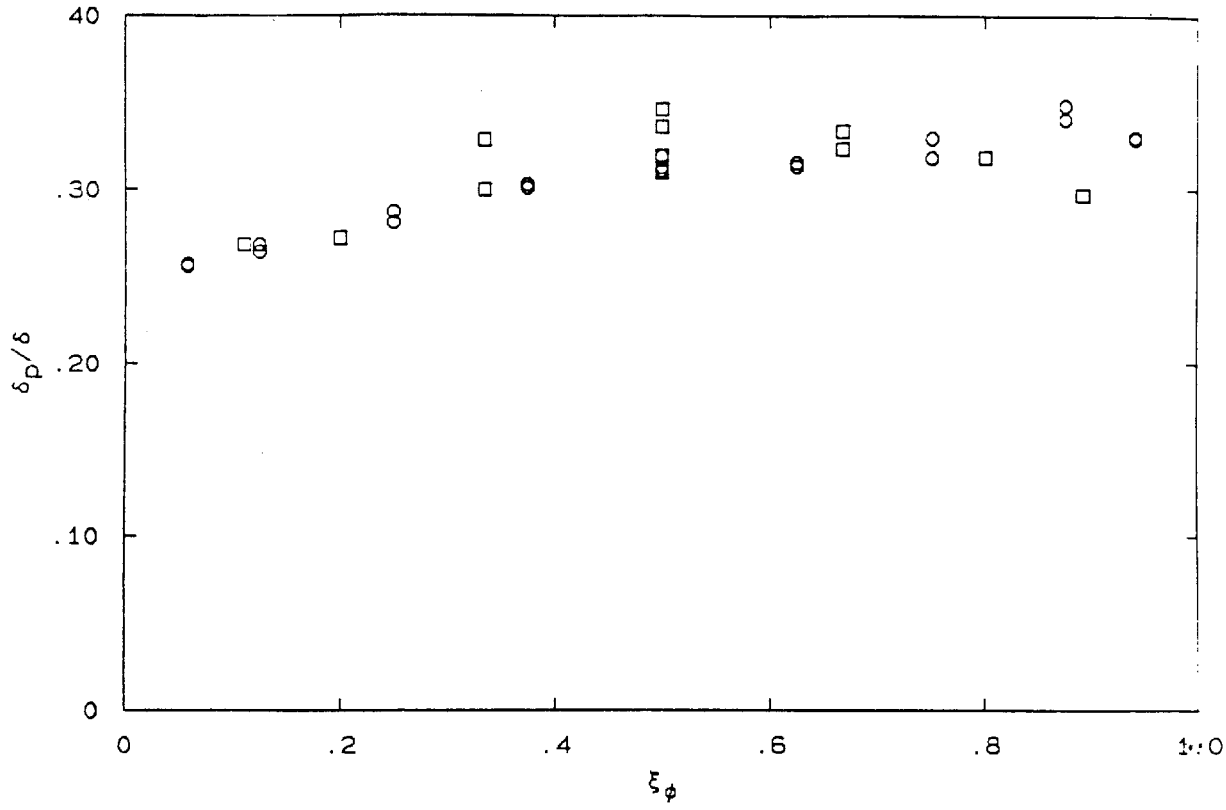

Figure 5.1 Product probability thickness versus stoichiometric composition.

$$\rho_1 = \rho_2\,,\ U_2/U_1 = .386\,,\ Re_\delta = 62{,}000$$

(1985) had used large concentrations of F_2 in high heat release experiments in this facility, and no indication of increased hazard or inadequacy of the post-run gas handling apparatus had appeared. Since extensive experience with the handling and use of F_2 had been gained, it was felt that keeping F_2 the lean reactant was no longer required for safety. All present experiments (circles) appearing in Figure 5.1 were performed with H_2 on the high-speed side, and therefore runs for $\phi > 1$ were performed with F_2 the rich reactant carried on the low-speed side.

The data in Figure 5.1 demonstrates that the amount of product formed depends on whether the rich reactant is H_2 or F_2 . This is an unsettling discovery,

and calls into question many of the assumptions which had been used in previous analysis and interpretation of the data. A set of four experiments were then performed which confirmed this observation.

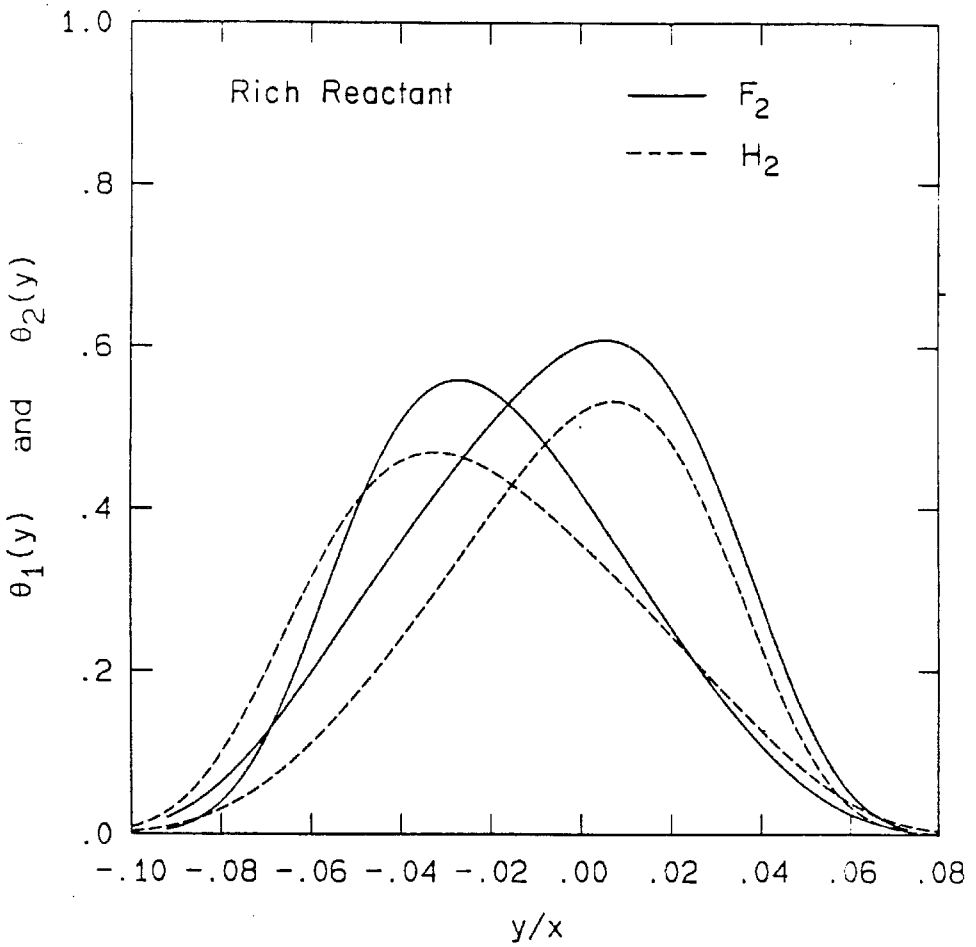

Figure 5.2 Reduced temperature profiles for F_2-richand H_2-rich.

$\phi = 7, 1/7$

Figure 5.2 shows the results of two flip experiments. In two, the velocities were set so that H_2 was carried in the high-speed stream, and the stoichiometries were flipped, $\phi = 7, 1/7$. The velocities were then interchanged, and with F_2 now on the high-speed side, another flip pair were performed. First, it can be seen

that the growth rate changed noticeably between the two sets of experiments. This has been covered in detail in Chapter 2, and is the result of the differences in initial conditions. The contraction sections for these experiments were $5\,cm$ on the H_2 side and $7.5\,cm$ on the F_2 side. Therefore a velocity flip changed both the boundary layers at the splitter tip, and because of the increased flow in the F_2 side, possibly changed the acoustic disturbance felt by the layer. As has repeatedly been suggested, the differences in growth rate may be discounted and the differences in peak height and normalized integral considered. In these quantities, the difference is clearly above the repeatability and also well above the accuracy expected from this facility. In both cases, the experiments performed with F_2 being the rich reactant, showed higher peak temperatures and a greater integral of product.

This brings up a serious and puzzling question. The velocities were all carefully set. The kinematic viscosities changed by a very slight amount. The streams were very carefully density matched. The specific heats of each stream were matched. The adiabatic flame temperatures were identical. Negligible pressure gradients existed in the test section. None of the macroscopic quantities used up to this time to characterize the mixing and reaction in the HF shear layer could therefore account for this observation. The molar possibilities above discounted, what molecular property could possibly be responsible? Although conventional thought at the time held that molecular transport coefficients could not effect high Reynolds number turbulent flows, the experiments of Konrad (1976) and Breidenthal (1981) had shown this to be incorrect. In separate studies, these experimenters demonstrated that the amount of mixing and reaction that occurs in the 2D mixing layer significantly depended upon the molecular diffusivity. It seemed some related phenomena could be taking place, because at

room temperature the diffusivity of H_2 is a factor of $3\frac{1}{2}$ higher than that of F_2 . To confirm this hypothesis a set of fast gas-phase reactants with intermediate diffusivities would be required. Unfortunately, no experimental test seemed possible because no such reactants were known.

As an alternative, a simple calculation was performed to evaluate the effects of differing diffusivity upon the Broadwell-Breidenthal (1982) model. This elegantly simple decomposition of the mixing and reaction inside turbulent flows uses two components. The first is a homogeneously mixed portion of the flow in which all species are uniformly distributed. Because of the uniformity, the diffusive transport (which is proportional to spatial gradients) could not possibly effect the amount of product formed in this part of the flow. The second component of the model is the laminar strained diffusion flame. Here the importance of the diffusive transport coefficients are immediately apparent. Since Mungal et al.(1983) had estimated a roughly 50/50 split between the two components in these gas-phase experiments, it was conceivable that an effect large enough to account for the differences in the data could occur.

Shown in Figures 5.3 and 5.4 are calculations which test this possibility. The Equations $D.13$ were solved for the non-reacting case, and the profiles of several species have been plotted versus the similarity space variable based on the diffusivity of N_2 . Two cases are shown in each plot. The first is the profiles that would result if all the diffusivities were identical, and equal to that of N_2 . The second in each case is the profile that results if the actual diffusivity in N_2 of the species in question is used. It is clear that the differences in the F_2 profiles are completely negligible, however, differences in the H_2 profile are significant. Unfortunately, it would appear from these plots that in the fast chemistry limit, the amount of product, which can be estimated by the intersection of the H_2 and

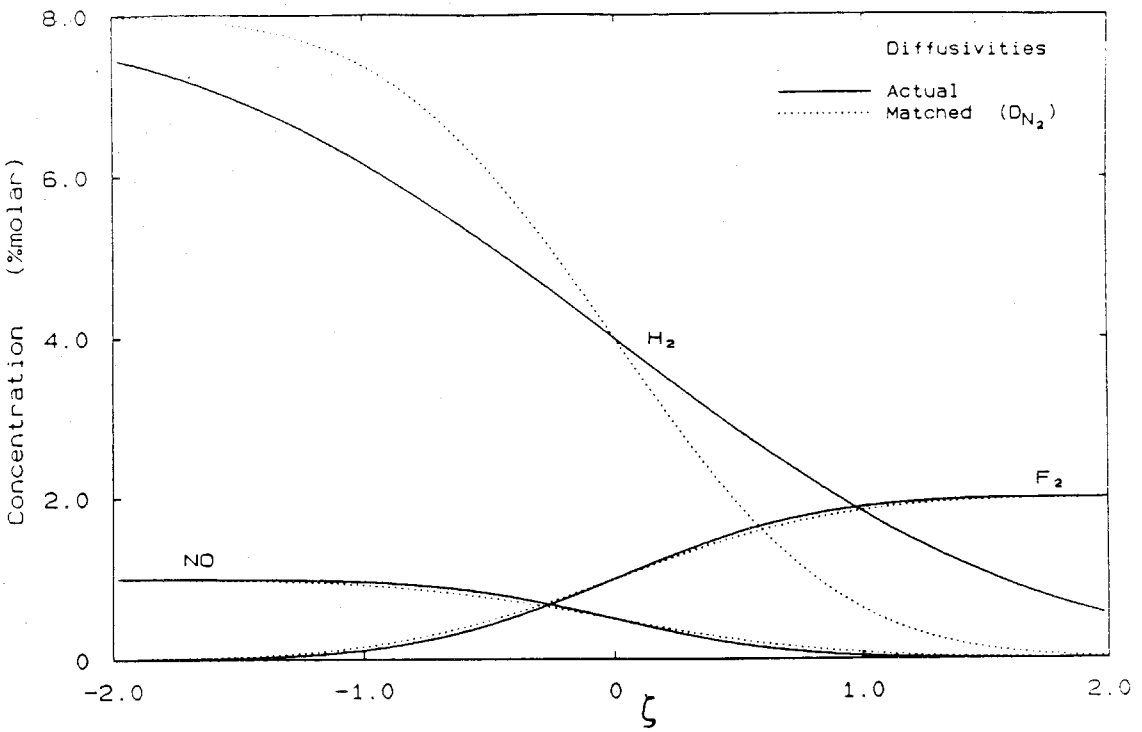

Figure 5.3 H_2-richdiffusion profiles.

F_2 profiles, is actually larger in the case where H_2 is the rich reactant. This is exactly the reverse of the observed effect.

The curves in Figure 5.5 show the integral amount of product in the laminar strained diffusion flame in the limit of fast kinetics as it is effected by differing diffusivities. The horizontal axis is the stoichiometric composition and is related to the freestream concentrations of the reactants. These solutions have been normalized by the results for equal diffusivity (given analytically in Equation $D.21$), which appears as a straight line at a value of 1. The additional constraint,

$$\mathcal{D}_1 \, \mathcal{D}_2 \;=\; 1. \tag{5.4}$$

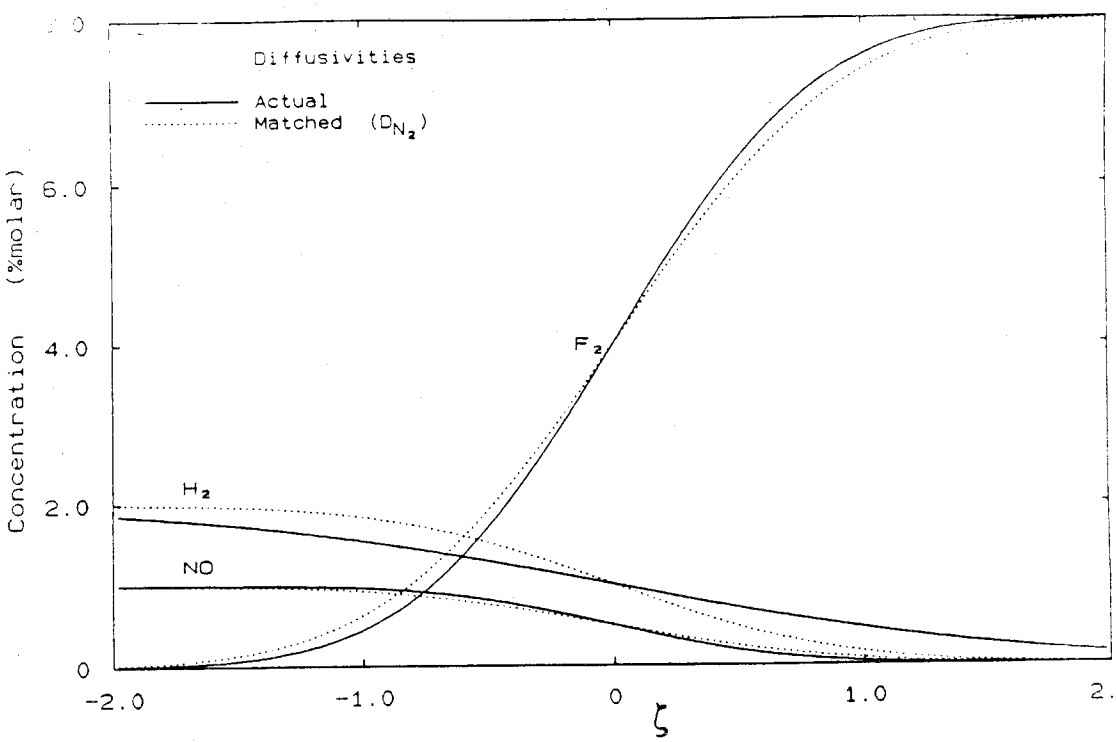

Figure 5.4 F_2-richdiffusion profiles.

has been imposed which allows the results to be plotted with the ratio $\mathcal{D}_2/\mathcal{D}_1$ as a single parameter. It also makes comparisons where the roles of species with different diffusivities are switched, particularly simple. As an example, consider a flip pair of experiments performed with H_2 carried in the high-speed stream and F_2 in the low-speed stream. The curve of interest is $\mathcal{D}_2/\mathcal{D}_1 = \mathcal{D}_2(F_2)/\mathcal{D}_1(H_2) \approx 1/4$. At a stoichiometry of $\phi = 7$ (ie. F_2-rich), $\xi_\phi = .125$ and from Figure 5.5, the normalized amount of product in laminar strained flame would be 0.8. Comparing these results to the case where H_2 is the rich reactant, $\phi = 1/7$, $\xi_\phi = .875$ and the amount of product would be 1.35. The amount of product in the H_2-richcase is nearly 75% greater than in the F_2-richcase. In the laminar strained diffusion flame, in the fast chemistry limit, the amount of product is greater if the

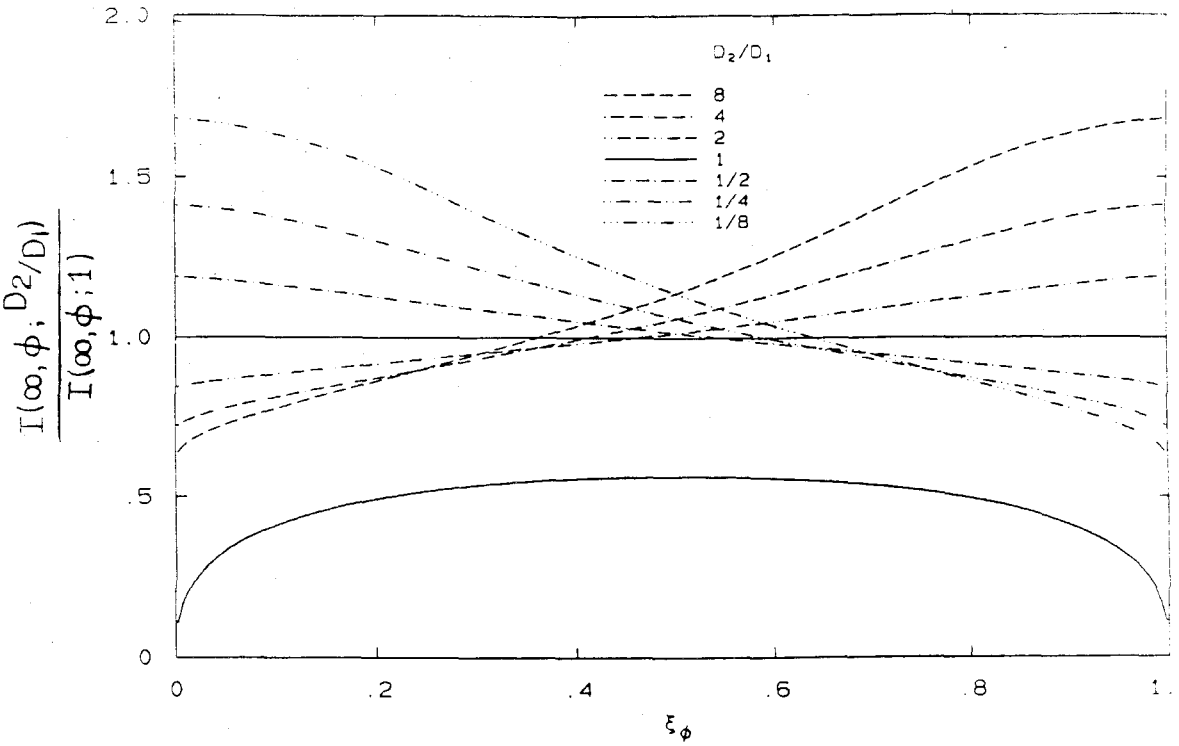

Figure 5.5 Product in the LSDF for several diffusivity ratios.

rich reactant diffuses faster, than if the lean reactant diffuses faster. The effects of differing diffusivity are opposite the observations. If any part of the flow exists in a spatially non-uniform condition, then the amount of product in that fraction of the flow should be greater for the H_2-richcase. In an approximate sense, the analysis in Appendix B suggests that the F_2-richcase measures the amount of mixed fluid from the H_2 stream at a Schmidt number corresponding to the diffusivity of F_2 . Similarly, the H_2-richcase measures the amount of mixed fluid from the F_2 stream at a Schmidt number corresponding to the diffusivity of H_2 . Clearly, the amount of product must be greater at the lower Schmidt number of the H_2-richcase. The effects of differing diffusivity alone could not account for the data in Figure 5.2.

The next possibility to be pursued was chemical kinetics. The experimental investigations of Mungal and Frieler (1988) had estimated the Damköhler number necessary for the amount of product to reach an asymptotic value. The Damköhler number is defined as the ratio of the fluid mechanical time, to the chemical time. This was expressed as the ratio of the large-structure turn-over time, to the chemical time determined from a numerical simulation of the reactions in a simplified geometry. The overall reaction rate hinged on Reaction 5.3, which in turn depends on the concentration of NO . This chemical time was therefore varied by performing experiments with different freestream concentrations of NO . Unfortunately, the present experiments were performed at well beyond this criterion. This implied that if chemical rates were responsible for the difference observed in Figure 5.2, then another rise in product for the $\phi = 1/8$ case must occur at NO concentrations beyond those investigated.

This possibility was addressed in an extensive set of experiments. Experiments were performed which investigated the effects of kinetics upon three distinct stoichiometries. For the case $\phi = 1/7$, the range of NO concentrations used in Mungal and Frieler was considerable extended, with no further increase in product measured. Hoping to shed some light on this dilemma, two other stoichiometries were also investigated. Velocities for these experiments were 22 m/sec on the high-speed side using a 5 cm contraction, and 8.5 m/sec on the low-speed side using a 7.5 cm contraction. All data for these are shown in Figure 5.6.

The vertical axis is a normalized integral of the temperature rise, the product probability thickness normalized by the width of the mixing region Definition and discussion of δ_p/δ appears in Appendix B and demonstrates that for the extreme stoichiometry cases, it is proportional to the volume fraction of the layer occupied by mixed fluid from the lean reactant free stream. The horizontal axis is the

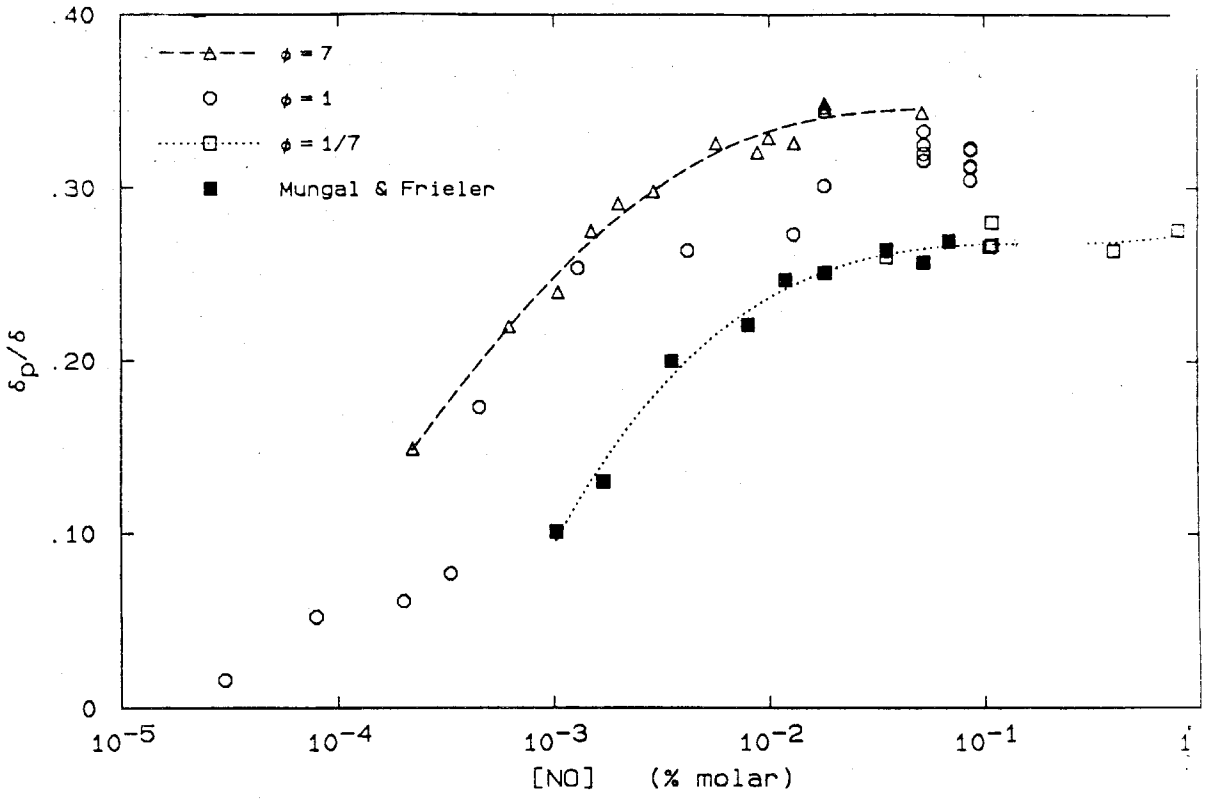

Figure 5.6 Product probability thickness versus NO concentration.

concentration of NO diluted in the high-speed hydrogen stream, in mole percent. The circles are data for $\phi = 1$, which do not follow a simple curve to as do the other two stoichiometries. A dashed line has been drawn through the data for the case $\phi = 7$, which are indicated by the triangles. Note the factor of 10 difference in the amount of NO required to rise to a specific level of product. Also note the higher level of the "fast" chemistry asymptote when F_2 is the rich reactant. The filled symbols are the results previously published in Mungal and Frieler ($\phi = 1/8$), and a dotted line has been added to aid the reader. For readers familiar with that work, note that the NO concentrations for this data have all been revised based on a careful calibration of the NO delivery system. The experiments for $\phi = 1/7$ in the present work show that a factor of 10 increase in the NO concentration did

not lead to an increase in the amount of product beyond the asymptote determined by the filled symbols. At some point, increased product would be expected due to NO becoming a major reactant. However, the data suggests that for reasonable concentrations of NO , the amount of product has indeed asymptoted.

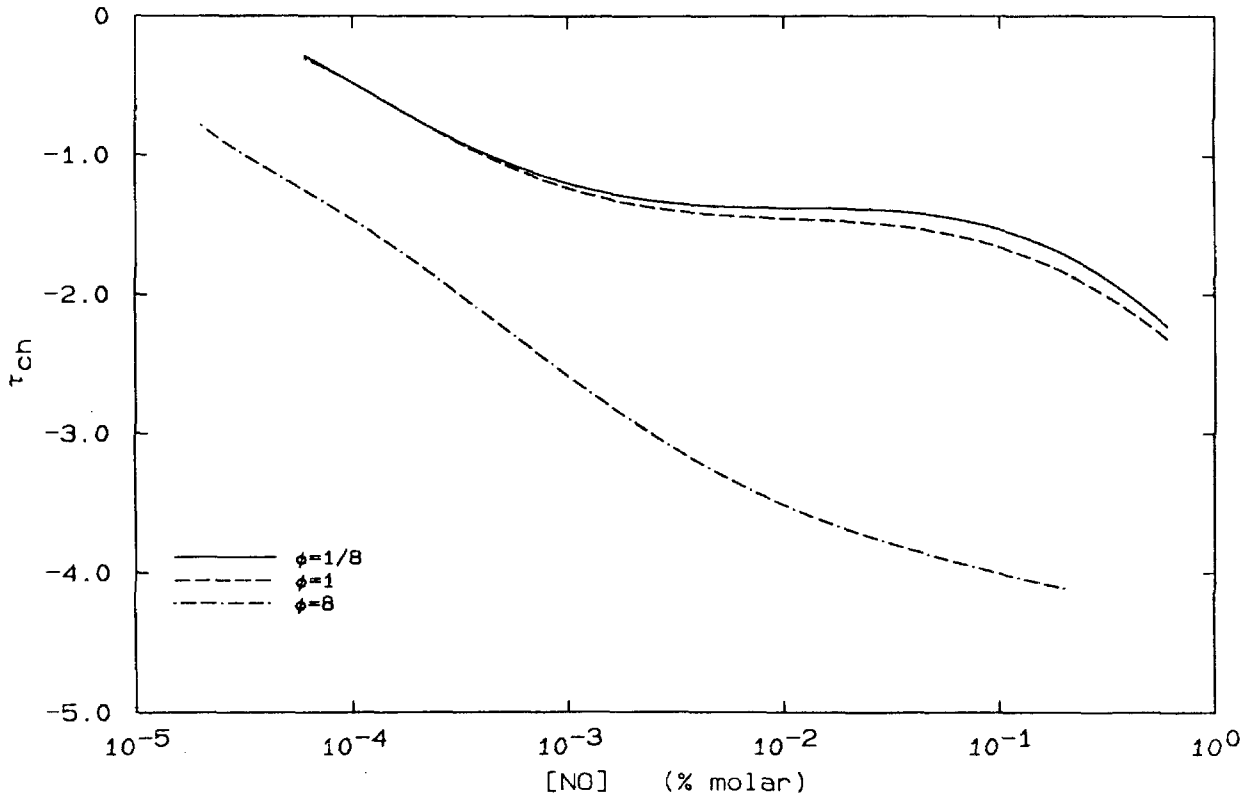

Figure 5.7 Calculated chemical times in homogeneous reactor.

Shown in Figure 5.7 are the results of many CHEMKIN simulations, described in Appendix E. These have been compiled to give the overall reaction rate of this system, expressed here as the chemical time (τ_{ch}), versus the concentration of NO . These calculations simulate the reaction occurring in the homogeneous part of the Broadwell and Breidenthal model (1982), including the rise of temperature. All relevant reactions for which rate data could be found were included in these

simulations, both the basic Reactions 5.2 and a host of others. These reactions and their associated rates and heat releases are summarized in Table 5.1.

Details of the interaction of these reactions and analysis of the effects each has on the overall process, is certainly beyond the qualifications of the author, and it is hoped also beyond the necessities of the present work. Suffice to say that significant changes between the calculations based on this set of reactions, the set used in Mungal and Frieler, and that used in Dimotakis and Hall do exist. The vertical axis on this plot is a measure of the overall reaction rate, in this case, the time (τ_{ch}) required for the system to reach 90% of the asymptotic value. A relevant timescale for comparison is the time of flight of the large-scale structure, from the splitter tip to the measuring station, which for these experiments, was approximately $30 msec$.

As discussed in Appendix E, the overall reaction rate increases in general as the amount of NO is increased. This dependence varies with the stoichiometry, as well as with the absolute concentrations of the major reactants H_2 and F_2 . However, because the curves for $\phi = 1$ and $\phi = 1/8$ are so similar, it can be seen that the rate does not depend strongly on the concentration of H_2 in cases where it is the rich reactant. Note the large difference between the curves for the H_2-richand F_2-richcases. The overall reaction rate for the F_2-richcase increases steadily as the concentration of NO increases, while the H_2-richcase becomes insensitive to increased NO over an intermediate range of nearly two decades. Results reported by Dimotakis and Hall (1988) do not indicate this feature. The sole difference is that several reactions have been added to the set used by Dimotakis and Hall. Some characteristic of this more complete reaction set must therefore be responsible for the differences. Results of the individual calculations for the H_2-richcases, shown in Figure E.6 and E.7, indicate that the initiation

Table5.1 : Rate Constants and Heat Release for Reactions in the $H_2/F_2/NO$ System.

Overall Reaction	Rate Constant(κ)	$^{298K}\Delta H^{o}_{rxn}(kJ/mol)$	
$H_2 + F_2 \rightarrow 2HF$			
$H_2 + F \rightarrow HF + H$	$2.7 \times 10^{12}\ T^{0.5}\ e^{-319/T}\ cm^3mol^{-1}s^{-1}$	-133.46	(A)
$H + HF \rightarrow H_2 + F$	$1.65 \times 10^{12}\ T^{0.6}\ e^{-16362/T}\ cm^3mol^{-1}s^{-1}$	133.46	(A)
$H + F_2 \rightarrow HF + F$	$2.9 \times 10^{9}\ T^{1.4}\ e^{-667/T}\ cm^3mol^{-1}s^{-1}$	-411.63	(A)
$HF + F \rightarrow H + F_2$	$1.33 \times 10^{13}\ e^{-50680/T}\ cm^3mol^{-1}s^{-1}$	411.63	(B)
$2NO + F_2 \rightarrow 2ONF$			
$NO + F_2 \rightarrow ONF + F$	$4.2 \times 10^{11}\ e^{-1150/T}\ cm^3mol^{-1}s^{-1}$	-77.069	(B)
$NO + F + M \rightarrow ONF + M$	$3.0 \times 10^{16}\ cm^6mol^{-2}s^{-1}$	-234.89	(B)
Others			
$F_2 + M \rightarrow 2F + M$	$2.12 \times 10^{13}\ e^{-16970/T}\ cm^3mol^{-1}s^{-1}$	157.82	(B)
$2F + M \rightarrow F_2 + M$	$3.25 \times 10^{8}\ T\ e^{+3190/T}\ cm^6mol^{-2}s^{-1}$	-157.82	(B)
$HF + M \rightarrow H + F + M$	$3.12 \times 10^{13}\ e^{-49980/T}\ cm^3mol^{-1}s^{-1}$	569.46	(B)
$H + F + M \rightarrow HF + M$	$3.6 \times 10^{18}\ T^{-1}\ cm^6mol^{-2}s^{-1}$	-569.46	(B)
$NO + H + M \rightarrow HNO + M$	$5.4 \times 10^{15}\ e^{+300/T}\ cm^6mol^{-2}s^{-1}$	-208.70	(C)
$HNO + M \rightarrow NO + H + M$	$3 \times 10^{16}\ e^{-24500/T}\ cm^3mol^{-1}s^{-1}$	208.70	(C)
$HNO + H \rightarrow H_2 + NO$	$4.8 \times 10^{12}\ cm^3mol^{-1}s^{-1}$	-227.28	(C)
$H_2 + NO \rightarrow HNO + H$	$3.2 \times 10^{6}\ cm^3mol^{-1}s^{-1}$	227.28	(C)
$2H + M \rightarrow H_2 + M$	$3.6 \times 10^{14}\ cm^6mol^{-2}s^{-1}$	-436.01	(D),(E)
$ONF + H \rightarrow NO + HF$		-334.57	(E)
$HNO + F \rightarrow NO + HF$		-361.23	(E)
$ONF + F_2 + M \rightarrow ONF_3 + M$		-97.487	(E)

(A) Cohen & Westberg (1983) (B) Baulch *et al.* (1981)

(C) Cohen & Bott (1982) (D) Mungal (1983)

(E) JANAF Tables (1985)

of the reaction does indeed become faster as the NO concentration is increased in this range. However, after the temperature has risen to roughly 60% of its asymptotic value, the rise slows drastically. This may indicate that the reactants end up in intermediate species which must then enter relatively slow reactions which release the heat required to reach the asymptotic temperature. Since this "plateau" occurs at times comparable with the transit time of the facility, it may be that a significant amount of these intermediates exist at the measuring station. This would lead to a decrease in the amount of reaction products measured in the H_2 case.

Several observations need to be made from a close comparison of results and data. Compare the values of NO at which the asymptote is reached in both Figures 5.6 and 5.7 for the H_2-richcase. The majority of the product thickness rise occurs during the region of NO concentrations where the reaction rate is not changing. It is possible that the rise in measured amount of product results from the initial 60% rise in temperature becoming faster as the NO concentrations increase. This would then imply that some fraction of the mixed fluid in the mixing layer remains unreacted even at the highest concentrations of NO . This reasoning would indicate that for the F_2-richcase, the calculations predict that the amount of product should begin to asymptote at $NO \sim 10^{-3}\%$. This does not actually occur until nearly a decade later, at $NO \sim 10^{-2}\%$. As discussed in Dimotakis and Hall, these difficulties may stem from details of the mixing process, particularly as it differs from the simplified model used for these calculations. Due to the strain rate history which the fluid undergoes as it is subdivided and reduced to the truly homogeneous mixture, the relevant fluid mechanic timescale may actually be substantially shorter than the time of flight.

For the moment the differences in the experimentally determined and calculated values of NO for which the chemistry becomes fast will be ignored. The results above suggest that the F_2-richcase may display more product (in Figure 5.2) because it has substantially faster chemistry. This conclusion may be partially correct, but additional complications exist. Figure 3.5 plots the distributions of mixed fluid, along with the mean number density for several different flip experiments. In these experiments, the adiabatic flame temperature was varied by changing both the stoichiometry and the absolute concentrations of the reactants. F_2 was the rich reactant in each experiment, with a mixture of H_2 and NO in the other stream. Note that for the lowest heat release cases the distribution of mixed fluid actually exceeds the mean number density. This is physically impossible, implying that at the center of the mixing region, more mixed fluid existed than total fluid, both mixed and unmixed. The result is obviously repeatable and indicates an experimental or analytical error. Since fluid mechanic reasons for this phenomena have been examined and dismissed, these experiments indicate that some reaction is taking place which is not properly accounted for in the calculation of the stoichiometric mixture ratio and the adiabatic flame temperature. No evidence for an excess amount of heat released by these reactions was indicated in the CHEMKIN calculations discussed above. In each case, the asymptotic temperature matched the estimated result assuming Reactions 5.2 and 5.3 proceeded to completion. This returned attention to the second component of the Broadwell-Breidenthal model, the laminar strained diffusion flame.

Calculations of the effects of finite kinetics on the laminar strained diffusion flame were next undertaken. Shown in Figure 5.8 are the results of several calculations chosen to represent the experimental results in Figure 5.6. The concentrations of each of the reactants, including NO , used in the calculations

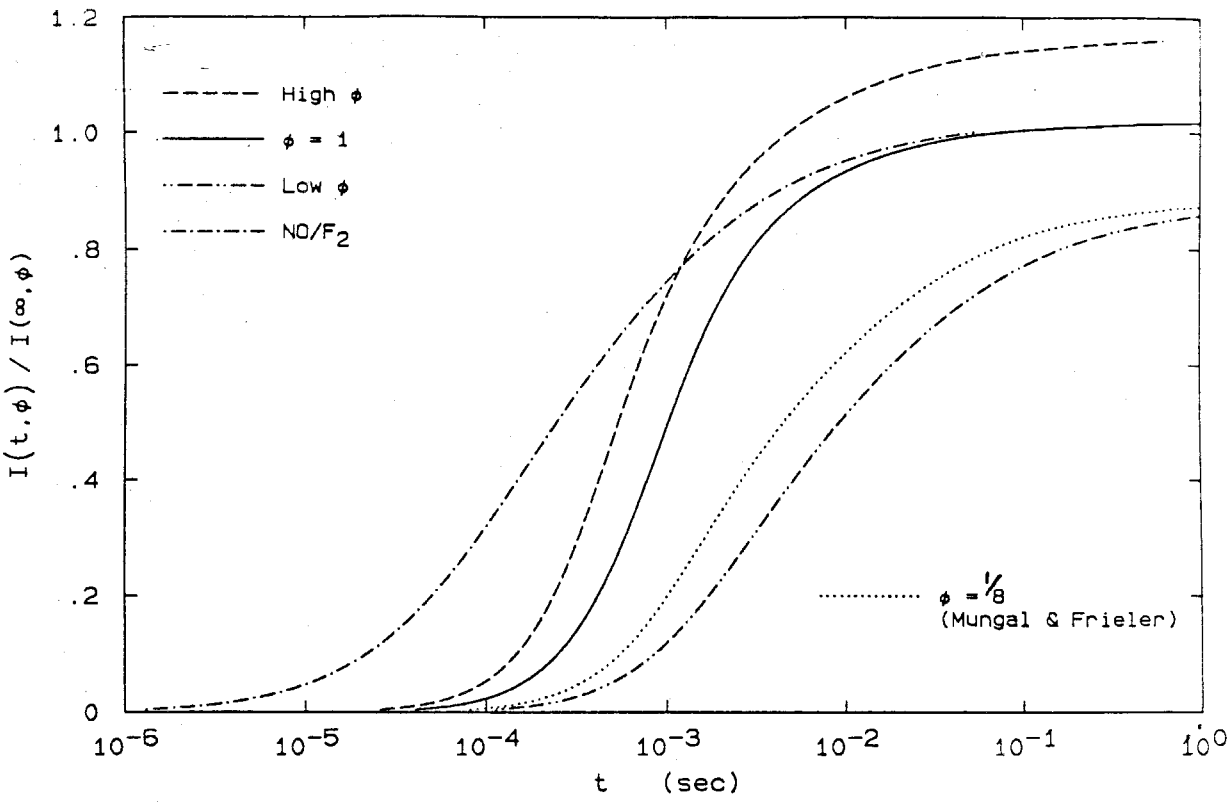

Figure 5.8 LSDF solution versus time for several cases.

match the values used in the experiments. The vertical axis in this plot represents the integrated temperature rise normalized by the temperature rise which would result if Reactions 5.2 and Reaction 5.3 were to proceed to completion. The calculations proceeded under the assumptions detailed in Appendix D and correspond to solution of Equations *D*.13. The reaction set used for these calculation was by necessity somewhat restricted. Those included were

$$NO + F + M \rightarrow ONF + M$$

$$NO + H + M \rightarrow NOH + M$$

$$2\,F + M \rightarrow F_2 + M$$

$$2\,H + M \rightarrow H_2 + M$$

$$H + F + M \rightarrow HF + M \tag{5.5}$$

in addition to the basic Reactions 5.2 and Reaction 5.3. Note that this differs from the set used in the homogeneous mixing calculations above. For future reference, the solution for a NO/F_2 flame similar to the experiments discussed in Chapter 6 is shown. The horizontal axis is labeled time and may be thought of as simply the physical time in seconds if the transient interface is the problem of interest. Hence, at 1 *msec* the 8% NO / .5% F_2 flame shown in the figure has reached roughly 75% of its asymptotic temperature distribution in similarity coordinates. Note that although this reaction is initiated much sooner, it finishes at about the same time as the faster of the H_2/F_2 flames. As an example of the application of this family of similarity solutions to a laminar strained diffusion flame, one might suggest that a relevant strain history is that of a flame which convects at the large-structure celerity, and undergoes the large-structure induced strain rate. For the experiments conducted here, this would indicate a reduced time of approximately 15 *msec*.

Two cases are calculated for low ϕ. The first corresponds to the experiments of Mungal and Frieler, and is plotted with a dotted line. The second is the $\phi = 1/7$ case plotted in Figure 5.6 and is the slowest rising curve on this plot. The remaining two H_2 / F_2 calculations for $\phi = 1$ and $\phi = 7$ are shown by the solid and dashed lines respectively. Note that the overall reaction rates inferred for each of these chemical systems from the laminar strained diffusion flame differ substantially. Specifically, the two low ϕ curves are nearly a decade slower than the high ϕ and stoichiometric curves.

Several disturbing features present themselves in this figure. First, note that the curve for the NO / F_2 flame appears to asymptote nicely to the fast-chemistry limit and the curve for H_2 2/ F_2 , $\phi = 1$ asymptotes to slightly greater than 1.

However, the curve for H_2 / F_2 , $\phi = 7$ has exceeded the estimated fast-chemistry limit by nearly 20%. Also, the curve for H_2 / F_2 , $\phi = 1/7$ appears to have asymptoted to a value significantly below its fast-chemistry limit. The later is not too difficult to understand. Reactions have been neglected (by necessity), which provide paths for the intermediate species to reach completion. The system is therefore trapped in a higher potential state, and the full adiabatic flame temperature cannot be reached. This phenomena has the same cause as the "plateau" in the chemical time calculations based on the homogeneous reactor, however in that case, the additional reactions could eventually occur. The former is slightly more difficult. When the laminar strained flame is F_2-richthe flame interface (in the fast-chemistry limit) resides well into the region which contains NO . Perhaps reactions which produce intermediates in the H_2-richcase, reactions such as

$$NO + H + M \rightarrow 2\,NOH + M \tag{5.6}$$

are occurring with H_2 or H which would not ordinarily come into contact with the F_2 . Since this H_2 or H would normally not contact F_2 , it would not be included in an *a priori* estimate of the amount of heat to be released in the fast-chemistry limit. It could then appear as excess heat release, and could account for the experimental results. Detailed examination of the species profiles produced in these calculations would probably shed some light on these issues, but time dictates that this be left for the future.

For the present, it suffices to state that there are indications that the laminar strained flame does indeed release less heat in the H_2-richcases than in the F_2-richcase, relative to the estimated fast-chemistry limit for each case.

The calculations performed above, can be rephrased in a form which is much more convenient for comparison to the experimental data. Instead of asking what

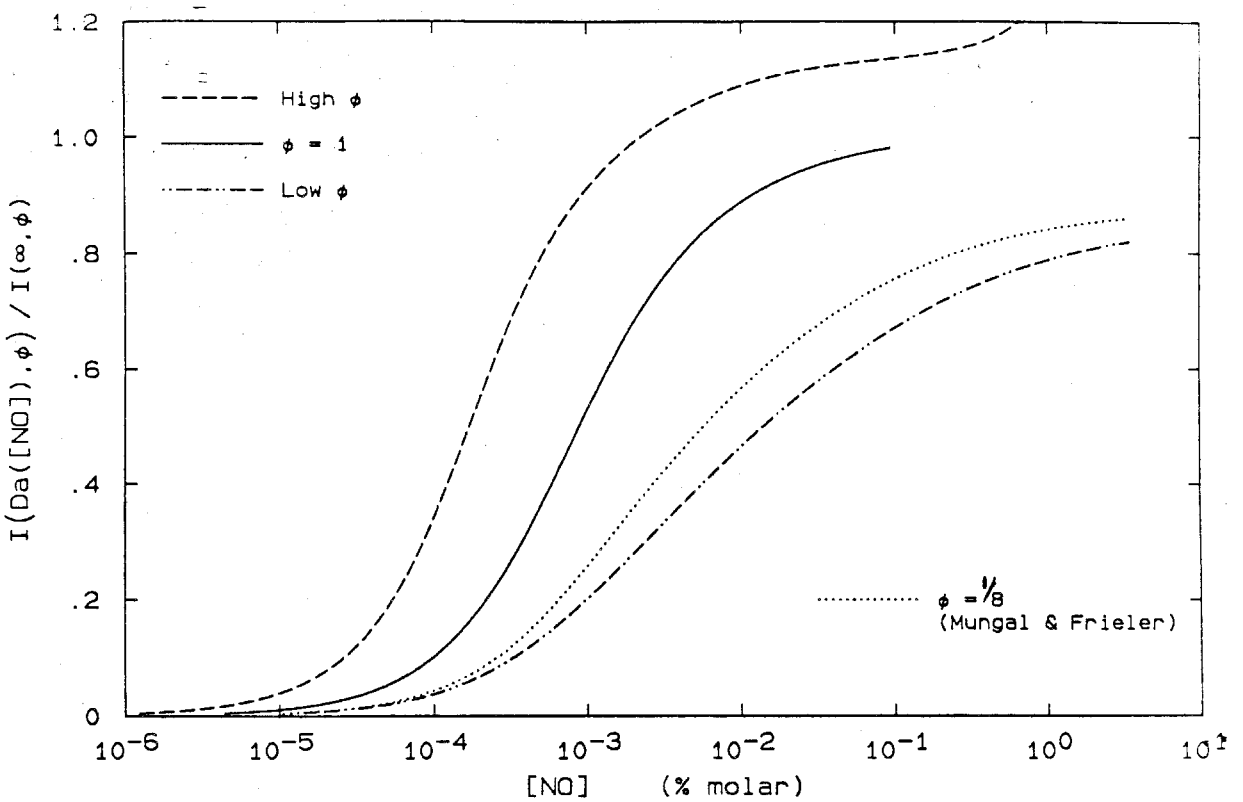

Figure 5.9 LSDF solution at a specific time versus NO concentration.

the similarity time dependence of the laminar strained flame is for a specific set of reactant concentrations, we can ask, what concentrations are required to achieve a certain response at a specific similarity time. The results of such calculations are shown in Figure 5.9. The specific time chosen for these calculations was the one mentioned above, that of a reacting interface convecting at the large-structure celerity and undergoing the large-scale strain rate. Note the striking similarity between this plot and the experimental data, Figure 5.6. For the F_2-richcase, product begins to appear at NO concentrations like 10^{-5}, and the curve asymptotes at about $NO \sim 10^{-2}$. Also note the upturn of this curve when the concentration of NO becomes comparable with that of H_2 . This is to be expected, since for these calculations, the fast-chemistry limit which these

curves were normalized by was based solely on the concentrations of H_2 and F_2 . Therefore when NO becomes a major reactant, the estimates for both the stoichiometry and the adiabatic flame temperature need to be revised. However, at concentrations far below those at which NO becomes a major reactant, the amount of heat released in the F_2-richflame is greater than the estimated fast-chemistry limit. For the H_2-richcases, the product begins to appear at NO concentrations of about 10^{-4}, however the asymptote is not reached until $NO \sim 10^0\%$. This is substantially beyond the concentration at which the data in Figure 5.6 asymptotes.

The final curve appearing in Figure 5.9 is for $\phi = 1$, denoted by the solid line. Interestingly, in the laminar strained diffusion flame, the overall reaction rate for this case appears to be much faster than the H_2-rich(low ϕ) case. This is in contrast to results from the homogeneously mixed reactor, where the two were found to be very similar. This difference may serve to explain the unusual dependence of the product thickness at this stoichiometry upon the NO concentration.

The Broadwell-Breidenthal model needs to be reexamined in view of several results. The laminar strained flame component has been envisioned as an interface existing between volumes of pure fluid from the freestreams. Measurements of the probability of mixed fluid (Figures 4.12 and 6.5) indicate that a very small amount of unmixed fluid exists at the center of the layer. This implies that rarely will an interface exist between pure fluids, because pure fluids do not coexist at a given location to a significant degree. Since unmixed fluid from the freestreams cannot come into direct contact, mixing is occurring between previously mixed fluid at the edges of the shear layer and the freestream on that side.

This implies that in cases where the chemistry is fast and there is excess of one reactant, the majority of the reaction will be occurring on the lean reactant side of the mixing layer. Entrainment on the rich reactant side merely supplies fresh reactant to the homogeneously mixed region, and it is in interfaces between this homogeneously mixed region and the lean reactant freestream that reaction takes place. This process has been recognized as the reason for the symmetry shift in the mean temperature profiles with changes in the stoichiometry (*e.g.,* Mungal and Dimotakis 1984). It is also consistent with the formation of the ramp-like structure in the temperature time-series. This perhaps explains why, at low heat release and extreme stoichiometry, the results of the laminar strained diffusion flame so closely correspond to the actual dependence of product formation upon the concentration of NO .

This description does not apply to the case where the freestream reactants are nearly equal. When one reactant is not in excess and the chemistry is fast, the homogeneously mixed region has been largely depleted of reactants. Therefore on the edges of the layer where the entrainment of fresh reactants is occurring, they are being mixed into a stream with a small concentration of the complementary reactant. It is likely that for this case, the majority of reaction occurs in the homogeneously mixed region. However, as shown by the calculations in Figure 5.9, the laminar strained flame in this case begins formation of product at substantially lower NO concentrations than the homogeneously mixed region. Thus the data in Figure 5.6 may depict the following sequence. As the level of NO is gradually increased, the laminar strained flames between the homogeneously mixed region and either freestream begin to form product. When sufficient reaction is occurring, say at a concentration $NO \sim 3 \times 10^{-4}\%$, the laminar strained flames are forming and dumping a sufficient number of radicals into the homogeneously mixed region

to initiate formation of product in this region. This transition, from slow to fast chemistry in the homogeneously mixed region, could be artificially shortened by the addition of the reaction products formed in the strained flames. The transition to fast chemistry in the laminar strained flames, however, is not complete until $NO \sim 10^{-2}\%$. This scenario may explain why this particular stoichiometry behaves differently than cases at either extreme.

It has been demonstrated that the H_2/F_2 system is not as simple as had previously been thought. Admittedly, most of the complications stem from reactions involving NO . Several play important roles in the overall progress of the primary reactions. However, it must be observed that while the amount of analytical difficulty introduced might be proportional to the fraction of NO , so is the overall reaction rate. Therefore, to a large extent, these difficulties are unavoidable.

$\underline{NO\,/\,F_2}$

In experiments for which NO serves as the primary reducing agent, the reaction is

$$2\,NO + F_2 \;\rightarrow\; 2\,ONF \tag{5.7}$$

and the probable mechanism is a second order homogeneous reaction combined with one of third order, i.e.,

$$\begin{aligned} NO + F_2 &\rightarrow ONF + F \\ NO + F + M &\rightarrow ONF + M. \end{aligned} \tag{5.8}$$

It was thought that this simple chemical system could be used to perform a set of experiments which avoided the complications found in the HF system. However, early experiments displayed the same difficulty found in the F_2-richexperiments.

Flip experiments performed by setting the velocities and interchanging the concentrations of NO and F_2 produced probability profiles which exceeded 1. Again, an additional reaction was occurring which made the estimate of the stoichiometry and the adiabatic flame temperature inaccurate. Further research, many phone calls to knowledgeable chemists and an extensive search of the existing literature for information on gas-phase reactions involving fluorine and nitric oxide, finally turned up a potential cause. As is known by any sophomore chemist, nitrogen has several oxidation states. It appears that further oxidation of ONF was occurring through the reaction

$$ONF + F_2 + M \rightarrow ONF_3 + M \tag{5.9}$$

This additional reaction releases 30% the enthalpy of the basic reaction set 5.7. Ordinarily, this would leave the same difficulties which occur in the HF system discussed above,however, a solution was found. Although a very small amount has been published on this reaction, no rate data has been reported. The experts consulted were of the opinion that Reaction 5.8 would be a relatively fast reaction, but probably much slower than Reactions 5.7. Using this as an assumption, it can be shown that this additional reaction will only be of importance when the flow contains excess F_2 .

Figure 5.10 shows the resulting temperature-composition transform for three different stoichiometries, $\xi_\phi = 1/9,\ 1/2,\ 8/9$ $(\phi = 1/8,\ 1,\ 8)$. The solid line for each stoichiometry is the temperature which results from Reactions 5.7. The dotted lines indicate the additional heat which is released when Reaction 5.8 occurs for compositions which are F_2-rich. It can easily be seen that the additional heat release from Reaction 5.8 is not as great an effect when the composition is NO-rich. For this case, the adiabatic flame temperature calculated for Reaction 5.8

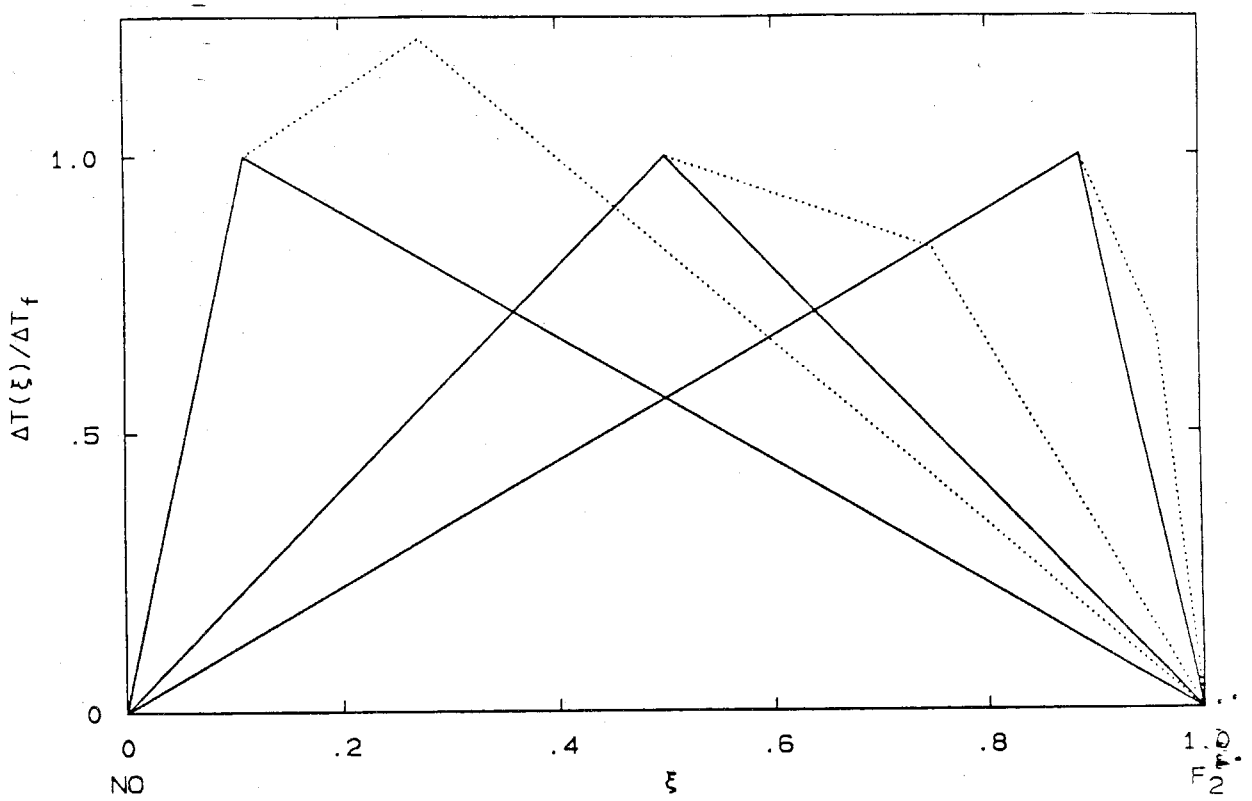

Figure 5.10 Temperature-Composition Relationship for NO/F_2 System.

$\phi = 1/8, 1, 8$

is not exceeded at any composition. This is a key element in the proper use of the ONF system as a diagnostic tool. In fact, using the analysis in Appendix B, it can be seen that this case can be used to give a slightly better approximation of the amount of mixed fluid from the F_2 stream than would be possible if the additional reaction did not occur. Therefore, the flip experiments discussed in Chapter 6, using NO/F_2, were performed with an excess of NO . Specifically, the stoichiometry appearing in Figure 5.10 farthest to the right was used for all experiments.

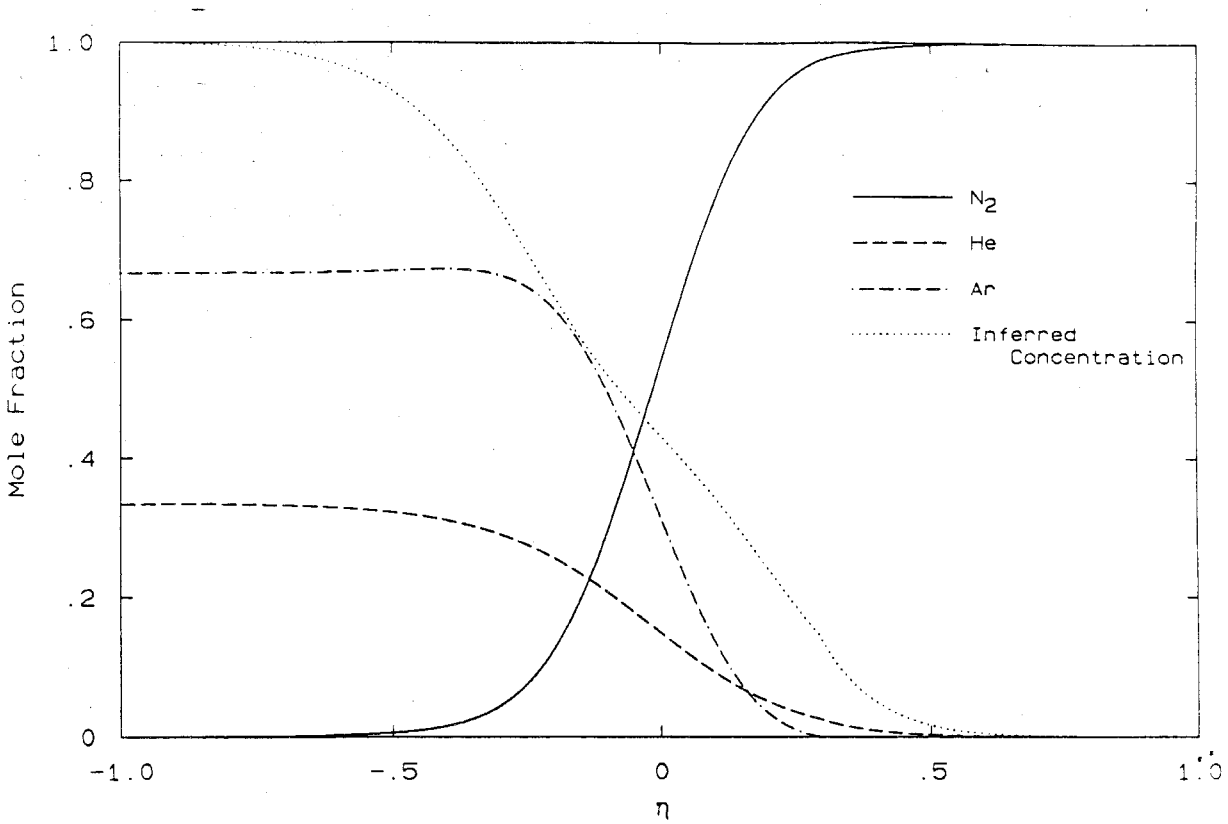

Figure 5.11 Tertiary diffusion solution and estimated probe response for Konrad's equal density experiments.

Effects of Tertiary Diffusion

Finally, as a note of caution. It has been demonstrated that the effects of molecular diffusion have a measurable impact on the mixing and reaction in the turbulent shear layer, particularly in the presence of chemical reaction. In fact, some questions remain as to what extent the present results regarding the effects of density ratio are intermixed with the effects of differing diffusivity. However, these effects are not restricted to reacting flows. Konrad used an aspirating probe to directly measure concentration. To infer composition from the response of the probe, a calibration technique was used in which mixtures of intermediate composition were sampled. This simple procedure posses no problem if the

flow is composed of only two gases, however, this calibration technique cannot accommodate the effects of differing diffusivity.

Figure 5.11 shows the results of a calculation of the diffusive interface produced in Konrad's equal density experiments. These experiments were performed with N_2 in one stream and a mixture of He and Ar in the other. Shown in the figure are the profiles of the concentration of each species when the Equations $D.12$ are solved. Also shown is a curve depicting the estimated probe response to the concentrations at that position. Note that in some regions, the probe response would indicate N_2 concentration significantly in error. It is not felt that these effects were large, or that any particular conclusion may have been in error. However, it is not clear that the potential for difficulty has been fully appreciated.

Summary

The preceeding discussion has been presented as somewhat of a chronological history of a year and a half of experimentation and musings. It is perhaps relevant to point out that although a dilemma appeared, it was a dilemma only in the understanding of turbulent mixing and reaction, and usually in the application of analysis based on simplifying assumptions. In every case, the difficulty was caused by assuming the reaction system was simpler than it is.

The data given in Figures 5.1 and 5.6, when presented in unnormalized form, are the results which will be measured in these reacting flows if the specified reactants are used at the given concentrations. They represent the results which modelers and numericists must be able to reproduce if they are to recreate, let alone predict, these reacting flows. The phenomena displayed in these figures, and especially Figure 5.2, stand as perhaps the toughest tests proposed to date for modeling turbulent reacting flow. Involved are details of molar transport and

the influence of the large-scale structure, molecular transport and the effects of differing diffusivities, and finally, a (moderately) complicated reaction system. As shown in the data, these effects are measurable and it is doubtful that a more common combustion system, say involving hydrocarbons, will not be similarly influenced. It that been demonstrated that the amount of heat released when the mixing layer contains excess F_2 is greater than when it is H_2-rich. This appears to be primarily due to the overall reaction rate for the HF system being substantially faster in the former case. However this is not a complete explanation, and a significant coupling of the effects of differing diffusivities with this chemical system is indicated. The dependence of the formation of product upon the concentration of NO has been found to be represented well by the results of calculations of the laminar strained diffusion flame when there is a large excess of one reactant. Correspondence was not good for either the LSDF or the homogeneous reactor calculations when the freestream reactant concentrations were equal, or more generally, where the ratio of the stoichiometric mixture ratio to the entrainment ratio equals unity. Because the reaction is not localized, as it is in the case of extreme stoichiometry, this situation presents a unique test for modeling the interaction of the components of the Broadwell-Breidenthal model.

It has been demonstrated that the H_2/F_2 system is not as simple as had previously been thought. There also appears to exist additional reactions for the ONF system, with formation of higher oxidation states of NO complicating the association of temperature rise with composition. However, if an excess of NO is used the problems are largely avoided. For use as a diagnostic tool, the NO/F_2 system used in this fashion appears to be the most promising.

Chapter 6. The Effects of Reynolds Number

The effects of Reynolds number on the mixing and reaction in an equal density, subsonic, gas-phase, non-buoyant, two-dimensional turbulent mixing layer, were investigated next. In experiments with very high and very low stoichiometric mixture ratios ("flip" experiments), the heat release from an exothermic reaction serves as a quantitative label for molecularly mixed fluid originating in the lean reactant freestream. The probability and number density profiles of the mixed fluid can be inferred from temperature measurements. Although the Reynolds number in these experiments was varied by a factor of 15, profiles of these quantities show little variation, with integrals varying by less than 7%.

Several investigations in the past have dealt directly with the subject of the present work. Konrad (1976) performed a series of experiments in subsonic non-homogeneous layers using pitot static pressure measurements and the Brown-Rebollo aspirating probe. Using the concentration measurements to infer the amount of product that would be formed in a fast reaction, he concluded that beyond the mixing transition, the amount of product was independent of the Reynolds number. Mungal *et al.* (1985) performed a study of the uniform density case using the same combustion facility as the present work. Using the HF chemical system, they performed a set of chemically reacting experiments over a range of Reynolds numbers significantly higher than that of Konrad. Measuring the mean temperature profile produced with the high-speed stream carrying a great excess of H_2 , they concluded that the amount of product actually decreased as the Reynolds number increased.

Although it has been the subject of study in the past, there are several reasons why the present work focuses on the effects of Reynolds number on the shear layer. It was felt that some part of the variation in product formation found by Mungal, *et al.* (1985) might have in fact been due to the complications found in the HF reaction system. As discussed in Chapter 5, some indications exist that the H_2 rich case used in Mungal's experiments might not represent a fast chemistry limit. At the same time, realization had been made that experiments at a single stoichiometry do not indicate the amount of mixing unambiguously. In interpreting experiments at a single stoichiometry, one cannot distinguish between a change in the amount of mixed fluid, and a change in the composition of the mixed fluid.

Experiments involving chemical reaction between mixtures of nitric oxide and nitrogen (8% NO / 92% N_2) in one stream and fluorine and nitrogen (.5% F_2 / 99.5% N_2) in the other have been performed. The practical range of velocities allowed experiments to be carried out over the range of Reynolds number 10^4 *to* 2×10^5. Table 6.1 shows the velocities used for each of the experiments.

Table 6.1 : Velocities for Reynolds Number Experiments

$\mathbf{Re}_\delta$ $(\times 10^{-4})$	$\mathbf{U_1}$ (m/sec)	$\mathbf{U_2}$ (m/sec)
1.05	2.2	0.85
1.50	3.5	1.35
3.65	9.9	3.8
6.53	22.	8.5
9.19	44.	17.
17.2	83.	32.

This produces a Reynolds number range, based on the downstream measuring station and mean velocity, of $5 \times 10^4 < Re_x < 2 \times 10^6$. The Reynolds number used throughout the remainder of this chapter will be based on the local layer width, δ, and is defined as

$$Re_\delta = \frac{\Delta U \delta}{\nu} \tag{6.1}$$

where ΔU is the velocity difference between the two streams. The contraction sections used for these experiments had $7.5cm$ exits for both streams and "flips" were performed by interchanging velocities. Experiments were performed with the heat release at levels well below the threshold suggested by Wallace (1981) and confirmed by Hermanson *et al.* (1985), (and Chapter 3) beyond which heat release begins to measurably affect the fluid mechanics of the turbulent shear layer. The adiabatic flame temperature was $48K$ for all of the experiments. The magnitude of possible buoyancy effects can be estimated from the Richardson number. For the lowest velocities used,

$$Ri = \frac{\Delta \rho}{\rho_o} \frac{g\ \delta}{(\Delta U)^2} = 0.06 \tag{6.2}$$

which is at the threshold suggested by Koop and Browand (1979) above which buoyancy becomes important. No obvious effects of buoyancy are observed for this case, and higher velocities are well below this value. Measurements of temperature rise were made using a rake of eight resistance wire ($2.5\mu m$) thermometers, as described Chapter 1. As discussed in Chapter 5, kinetic rates for these experiments were all more than a factor of five higher than rates at which product formation may be assumed to be mixing limited.

Figure 6.1 shows the results of two techniques for determining the extent of the mixing region, plotted versus the Reynolds number. The edges of the temperature profile have been used as an estimate of the layer width and the results are labeled

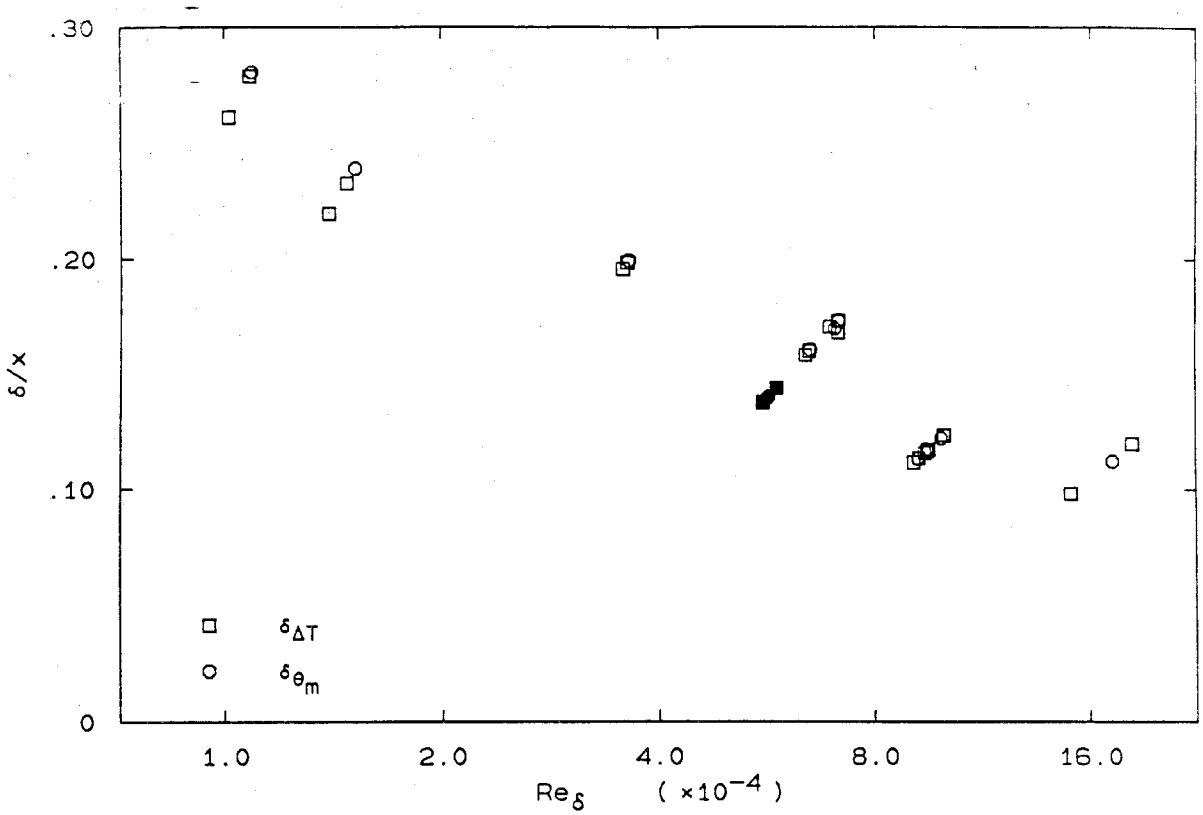

Figure 6.1 Growth rate of mixing layer versus Reynolds number.

(Filled symbols ⇒ tripped.)

$\delta_{\Delta T}$. Also, the edges of the mixed-fluid profile were used to estimate the layer width. Labeled here δ_{θ_m} , this width is the distance between the 1% points of the distribution of mixed fluid determined from the flip. Both of these estimates were shown in Chapter 4 to correspond well with the visual thickness. Both show substantial dependence upon the Reynolds number with the layer width changing by nearly a factor of 3 over the range investigated. Throughout this chapter, the thickness determined from the mixed-fluid profile will serve as a reference length scale and will be labeled simply δ from this point on. Uncertainty in the estimates of growth rate of the layer, at a given absolute velocity and for a specific fluid,

would scatter the data roughly along diagonals, since both the layer width and Re_δ are decreasing. This can be seen to occur for most of the Reynolds numbers. The experimental error in determining this width can be best estimated from the data near Reynolds number of 10^5. Six independent experiments are shown here, and the scatter is roughly 10%. The data about $Re_\delta = 6 \times 10^5$ is scattered along a diagonal for different reasons. Shown are three very different pairs of experiments. The center group of three points are the data taken at conditions comparable to the rest of the Reynolds number data. Another pair are the equal density case from the density ratio flips. These were performed with a different high-speed contraction, and therefore different high-speed boundary layer. The third pair of experiments were performed at the same velocity and with the same contraction sections as the remainder of the data, however both the high and low-speed sides had tripping devices placed in the boundary layers upstream of the splitter tip. These devices consisted of $0.75mm$ dia. wires attached to the splitter plate, parallel to the trailing edge, $40mm$ upstream. The comparison of tripped and untripped data is, strictly speaking, an examination of initial condition effects. However, even without deliberate introduction, these effects exist throughout the Reynolds number range. In particular, for the highest two Reynolds numbers investigated, natural transition of the inlet boundary layers is expected to occur. Therefore, conclusions regarding high Reynolds number limits are best formed with some measure of the effects of initial conditions in mind. Filled symbols will be used exclusively for data from these tripped experiments throughout this chapter.

Mixed Fluid Profiles

Figures 6.2 and 6.3 show, respectively, the profiles of mixed high-speed fluid and the profiles of mixed low-speed fluid for each of the Reynolds number. As in the plots appearing in Chapter 4, the horizontal axis has been shifted to align

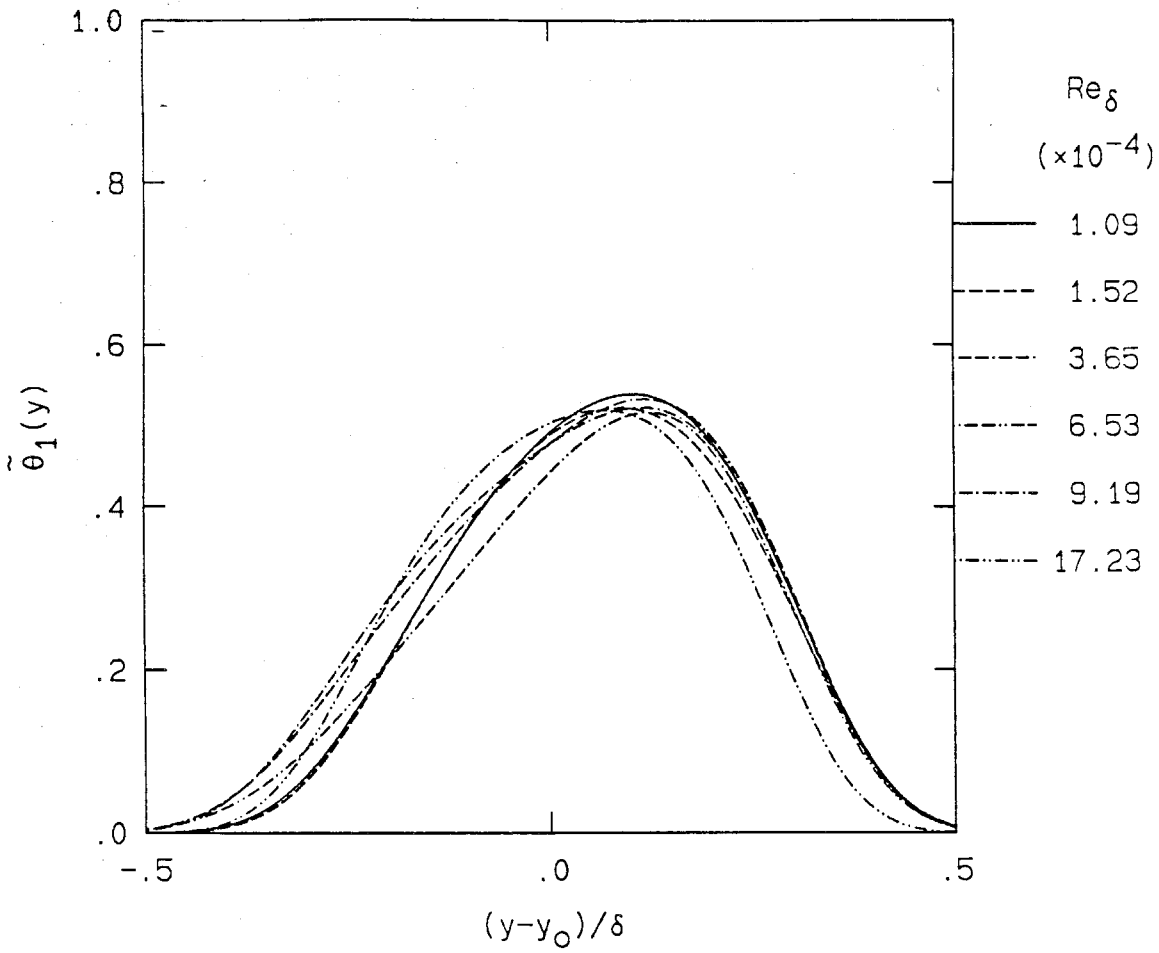

Figure 6.2 Mixed high-speed fluid profiles for each Reynolds number.

the edges of the mixed fluid profile for each pair of experiments, and has been scaled by the layer width δ. The scaling is particularly necessary, because the factor of 3 difference in growth rate would completely obscure several important observations. The most obvious of these is the similarity of the profiles in Figure 6.2. The symmetry and height of each of these profiles is nearly identical, with just a hint that the profiles may be changing symmetry slightly as the Reynolds

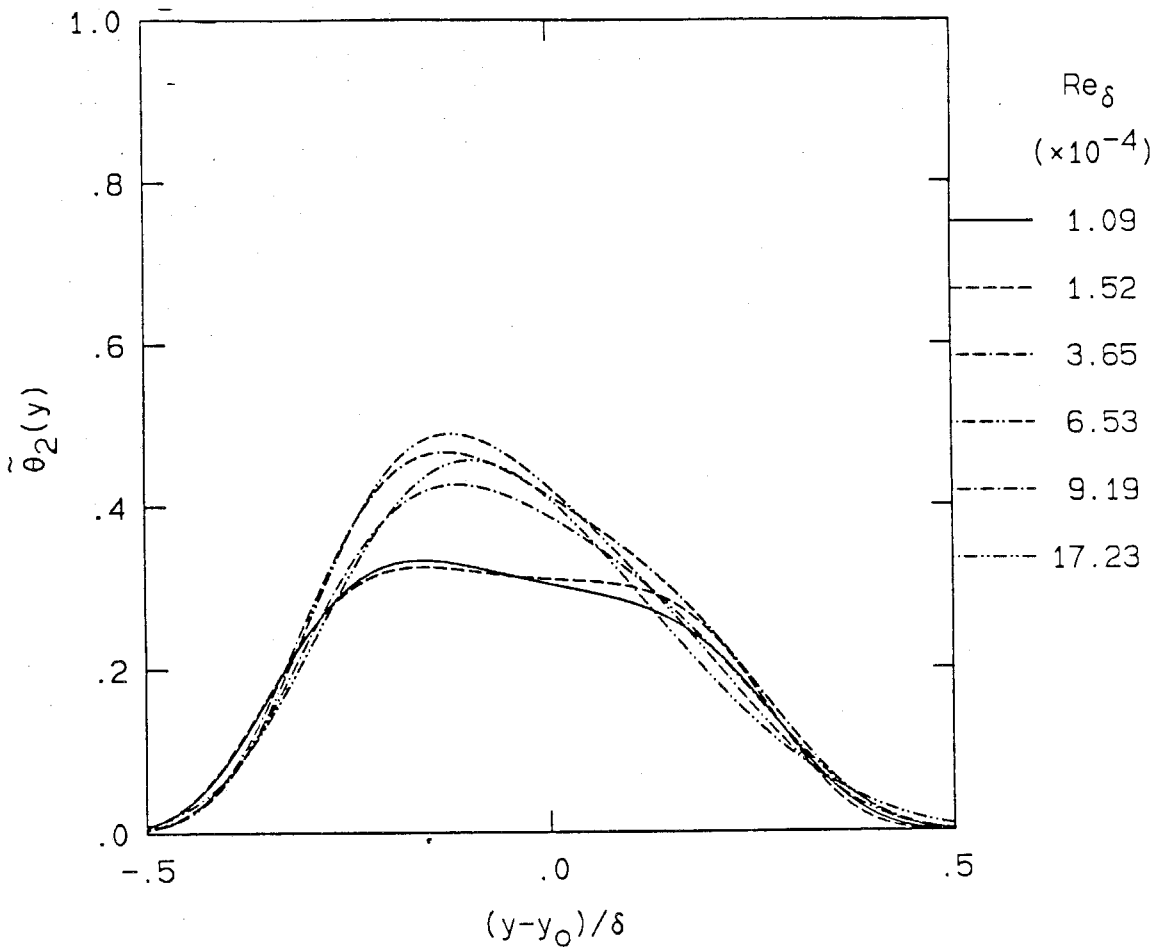

Figure 6.3 Mixed low-speed fluid rrofiles for each Reynolds number.

number increases. If instead of the shift and scale being determined by the mixed-fluid profile, these were based on the individual mixed high-speed fluid profile, these curves would lie nearly on top of each other.

The same cannot quite be said for the mixed low-speed fluid profiles shown in Figure 6.3. A large shift in the character of the profile occurs between Reynolds number 15,000 and 30,000. Both profiles below Reynolds number 20,000 are markedly flat over the center third of the mixing region. Konrad (1976) found that a mixing transition occurred at a particular Reynolds number. The distribution

and amount of mixed fluid changed during that transition, which he determined to begin at $Re_\delta \sim 10^4$, for the unequal density case $\rho_2/\rho_1 = 7$. This Reynolds number was based on the viscosity of N_2, a logical, if somewhat arbitrary choice, for his experiments. Since the viscosity of He is a factor of seven higher and the relevant figure lies somewhere in between, the expected value of the transition Reynolds number for equal viscosities is certainly lower. It is expected that the transition in the current equal viscosity gas-phase experiments will have occurred at the same Reynolds number found by Breidenthal (1979) in liquid experiments, i.e., begin at about $Re_\delta \sim 2,000$ and be completed by $Re_\delta \sim 10^4$. It is possible that the change in the profile of mixed low-speed fluid represents a remnant of the transition and some additional time is required to redistribute the mixed fluid into self similar form. Another possibility is that the forcing due to resonance with the acoustic mode of the facility causes these changes.

Note that the quantities plotted ($\tilde{\theta}_i(y)$), are dilatation corrected. Because the heat release was low ($1 - \tilde{\delta}/\delta \sim .05$) the changes involved in correcting for dilatation are very small. The corrected quantities were selected because they seem the most relevant. Remember that, in the limit of zero heat release, plots of $\tilde{\theta}_i(y)$ and $\theta_i(y)$ would be identical and the number density $\overline{n}(y)$ would equal 1.0 identically.

Figure 6.4 shows the mixed-fluid thickness and probability thickness from each of the streams as a function of the Reynolds number. The difference between dilatation corrected and uncorrected quantities can be seen, here in integral form, to be inconsequential. Note that there does not appear to be a substantial trend. The normalization for this plot has been chosen differently in order to facilitate comparison with the previous work of Mungal, et al.(1985). Instead of using the mixed-fluid profile to measure the layer width, the normalization used here is the

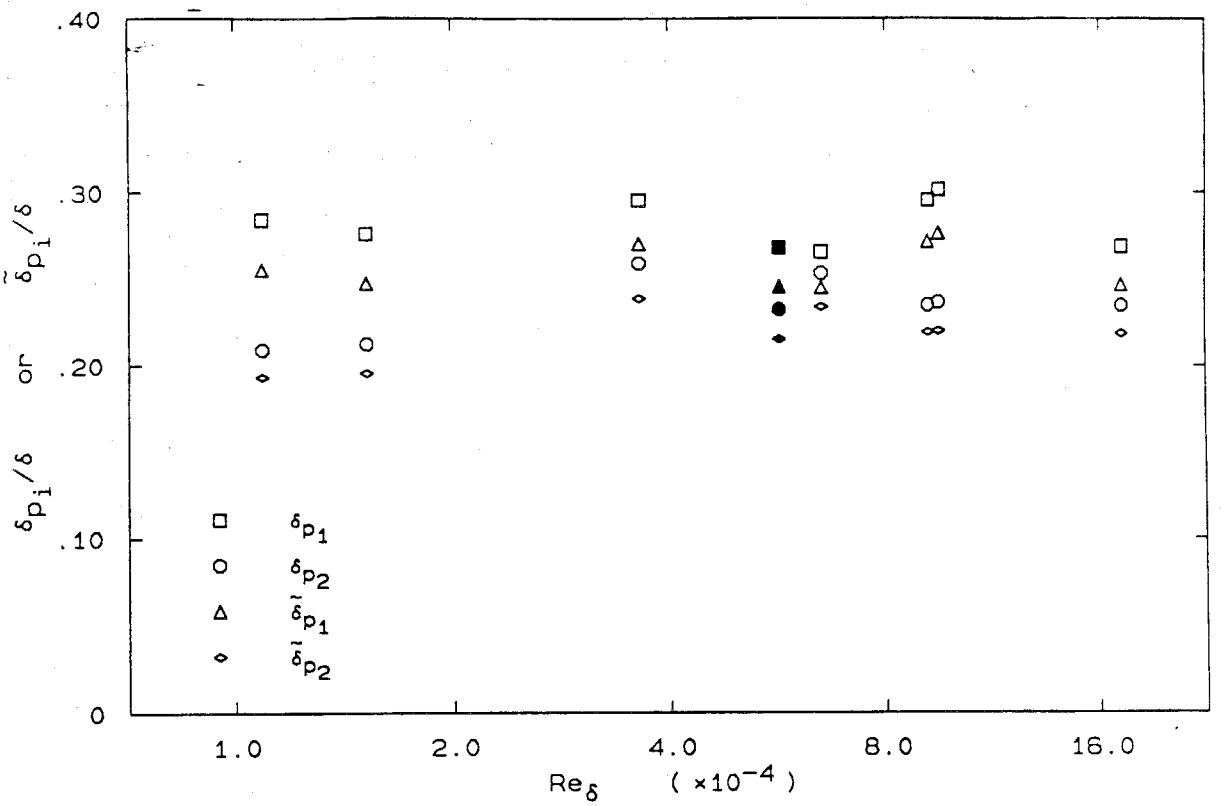

Figure 6.4 Mixed high and low-speed fluid thicknesses and probability thicknesses.

width determined from the individual profile whose integral is δ_p. Comparison of the present values for δ_{p_2}/δ with those of Mungal et al.(1985) reveals good agreement. If the last four Reynolds numbers are considered (excluding the tripped case), a decline in the amount of product of 16% per decade is indicated, just slightly less than their value of 20%. It is felt however, that the majority of this decline represents the effects of initial conditions. Comparing the values for the tripped case with the highest Reynolds number case where the boundary layers had naturally transitioned, very little difference is found.

Figure 6.5 shows the result of adding the mixed-fluid profiles for the flip, along with the mean number density for the pair of experiments. It can be seen that the

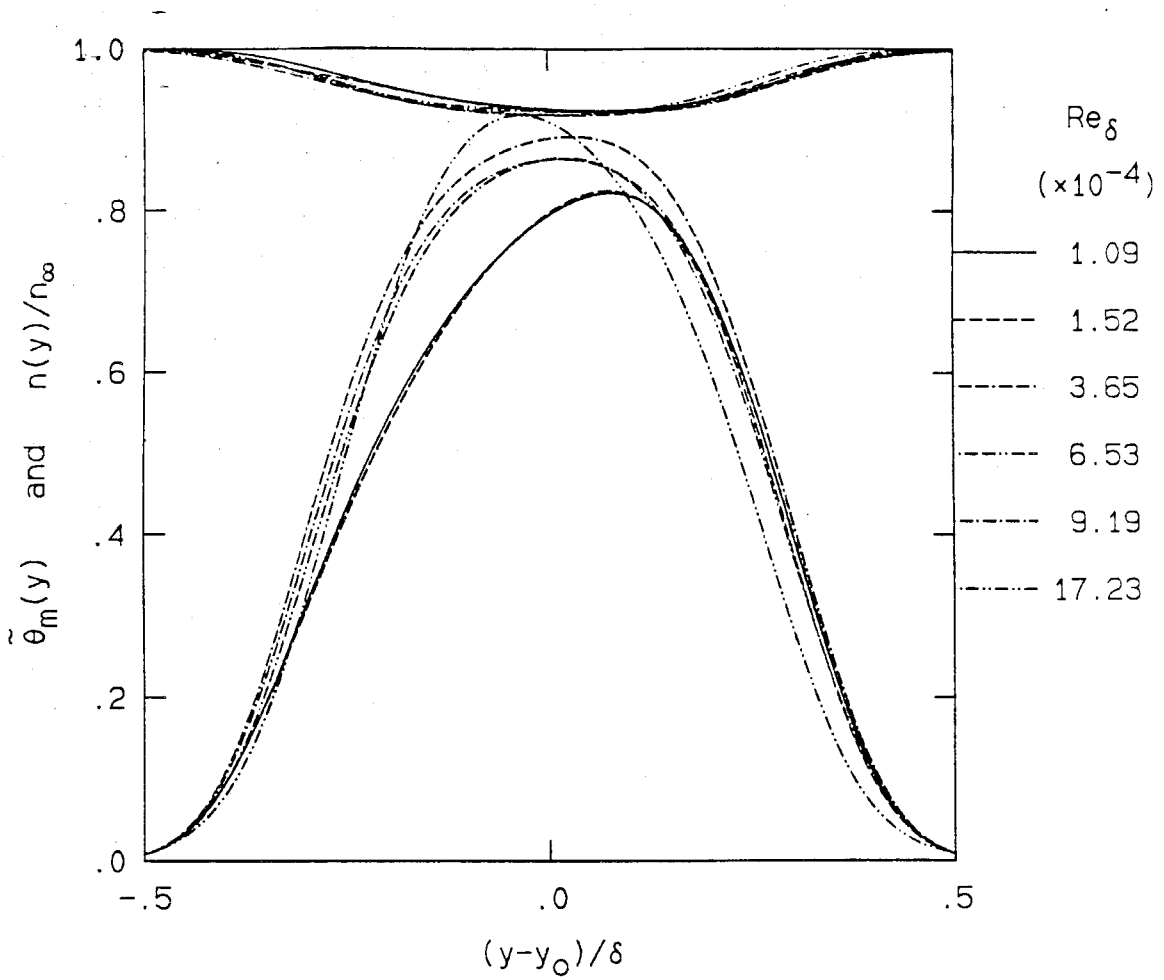

Figure 6.5 Mixed-fluid and mean number density profiles for each Reynolds number.

amount of unmixed fluid in the center third of the layer is very low, confirming the equal density results of Konrad (1976) and the equal density case in Chapter 4. Estimated here by the distance between $\tilde{\theta}_m(y)$ and $\overline{n}(y)$ for a given Reynolds number it is less than 10% for all of the data. The symmetry appears to shift slightly, a reflection of the change in the profiles in Figures 6.2 and 6.3. Again, this may be a remnant of transition or a feature induced by effects of initial conditions.

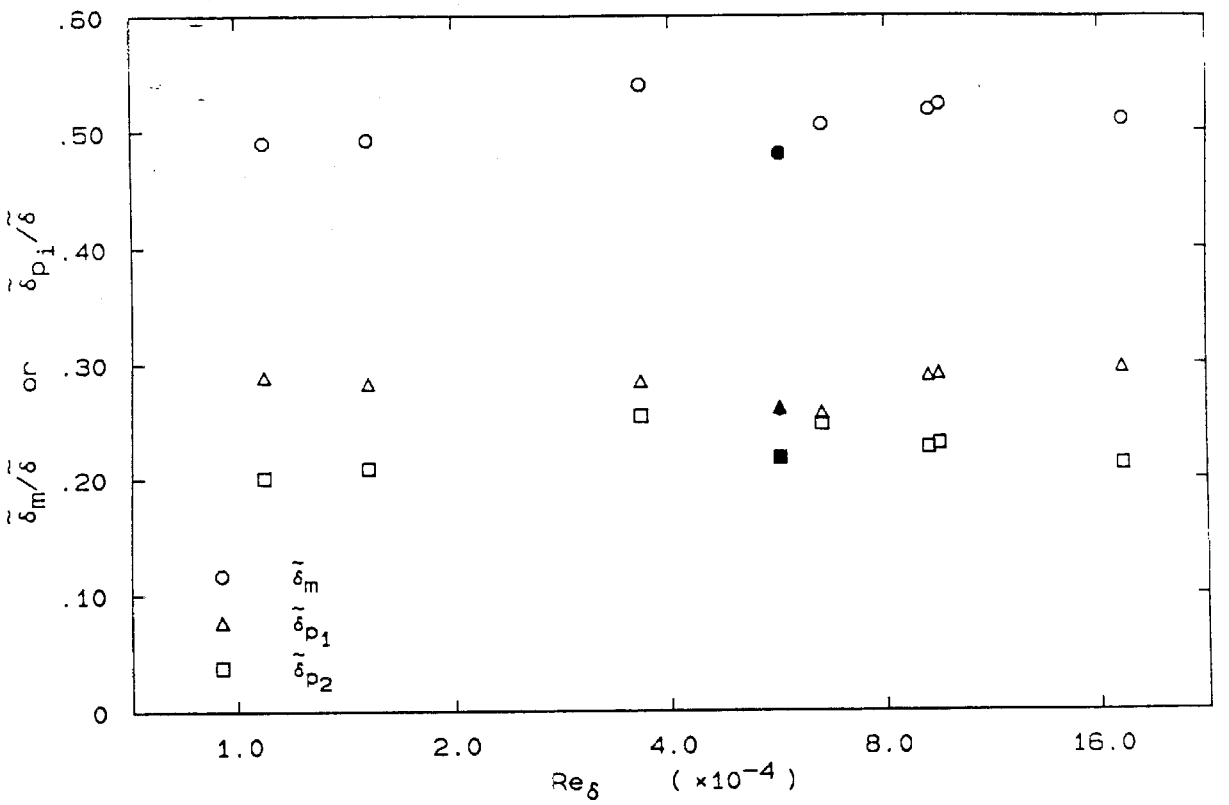

Figure 6.6 High-speed, low-speed and total mixed-fluid mole fractions.

Despite these small changes, note the striking similarity in these despite a factor of 3 change in the growth rate, and a factor of 15 increase in the Reynolds number.

Three integral quantities, $\tilde{\delta}_m$, $\tilde{\delta}_{p_1}$ and $\tilde{\delta}_{p_2}$ are plotted in Figure 6.6 versus the Reynolds number. Normalized by the mole thickness, $\tilde{\delta}$, these may be interpreted as mole fractions. Hence, the mixed-fluid thickness, $\tilde{\delta}_m/\tilde{\delta}$, represents the mole fraction of mixed fluid at any composition within the layer, when normalized in this fashion. The lack of variation with the Reynolds number shown by this quantity is particularly noteworthy. The variation is less than .07 over the entire range (.05 if the two low Reynolds number cases are excluded) with the average value $\tilde{\delta}_m/\tilde{\delta} = 0.50$. This variation is felt to be completely within the "noise" introduced by the effects of initial conditions. Note that the mixed-fluid

mole fraction for the tripped case is as low as the highest Reynolds number case where turbulent boundary layers also exist. Also plotted are $\tilde{\delta}_{p_1} / \tilde{\delta}$ and $\tilde{\delta}_{p_2} / \tilde{\delta}$, which represent, respectively, the mixed high-speed fluid and mixed low-speed fluid mole fractions. As shown previously in Figure 6.4, $\tilde{\delta}_{p_2}$ decreases over the upper range of the Reynolds number investigated. However, note that over the same range of the Reynolds number, the mixed high-speed fluid $\tilde{\delta}_{p_1}$ increases almost in proportion. This demonstrates how the inference of the amount of mixed fluid from the results of reacting experiments at a single stoichiometry can be misleading. Although the amount of product formed at low ϕ does decrease, this represents a change in the composition, rather than the amount of mixed fluid.

Using the approximations detailed in the Appendix B, the mixed-fluid composition profile, $\xi_m(y)$, was also estimated. Shown in Figure 6.7 are the profiles for each of the Reynolds number investigated. Comparing cases with similar Reynolds number, these curves are consistent with those measured by Konrad, and with Wallace when scaled in his fashion. At low Reynolds number, a marked region of uniform composition exists over the center third of the layer, and the composition extends over the entire range of values, $0 < \xi_m < 1$. As the Reynolds number increases this flat spot disappears and the slope in the center of the curve increases until $Re_\delta \sim 65,000$. At the same time, the composition of mixed fluid near the edges of the layer becomes more nearly that found in the center. For Reynolds number higher than 65,000, it appears that the trend is reversed. The center third becomes more uniform as the Reynolds number increases and again the edges extend over a wide range of compositions. What portion of this behavior results from the acoustic mode of the facility interacting with the layer at the lowest Reynolds number, then the region of interaction moving out of the test section as the Reynolds number increases, cannot be determined.

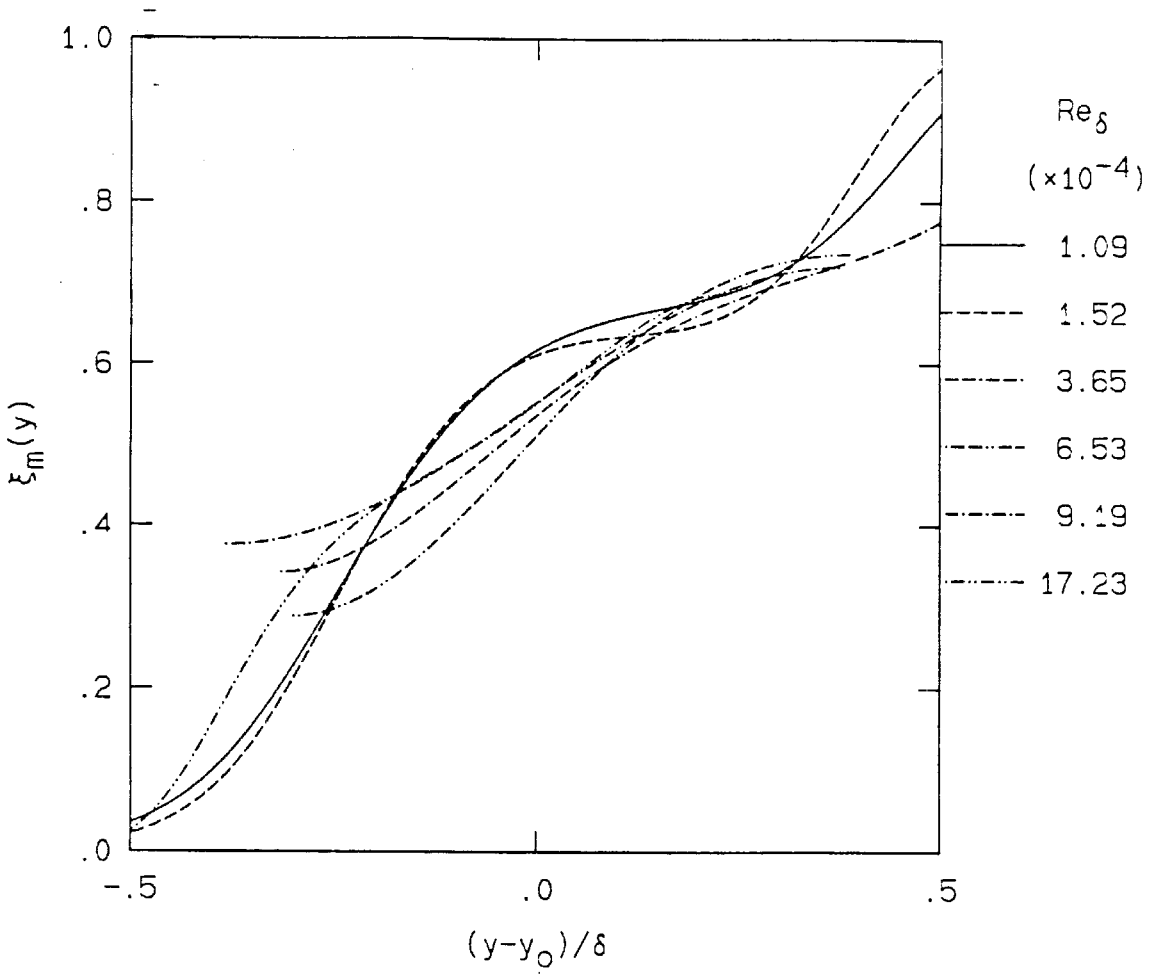

Figure 6.7 Mixed-fluid composition profiles for each Reynolds number.

There are reasons why the behavior of the composition profile near the edges of the layer must be separately qualified. As can be seen by the mixed-fluid profiles, these regions of the profile are based on measurements of a few degrees of temperature rise in the mean, and are therefore more effected by the accuracy limits. Alternately, this can be viewed as being a statistically insignificant sample of the mixed fluid. As displayed in Mungal and Dimotakis (1984) and others, the mean temperature at any location is achieved by the passage of hot fluid for some interval, followed by a period of cold fluid. Hence the low mean temperature near

the layer edges results from cold fluid being observed more often than hot. This implies that the amount of mixed (hot) fluid measured during the time series is low at these positions, which may be interpreted as having poor statistics from which the estimate of mixed-fluid composition is made.

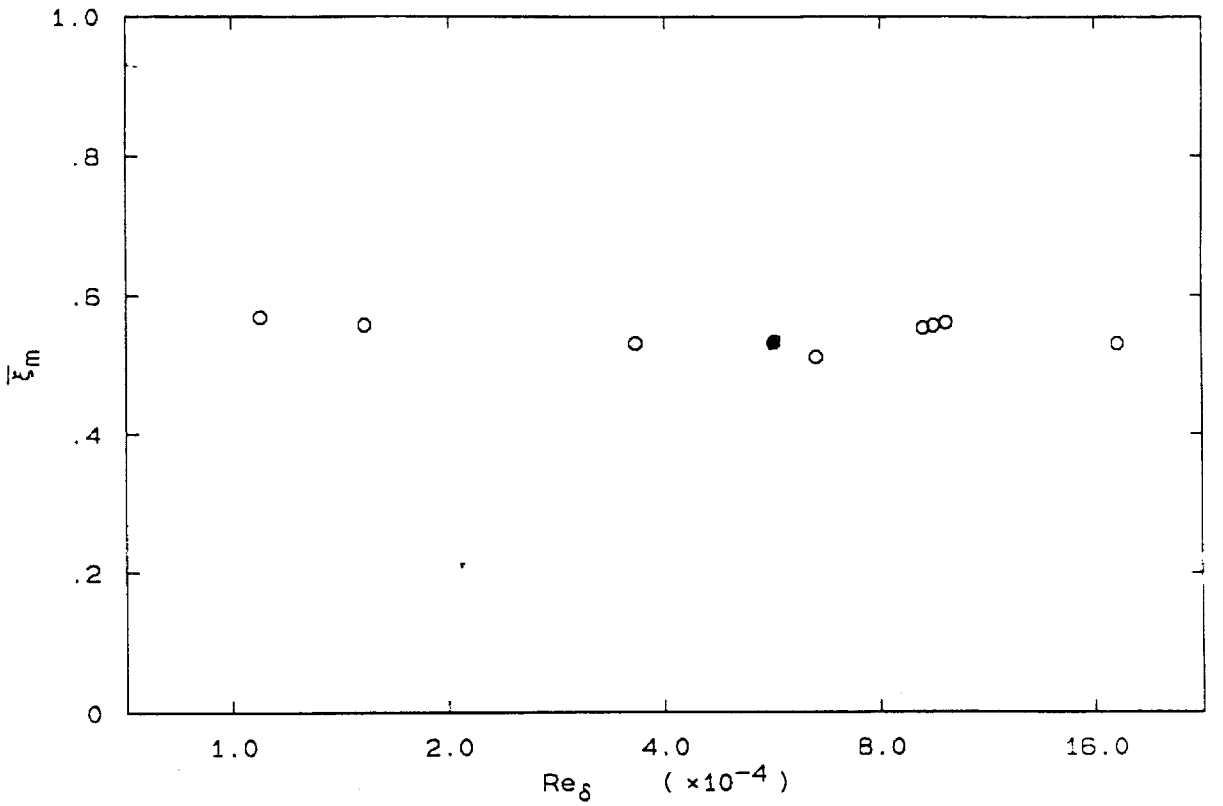

Figure 6.8 Mean mixed-fluid composition versus Reynolds number.

While the profile of mixed-fluid composition in the previous figure changed substantially over the Reynolds numbers investigated, the mean composition of the mixed fluid did not. Figure 6.8 is the average composition for the mixed fluid in the layer, defined by Equation $B.10$. This quantity shows little dependence upon the Reynolds number with the total variation being less than .06 and the mean at about .525. The first four (untripped) points do show a gradual decline in

this quantity, from a high of .57 to a low of .51. This is felt to arise from the very asymmetric entrainment which occurs in the initial roll-up and its subsequent dilution. This "gulp" of high-speed fluid has been observed by Koochesfahani (1984) and others.

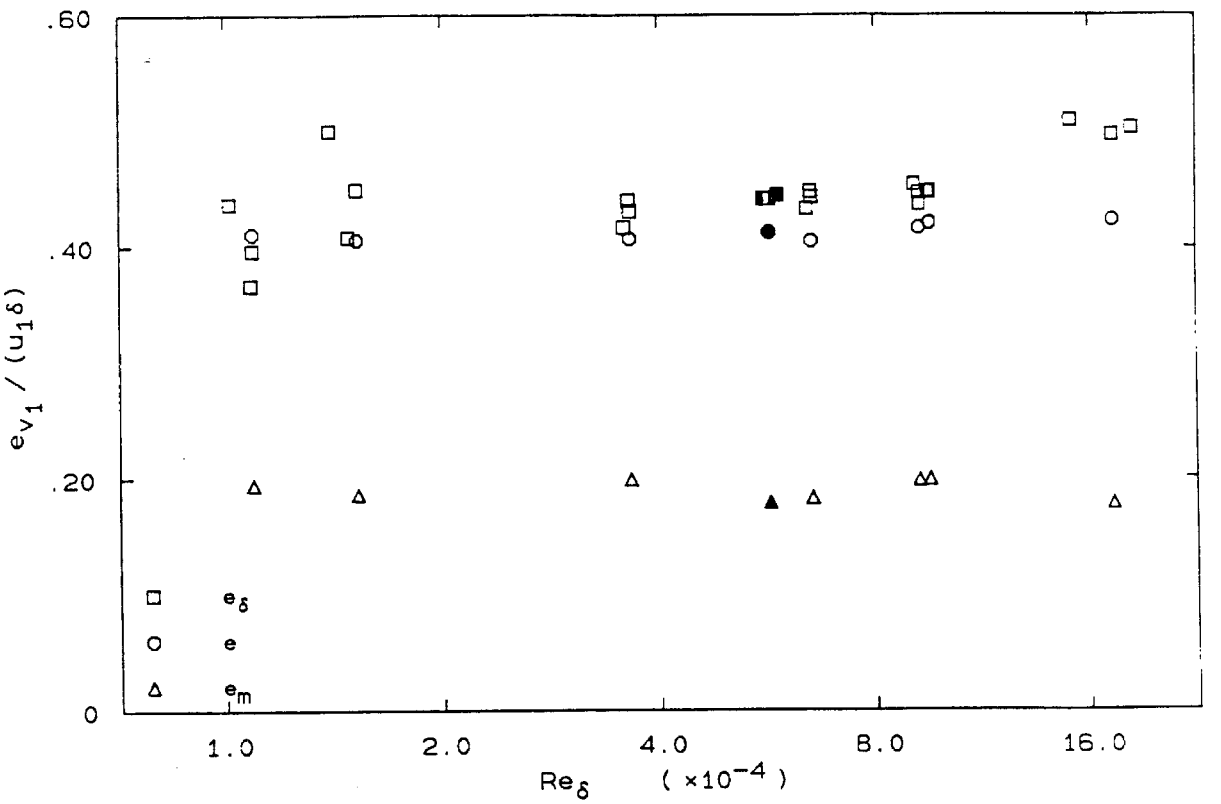

Figure 6.9 Entrainment of high-speed fluid versus Reynolds number.

Entrainment

The volume entrainment rate from each stream, e_{v_i} , and the total volume entrainment rate, e_v, were estimated for each of the Reynolds number by several techniques. In Figures 6.9, 6.10 and 6.11 these are shown normalized by the high-speed velocity and the layer width. As discussed in Chapter 4 and Appendix B,

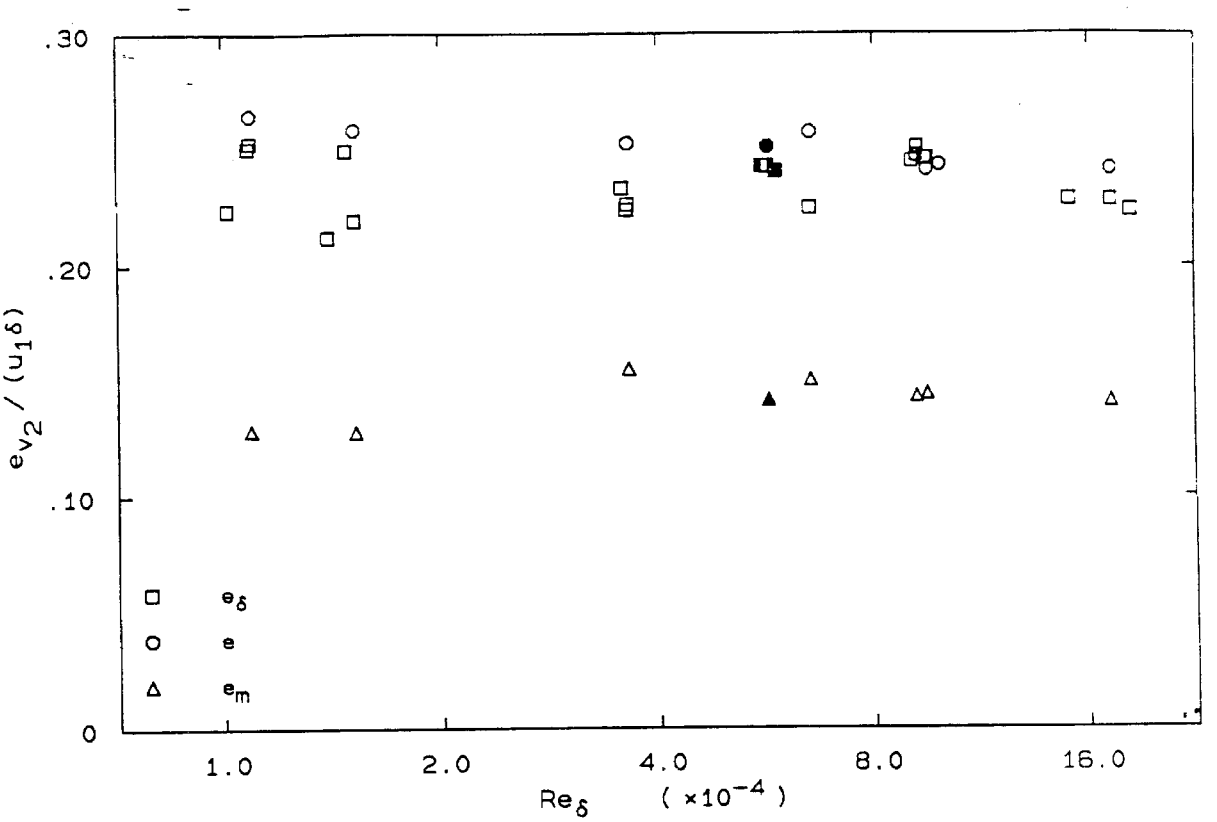

Figure 6.10 Entrainment of low-speed fluid versus Reynolds number.

e_δ in these figures represents the entrainment estimated by the layer geometry. For the calculations involving flux quantities, a velocity had to be assumed due to lack of measurements. This was chosen as the velocity profile of the equal density case reported in Chapter 4, and was scaled in each case to correspond to the mixed-fluid profile width, δ. Self-similarity of the profiles in Figure 6.2 strongly suggests that this is probably adequate for the purpose of qualitative comparison. Using the assumed velocity profiles, the mean flux of fluid from each stream, e , was calculated from the composition profiles determined from the flip experiment. The flux of mixed fluid from each stream, e_m , was calculated using the velocity profile along with the mixed-fluid profiles, $\tilde{\theta}_i(y)$. Each estimate in Figures 6.9, 6.10 and 6.11, are nearly independent of the Reynolds number. Any slight trend

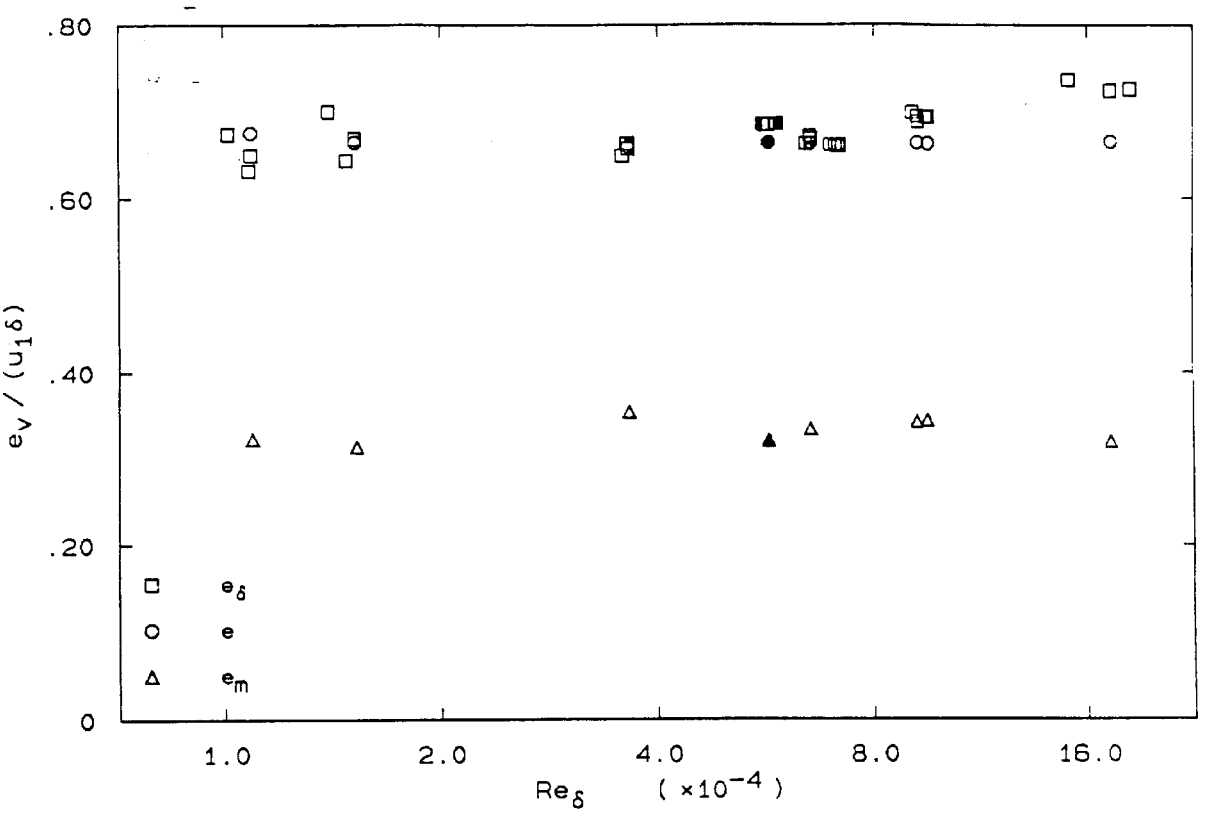

Figure 6.11 Total volume entrainment rate versus Reynolds number.

that might be observed cannot be attributed to an effect of the Reynolds number, since the trend is certainly less than the possible changes in the actual velocity profile. In essence, these figures simply verify some measure of similarity.

The ratios of entrainment estimated by each technique are plotted in Figure 6.12. Significant scatter can be seen for each of the estimates, and therefore does not reflect on a particular technique. Several items of interest can be noted, however. Most obviously, the entrainment ratio of fluid into the layer is substantially higher than the mixed-fluid flux ratio. While nearly twice as much high-speed fluid enters the mean boundaries of the layer, only 35% more flows past a fixed location in a mixed state. This has been previously noted by Hermanson and Dimotakis (1989). The mixed-fluid flux ratio, the quantity most

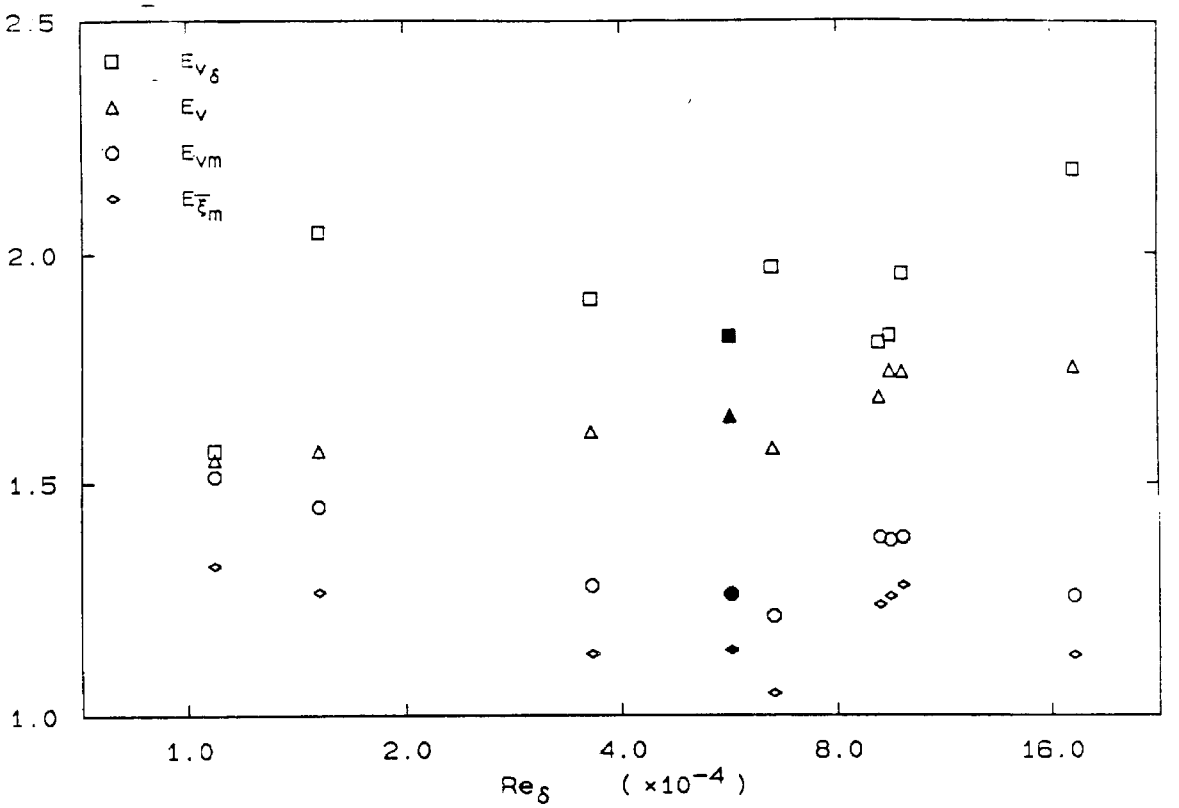

Figure 6.12 Volume entrainment ratios versus Reynolds number.

closely related to Konrad's entrainment ratio, can be seen to vary substantially with the Reynolds number. The data ranges from $1.2 < E_{vm} < 1.5$ centered about Konrad's measurement of $E_v = 1.33$. The variations are most likely the result of initial conditions, and in light of the differences in technique, this is felt to be adequate agreement. As discussed in Chapter 4, the ratio of mean velocities of the mixed fluid can be estimated from the difference between the mixed-fluid flux ratio E_{vm} and the composition ratio $E_{\bar{\xi}_m}$. For the present experiments, it appears there is a slight decrease in this quantity, with the value being 1.3 at Red = and closer to 1.1 at high Reynolds number.

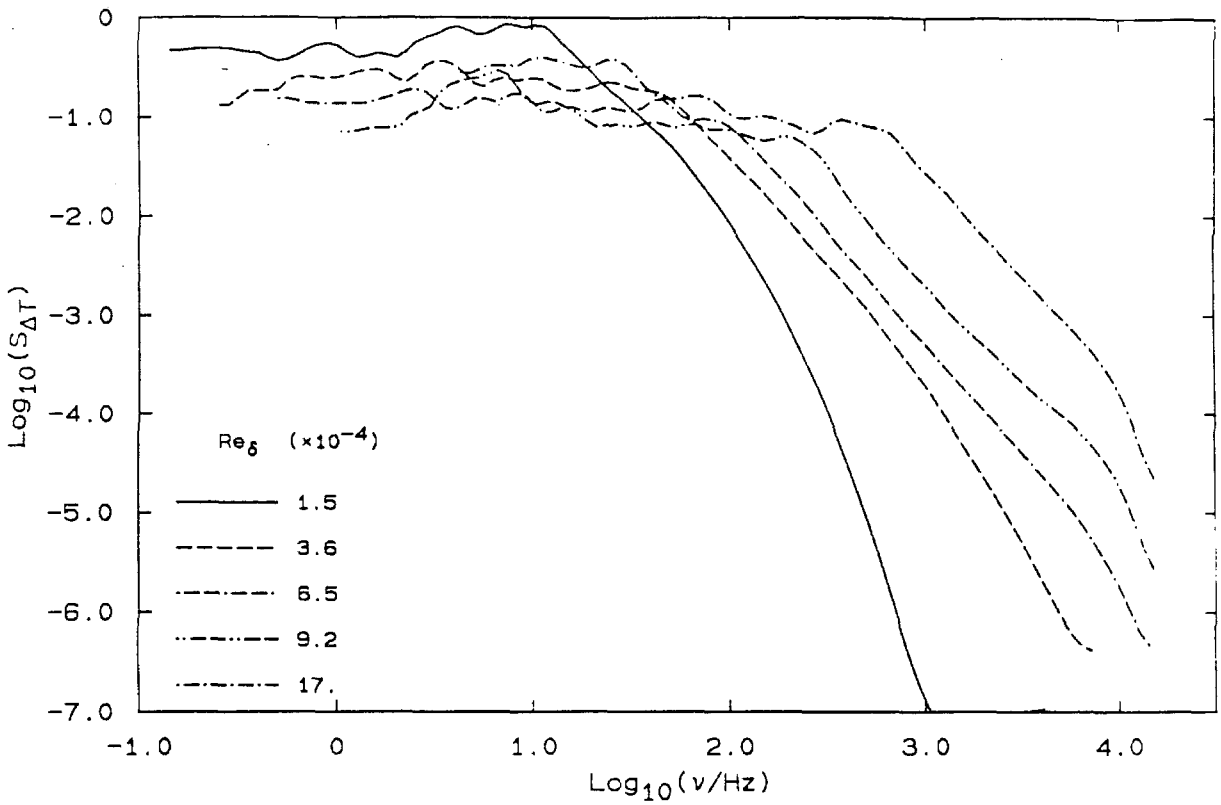

Figure 6.13 Power spectral density for each Reynolds number.

Spectra and Autocorrelations

Figure 6.13 shows the power spectral density (PSD) for each of the Reynolds numbers. In this plot, the probe response is near 3.0 on the lower axis for the lowest Reynolds number, and closer to 4.0 at the highest. The fundamental mode of the apparatus ($\sim 12Hz$) and its first harmonic can be seen in the lowest Reynolds number and the highest Reynolds number as slight bumps when plotted on this logarithmic scale. Three distinct regions can be seen. Below a certain frequency for each Reynolds number, the spectra is relatively flat, and appears to continue that way to very low frequencies. There is a break, at a position which depends on the Reynolds number, beyond which the spectra decays as ν^{-2}. For the two lowest Reynolds numbers, there is a second, very broad transition in the spectra

to a steeper decay. Finally, each of the spectra run into a boundary, either the noise floor ($\sim 10^{-7}$ at $1kHz$, $\sim 10^{-6}$ at $10kHz$) or the beginning of the passive filter in the amplification circuits at $10kHz$.

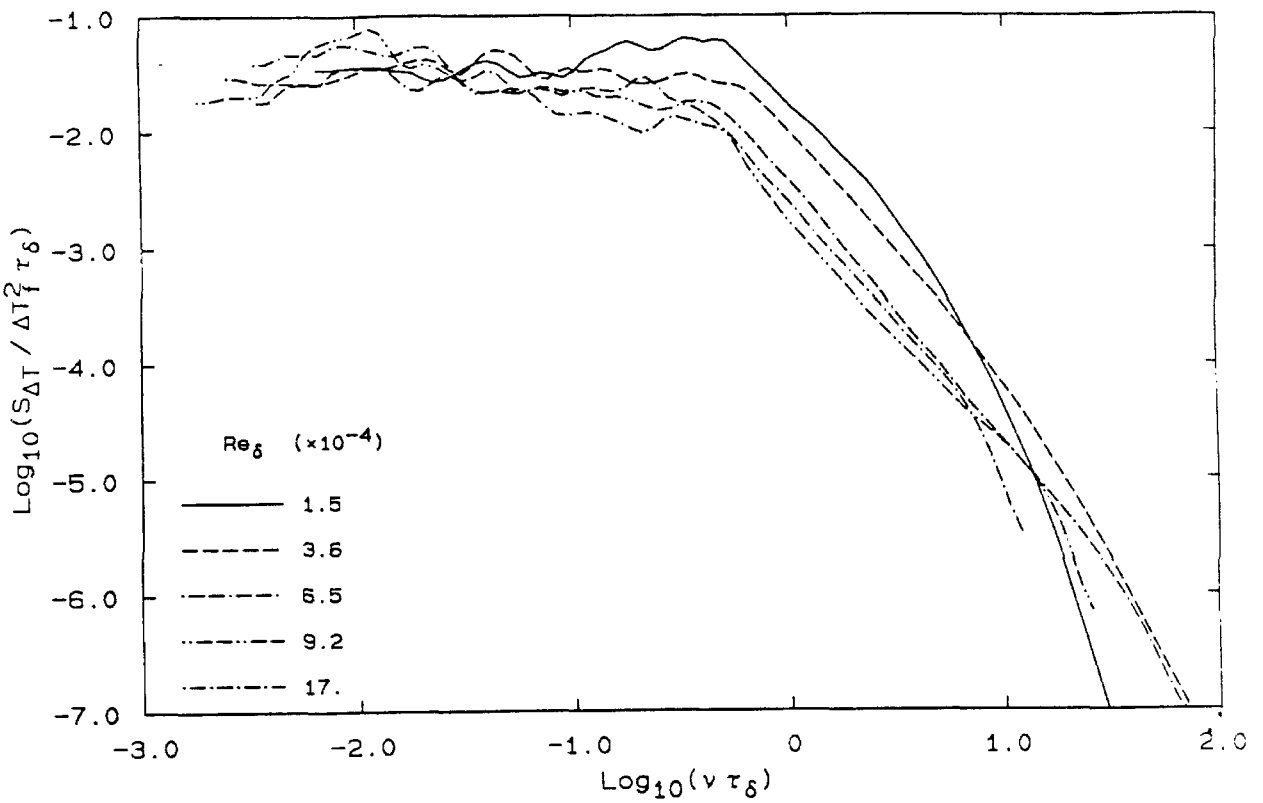

Figure 6.14 Normalized power spectral density for each Reynolds number.

Individual probes displayed the same transverse coordinate dependence found by Konrad, with greater high-frequency content on the high speed side of the layer than on the low-speed side. If the spectra are averaged for the entire layer, and normalized by the large structure convection time and flame temperature, the collapse shown in Figure 6.14 is obtained. It is not clear which of the remaining differences are due to changes of the Reynolds number. It is believed that the majority of the differences are the result of initial conditions, as discussed in

Chapter 2. Similar to the dramatic collapse found in Chapter 3 for several values of heat release, and also in Chapter 4 over a wide range of density ratios, these spectra might fall directly on top of each other if the effects of initial conditions could be removed. However, the break to a slope less than -2 is clearly seen to be dependent upon Reynolds number. Only the break point on the lowest three Reynolds numbers are of interest, the other two being an artifact of the electronics. If these are fit with a power law dependence, the result is

$$\frac{\lambda_B}{\delta} \sim Re_\delta^{-5/3} \tag{6.3}$$

where λ_B denotes the Bachelor scale, which this break is thought to indicate. It must be cautioned that these 3 cases have already been seen to be in the late stages of a transition from the largely $2D$ motion of the pre-transitional mixing layer to the "fully developed" turbulent state. This power law could indicate a transitional dependence and does not necessarily represent an asymptotic dependence thought to be achieved at "high" Reynolds number. It will be left to the reader to conjecture on the significance of this result.

In the same fashion as Chapter 3, the instantaneous temperature integral auto-correlations were calculated for each Reynolds number. Dramatic variation of these curves can be seen, however it is again not clear what amount is due to the Reynolds number. The results for each Reynolds number, and two additional cases, are shown in Figure 6.15. The position of the first minimum and the second maximum for each of these curves has also been calculated. Figure 6.16 shows the inferred length scale (discussed in Chapter 3) for each as estimated by these positions. Plotted with the circles are twice the distance to the first minimum in each case, and the triangles denote the position of the second maximum. The data in Figure 6.16 suggest that as the Reynolds number is increased, the position

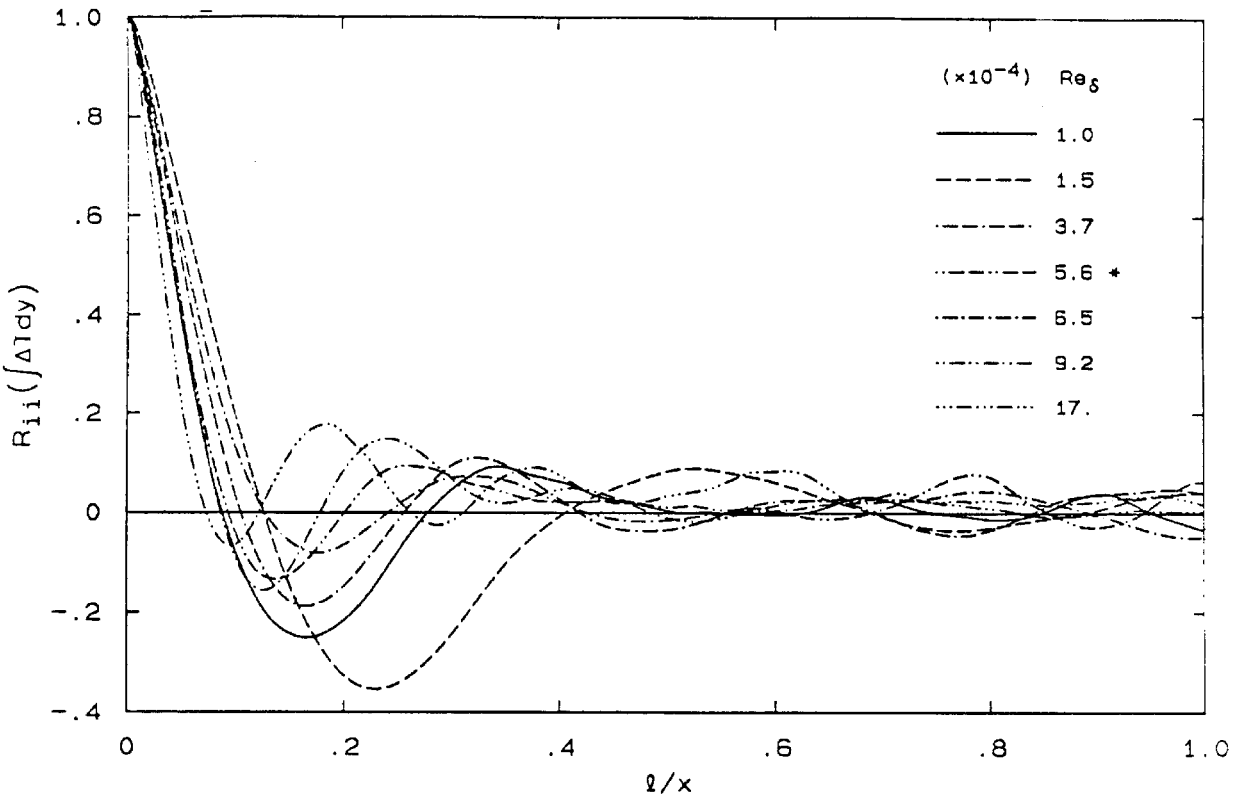

Figure 6.15 Autocorrelation of integral temperature rise.

of both the first minimum and the second maximum decreases. However, there are several exceptions to this trend which indicate that these changes may result from changes of initial conditions rather than the Reynolds number. Note the three sets of data at or near $Re_\delta = 60,000$. As described in the discussion of Figure 6.1, these are data from two different set of contractions and also one case where the inlet boundary layers have been tripped (denoted by the filled symbols). The variations induced by these initial condition changes nearly span the range of values for all Reynolds numbers. Similarly, it might be observed that increasing the Reynolds number seems to decrease the depth of the first minimum and increases the height of the second maximum. This seems intuitively reasonable, implying a decreased coherence of the structures as the Reynolds number increases. However,

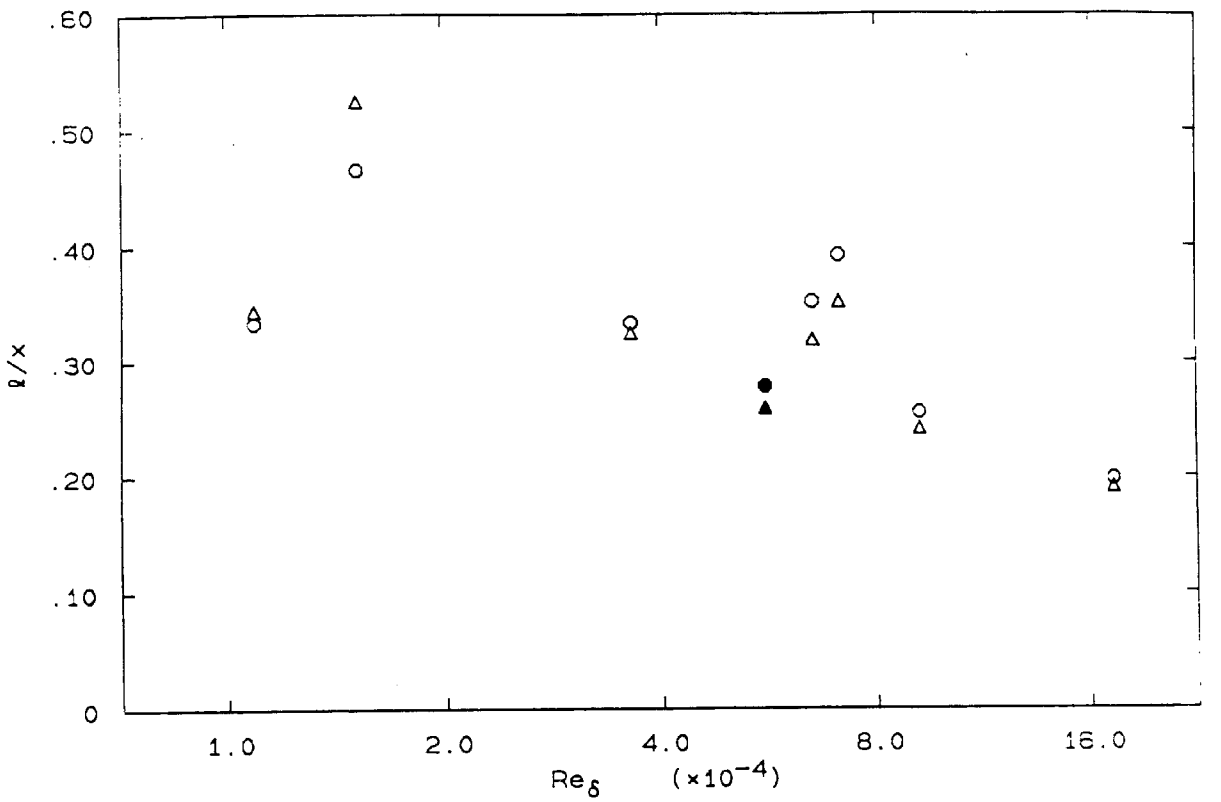

Figure 6.16 Large-structure spacing versus Reynolds number.

the Reynolds number 10,000 layer is significantly less correlated than at Reynolds number 15,000, and the inferred structure spacings are substantially less. Denoted in the legend by the asterisk (∗) in Figure 6.15, the autocorrelation for the tripped case is another exception. Compared to the untripped case at the same velocity, the amplitude of the autocorrelation is increased while the inferred spacing for the structures have decreased. In view of these and other contradictions, it is apparent that the layer is significantly effected, but the majority of the cause may be the changes occurring in the initial conditions.

The changes in the inferred structure spacings indicate that one of two quantities are changing within the layer. Either there is a distinct change in the nature of the large scale structure or the velocity at which it is convecting is

changing._As was the case in Chapter 4, assuming that the large scale structure remains unchanged, leads to unrealistic convection velocities. Therefore, some change is occurring in the structure. Also as was found in Chapter 4, this change in structure spacing is not reflected in the entrainment as expected from theory.

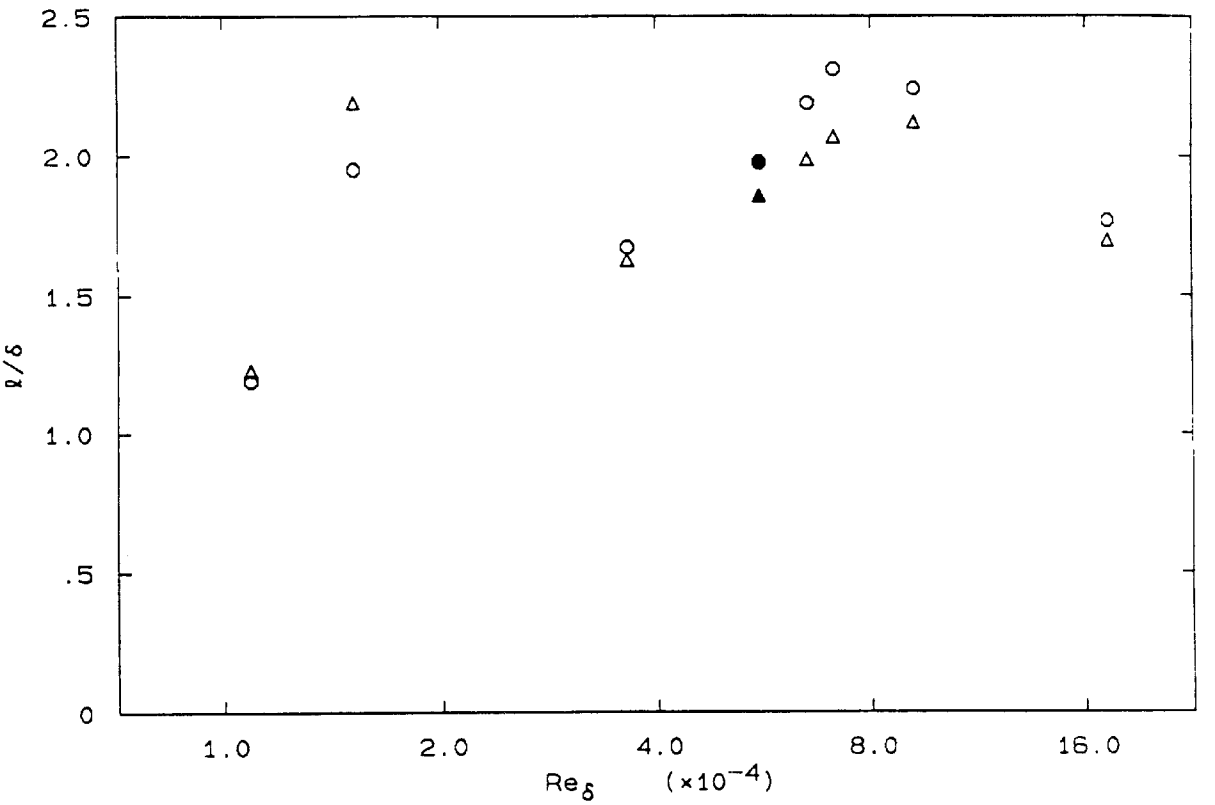

Figure 6.17 Large-structure spacing normalized by mixing-layer width.

Figure 6.17 plots these length scales normalized by the layer width, δ. For comparison, Brown and Roshko (1974), Winant and Browand (1974), Koochesfahani et al.(1979) and Bernal (1981) all find the inter-structure spacing to be in the range 1.4-1.8 . Several of the results plotted in Figure 6.17 fall in this range, however, just as many are substantially higher. As commented upon in Chapter 3, technique may explain some of the difference, however the variation

with respect to the Reynolds number is again felt to stem from the influence of initial conditions.

Probability Density Functions

The last six figures in this chapter are the result of the analysis detailed in Appendix C. Shown are the probability density functions (PDF's) of composition for the lower Reynolds number cases. The vertical axis is the probability density, $P(\xi, y)$, which depends on both the composition and the position within the mixing layer. Delta function singularities at the edges of this plot, representing the existence of pure fluid from the corresponding free-stream, have been plotted with the height scaled by the integral. The data is also plotted as a contour plot for each of the Reynolds number. In these plots two other calculations have been made. The dashed line in each is the mean composition ($\bar{\xi}$), calculated from the PDF and the point denoted by the asterisk on both the plot and the accompanying bar graph is the peak probability location and value. The least squares fitting technique converged to these solutions with the residual in each case being on the order of 1%. Similar fits were attempted for the two higher Reynolds numbers, however the residual was found to be higher for these cases, perhaps indicating inadequate resolution of the temperature fluctuations. For this reason, these results are not shown.

Figures 6.18 and 6.19 show the results for $Re_\delta = 15,000$. Several of the features in these figures are striking, and it might appear that some result from an inability of the imposed functional form to fit the data. However, the residual is an unambiguous measure of the success of the analysis and indicates that these figures fit the temperature data well. Note the trend in appearance of the unmixed, or nearly unmixed, fluid from either freestream represented by the features of the distributions along the edges $\xi = 0$ and 1 in the plots. These distributions of

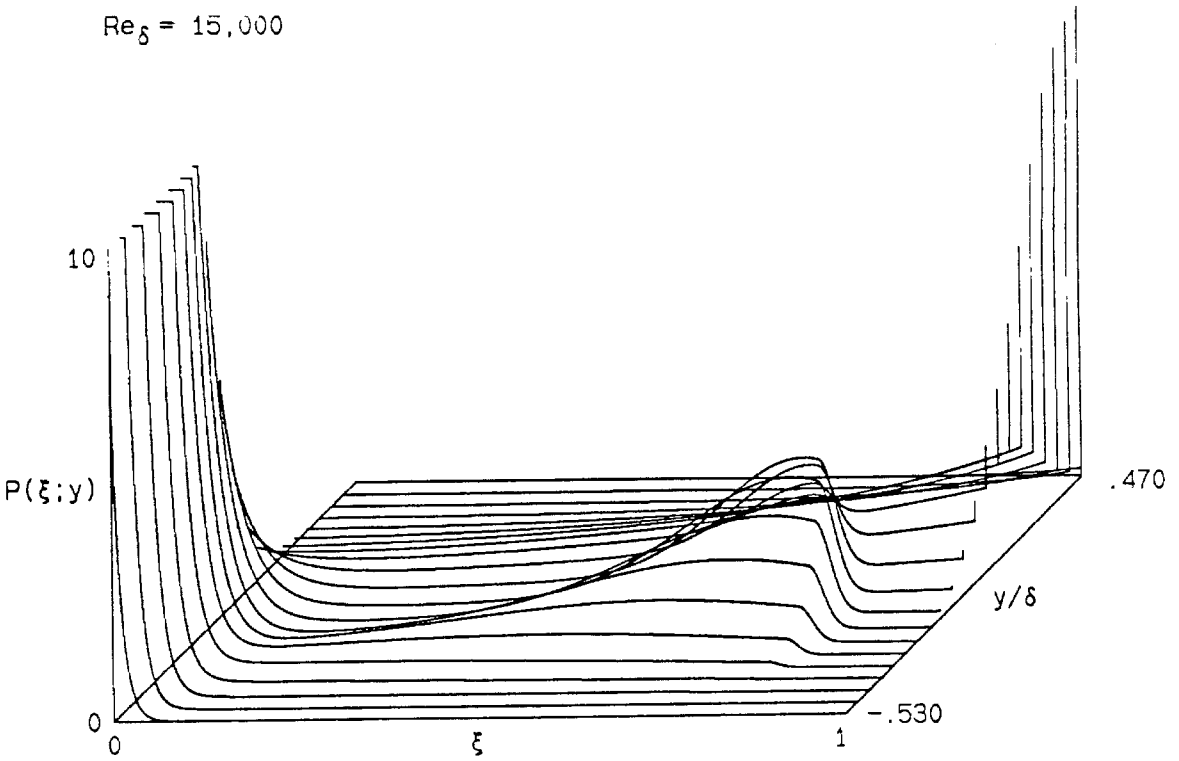

Figure 6.18 PDF of composition for Reynolds number= 15,000.

unmixed fluids reach into the layer, yet even at this lowest Reynolds number, do not quite coexist in the center of the layer. As the Reynolds number increases, it can be seen that these recede even further and a significant portion of the layer contains no unmixed fluid from either stream. The preferred composition which was found to exist in the density difference work has again been found. In the lowest Reynolds number case, however, the Gaussian distribution is far from the mean composition of mixed fluid ($\overline{\xi}_m$ = .57) and is strongly asymmetric. Inspection of the individual experiments temperature data indicates that the asymmetry and location of this distribution is a real feature of the flow. This suggests that some large amount of high-speed fluid has been mixed with a smaller

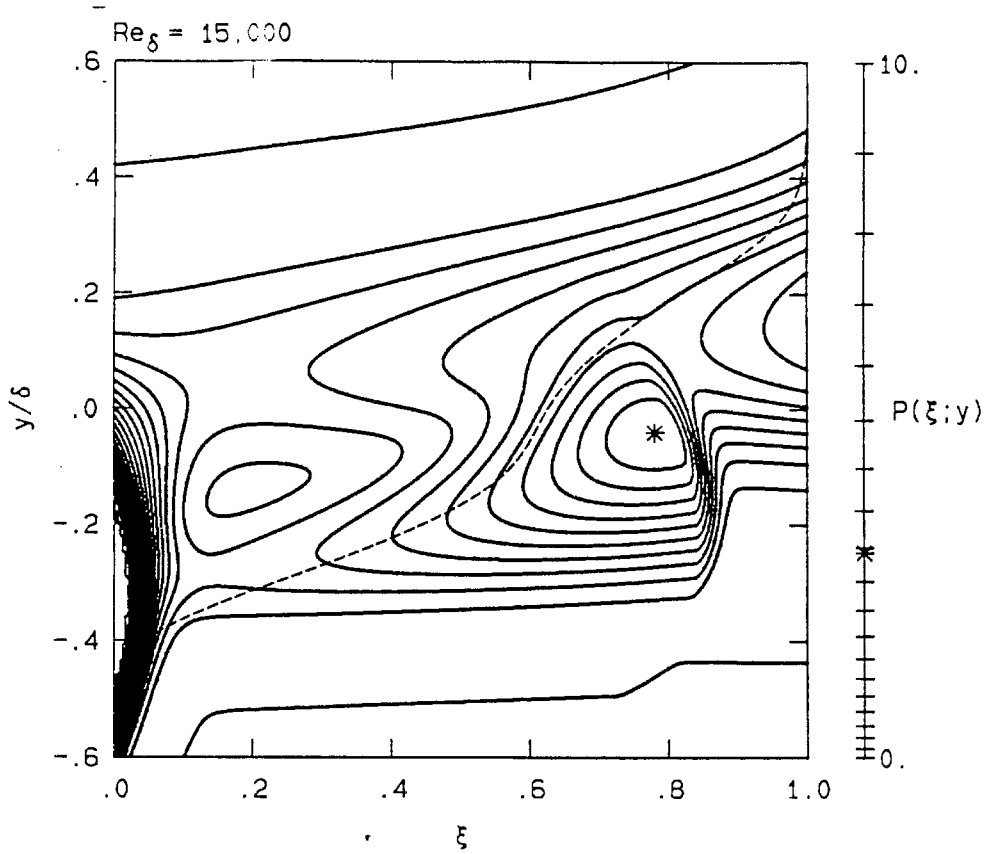

Figure 6.19 PDF of composition for Reynolds number= 15,000.

amount of low-speed fluid to a relatively uniform composition, exactly what is thought to occur when the asymmetric entrainment occurring in the initial roll-up is homogenized during the mixing transition. The composition at which this "lump" of probability is located shifts as the Reynolds number increases until at $Re_\delta = 62,000$ it is located at $\xi = .5$ and the entire distribution appears symmetric about this center. The PDF in this last case supports a slightly different view of mixing in the shear layer. Since the probability of unmixed fluid in the center third of the layer is very rare, mixing between volumes of unmixed fluid from each freestream does not occur. Hence the mixing occurs between unmixed fluid in either stream and the previously mixed fluid in the center of the layer. Therefore

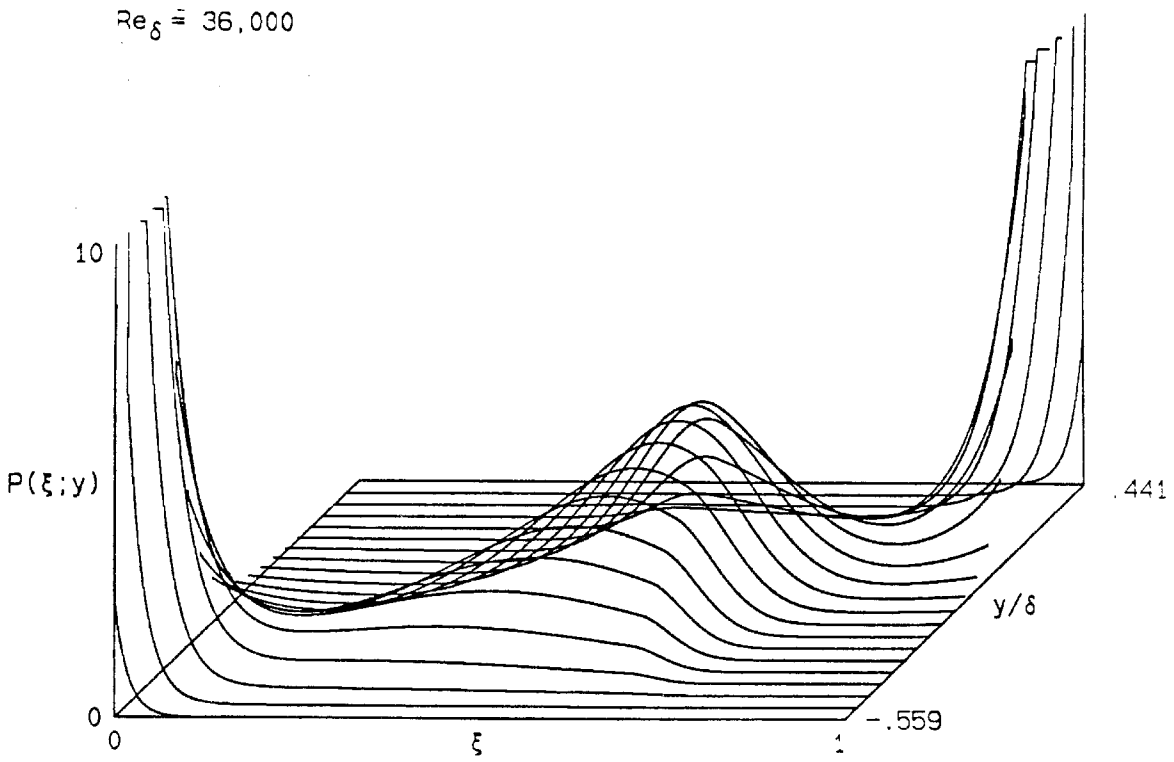

Figure 6.20 PDF of composition for Reynolds number= 36,000.

any portion of the flow which resembles the laminar strained diffusion flame must be an interface between the previously mixed fluid and either freestream.

Summary

The investigation of the effects of Reynolds number is severly hampered in this type of facility. Many things change when velocity is increased and these can have as much or more impact on the measurements as the change in the Reynolds number which was desired. In particular, the growth rate of the uniform density shear layer has been found to change by nearly a factor of three in these experiments, and the majority is thought to be induced by changes in the initial

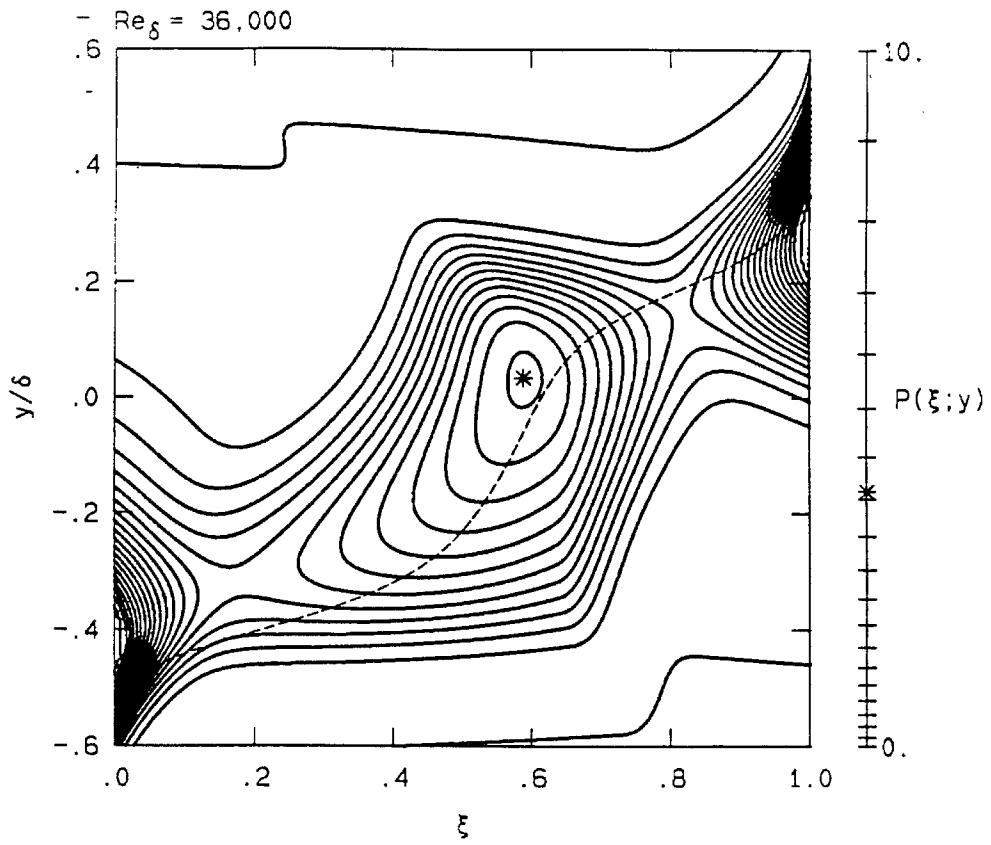

Figure 6.21 PDF of composition for Reynolds number= 36,000.

conditions. Entrainment ratios, spectra of the temperature fluctuations and large structure spacing all vary significantly as the velocity is changed. However these are also felt to result from initial conditions effects rather than a true Reynolds number effect.

A separate class of changes has been observed which are believed to be remnants of the mixing transition. Profiles of mixed low-speed fluid and of composition of mixed fluid as well as the PDF of composition show evidence of this. However measures of mixing in integral form show that transition has indeed been traversed by the lowest Reynolds number investigated, $Re_\delta = 10,000$.

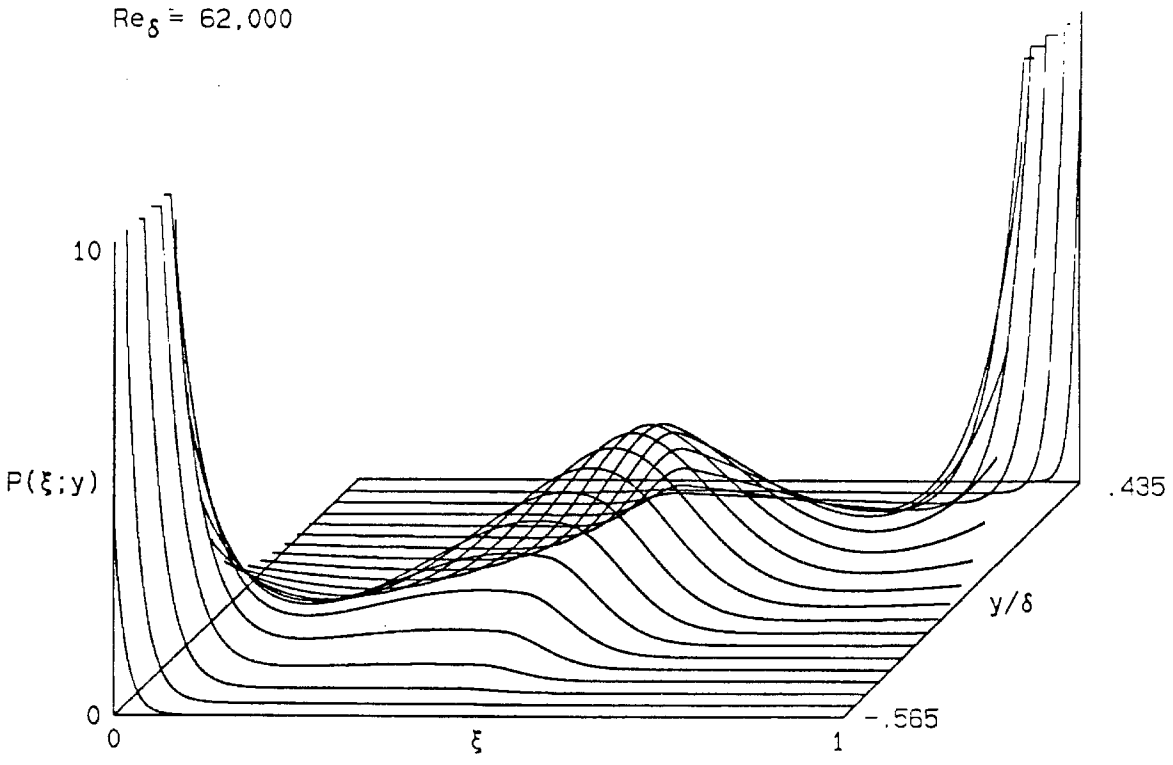

Figure 6.22 PDF of composition for Reynolds number= 62,000.

Based on the similarity of the profiles in Figure 6.2, 6.3 and 6.5, it can be concluded that the distribution of mixed fluid within the two-dimensional shear layer is relatively insensitive to the Reynolds number. This is reinforced by the invariance of the integral amounts, Figure 6.4 and 6.6, which differ by only 10% for all Reynolds numbers investigated. This point deserves repetition. Despite the serious effects of initial conditions on many aspects of mixing and growth in the shear layer, the amount of mixed fluid within the turbulent region does not vary significantly with the Reynolds number.

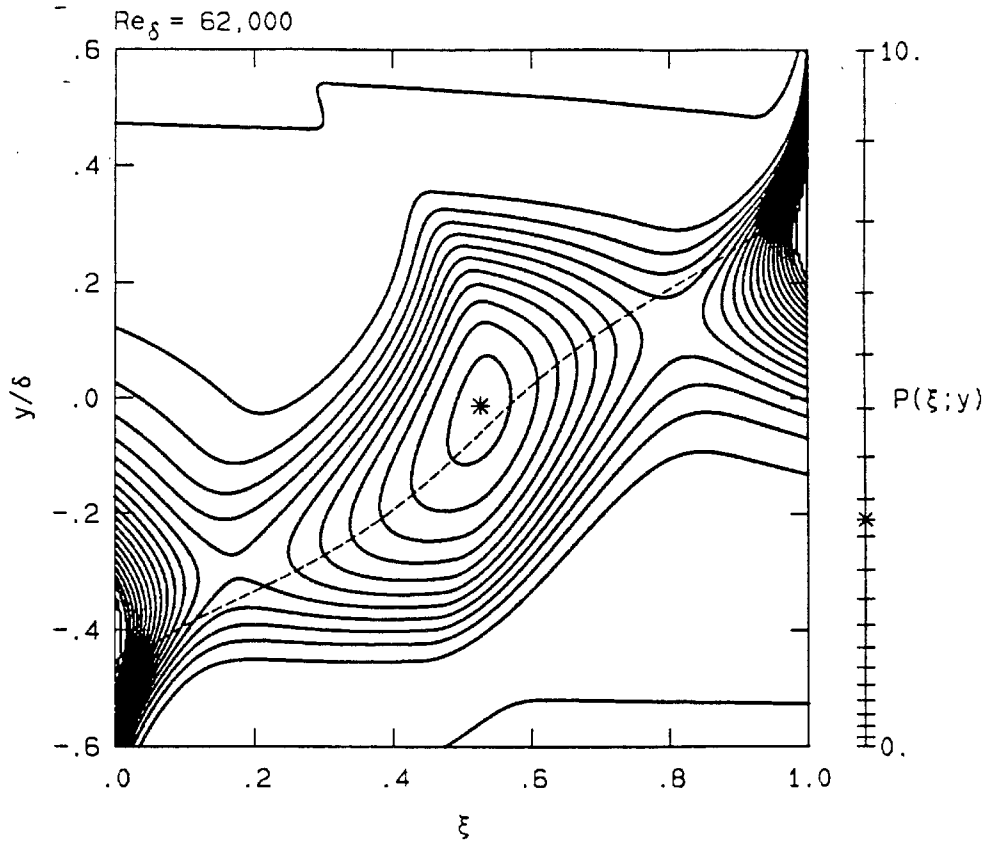

Figure 6.23 PDF of composition for Reynolds number= 62,000.

Conclusions

The two-dimensional turbulent shear layer has been the subject of investigation for many years, particularly the gas-phase layer with uniform freestream densities. This flow represents one of the simplest in which turbulent mixing occurs between two separate streams. Relatively simple boundary conditions and strong similarity properties combine to make this one of the more attractive flows to experimentalists, theorists and modelers.

In the same gas-phase facility used by Mungal and Hermanson, the present study has extended the range of topics to include the effects of freestream density ratio and has gone into considerable depth on the subjects of the effects of Reynold's number and finite kinetics. Several aspects of mixing and reaction in a turbulent two-dimensional shear layer have been studied. Experiments have been performed which react mixtures of H_2 , F_2 and NO in inert diluent gases. Using the heat release by these reactions to indicate the presence and amount of chemical product, several aspects of the mixing process have been examined.

The effects of initial conditions are of primary importance when comparisons to other studies are undertaken. Aspects as fundamental as growth rate of the turbulent region, or as obscure as the mixed-fluid flux ratio depend strongly on the boundary conditions of this flow. These effects are examined in conjunction with those of Reynolds number and density ratio. Growth of the shear layer was found to depend very strongly on the velocity in this facility. It is concluded that, at low velocities, this resulted from an interaction between the large structure and the accoustic mode of the facility. Some change in the growth rate at higher Reynolds numbers is shown to be due to the condition of the inlet boundary layers. In particular, tripping the inlet boundary layers is shown to reduce the growth. This

particular result holds for most cases studied here, *i.e.*, tripping of the high-speed boundary layer led to growth rate decreases. However, an exception was found for the case of high density ratio, where the opposite effect was observed. This anomolous result occurred at conditions under which a new mode of instability has been shown to exist. Parallels exist between this unusual result and those of J.L.Brown (1978) which suggest that non-linear interaction of modes may be responsible.

An extensive study of the effects of density ratio on the mixing and reaction in the 2-D shear layer has been performed. Results indicate that several aspects of the mixing process are remarkably similar. Profiles of mixed fluid change little as the density ratio varies by a factor of 30. The integral amount of mixed fluid varies less than 6% for all density ratios examined. This insensitivity contrasts with that of the profiles of mixed-fluid composition. While having very similar shapes, the profiles are offset by an amount which depends very strongly upon the density ratio. The entrainment into the mixing layer has also been examined and found to vary substantially with the density ratio, albeit not according to theory. Power spectral densities of temperature fluctuations were calculated and found to collapse upon normalization with the adiabatic flame temperature and large-structure passage frequency. Least squares fits of the probability density functions were also examined and found to demonstrate several important features. Most notably, a preferred composition of the mixed fluid was found to exist for all density ratios. This preffered composition tends toward the low-density fluid and depends strongly on the density ratio, as found by Konrad. Also, the absence of unmixed fluid in the center of the mixing region is confirmed.

The initial experimental work of Mungal and Frieler (1988) on the effects of chemical kinetics on the formation of product in the 2-D mixing layer has

been greatly expanded. Measurements have been extended to include a wider range of NO concentrations and have been performed for 2 other stoichiometries. Results indicate that the simple model envisioned in Mungal and Frieler may only be suited for cases with extreme stoichiometry (very high or very low). Further investigations have turned up a serious discrepancy reflecting both on the experimental technique and on theory and modeling of this reacting flow. Experiments run under otherwise identical conditions demonstrate that more product is formed when F_2 is the rich reactant than when H_2 is the rich reactant. This dependence upon molecular species is counterintuitive and is shown to stem from a coupling of the effects of differing diffusivity and chemical kinetics. Numerical calculations based on simplified flow models are reported which demonstrate this coupling.

The effects of Reynolds number on mixing and reaction in the 2-D turbulent mixing layer have been re-examined. Evidence of the remnants of the initial roll up and mixing transition are seen for Reynolds numbers as large as 30,000. Indications of a resonance with the acoustic mode of the apparatus exist, which may affect results for Reynolds numbers ($Re_\delta = \frac{\Delta U \delta}{\nu}$) up to 60,000. Natural transition of the high and low-speed boundary layer on the splitter plate complicate interpretation of the high Reynolds number data. In spite of these qualifications, the amount of mixed fluid is nearly constant. Over the range of Reynolds numbers 10,000 to 200,000, it varies by less than 12%, with the majority of this probably caused by the influence of initial conditions. No evidence for an asymptotic decline in the amount of mixed fluid is observed. Barring the effects of the initial conditions, the spectra of temperature fluctuations may collapse in the same fashion as was observed for the density ratio experiments. Normalized by the adiabatic flame

temperature and the large-structure passage frequency, the data suggests that the spectra have the following features:

i. A relatively uniform low-frequency spectrum.

ii. A break at the large-structure passage frequency

iii. A decay displaying a slope of ν^{-2}

(for nearly two decades at $Re_\delta = 60,000$) .

iv. A second break to a steeper slope which occurs at a Reynolds number dependent frequency.

Appendix A. Temperature Measurements and Probe Response

Temperature

The temperature in the shear layer was measured by a rake of 8 resistance thermometers (cold wires). The construction and use of these sensors have been discussed in Chapter 1. A sample of the results of a single experiment appears below.

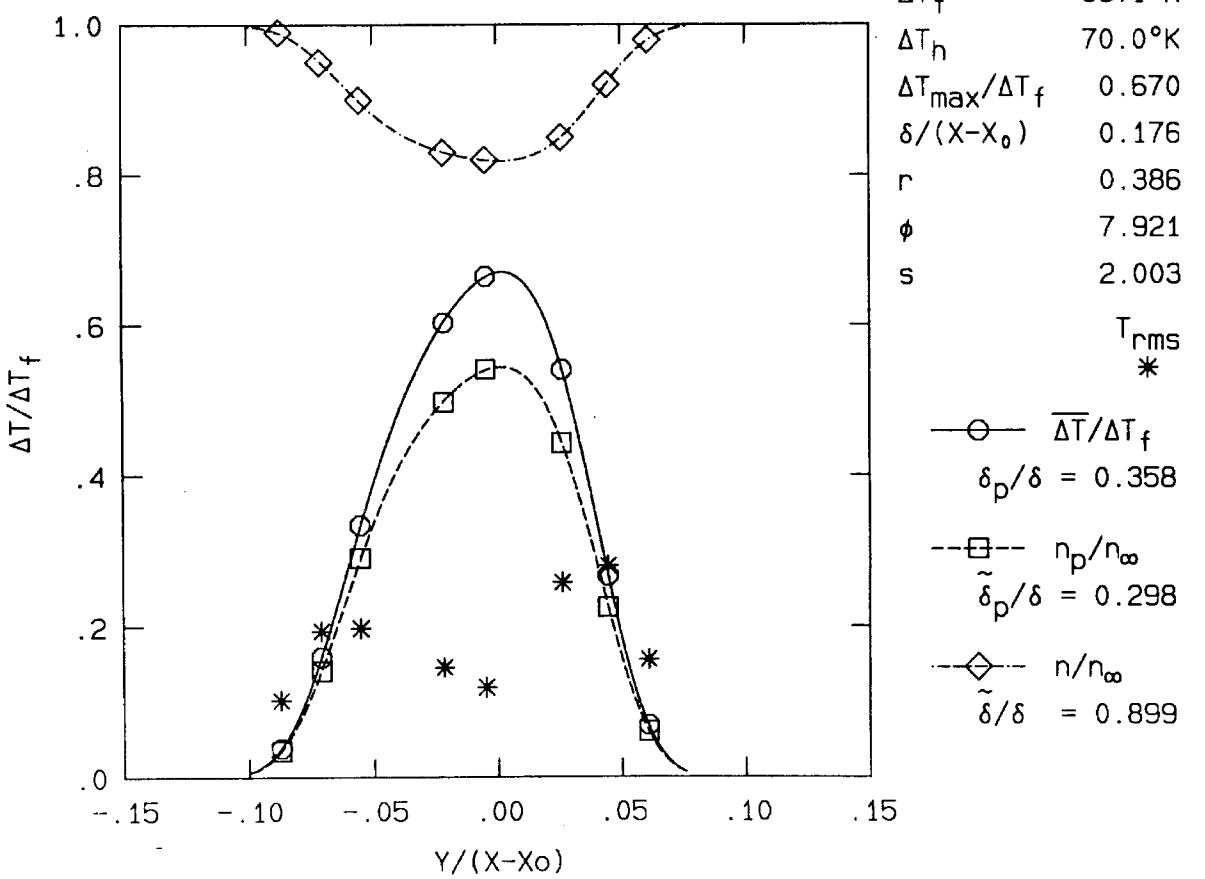

Figure A.1 Experimental results for the case $\rho_2/\rho_1 = 2$.

Measured mean temperatures, ΔT_{ave} , at each of the eight probe locations are indicated by the circles and have been plotted normalized by the adiabatic flame temperature for the flow, ΔT_f. Fitted profiles are also shown for the normalized mean temperature $\theta(y) = \Delta T_{ave}(y)/\Delta T_f$. In addition, fitted profiles for two other quantities are shown. The second bell-shaped profile is the mean number density of product n_p normalized by the number density of product which would be formed at the stoichiometric composition n_ϕ. The final curve is the mean total number density normalized by the number density in the freestream, $n(y)/n_\infty$. These curves are of the form

$$\theta(\eta) = e^{-(\alpha_0 + \alpha_1\eta + \alpha_2\eta^2 + \alpha_3\eta^3 + \alpha_4\eta^4)} \qquad (A.1)$$

with the exception of $n(y)/n_\infty$, which has the form

$$n(\eta)/n_\infty = .1 - e^{-(\alpha_0 + \alpha_1\eta + \alpha_2\eta^2 + \alpha_3\eta^3 + \alpha_4\eta^4)} \qquad (A.2)$$

In these expressions, $\eta = y/x$ is the similarity coordinate for this flow and is the ordinate for Figure A.1. The origin for these coordinates is at the splitter tip with the transverse or cross-stream coordinate denoted as y. The x axis is oriented parallel to the high-speed stream lines, as experimentally enforced by the upper guide wall. A diagram of the flow and these coordinates appears in Figure 1.4. Table A, at the end of this appendix, is a compilation of the detailed run conditions and selected results for the experiments reported. The Run# is an identification tag related to the chronological order in which these experiments were performed. A list of freestream flow conditions and compositions appears next with the high-speed stream labeled HSS and the low-speed stream labeled LSS. Tabulated for each stream are the freestream velocity U , the density ρ , and the mole fraction of each species present. Next in the table are the positions of

each of the eight temperature probes followed by three rows of selected quantities measured at these locations. The first two are the mean temperature rise ΔT and the rms temperature fluctuation T', both in degrees Kelvin (K). The third is the normalized number density of product n_p/n_ϕ. The last three rows are coefficients resulting from a least squares fit to each of the subscripted data quantities. Using the functional forms given in Equation $A.1$ and $A.2$, these are fitted profiles of mean temperature ΔT, normalized mean number density of product n_p/n_ϕ and the mean total number density n/n_∞.

Temperature Measurement Compensation

The driving and amplification circuit provided $0.1\,mA$ constant current through each wire. Changes in voltage required to drive this current correspond to changes in wire resistance due to heating by the flow. The resistance may be related to the average temperature T_w along the wire by

$$R = R_o\,[1 + \alpha_T(T_w - T_o)] \qquad (A.3)$$

where R is the measured resistance, R_o is the value at the reference temperature T_o and the temperature coefficient of resistivity is α_T. For the present sensors, which are $Pt/10\%Rh$, $\alpha_T = .0016\ K^{-1}$.

Assuming that the wire temperature T_w follows the gas temperature T, Equation $A.3$ can be used to accurately determine the mean temperature of the flow and has also been used to give approximate time series (*e.g.*, Mungal and Dimotakis (1984), Hermanson and Dimotakis (1985), etc.). This use requires several approximations which are valid in the present work. The non-linearity in the sensor temperature dependence has been neglected, being three orders of magnitude smaller than the linear term's contribution. Radiative heat transfer to and from the wires has been shown by Hermanson (1985) to be negligible at the

temperatures involved in the present work. Additionally, ohmic heating induced by the sensor current has been ignored. However, there are physical phenomena which complicate the probe response and require further attention. The most important are thermal inertia of the sensing element and heat conduction to the wire supports. An approximate correction for these effects in the present work has been based on a model of probe response found in Mungal (1983), Sandborn (1972) and elsewhere. A more detailed model of probe response may be found in Paranthoen *et al.* (1982) including effects such as the heat transport through the fluid boundary layers adjacent to the sensors. These two models share several necessary approximations. In light of the accuracy of these approximations it was decided the additional complexity of Paranthoen's model was not warranted.

The partial differential equation governing the temperature of the wire $T_w(x,t)$, dependent upon both time and the position along its length, is given by

$$\tau \frac{\partial T_w}{\partial t} = \ell^2 \frac{\partial^2 T_w}{\partial x^2} + T - T_w \qquad (A.4)$$

This is in the form of an evolution equation for the wire temperature with the gas temperature T appearing as a forcing function. The two constants which appear, τ and ℓ, are the thermal response time and thermal conduction length, respectively, for the sensing element. Details of how these may be calculated from flow properties may be found in Sandborn (1972) and in Mungal (1983). The boundary conditions for this equation are an initial temperature distribution and the heat transfer or temperature conditions provided by the wire supports. The gas temperature T is a function of both space and time, however, it will be assumed that the probe is smaller than non-uniformities in the flow. Therefore T is assumed constant with respect to position along the wire, x, and the gas temperature inferred from these measurements can be thought of as a spatial

average over the sensor length. Experimental data indicates that the support temperature, which provides a spatial boundary condition for Equation $A.4$, can approximated as constant at the mean temperature of the gas. Using these assumptions and separation of variables, Equation $A.4$ may be integrated along the wire to obtain

$$\tau \frac{\partial V}{\partial t} \cong \lambda (\overline{V} - V) + (T - V) \qquad (A.5)$$

where the overbar indicates the time averaged value. In this expression, V represents the temperature integral along the wire, since this integral is proportional to the measured voltage. This is also proportional to the wire resistance, therefore V is the temperature inferred from the uncompensated signal. Equation $A.5$ may be rearranged to give the gas temperature T as a function of the measured probe response,

$$T \cong V + \tau \frac{\partial V}{\partial t} + \lambda (V - \overline{V}) \qquad (A.6)$$

Here the gas temperature is related to the measurement, V , its time rate of change and the difference between the instantaneous value and the mean. This relationship is used for compensating the temperature time series. The two constants which appear, τ and λ , depend on the wire geometry, the gas properties and the velocity of the flow, which has to this point been assumed to be time independent. Since the flow does vary with time, the response constants vary with time and compensation using Equation $A.6$ will be approximate. The theoretical response time for the present wires is $130\,\mu sec$ in N_2 at $20\,m/s$, while the experimentally observed value is somewhat greater. The conduction error constant, λ, is estimated at .09 for these conditions and appears to match the experimental observations quite well. Non-physical values of temperature, such as temperature drop below ambient in a flow with only exothermal reactions,

may result if poor estimates of response characteristics are used. These potential flaws in compensation occur only when sensor performance is underestimated, *i.e.*, when values for τ and λ are too large. Since the theoretical estimates appear to be slightly optimistic and therefore provide underestimates of τ and λ, they have been used throughout.

It is important to note that compensation does not effect inferred values of the mean temperature. Its primary influence is on the fluctuation spectra, and to a lesser extent, the inferred values of the product number density and total number density.

Noise Measurements

As mentioned previously, the driving and amplification circuit provided $0.1\,mA$ current through each wire. Operated in this constant current mode, velocity sensitivity arising from the overheat can at most produce signals the size of the overheat. It is estimated that under natural convection (a worst case) the electrical heating causes a temperature rise of less than $0.1K$, which is negligible compared to the temperatures of interest in the flow. This arrangement produced satisfactory signals with a measured rms noise on the order $\sim 0.2K$.

Figure A.2 shows two power spectral densities of temperature rise in the shear layer, this particular experiment having an adiabatic flame temperature ΔT_f of $166\,K$. The upper trace is from a probe near the peak of the temperature rise profile. The lower trace is for a probe which was located completely outside the region where reaction was taking place, and therefore represents a measurement of all signal in the system not due to reaction induced temperature rise. The sources contributing to this include temperature fluctuations in the freestreams, velocity sensitivity of the thermistor, noise from the amplifiers, cross-talk between amplifiers and induced noise from the surrounding lab equipment. The peaks

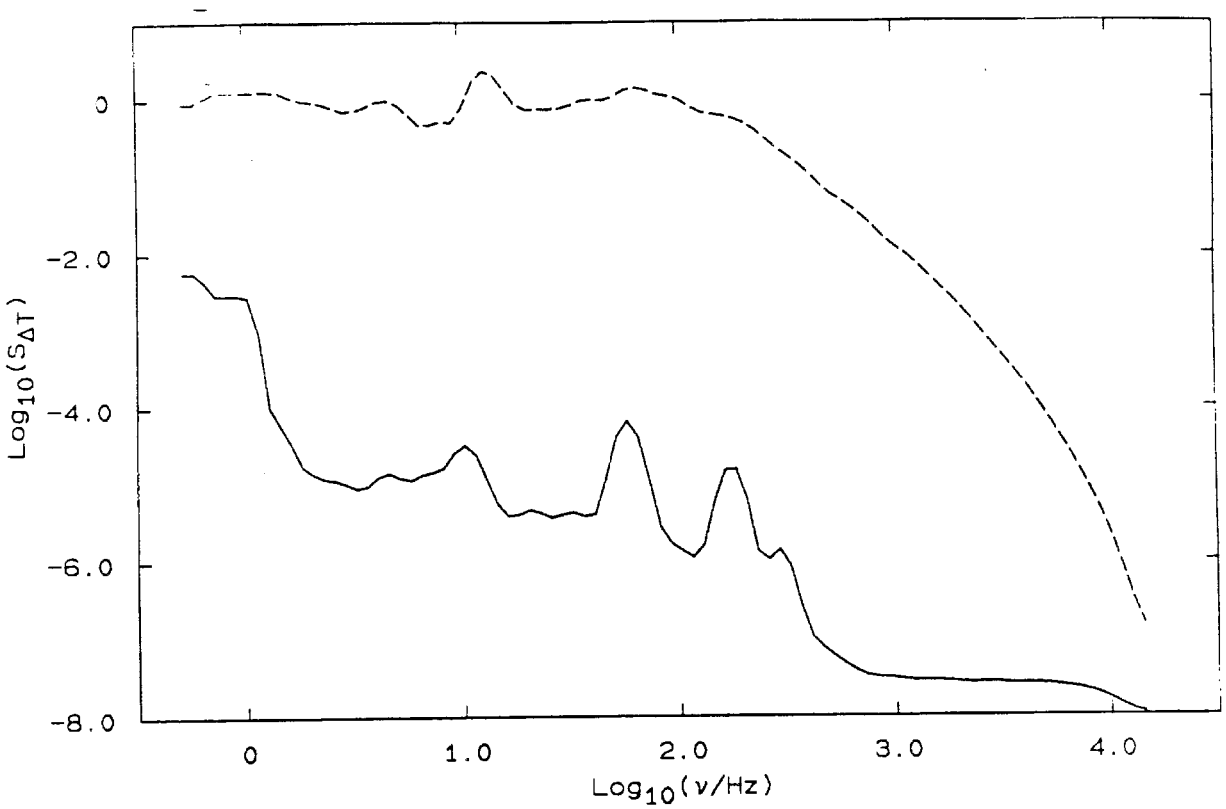

Figure A.2 Temperature fluctuation spectra.

in this "noise" spectra correspond to $60Hz$ and its harmonics, leaving a signal to noise ratio of about 10^4 over the midrange frequencies. This agrees with the direct measurements of rms noise levels.

An example of the effects of compensation upon the temperature fluctuation spectra is shown in Figure A.3. Using the same two time series which produced Figure A.2, compensation for sensor characteristics was performed using Equation $A.6$ and the new time series spectra calculated. Note the very slight change in the spectra for mid and low frequencies. The most notable effect is the rise in the noise spectrum starting at the estimated response time. The spectrum of the temperature fluctuations has also undergone subtle changes. The uncompensated spectrum contained a bend at the subharmonic of the large-structure passage

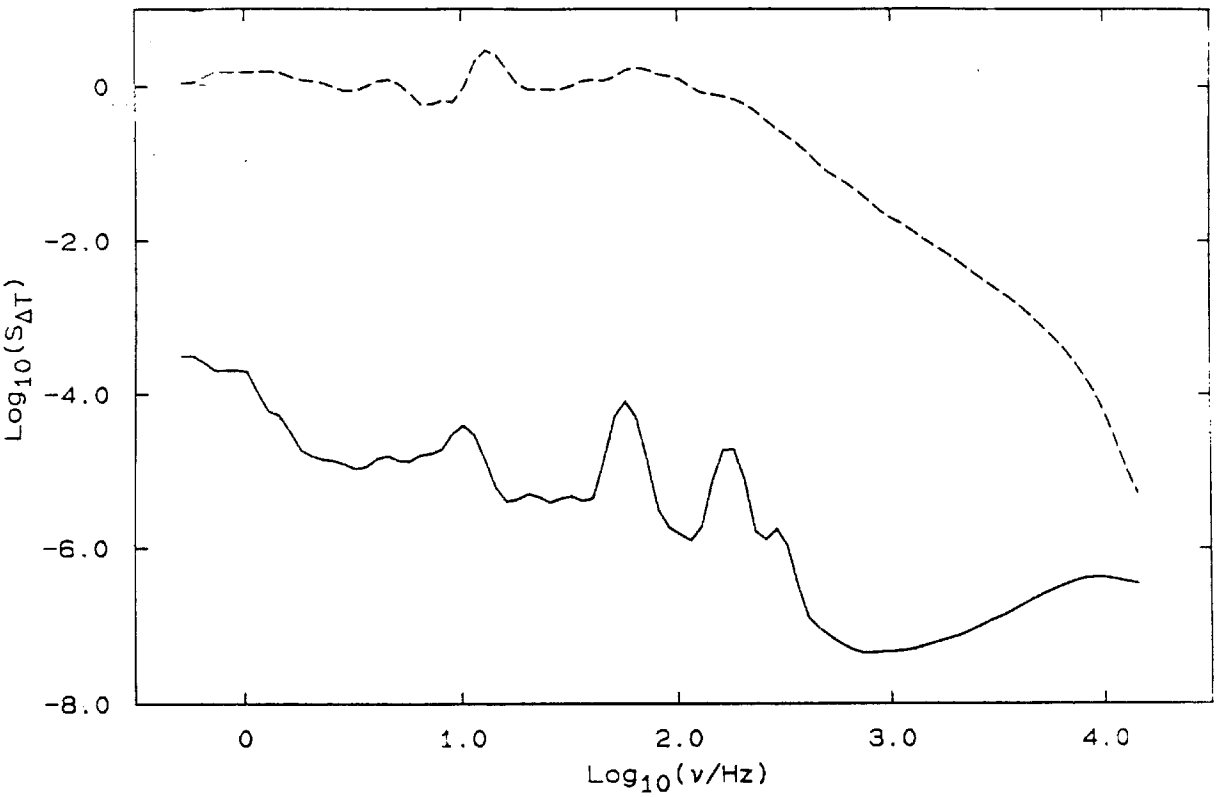

Figure A.3 Compensated temperature fluctuation spectra.

frequency, roughly a decade of ν^{-2}, and then a gradual roll off. The compensated spectrum has nearly two decades of ν^{-2}, with a faster roll-off occurring only at frequencies affected by the Butterworth filter. The extension of a constant slope region is a rather unique result, and it is felt unlikely that it is the result of over-compensation. Also, note that the amplitude of the altered part of the spectrum is smaller than the low-frequency range by two orders of magnitude. This indicates that estimated values for quantities such as the rms temperature fluctuation are not substantially altered.

Table A : Detailed Experimental Parameters and Results

Run#215	U (m/s)	ρ (kg/m^3)	% H_2	% F_2	% N_2	% Ar	% He	% NO
HSS	22.00	1.160	1.00		98.00	1.00		0.045
LSS	8.50	1.160		1.00	98.00		1.00	
y/x	0.061	0.044	0.026	-.005	-.022	-.055	-.071	-.087
ΔT(K)	2.67	12.08	32.25	55.87	58.15	31.98	14.98	4.14
T'(K)	8.89	18.65	23.98	15.11	14.25	23.11	21.41	11.66
n_p/n_ϕ	0.026	0.113	0.294	0.494	0.511	0.292	0.138	0.039
$\alpha_{\Delta T}$	3.9919	-.21220	-.16055	-.23485E-1	-.93882E-2			
α_{n_p}	-.73379	-.19316	-.15067	-.25332E-1	-.99175E-2			
α_n	-1.8798	-.20053	-.15387	-.18598E-1	-.85566E-2			

Run#216	U (m/s)	ρ (kg/m^3)	% H_2	% F_2	% N_2	% Ar	% He	% NO
HSS	22.00	1.140	4.00		93.00	3.00		0.100
LSS	8.50	1.140		0.50	96.50		3.00	
y/x	0.060	0.044	0.026	-.005	-.021	-.055	-.070	-.086
ΔT(K)	1.62	7.83	18.96	34.24	41.65	34.25	17.16	3.45
T'(K)	4.91	10.72	13.07	11.63	11.92	19.94	21.84	10.17
n_p/n_ϕ	0.018	0.087	0.207	0.363	0.432	0.355	0.178	0.037
$\alpha_{\Delta T}$	3.4791	-.31172	-.77808E-1	-.23026E-1	-.14285E-1			
α_{n_p}	-1.0653	-.28464	-.75560E-1	-.24955E-1	-.14446E-1			
α_n	-2.3448	-.27571	-.72759E-1	-.27358E-1	-.15071E-1			

Run#218	U (m/s)	ρ (kg/m^3)	% H_2	% F_2	% N_2	% Ar	% He	% NO
HSS	22.00	1.180	0.50		98.00	1.50		0.010
LSS	8.50	1.180		4.00	94.50		1.50	
y/x	0.060	0.044	0.026	-.005	-.021	-.055	-.070	-.086
ΔT(K)	3.26	16.41	42.98	54.36	46.40	21.72	10.34	2.77
T'(K)	10.40	23.10	25.30	13.17	14.71	16.06	14.73	7.64
n_p/n_ϕ	0.035	0.168	0.428	0.541	0.471	0.232	0.111	0.031
$\alpha_{\Delta T}$	4.0196	0.60235E-1	-.16107	-.47668E-1	-.12421E-1			
α_{n_p}	-.59353	0.47828E-1	-.14982	-.46391E-1	-.12659E-1			
α_n	-1.8232	0.15978E-1	-.15260	-.41152E-1	-.11887E-1			

Run#219	U (m/s)	ρ (kg/m^3)	% H_2	% F_2	% N_2	% Ar	% He	% NO
HSS	22.00	0.709	1.00		53.40		45.60	0.060
LSS	8.50	1.410		1.00	53.40	45.60		
y/x	0.060	0.044	0.026	-.005	-.021	-.055	-.070	-.086
ΔT(K)	3.43	12.85	29.81	55.84	63.49	45.37	21.62	5.01
T'(K)	8.91	15.93	20.63	17.54	16.64	28.89	28.23	14.64
n_p/n_ϕ	0.029	0.107	0.240	0.427	0.477	0.345	0.167	0.040
$\alpha_{\Delta T}$	3.9603	-.29565	-.11103	-.16698E-1	-.10767E-1			
α_{n_p}	-.90653	-.26208	-.10278	-.18719E-1	-.11128E-1			
α_n	-1.8917	-.26320	-.91693E-1	-.20463E-1	-.13270E-1			

Run#220	U (m/s)	ρ (kg/m^3)	% H_2	% F_2	% N_2	% Ar	% He	% NO
HSS	22.00	0.679	4.00		50.00		46.00	0.080
LSS	8.50	1.430		0.50	53.50	46.00		
y/x	0.060	0.044	0.026	-.005	-.021	-.054	-.070	-.086
ΔT(K)	2.29	7.02	15.81	31.01	39.93	46.54	30.24	10.15
T'(K)	5.44	8.58	10.73	12.32	13.78	18.76	27.23	18.75
n_p/n_ϕ	0.023	0.069	0.153	0.289	0.362	0.410	0.266	0.092
$\alpha_{\Delta T}$	3.3461	-.38499	-.49231E-1	-.19412E-1	-.11617E-1			
α_{n_p}	-1.3239	-.35295	-.50013E-1	-.20754E-1	-.11553E-1			
α_n	-2.4105	-.35479	-.55425E-1	-.25191E-1	-.12450E-1			

Run#221	U (m/s)	ρ (kg/m^3)	% H_2	% F_2	% N_2	% Ar	% He	% NO
HSS	22.00	0.719	0.50		53.90		45.60	0.010
LSS	8.50	1.440		4.00	50.40	45.60		
y/x	0.061	0.044	0.026	-.005	-.022	-.055	-.071	-.087
ΔT(K)	6.63	25.64	51.96	63.88	57.96	32.13	15.36	3.72
T'(K)	15.01	26.94	24.80	11.47	14.02	19.02	18.66	9.85
n_p/n_ϕ	0.061	0.225	0.443	0.541	0.498	0.291	0.142	0.035
$\alpha_{\Delta T}$	4.1651	0.19613E-1	-.10557	-.34066E-1	-.12498E-1			
α_{n_p}	-.60879	0.13237E-1	-.94129E-1	-.33195E-1	-.12681E-1			
α_n	-1.7072	0.85179E-2	-.78975E-1	-.32120E-1	-.13735E-1			

Run#222	U (m/s)	ρ (kg/m^3)	% H_2	% F_2	% N_2	% Ar	% He	% NO
HSS	22.00	0.389	1.00		22.30		76.70	0.045
LSS	8.50	1.550		1.00	22.30	76.70		
y/x	0.061	0.044	0.026	-.005	-.022	-.055	-.071	-.087
ΔT(K)	11.90	22.81	36.94	62.22	68.80	42.06	16.79	1.94
T'(K)	14.72	16.67	18.79	21.22	24.39	37.82	30.71	10.77
n_p/n_ϕ	0.090	0.170	0.266	0.420	0.455	0.280	0.113	0.013
$\alpha_{\Delta T}$	4.0603	-.27605	-.78451E-1	0.12235E-1	-.78772E-2			
α_{n_p}	-.92849	-.23712	-.69621E-1	0.10102E-1	-.82814E-2			
α_n	-1.8124	-.24633	-.82991E-1	0.13387E-1	-.58280E-2			

Run#223	U (m/s)	ρ (kg/m^3)	% H_2	% F_2	% N_2	% Ar	% He	% NO
HSS	22.00	0.389	4.00		22.10		73.90	0.100
LSS	8.50	1.550		0.50	25.60	73.90		
y/x	0.061	0.044	0.026	-.005	-.022	-.055	-.071	-.087
ΔT(K)	5.50	11.11	18.65	34.95	43.91	31.26	10.61	1.75
T'(K)	6.86	8.11	9.55	13.96	17.33	26.67	21.90	8.68
n_p/n_ϕ	0.050	0.100	0.164	0.293	0.357	0.252	0.085	0.015
$\alpha_{\Delta T}$	3.4636	-.39624	-.46205E-1	0.17104E-1	-.10929E-1			
α_{n_p}	-1.3141	-.35751	-.42086E-1	0.14772E-1	-.11266E-1			
α_n	-2.2983	-.35130	-.54624E-1	0.17556E-1	-.90752E-2			

Run#224	U (m/s)	ρ (kg/m^3)	% H_2	% F_2	% N_2	% Ar	% He	% NO
HSS	22.00	0.399	0.50		22.60		76.90	0.010
LSS	8.50	1.590		4.00	19.10	76.90		
y/x	0.077	0.044	0.026	-.005	-.022	-.055	-.071	-.087
ΔT(K)	4.44	50.84	75.92	82.92	71.85	32.36	10.82	1.70
T'(K)	15.24	35.48	27.33	16.53	24.41	32.30	23.29	8.66
n_p/n_ϕ	0.035	0.378	0.548	0.597	0.527	0.248	0.084	0.014
$\alpha_{\Delta T}$	4.4299	0.55000E-1	-.87315E-1	-.84709E-2	-.10303E-1			
α_{n_p}	-.50743	0.45203E-1	-.74844E-1	-.74715E-2	-.10698E-1			
α_n	-1.5080	0.29414E-1	-.65131E-1	-.59600E-2	-.11859E-1			

Run#225	U (m/s)	ρ (kg/m^3)	% H_2	% F_2	% N_2	% Ar	% He	% NO
HSS	22.00	0.212	1.00		4.00		95.00	0.045
LSS	8.50	1.690		1.00	4.00	95.00		
y/x	0.076	0.044	0.026	-.005	-.021	-.055	-.070	-.086
ΔT(K)	1.31	15.29	27.21	50.13	58.01	18.89	1.90	0.07
T'(K)	4.25	12.75	17.19	21.51	23.80	28.13	10.69	1.34
n_p/n_ϕ	0.010	0.109	0.187	0.323	0.364	0.121	0.012	0.000
$\alpha_{\Delta T}$	3.8332	-.36183	-.80868E-1	0.34227E-1	-.17929E-1			
α_{n_p}	-1.2035	-.32004	-.74280E-1	0.31483E-1	-.17824E-1			
α_n	-1.9718	-.30128	-.11634	0.27664E-1	-.13471E-1			

Run#227	U (m/s)	ρ (kg/m^3)	% H_2	% F_2	% N_2	% Ar	% He	% NO
HSS	22.00	1.370	1.00		51.60	47.40		0.045
LSS	8.50	0.687		1.00	51.60		47.40	
y/x	0.052	0.035	0.017	0.003	-.028	-.047	-.063	-.079
ΔT(K)	4.93	22.48	48.82	61.31	62.14	47.58	29.34	12.50
T'(K)	14.31	26.17	27.87	19.66	19.30	22.00	23.99	17.37
n_p/n_ϕ	0.040	0.177	0.372	0.463	0.469	0.370	0.234	0.103
$\alpha_{\Delta T}$	4.1489	-.15789	-.17730	-.48533E-1	-.12307E-1			
α_{n_p}	-.74003	-.14418	-.16592	-.49735E-1	-.12688E-1			
α_n	-1.7332	-.11920	-.18292	-.63235E-1	-.14222E-1			

Run#228	U (m/s)	ρ (kg/m^3)	% H_2	% F_2	% N_2	% Ar	% He	% NO
HSS	22.00	1.350	4.00		47.40	48.60		0.100
LSS	8.50	0.675		0.50	50.90		48.60	
y/x	0.052	0.035	0.017	0.003	-.028	-.047	-.063	-.079
ΔT(K)	3.00	12.68	28.57	38.17	52.53	47.54	29.95	11.39
T'(K)	8.44	15.80	16.93	13.38	11.42	16.51	24.89	18.65
n_p/n_ϕ	0.029	0.119	0.263	0.347	0.461	0.419	0.266	0.104
$\alpha_{\Delta T}$		3.7082	-.33338	-.13129		-.36214E-1	-.14067E-1	
α_{n_p}		-1.0002	-.30291	-.12703		-.39319E-1	-.14556E-1	
α_n		-2.1377	-.26726	-.97601E-1		-.46242E-1	-.18416E-1	

Run#229	U (m/s)	ρ (kg/m^3)	% H_2	% F_2	% N_2	% Ar	% He	% NO
HSS	22.00	1.400	0.50		51.30	48.20		0.010
LSS	8.50	0.701		4.00	47.80		48.20	
y/x	0.052	0.035	0.017	0.003	-.028	-.047	-.063	-.079
ΔT(K)	6.27	27.13	52.28	57.24	40.04	27.72	16.01	5.61
T'(K)	15.38	26.99	22.89	16.03	16.24	14.62	13.81	8.81
n_p/n_ϕ	0.056	0.237	0.446	0.489	0.357	0.256	0.151	0.054
$\alpha_{\Delta T}$		4.0302	0.10992	-.17333		-.70151E-1	-.16408E-1	
α_{n_p}		-.73148	0.93372E-1	-.15931		-.68001E-1	-.16574E-1	
α_n		-1.8342	0.91080E-1	-.16459		-.62651E-1	-.14411E-1	

Run#235	U (m/s)	ρ (kg/m^3)	% H_2	% F_2	% N_2	% Ar	% He	% NO
HSS	22.00	1.160	1.00		98.00	1.00		0.045
LSS	8.50	1.160		1.00	98.00		1.00	
y/x	0.060	0.043	0.026	-.007	-.023	-.055	-.073	-.088
ΔT(K)	3.04	14.71	32.64	55.89	55.97	33.26	15.62	4.23
T'(K)	9.85	19.61	22.73	15.57	14.56	25.06	19.69	12.25
n_p/n_ϕ	0.029	0.138	0.299	0.494	0.495	0.301	0.146	0.040
$\alpha_{\Delta T}$		3.9848	-.17307	-.14889		-.28903E-1	-.99942E-2	
α_{n_p}		-.73939	-.15901	-.13967		-.29481E-1	-.10239E-1	
α_n		-1.8582	-.13456	-.13610		-.39089E-1	-.12647E-1	

Run#236	U (m/s)	ρ (kg/m^3)	% H_2	% F_2	% N_2	% Ar	% He	% NO
HSS	22.00	1.510	1.00		20.60	78.40		0.045
LSS	8.50	0.379		1.00	20.60		78.40	
y/x	0.059	0.043	0.026	-.008	-.023	-.055	-.072	-.088
ΔT(K)	0.71	10.03	45.28	82.27	69.68	28.34	12.23	3.53
T'(K)	6.05	23.73	41.15	22.93	23.41	21.83	15.08	8.57
n_p/n_ϕ	0.005	0.068	0.295	0.526	0.459	0.204	0.092	0.027
$\alpha_{\Delta T}$		4.4260	-.56338E-1	-.29040		-.73683E-1	-.12897E-1	
α_{n_p}		-.63119	-.65085E-1	-.26716		-.72333E-1	-.13487E-1	
α_n		-1.5429	-.79237E-1	-.25895		-.64071E-1	-.12121E-1	

Run#237	U (m/s)	ρ (kg/m^3)	$\%H_2$	$\%F_2$	$\%N_2$	$\%Ar$	$\%He$	$\%NO$
HSS	22.00	1.450	4.00		20.60	78.90		0.045
LSS	8.50	0.339		0.50	17.10		78.90	
y/x	0.043	0.027	0.010	-.006	-.023	-.055	-.072	-.087
ΔT(K)	7.67	27.93	49.70	63.50	69.93	44.39	20.33	5.79
T'(K)	17.19	24.83	22.94	18.04	14.48	29.68	25.59	15.41
n_p/n_ϕ	0.060	0.217	0.374	0.467	0.508	0.331	0.157	0.045
$\alpha_{\Delta T}$	4.0866		-.31927	-.19412	-.40827E-1		-.11950E-1	
α_{n_p}	-.81613		-.28464	-.18562	-.44972E-1		-.12741E-1	
α_n	-1.8050		-.28132	-.19556	-.45562E-1		-.11727E-1	

Run#238	U (m/s)	ρ (kg/m^3)	$\%H_2$	$\%F_2$	$\%N_2$	$\%Ar$	$\%He$	$\%NO$
HSS	22.00	1.500	0.50		20.10	79.40		0.045
LSS	8.50	0.376		4.00	16.60		79.40	
y/x	0.043	0.027	0.010	-.006	-.023	-.055	-.072	-.088
ΔT(K)	11.45	37.97	54.70	52.87	40.58	17.04	8.63	2.68
T'(K)	22.40	29.32	22.18	17.56	16.25	12.72	9.19	5.48
n_p/n_ϕ	0.088	0.289	0.412	0.403	0.320	0.143	0.074	0.023
$\alpha_{\Delta T}$	4.0154		0.11008	-.24148	-.72984E-1		-.12386E-1	
α_{n_p}	-.86598		0.89734E-1	-.22720	-.71109E-1		-.12662E-1	
α_n	-1.8572		0.62214E-1	-.25106	-.68171E-1		-.10149E-1	

Run#239	U (m/s)	ρ (kg/m^3)	$\%H_2$	$\%F_2$	$\%N_2$	$\%Ar$	$\%He$	$\%NO$
HSS	22.00	1.580	1.00		4.10	94.90		0.045
LSS	8.50	0.216		1.00	4.10		94.90	
y/x	0.041	0.025	0.009	-.007	-.025	-.057	-.073	-.090
ΔT(K)	5.68	36.17	74.26	81.09	64.24	23.13	9.67	2.93
T'(K)	19.50	40.43	37.19	28.35	25.71	18.51	11.85	6.33
n_p/n_ϕ	0.036	0.223	0.442	0.485	0.401	0.160	0.070	0.022
$\alpha_{\Delta T}$	4.4116		-.89725E-1	-.38151	-.11026		-.17709E-1	
α_{n_p}	-.71291		-.10116	-.35268	-.10764		-.18325E-1	
α_n	-1.5545		-.93739E-1	-.33798	-.96788E-1		-.16031E-1	

Run#240	U (m/s)	ρ (kg/m^3)	$\%H_2$	$\%F_2$	$\%N_2$	$\%Ar$	$\%He$	$\%NO$
HSS	22.00	1.540	4.00		0.80	95.20		0.045
LSS	8.50	0.209		0.50	4.30		95.20	
y/x	0.043	0.027	0.009	-.008	-.023	-.039	-.056	-.071
ΔT(K)	4.81	29.49	57.97	75.94	82.83	75.65	51.21	24.68
T'(K)	14.55	28.92	27.31	21.13	15.58	23.51	30.60	28.14
n_p/n_ϕ	0.037	0.218	0.414	0.526	0.567	0.522	0.367	0.183
$\alpha_{\Delta T}$	4.2448		-.34135	-.22505	-.66637E-1		-.18104E-1	
α_{n_p}	-.71530		-.29941	-.21167	-.71016E-1		-.18955E-1	
α_n	-1.6770		-.26775	-.21685	-.88880E-1		-.23075E-1	

Run#241	U (m/s)	ρ (kg/m^3)	% H_2	% F_2	% N_2	% Ar	% He	% NO
HSS	22.00	1.610	0.50		3.50	96.00		0.045
LSS	8.50	0.220		4.00			96.00	
y/x	0.043	0.027	0.011	-.006	-.023	-.039	-.056	-.071
ΔT(K)	6.67	32.97	53.05	50.50	38.08	25.11	13.70	6.39
T'(K)	19.33	31.05	25.60	20.74	17.37	15.11	10.77	7.66
n_p/n_ϕ	0.047	0.234	0.373	0.361	0.283	0.193	0.109	0.052
$\alpha_{\Delta T}$	3.9889		0.13956	-.28076		-.10537	-.20610E-1	
α_{n_p}	-.95927		0.11438	-.26422		-.10335	-.21136E-1	
α_n	-1.8943		0.13172	-.24948		-.11107	-.25316E-1	

Run#345	U (m/s)	ρ (kg/m^3)	% H_2	% F_2	% N_2	% Ar	% He	% NO
HSS	22.00	1.140	0.50		99.50			0.011
LSS	8.50	1.170		4.00	96.00			
y/x	0.061	0.045	0.030	-.004	-.020	-.053	-.070	-.086
ΔT(K)	0.86	7.49	30.16	54.39	46.88	22.40	9.61	2.29
T'(K)	3.88	13.19	28.57	10.21	10.25	13.17	10.77	4.54
n_p/n_ϕ	0.010	0.081	0.303	0.547	0.482	0.244	0.107	0.026
$\alpha_{\Delta T}$	4.0139		0.32738E-1	-.21301		-.74539E-1	-.17520E-1	
α_{n_p}	-.58954		0.13005E-1	-.20064		-.70229E-1	-.16954E-1	
α_n	-1.8553		0.35790E-1	-.18028		-.78615E-1	-.20916E-1	

Run#346	U (m/s)	ρ (kg/m^3)	% H_2	% F_2	% N_2	% Ar	% He	% NO
HSS	22.00	1.170		4.00	96.00			
LSS	8.50	1.150	0.50		99.50			0.011
y/x	-.082	-.065	-.050	-.016	0.000	0.032	0.049	0.065
ΔT(K)	1.67	12.67	36.15	48.81	37.77	15.52	4.76	0.80
T'(K)	7.66	18.18	30.01	11.25	9.76	10.40	7.16	2.28
n_p/n_ϕ	0.018	0.135	0.359	0.498	0.398	0.173	0.054	0.009
$\alpha_{\Delta T}$	3.6401		-.39706	-.89874E-1		-.78318E-2	-.19295E-1	
α_{n_p}	-.91314		-.35369	-.91345E-1		-.10510E-1	-.18620E-1	
α_n	-2.1866		-.35580	-.97959E-1		-.24480E-2	-.14397E-1	

Run#347	U (m/s)	ρ (kg/m^3)	% H_2	% F_2	% N_2	% Ar	% He	% NO
HSS	22.00	1.170		4.00	96.00			
LSS	8.50	1.150	0.25		99.70			0.011
y/x	-.082	-.065	-.050	-.016	0.000	0.032	0.049	0.065
ΔT(K)	0.98	6.67	19.07	24.41	19.11	7.92	2.42	0.44
T'(K)	4.14	9.13	15.09	5.81	4.92	5.29	3.55	1.06
n_p/n_ϕ	0.021	0.141	0.387	0.504	0.401	0.171	0.053	0.010
$\alpha_{\Delta T}$	2.9628		-.39458	-.99593E-1		-.90413E-2	-.17661E-1	
α_{n_p}	-.90133		-.37726	-.10333		-.91547E-2	-.16734E-1	
α_n	-2.7881		-.32581	-.16197E-1		-.13414E-1	-.27996E-1	

Run#348	U (m/s)	ρ (kg/m^3)	% H_2	% F_2	% N_2	% Ar	% He	% NO
HSS	22.00	1.150	0.25		99.70			0.011
LSS	8.50	1.170		4.00	96.00			
y/x	0.061	0.045	0.031	-.004	-.020	-.053	-.070	-.086
ΔT(K)	1.85	10.46	23.42	27.87	22.66	9.31	3.38	0.74
T'(K)	4.93	10.73	14.13	5.74	5.96	6.76	4.77	1.75
n_p/n_ϕ	0.039	0.219	0.474	0.569	0.470	0.199	0.073	0.016
$\alpha_{\Delta T}$	3.3921	0.18573	-.15308	-.48683E-1	-.14331E-1			
α_{n_p}	-.49983	0.17459	-.14770	-.47507E-1	-.14219E-1			
α_n	-2.4262	0.87466E-1	-.12390	-.30004E-1	-.15249E-1			

Run#351	U (m/s)	ρ (kg/m^3)	% H_2	% F_2	% N_2	% Ar	% He	% NO
HSS	22.00	1.140	1.00		99.00			0.011
LSS	8.50	1.180		8.00	92.00			
y/x	0.061	0.045	0.031	-.004	-.020	-.053	-.070	-.086
ΔT(K)	2.41	22.20	72.81	104.73	85.09	35.08	13.12	2.35
T'(K)	10.30	30.62	56.94	19.75	20.30	24.33	17.76	6.08
n_p/n_ϕ	0.013	0.111	0.317	0.463	0.394	0.181	0.071	0.013
$\alpha_{\Delta T}$	4.6976	0.16402	-.17511	-.73165E-1	-.20453E-1			
α_{n_p}	-.73509	0.11248	-.15411	-.63675E-1	-.19141E-1			
α_n	-1.3046	0.12889	-.16037	-.66588E-1	-.18795E-1			

Run#353	U (m/s)	ρ (kg/m^3)	% H_2	% F_2	% N_2	% Ar	% He	% NO
HSS	22.00	1.180		8.00	92.00			
LSS	8.50	1.140	1.00		99.00			0.011
y/x	-.084	-.068	-.050	-.017	-.001	0.033	0.048	0.064
ΔT(K)	3.07	24.23	71.03	87.99	68.09	27.21	8.94	1.41
T'(K)	13.24	34.08	58.26	20.17	17.06	17.59	12.64	3.88
n_p/n_ϕ	0.016	0.119	0.308	0.405	0.331	0.145	0.050	0.008
$\alpha_{\Delta T}$	4.2164	-.38318	-.81672E-1	-.14859E-1	-.19207E-1			
α_{n_p}	-1.1068	-.31142	-.88650E-1	-.18345E-1	-.17562E-1			
α_n	-1.6983	-.33801	-.97433E-1	-.11537E-1	-.14952E-1			

Run#354	U (m/s)	ρ (kg/m^3)	% H_2	% F_2	% N_2	% Ar	% He	% NO
HSS	22.00	1.160		2.00	98.00			
LSS	8.50	1.150	0.13		99.90			0.011
y/x	-.084	-.068	-.050	-.017	-.001	0.033	0.048	0.064
ΔT(K)	0.39	3.23	9.62	13.36	10.82	5.07	2.03	0.58
T'(K)	1.48	4.27	7.02	2.98	2.69	3.05	2.35	0.92
n_p/n_ϕ	0.017	0.139	0.406	0.565	0.461	0.219	0.088	0.026
$\alpha_{\Delta T}$	2.3777	-.32768	-.74818E-1	-.33212E-2	-.16399E-1			
α_{n_p}	-.77755	-.31655	-.75133E-1	-.39887E-2	-.16133E-1			
α_n	-3.2612	-.12834	-.57884E-1	-.32914E-1	-.22086E-1			

Run#355	U (m/s)	ρ (kg/m^3)	% H_2	% F_2	% N_2	% Ar	% He	% NO
HSS	22.00	1.150	0.13		99.90			0.011
LSS	8.50	1.160		2.05	98.00			
y/x	0.063	0.047	0.031	-.003	-.018	-.052	-.068	-.084
ΔT(K)	0.76	4.03	10.22	14.03	11.65	4.58	1.74	0.42
T'(K)	1.69	4.28	6.26	2.66	2.90	3.23	2.24	0.83
n_p/n_ϕ	0.033	0.172	0.430	0.589	0.493	0.197	0.075	0.019
$\alpha_{\Delta T}$	2.6664		0.11614	-.17564		-.36251E-1	-.11309E-1	
α_{n_p}	-.50226		0.11105	-.17394		-.35416E-1	-.11069E-1	
α_n	-3.0026		0.10586	-.17414		-.65107E-1	-.17008E-1	

Run#359	U (m/s)	ρ (kg/m^3)	% H_2	% F_2	% N_2	% Ar	% He	% NO
HSS	22.00	1.150			92.00			8.000
LSS	8.50	1.150		0.50	99.50			
y/x	0.063	0.047	0.031	-.001	-.018	-.050	-.068	-.084
ΔT(K)	0.55	3.18	8.94	21.80	27.58	21.01	7.15	0.88
T'(K)	2.05	4.12	7.84	6.29	5.37	11.57	10.00	3.09
n_p/n_ϕ	0.011	0.064	0.177	0.420	0.523	0.400	0.139	0.018
$\alpha_{\Delta T}$	3.0664		-.38104	-.10228		-.13843E-1	-.17382E-1	
α_{n_p}	-.88358		-.36115	-.99649E-1		-.15391E-1	-.17391E-1	
α_n	-2.7204		-.29357	-.76897E-1		-.27219E-1	-.22828E-1	

Run#360	U (m/s)	ρ (kg/m^3)	% H_2	% F_2	% N_2	% Ar	% He	% NO
HSS	22.00	1.150		0.50	99.50			
LSS	8.50	1.150			92.00			8.000
y/x	-.082	-.065	-.048	-.016	0.001	0.033	0.049	0.065
ΔT(K)	0.89	3.32	9.76	23.66	28.80	21.60	7.51	1.06
T'(K)	3.19	4.90	8.34	6.09	4.63	10.02	9.04	2.80
n_p/n_ϕ	0.018	0.067	0.192	0.453	0.545	0.413	0.147	0.022
$\alpha_{\Delta T}$	3.3775		0.19591	-.16878		-.42846E-1	-.13270E-1	
α_{n_p}	-.59028		0.18631	-.15901		-.41435E-1	-.13595E-1	
α_n	-2.4200		0.27478	-.10529		-.67808E-1	-.27141E-1	

Run#361	U (m/s)	ρ (kg/m^3)	% H_2	% F_2	% N_2	% Ar	% He	% NO
HSS	2.20	1.150		0.50	99.50			
LSS	0.90	1.150			92.00			8.000
y/x	-.082	-.065	-.048	-.016	0.001	0.033	0.049	0.065
ΔT(K)	14.00	19.73	25.00	31.89	32.60	27.12	19.75	12.11
T'(K)	14.54	13.48	14.36	11.65	10.73	15.00	16.18	15.16
n_p/n_ϕ	0.265	0.374	0.468	0.591	0.605	0.504	0.370	0.228
$\alpha_{\Delta T}$	3.4887		-.29335E-2	-.62573E-1		-.83174E-2	-.19846E-2	
α_{n_p}	-.49968		-.32175E-2	-.60204E-1		-.83490E-2	-.20414E-2	
α_n	-2.2980		-.42639E-1	-.62351E-1		-.27172E-2	-.16034E-2	

Run#362	U (m/s)	ρ (kg/m^3)	% H_2	% F_2	% N_2	% Ar	% He	% NO
HSS	2.20	1.150			92.00			8.000
LSS	0.90	1.150		0.50	99.50			
y/x	0.065	0.049	0.033	0.000	-.016	-.048	-.065	-.082
ΔT(K)	4.27	7.96	12.25	16.24	17.04	18.35	19.62	19.41
T'(K)	10.41	11.62	13.52	10.54	8.69	9.44	10.19	11.71
n_p/n_ϕ	0.081	0.153	0.234	0.314	0.331	0.354	0.377	0.371
$\alpha_{\Delta T}$	2.7892	-.85361E-1	-.37821E-1	-.17843E-1	-.27670E-2			
α_{n_p}	-1.1575	-.88958E-1	-.39550E-1	-.17585E-1	-.26971E-2			
α_n	-2.9930	-.79884E-1	-.40187E-1	-.24275E-1	-.42058E-2			

Run#363	U (m/s)	ρ (kg/m^3)	% H_2	% F_2	% N_2	% Ar	% He	% NO
HSS	3.47	1.150		0.50	99.50			
LSS	1.34	1.150			92.00			8.000
y/x	-.098	-.065	-.048	-.016	0.001	0.033	0.049	0.082
ΔT(K)	1.27	10.07	18.01	28.84	31.24	28.25	21.27	5.47
T'(K)	4.19	12.52	17.11	15.14	12.84	14.74	16.55	11.25
n_p/n_ϕ	0.025	0.193	0.336	0.534	0.579	0.524	0.397	0.104
$\alpha_{\Delta T}$	3.4452	0.58318E-1	-.70510E-1	-.22115E-2	-.40263E-2			
α_{n_p}	-.54368	0.57605E-1	-.69506E-1	-.23543E-2	-.39002E-2			
α_n	-2.3535	-.23458E-2	-.68870E-1	0.73310E-2	-.49312E-2			

Run#364	U (m/s)	ρ (kg/m^3)	% H_2	% F_2	% N_2	% Ar	% He	% NO
HSS	3.47	1.150			92.00			8.000
LSS	1.34	1.150		0.50	99.50			
y/x	0.079	0.047	0.031	-.002	-.018	-.050	-.068	-.100
ΔT(K)	1.38	11.14	15.00	17.73	18.65	18.89	18.30	8.23
T'(K)	6.61	13.01	14.67	10.21	9.17	11.27	12.61	12.47
n_p/n_ϕ	0.026	0.213	0.284	0.342	0.360	0.362	0.349	0.157
$\alpha_{\Delta T}$	2.8854	-.17538E-1	-.16268E-1	-.22512E-1	-.59131E-2			
α_{n_p}	-1.0648	-.22216E-1	-.19134E-1	-.22279E-1	-.57976E-2			
α_n	-2.7947	0.43451E-1	-.37529E-1	-.42294E-1	-.84412E-2			

Run#365	U (m/s)	ρ (kg/m^3)	% H_2	% F_2	% N_2	% Ar	% He	% NO
HSS	9.90	1.150			92.00			8.000
LSS	3.80	1.150		0.50	99.50			
y/x	0.064	0.049	0.032	0.000	-.016	-.050	-.065	-.083
ΔT(K)	1.96	6.14	11.88	21.03	24.76	26.99	20.32	10.39
T'(K)	5.66	7.11	10.44	6.80	6.53	8.92	13.34	12.61
n_p/n_ϕ	0.038	0.122	0.231	0.406	0.473	0.510	0.385	0.199
$\alpha_{\Delta T}$	3.0580	-.22458	-.50095E-1	-.19693E-1	-.91227E-2			
α_{n_p}	-.89308	-.21692	-.49642E-1	-.19172E-1	-.89239E-2			
α_n	-2.6644	-.25818	-.71325E-1	-.60647E-2	-.51184E-2			

Run#366	U (m/s)	ρ (kg/m^3)	$\%H_2$	$\%F_2$	$\%N_2$	$\%Ar$	$\%He$	$\%NO$
HSS	9.90	1.150		0.50	99.50			
LSS	3.80	1.150			92.00			8.000
y/x	-.084	-.068	-.050	-.018	-.002	0.030	0.047	0.063
ΔT(K)	4.77	10.11	17.02	27.69	30.65	26.97	16.60	5.99
T'(K)	6.84	8.16	11.50	7.19	5.75	9.42	13.28	9.52
n_p/n_ϕ	0.095	0.199	0.327	0.524	0.576	0.509	0.316	0.116
$\alpha_{\Delta T}$	3.4386	0.86876E-1	-.88593E-1	-.23043E-1	-.68540E-2			
α_{n_p}	-.53138	0.89741E-1	-.86866E-1	-.23749E-1	-.67947E-2			
α_n	-2.3772	0.10252	-.10649	-.22986E-1	-.40264E-2			

Run#369	U (m/s)	ρ (kg/m^3)	$\%H_2$	$\%F_2$	$\%N_2$	$\%Ar$	$\%He$	$\%NO$
HSS	44.00	1.150			92.00			8.000
LSS	17.00	1.150		0.50	99.50			
y/x	0.047	0.032	0.016	0.001	-.017	-.033	-.050	-.066
ΔT(K)	0.65	4.70	13.18	21.07	26.65	20.28	4.43	0.20
T'(K)	2.01	4.29	8.38	5.32	4.84	8.26	6.46	0.85
n_p/n_ϕ	0.013	0.095	0.258	0.407	0.507	0.391	0.088	0.004
$\alpha_{\Delta T}$	3.0700	-.45723	-.21790	-.18670E-1	-.55158E-1			
α_{n_p}	-.87928	-.43435	-.21016	-.22038E-1	-.55011E-1			
α_n	-2.6837	-.42230	-.20785	0.87750E-3	-.53253E-1			

Run#372	U (m/s)	ρ (kg/m^3)	$\%H_2$	$\%F_2$	$\%N_2$	$\%Ar$	$\%He$	$\%NO$
HSS	44.00	1.150			92.00			8.000
LSS	17.00	1.150		0.50	99.50			
y/x	0.047	0.032	0.016	0.001	-.017	-.033	-.050	-.066
ΔT(K)	0.29	4.45	13.16	20.13	24.91	20.17	4.36	-0.04
T'(K)	1.98	4.35	8.04	5.00	4.67	7.85	6.45	1.18
n_p/n_ϕ	0.006	0.090	0.258	0.390	0.477	0.389	0.086	-.001
$\alpha_{\Delta T}$	3.0184	-.39663	-.18088	-.54052E-1	-.70869E-1			
α_{n_p}	-.92708	-.37251	-.17068	-.59298E-1	-.72139E-1			
α_n	-2.7694	-.43396	-.17402	-.68076E-1	-.93698E-1			

Run#373	U (m/s)	ρ (kg/m^3)	$\%H_2$	$\%F_2$	$\%N_2$	$\%Ar$	$\%He$	$\%NO$
HSS	83.40	1.150			92.00			8.000
LSS	32.20	1.150		0.50	99.50			
y/x	0.047	0.032	0.016	0.001	-.017	-.033	-.050	-.066
ΔT(K)	1.33	6.09	14.77	22.48	26.08	14.20	1.68	0.30
T'(K)	2.47	3.74	6.12	3.90	4.48	13.52	2.93	0.54
n_p/n_ϕ	0.027	0.123	0.290	0.433	0.497	0.271	0.034	0.006
$\alpha_{\Delta T}$	3.1639	-.44742	-.34208	0.59817E-1	-.32267E-1			
α_{n_p}	-.78728	-.42228	-.32777	0.56308E-1	-.33511E-1			
α_n	-2.6067	-.31819	-.28635	0.11073E-1	-.52198E-1			

Run#374	U (m/s)	ρ (kg/m^3)	$\%H_2$	$\%F_2$	$\%N_2$	$\%Ar$	$\%He$	$\%NO$
HSS	83.40	1.150		0.50	99.50			
LSS	32.20	1.150			92.00			8.000
y/x	-.064	-.049	-.033	-.018	0.000	0.016	0.033	0.049
ΔT(K)	-0.65	-0.01	6.76	20.45	30.06	29.11	10.35	0.70
T'(K)	0.65	1.97	7.52	4.70	3.47	9.83	7.24	2.28
n_p/n_ϕ	-.014	0.000	0.134	0.396	0.567	0.546	0.205	0.014
$\alpha_{\Delta T}$	3.4042		0.18959	-.23760		-.14306E-1	-.12056	
α_{n_p}	-.56668		0.16421	-.22112		-.50489E-2	-.11965	
α_n	-2.4088		0.24438	-.21015		-.46799E-1	-.13863	

Run#375	U (m/s)	ρ (kg/m^3)	$\%H_2$	$\%F_2$	$\%N_2$	$\%Ar$	$\%He$	$\%NO$
HSS	22.00	1.150			92.00			8.000
LSS	8.50	1.150		0.50	99.50			
y/x	0.055	0.039	0.023	0.005	-.027	-.042	-.059	-.075
ΔT(K)	0.66	4.26	11.62	17.79	25.82	18.14	5.40	1.03
T'(K)	3.50	5.47	9.78	5.73	6.22	14.81	8.25	4.29
n_p/n_ϕ	0.013	0.085	0.226	0.347	0.492	0.342	0.106	0.020
$\alpha_{\Delta T}$	3.0586		-.41622	-.18886		-.56302E-2	-.20071E-1	
α_{n_p}	-.88518		-.39550	-.18787		-.82353E-2	-.20187E-1	
α_n	-2.7044		-.29116	-.14000		-.59267E-1	-.38971E-1	

Run#376	U (m/s)	ρ (kg/m^3)	$\%H_2$	$\%F_2$	$\%N_2$	$\%Ar$	$\%He$	$\%NO$
HSS	22.00	1.150		0.50	99.50			
LSS	8.50	1.150			92.00			8.000
y/x	-.072	-.056	-.040	-.023	0.010	0.025	0.042	0.058
ΔT(K)	0.71	4.52	12.85	21.63	29.79	21.42	6.79	0.66
T'(K)	3.83	6.12	11.37	6.90	5.80	14.93	9.15	3.63
n_p/n_ϕ	0.014	0.090	0.248	0.416	0.561	0.402	0.133	0.013
$\alpha_{\Delta T}$	3.4035		0.95348E-1	-.23370		-.60034E-1	-.24009E-1	
α_{n_p}	-.56758		0.87429E-1	-.22503		-.58791E-1	-.24279E-1	
α_n	-2.4078		0.97500E-1	-.15135		-.62835E-1	-.44118E-1	

Appendix B. Analysis

The data acquired in the present work allow the examination of several quantities of interest in reacting turbulent flows. These fall into three categories; local, integral, and integral flux, each of which will be approached in turn.

Local

The major concepts involved in the analysis of the local data were derived for the laser induced fluorescence (LIF) technique in liquids by Koochesfahani & Dimotakis (1986). Differences between this developement and one appropriate for gas-phase measurements exist, however, and will be described here.

Starting with two distinguishable fluids, label pure fluid from the low-speed side as $\xi = 0$, and pure fluid from the high-speed side as $\xi = 1$. Identifying ξ as the composition, the intermediate values, $0 < \xi < 1$, correspond to the fraction of high-speed fluid in the mixture, or high-speed fluid mixture fraction. If we were able to make measurements with perfect resolution in both time and space, a properly normalized histogram of composition uniformly sampled at discrete times would approximate the probability density function (PDF) of composition, $P(\xi)$. Although laboratory measurements of sufficient resolution can not currently be made in high Reynolds number flows, the PDF is a useful construct in the present discussion. A conceptual model of the PDF of composition appears in Figure B.1.

Next we apply the change of variables from composition to temperature shown in Figure B.2. This temperature dependence, $\Delta T(\xi)$, represents the temperature rise above ambient which occurs when a fast, irreversible, exothermic reaction occurs between two fluids containing reactants mixed at a composition ξ . For

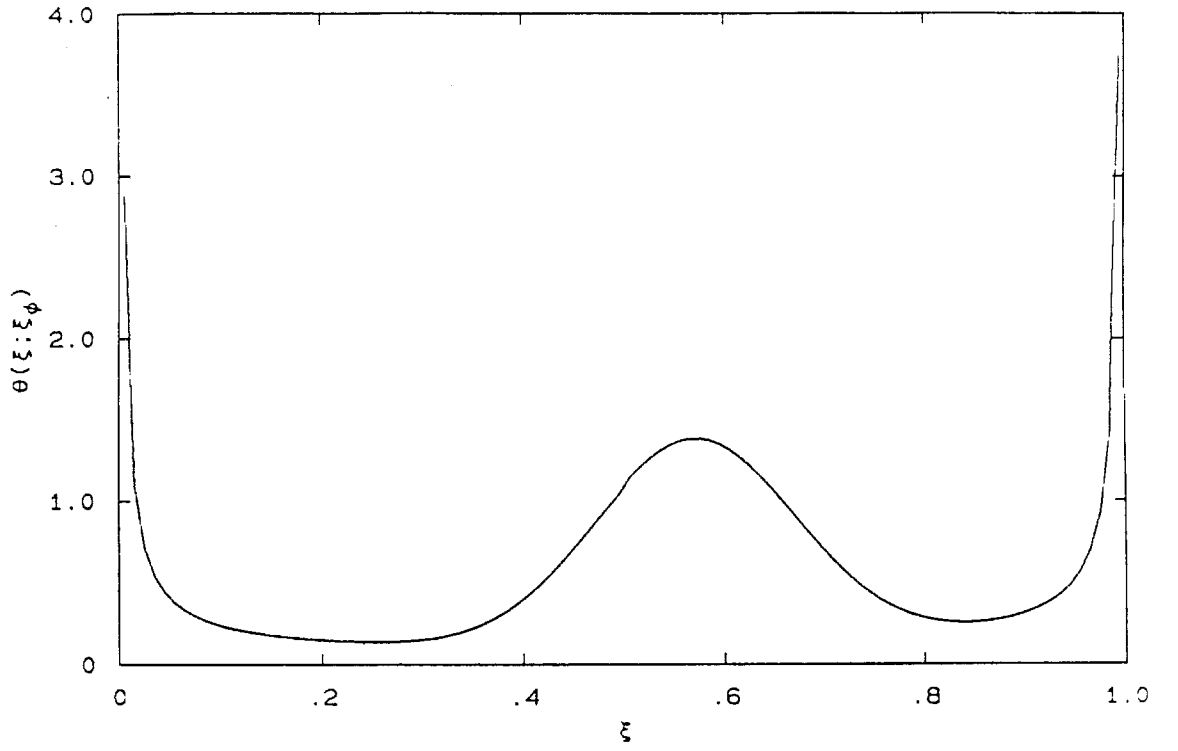

Figure B.1 Conceptual PDF of composition.

the H_2/F_2 system used in most of the experiments here, the stoichiometric mixture ratio is equal to the ratio of the freestream reactant concentrations, $\phi = c_2/c_1$. As an example, if the high-speed stream contained 4% H_2 and the low-speed stream carried 1/2% F_2 , the stoichiometric mixture ratio would be $\phi = \frac{1}{2}/4 = 1/8$. However, for the NO/F_2 system the freestream concentration of NO must be halved. If the high-speed stream contained 4% NO and the low-speed stream carried 1/2% F_2 , the stoichiometric mixture ratio would be $\phi = \frac{\frac{1}{2}}{4/2} = 1/4$. The value $\xi_\phi = \phi/(1+\phi)$ is the stoichiometric composition and the temperature rise at this composition is the adiabatic flame temperature rise, ΔT_f. Using standard

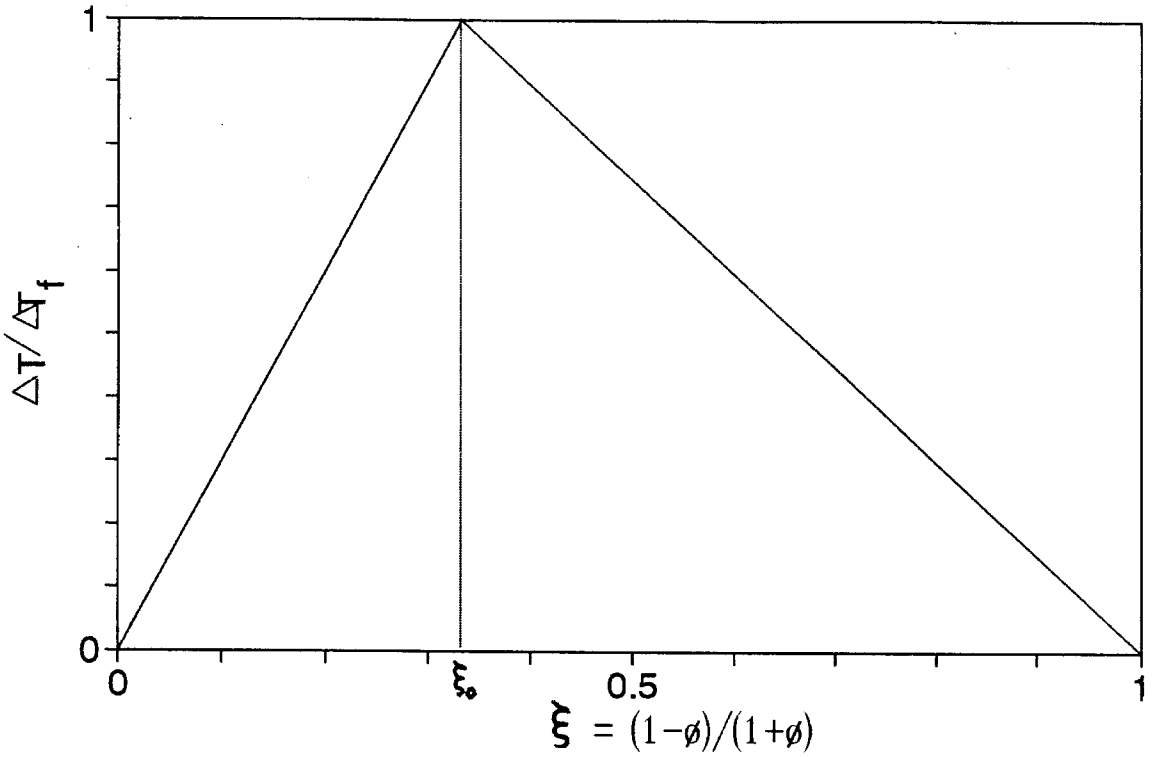

Figure B.2 Transform between temperature and composition for $\phi = 1/2$.

relations for change of independent variables, the PDF of temperature rise is given by

$$P_T(\Delta T) = \frac{1}{\Delta T_f}\left[\xi_\phi\, P\left(\xi_\phi \frac{\Delta T}{\Delta T_f}\right) + (1-\xi_\phi)\, P\left(1-(1-\xi_\phi)\frac{\Delta T}{\Delta T_f}\right)\right]. \tag{B.1}$$

Normalization of P_T is guaranteed by this transform if P is properly normalized. Note that the presence of two terms stems from the 'double-valued' nature of the transform $\Delta T(\xi)$. Having the probability of temperature rise, the mean temperature at a specific ϕ may be expressed simply as,

$$\frac{\overline{\Delta T}(\xi_\phi)}{\Delta T_f} = \int_0^{\Delta T_f} \frac{\Delta T}{\Delta T_f}\, P_T(\Delta T)\, d(\Delta T)\ . \tag{B.2}$$

Defining the normalized temperature rise, θ, to be the mean temperature divided by the adiabatic flame temperature, we can use Equation $B.1$ to relate it to the PDF of composition,

$$\theta(\xi_\phi) \;=\; \int_0^{\xi_\phi} \frac{\xi}{\xi_\phi}\, P(\xi)\, d\xi \;+\; \int_{\xi_\phi}^{1} \frac{1-\xi}{1-\xi_\phi}\, P(\xi)\, d\xi \;. \qquad (B.3)$$

There are two interesting limits immediately apparent from this expression. These are the "flip" experiments described in Koochesfahani *et al.* (1985). If we let the stoichiometric composition $\xi_\phi \rightarrow 1$, then the second integral disappears and we are left with

$$\lim_{\xi_\phi \rightarrow 1} \theta(\xi_\phi) \;=\; \int_0^1 \xi\, P(\xi)\, d\xi \;=\; \overline{\xi} \qquad (B.4)$$

where $\overline{\xi}$ is the mean composition. If we let $\xi_\phi \rightarrow 0$, the first integral vanishes and we are left with

$$\lim_{\xi_\phi \rightarrow 0} \theta(\xi_\phi) \;=\; \int_0^1 (1-\xi)\, P(\xi)\, d\xi \;=\; 1-\overline{\xi} \qquad (B.5)$$

In the latter case the roles of $\xi = 0$ and $\xi = 1$ have been reversed, *i.e.*, $\phi \rightarrow 1/\phi$, and $1-\overline{\xi}$ represents the mean low-speed fluid mixture fraction.

However, the analysis above has been too casual. Previous experimental work (Konrad 1976, Koochesfahani & Dimotakis 1984) has demonstrated that there is a finite probability of observing pure fluid from each of the freestreams in the interior of the layer. Consequently, we must admit integrable singularities (delta functions) in $P(\xi)$ at the values $\xi = 0$ and $\xi = 1$. The process of taking the limits discussed above, and eliminating one of the integrals in each case, relied on the integrand being finite at these points. Though delta functions at any other value of ξ would not pose a problem, their existance at these values invalidates

the association of mean temperature and mean composition. In retrospect this seems obvious, since even in the limits discussed above, measurements of temperature cannot distinguish between pure high-speed or pure low-speed fluid, *i.e.*, $\Delta T(0) = \Delta T(1) = 0$. Since this ambiguity in the transform arises from the probability of seeing pure fluid from the lean reactant freestream, this difficulty can be avoided if we restrict our attention to the molecularly mixed fluid (compositions $\xi \neq 0, 1$). As will be shown below, this "difficulty" becomes a benefit if reacting flows are used to investigate mixing.

We have examined how the mean temperature rise is related to the mean composition. Another useful, though perhaps less precise, interpretation is that in these limits $\theta(\xi_\phi)$ measures the *amount* of fluid originating in the lean reactant freestream. Building on this idea, we can define two reduced temperatures as

$$\theta_1(\xi_\phi) \;=\; \xi_\phi \frac{\overline{\Delta T}}{\Delta T_f}(\xi_\phi) \;\leq\; \int_0^{1-\epsilon} \xi\, P(\xi)\, d\xi$$

$$\theta_2(\xi_\phi) \;=\; (1-\xi_\phi) \frac{\overline{\Delta T}}{\Delta T_f}(\xi_\phi) \;\leq\; \int_\epsilon^{1} (1-\xi)\, P(\xi)\, d\xi \quad . \qquad (B.6)$$

An arbitrary small number, ϵ , has been introduced in the limits of integration solely to indicate that contributions from pure fluid from either stream have been excluded. The limits discussed above may now be reexamined. As $\xi_\phi \rightarrow 1$, the equality in the first expression is realized and $\theta_1(\xi_\phi)$ becomes equal to the amount of high-speed fluid which is molecularly mixed. Similarly, in the limit of $\xi_\phi \rightarrow 0$, $\theta_2(\xi_\phi)$ measures the amount of low-speed fluid which is molecularly mixed. As shown in Figure B.2, the normalization has been chosen such that for any other stoichiometric composition, $\theta_1(\xi_\phi)$ and $\theta_2(\xi_\phi)$ provide conservative estimates for the amount of mixed fluid which originated in the respective freestream. Measurements of θ_1 and θ_2 are made with the stoichiometry as close to these

limits as practical. For this reason, the explicit dependence of θ_1 and θ_2 upon ξ_ϕ will be omitted and these respective limits for the stoichiometry should be committed to memory.

These results provide a very powerful tool for investigation of turbulent mixing. Methods of directly measuring concentrations in gas-phase flows do exist, for example the Brown-Rebello aspirating probe, Rayleigh scattering or LIF. However, in any technique which directly measures concentration, complete resolution of all scales in the flow is required in order to determine the amount of mixing. Because chemical reaction will not occur where reactants are not in molecular contact, techniques which sense reaction products benefit from the molecular level resolution of the reaction. The measurement of temperature is an established technology and using the limits discussed above, several quantities of interest can be determined from reacting experiments in a manner which does not rely on resolution for accuracy.

If the reduced temperatures are now added, an estimate of the probability of mixed fluid at any composition, θ_m , is obtained.

$$\theta_m \;=\; \theta_1 + \theta_2 \;\leq\; \int_{\epsilon}^{1-\epsilon} (1-\xi)\, P(\xi)\, d\xi \;+\; \int_{\epsilon}^{1-\epsilon} \xi\, P(\xi)\, d\xi \;=\; \int_{\epsilon}^{1-\epsilon} P(\xi)\, d\xi \quad (B.7)$$

and this again provides a conservative estimate.

Dimotakis (1987) introduces this result in a somewhat more direct fashion. He defines a mixed-fluid function, $\Theta_m(\xi;\xi_o)$, to be the normalized sum of the temperature rises for the "flip" experiments, *i.e.*,

$$\Theta_m(\xi;\xi_o) \;=\; (1-\xi_o)\left(\frac{\Delta T(\xi;\xi_o)}{\Delta T_f(\xi_o)} \;+\; \frac{\Delta T(\xi;1-\xi_o)}{\Delta T_f(1-\xi_o)}\right) \;. \qquad (B.8)$$

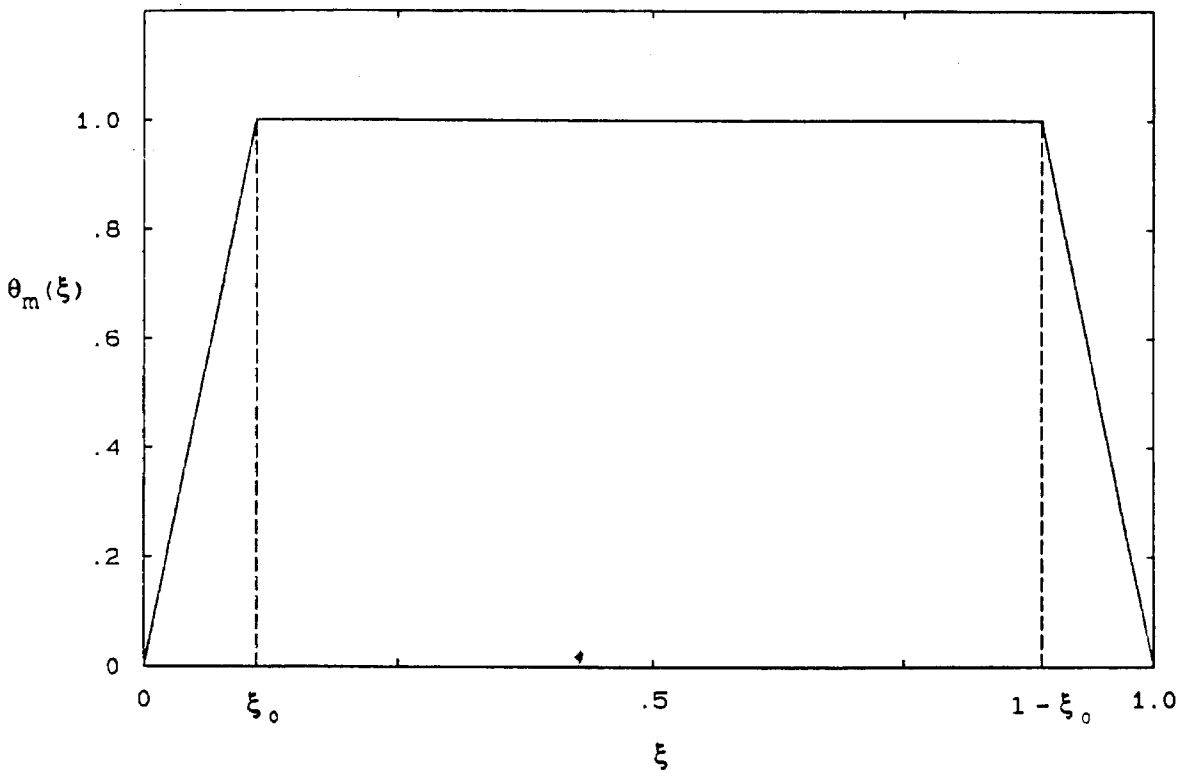

Figure B.3 Mixed-fluid function for $\xi_o = 1/9$.

This transform provides an estimate for the amount of mixed fluid through the relation

$$\theta_m = \int_0^1 \Theta_m(\xi;\xi_o)\, P(\xi)\, d\xi \quad . \tag{B.9}$$

As shown by Figure B.3, for small values of ξ_o , this estimate will be quite good. Note that the figure corresponds to the stoichiometry $(\xi_o = \xi_\phi)$ at which most of the flip experiments were performed. These two approaches are clearly equivalent.

Having a measure for the amount of mixed fluid from each stream separately we can also estimate the average composition of the mixed fluid,

$$\xi_m = \frac{\int_{\epsilon}^{1-\epsilon} \xi\, P(\xi)\, d\xi}{\int_{\epsilon}^{1-\epsilon} P(\xi)\, d\xi} \approx \frac{\theta_1}{\theta_1 + \theta_2} = \frac{\theta_1}{\theta_m} \,. \qquad (B.10)$$

Note that this expression differs from θ_m in one important respect. Here the quantity ξ_m is expressed as the quotient of two approximations and cannot *a priori* be said to represent a bound of its actual value.

Dilatation Considerations

As discussed above, measurements of a reaction marker such as temperature in the liquid shear layer can be considered equivalent to measuring the number density of product. In these gas-phase experiments, however, the total number density is not constant due to dilatation. This mandates reformulation of the previous analysis. Although the central issue is simply the distinction between volume and moles, an altered analysis of the data is required.

As a result of the careful matching of specific heats, the isobaric conditions and the simple chemical system with which these experiments were performed, we can still relate the measurements to the amount of product formed. In particular,

$$\Delta T \sim \frac{n_p}{n} \qquad (B.11)$$

where ΔT, n_p and n are respectively, the temperature rise above ambient, the number density of product and the total number density. The quantities n_p and n can be inferred separately from the temperature rise according to the relations

$$\frac{n_p}{n_\infty} \sim \frac{\Delta T}{T_\infty + \Delta T} \qquad \text{and} \qquad \frac{n}{n_\infty} = \frac{T_\infty}{T_\infty + \Delta T} \qquad (B.12)$$

where T_∞ is the absolute ambient temperature ($\sim 300K$) and n_∞ is the total number density in the freestreams at T_∞. Note that all three of the variables (ΔT, n_p and n) are functions of both space and time, *e.g.*, $n_p(\vec{x},t)$. As argued in Appendix A, the probes used in these experiments produce accurate measurements of the *mean* temperatures and therefore of the ratio n_p/n . The accuracy with which their time series can be determined, using Equation $B.12$ for n_p and n, and the accuracy of the averages for n_p and n rely upon measurement resolution. The mean total number density, $\overline{n}$, can be expressed using Equation $B.12$ as,

$$\frac{\overline{n}}{n_\infty} = \overline{\left(\frac{T_\infty}{T_\infty + \Delta T}\right)} = \int_0^{\Delta T_f} \frac{T_\infty}{T_\infty + \Delta T} P_T(\Delta T)\, d(\Delta T) \quad . \qquad (B.13)$$

Here the overbar represents a time average of the underlying time-dependent quantity.

Quantities discussed previously, such as the reduced temperature θ , were related to simply weighted integrals of the PDF. Because the *amount* of fluid is more precisely related to the number density, slightly revised connotations for these are necessary. The definition of θ implies that it is related to the probability of product at a specific stoichiometry. Accordingly, θ_1 and θ_2 may be referred to as the probability of mixed fluid from their respective free streams, while θ_m estimates the total probability of mixed fluid at any composition. If a tilde ($\tilde{}$) is used to denote quantities that have been corrected for dilatation, the amount of product is now given by

$$\tilde{\theta} = \overline{\left(\frac{\Delta T}{\Delta T_f}\,\frac{T_\infty}{T_\infty + \Delta T}\right)} = \int_0^{\Delta T_f} \frac{\Delta T}{\Delta T_f}\,\frac{T_\infty}{T_\infty + \Delta T} P_T(\Delta T)\, d(\Delta T) \quad . \quad (B.14)$$

In a fashion completely analogous to the derivation of Equations $B.6$ and $B.7$, we can associate $\tilde{\theta}_1$ with the amount of mixed fluid from the high-speed stream,

$\tilde{\theta}_2$ with the amount of mixed fluid from the low-speed stream and $\tilde{\theta}_m$ with the amount of mixed fluid from either stream.

The lone exception to this pattern of duplication and reinterpretation will be the mixed-fluid composition. Although the composition based on probabilities would be a relevant quantity, the individual probabilities, θ_1 and θ_2 , cannot be measured simultaneously. Since dilatation changes these probabilities during the flip experiment, the resulting estimate for "local composition" will be in error. The mixed-fluid composition will be defined as

$$\xi_m = \frac{\tilde{\theta}_1}{\tilde{\theta}_1 + \tilde{\theta}_2} = \frac{\tilde{\theta}_1}{\tilde{\theta}_m} \qquad (B.15)$$

the amount of mixed fluid from the high-speed stream, divided by the total amount of mixed fluid. Changes induced by dilatation differences in the flip will also cause this estimate to be flawed. Nevertheless, this quantity is chosen because the corresponding integral quantity, Equation B.25, is not effected.

Integral Quantities

The previous discussions have centered about local quantities in the mixing layer, and throughout, the dependence on spatial coordinates has been left implicit for clarity. Integral quantities will now be discussed, for which the dependence must be made explicit. Therefore, the local quantities discussed above will now become profiles dependent upon the transverse location within the mixing layer, *i.e.*, $\theta \rightarrow \theta(y)$.

The first and most obvious integral is the product probability thickness, δ_p , defined by

$$\delta_p = \int \theta(y)\, dy \quad . \qquad (B.16)$$

When normalized by the mixing layer width, the quantity δ_p/δ can be thought of as the average probability of product within the layer, or as the volume fraction occupied by product. Integrals of the reduced temperature profiles,

$$\delta_{p_1} = \int \theta_1(y)\, dy \qquad \text{and} \qquad \delta_{p_2} = \int \theta_2(y)\, dy \qquad (B.17)$$

may be interpreted as the probability of mixed fluid from their respective freestream. When normalized by the width δ, these become the volume fractions occupied by mixed fluid from each freestream. The mixed-fluid probability thickness, δ_m, is the integral of the mixed-fluid probability profile,

$$\delta_m = \int \theta_m(y)\, dy \qquad (B.18)$$

and δ_m/δ is a measure of the integral probability of mixed fluid within the layer. Alternatively, δ_m/δ can be interpreted as the volume fraction of the layer occupied by mixed fluid.

Integrals of the dilatation-corrected quantities follow a similar pattern. The product thickness $\tilde{\delta}_p$, is defined as

$$\tilde{\delta}_p = \int \tilde{\theta}(y)\, dy \ . \qquad (B.19)$$

The high and low-speed mixed-fluid thicknesses ($\tilde{\delta}_{p_1}$ and $\tilde{\delta}_{p_2}$), are defined as

$$\tilde{\delta}_{p_1} = \int \tilde{\theta}_1(y)\, dy \qquad \text{and} \qquad \tilde{\delta}_{p_2} = \int \tilde{\theta}_2(y)\, dy \ . \qquad (B.20)$$

The mixed-fluid thickness, $\tilde{\delta}_m$, is defined as

$$\tilde{\delta}_m = \int \tilde{\theta}_m(y)\, dy \ . \qquad (B.21)$$

Each of these quantities has the dimensions of a length, and indicates the thickness the relevant fluid would occupy at ambient temperature. Because the

dilatation effects how thicknesses within the layer are related, normalization of these quantities by the mixing layer width does not lead to a obvious interpretation. However, if the mole thickness ($\tilde{\delta}$) is defined as the integral of the total number density in the layer, *i.e.*,

$$\tilde{\delta} = \int \frac{\overline{n}(y)}{n_\infty}\, dy \qquad (B.22)$$

and is used to normalize the mixed-fluid thicknesses, the results can be interpreted as mole fractions. Hence, $\tilde{\delta}_p/\tilde{\delta}$ becomes the mole fraction of product, $\tilde{\delta}_{p_1}/\tilde{\delta}$ and $\tilde{\delta}_{p_2}/\tilde{\delta}$ become the mole fractions of mixed fluid from their respective freestreams, and $\tilde{\delta}_m/\tilde{\delta}$ becomes the mole fraction of mixed fluid at any composition. A measure of the dilatation for incompressible flow can be formed from the mole thickness. Defined as

$$1 - \frac{\tilde{\delta}}{\delta} = \int_{-\infty}^{\infty} \left[1 - \frac{\overline{n}(y)}{n_\infty}\right] d\left(\frac{y}{\delta}\right) \qquad (B.23)$$

it measures the integral decrease in number density for the layer. This is related to the mean density field in the equal freestream density case by the integral

$$1 - \frac{\tilde{\delta}}{\delta} = \int_{-\infty}^{\infty} \left[1 - \frac{\overline{\rho}(y)}{\rho_\infty}\right] d\left(\frac{y}{\delta}\right) \qquad (B.24)$$

which has been used previously by Hermanson (1984) to characterize the effects of heat release.

The last integral quantity which needs to be discussed is the mean composition of the mixed fluid. As was the case for the local composition, a single definition chosen for its compelling interpretation will be used, despite not being unique. The mean composition will be defined as

$$\overline{\xi}_m = \frac{\int \tilde{\theta}_1(y)\, dy}{\int \tilde{\theta}_1(y) + \tilde{\theta}_2(y)\, dy} = \frac{\int \tilde{\theta}_1(y)\, dy}{\int \tilde{\theta}_m(y)\, dy} = \frac{\tilde{\delta}_{p_1}}{\tilde{\delta}_m} \qquad (B.25)$$

and can be interpreted as the ratio of the integral amount of mixed high-speed fluid, divided by the integral amount of mixed fluid at any composition.

Flux Integrals

Several flux quantities of interest will be examined. These quantities are of particular interest because they are most directly related to the governing equations. Also, modeling efforts which rely on Lagrangian views of the mixing process are arguably more closely related to the Eulerian flux quantities than the simple field quantities discussed above.

The most fundamental of these fluxes is the volume entrainment rate. This is defined as the volume of fluid entering the layer through some boundary per unit time,

$$e_i = \int_{S_i} \overline{\vec{u}(\vec{x},t)} \cdot d\vec{S} \quad . \qquad (B.26)$$

The subscript indicates that the entrainment is from the i^{th} stream and the overbar again indicates a time-average of the underlying time-dependent quantity. The spatial integral is performed over the boundary of the mixing layer through which the fluid in question is introduced. The upstream edges of S_1 and S_2 are chosen as the end of the splitter tip (the origin of the layer), with each forming the boundary between the mixing region and their respective freestream. Defined in this fashion, the quantities e_i represent cumulative measures of the entrainment, from initial laminar growth onward. Dimotakis (1986) has related these quantities to the geometry of the mixing region in relation to the freestream streamlines. Using the closed nature of the apparatus to estimate the freestream lines, and using the temperature profile or visual edges to measure the boundaries of the layer, this estimate for the entrainment is denoted as $e_{\delta i}$.

Conservation of species may also be used to relate entrainment to an integral of the fluxes at the downstream end. Equation $B.26$ can be expressed as

$$\begin{aligned} e_i &= \frac{1}{n_\infty} \int_{S_i} \overline{\vec{u}(\vec{x},t)\, n_i(\vec{x},t)} \cdot d\vec{S} \\ &= \frac{1}{n_\infty} \int_{S_1+S_2} \overline{\vec{u}(\vec{x},t)\, n_i(\vec{x},t)} \cdot d\vec{S} \quad . \end{aligned} \tag{B.27}$$

The addition of the other boundary in each integral is permissable because in each case the integrand is zero there (*i.e.*, $n_1 = 0$ on S_2). Closing the contour at the downstream end and using conservation of species, the expression may be reduced to an integral of the x-component of the fluxes,

$$e_i = \frac{1}{n_\infty} \int_{y_1}^{y_2} \overline{u(\vec{x},t)\, n_i(\vec{x},t)}\, dy \quad . \tag{B.28}$$

Note that, in this expression, u represents the x-component of the velocity and is not a vector quantity. Note also that some care must be exercised in the choice of the limits of integration. Throughout this discussion, it will be implicit that if an integral occurs which depends on finite limits to remain well defined, those limits will be presumed to be the edges of the mean temperature profile.

The time average can be explicitly performed to yield

$$e_i = \frac{1}{n_\infty} \int \overline{u}\, \overline{n}_i + \overline{u'\, n_i'}\, dy \quad . \tag{B.29}$$

Here, primes refer to fluctuating quantities about the (overbarred) mean quantities and the remaining arguments of $\overline{u}(\vec{x})$ and $\overline{n}_i(\vec{x})$ have been omitted. While the potential for simultaneous measurements of time-resolved velocity and concentration exists, these measurements were not made and a separate estimate of this expression is not possible from the available data. Therefore, estimates

of entrainment will be calculated from the mean fluxes excluding the correlation. Denoted simply e, the estimates used in this work are

$$e_i = \frac{1}{n_\infty} \int \overline{u}\, \overline{n}_i \, dy \quad . \tag{B.30}$$

Experiments indicate a measurable difference between this estimate and the one determined from the layer geometry, $e_{i\delta}$. This difference can be used to estimate the fluctuation correlations, *i.e.*,

$$\begin{aligned} e_{i\delta} - e_i &= \frac{1}{n_\infty} \int \overline{u}\, \overline{n_i} + \overline{u'\, n_i'} \, dy - \frac{1}{n_\infty} \int \overline{u}\, \overline{n_i} \, dy \\ &= \frac{1}{n_\infty} \int \overline{u' n_i'} \, dy \quad . \end{aligned} \tag{B.31}$$

The flux of mixed fluid from each stream can be expressed conveniently in terms of the results of the flip experiments,

$$e_{im} = \int \overline{u}\, \tilde{\theta}_i \, dy \quad . \tag{B.32}$$

As before, these estimates exclude fluctuation correlations. The total volume entrainment is obtained by straightforward addition of the individual rates, *i.e.*,

$$e_v = e_1 + e_2 = \frac{1}{n_\infty} \int \overline{u}\, (\overline{n_1} + \overline{n_2}) \, dy \quad . \tag{B.33}$$

Mass entrainment rates can be obtained from these expressions simply by multiplication by the relevant density, *e.g.*,

$$e_s = \rho_1\, e_1 + \rho_2\, e_2 \tag{B.34}$$

where ρ_i is the density of the i^{th} freestream and the subscript s will be used to denote mass.

Several ratios of these entrainment rates are also of interest. $E_{v\delta}$ is the volume entrainment ratio determined from the mixing layer orientation. E_v is the ratio of

the mean flux estimates Equation $B.30$. E_{vm} denotes the mean flux ratio of the mixed fluid.

A last ratio which will be examined is the composition ratio. Defined as the ratio of integrals

$$E_{\bar{\xi}_m} = \frac{\int \tilde{\theta}_1 \, dy}{\int \tilde{\theta}_2 \, dy} \qquad (B.35)$$

it is not fundamentally linked to the mixed-fluid entrainment ratio. To be precise, because it involves integrals of fields rather than fluxes, $E_{\bar{\xi}_m}$ is not mathematically related to entrainment except in certain limits. Comparing Equation $B.35$ to the expression for E_{vm},

$$E_{vm} = \frac{\int \overline{u}\, \tilde{\theta}_1 \, dy}{\int \overline{u}\, \tilde{\theta}_2 \, dy} \qquad (B.36)$$

it can be seen that two cases exist for which E_{vm} and $E_{\bar{\xi}_m}$ are equivalent. If either the velocity field or the concentration field is uniform in space and steady in time, the expression for E_{vm} simplifies to the expression for $E_{\bar{\xi}_m}$. However, the difference between these two quantities in the present gas-phase experiments is significant and they cannot be casually interchanged. Experiments indicate that $E_{\bar{\xi}_m}$ is consistently less than E_{vm}, and it is believed that any contribution to E_{vm} from fluctuation correlations would enhance this difference.

Appendix C. PDF of Composition

Interest in the Probability Density Function (PDF) of Composition stems from several sources. It is a very compact representation of many of the quantities of engineering interest. If equilibrium chemistry is assumed, the PDF contains all that is needed to determine the concentrations of all species. If a reaction is taking place that releases heat, quantities such as temperature extremes, means and moments are simple integral transforms of the PDF. This distribution is used extensively in the preceeding appendixes as an analytical convenience. It is also of considerable interest in its own right. Much effort has been expended trying to model the process of turbulent mixing by equations which track the evolution of the PDF (*e.g.*, Kollman and Janicka 1982), rather than the concentration field itself. To establish confidence in a modeling technique, comparison with data is required and the most convincing comparison is with measurements of the entity being modeled. This necessitates independent determination of the PDF, the most successful means of which has been the direct measurement of this distribution. Measurements by Konrad (1976) in gases and Koochesfahani and Dimotakis (1986) in liquids, showed several features of the PDF which did not agree with contemporary modeling. Because direct measurement imposes stringent resolution requirements to guarantee accuracy, comparison was restricted to qualitative aspects.

Wallace (1981) suggested that the results of reacting experiments could be used to determine the PDF. Using the mean temperature measurements from many experiments at different stoichiometries, Wallace analytically inverted the data to give an approximate representation. Most of the difficulties he encountered

in determining the PDF stem from the ill-conditioned inversion technique he used. In his method, a somewhat unphysical representation for the PDF was chosen, consisting of a number of delta functions at discrete values of composition, whose height varied with position within the layer. The heights were not constrained *a priori* to positive values. His technique was sound, in that measurements of sufficiently accuracy would produce correct results. However, he found it necessary to discard most of the data in order to prevent negative values of probability from resulting and attributed his difficulties to the data's quality.

A fundamentally better technique would be to least squares fit a model for the PDF to the data. Accepting the resulting non-linear characteristics, the functional form could be chosen or constrained to conform to physical "reasonableness", such as being positive definite. Two methods following this approach are outlined below.

Mean Temperature Technique

The normalized mean temperature has been previously related to the PDF of composition by the two term integral relation

$$\theta(\xi_\phi) \;=\; \int_0^{\xi_\phi} \frac{\xi}{\xi_\phi}\, P(\xi)\, d\xi + \int_{\xi_\phi}^{1} \left(\frac{1-\xi}{1-\xi_\phi}\right) P(\xi)\, d\xi \qquad (C.1)$$

where ξ_ϕ is the stoichiometric composition. If the spatially dependent PDF is approximated by a functional form which depends on the constants α_n,

$$P(\xi, y) \;\approx\; \mathrm{P}(\xi, y; \alpha_n) \qquad (C.2)$$

then the mean temperature can be expressed as a function of these constants. Evaluated at the experimental conditions, stoichiometric composition ξ_{ϕ_i} and position y_j , the fit mean temperature would be,

$$\theta(\xi_{\phi_i}, y_j) \;\approx\; \theta(\xi_{\phi_i}, y_j; \alpha_n) \qquad (C.3)$$

Using a common convention for measured quantities, θ_{ij} will represent the corresponding measured quantity,

$$\theta(\xi_{\phi_i}, y_j) \quad \rightarrow \quad \theta_{ij} \tag{C.4}$$

The scalar residual is defined to be the sum of squares of the difference between fit and measured values,

$$\Phi(\alpha_n) \quad = \quad \sum_{ij} \left(\theta(\xi_{\phi_i}, y_j; \alpha_n) - \theta_{ij}\right)^2 \tag{C.5}$$

The summation is over the i separate experiments, each of which consists of mean temperature measurements at j positions. The least squares fit is found by minimization of this scalar.

Technique Based on Measured PDF of Temperature

A second direct method to determine the PDF from reacting flow measurements was attempted by Mungal (1983). Using the PDF of temperature rise measured in several experiments at different stoichiometries, he attempted to directly invert these to give the PDF of composition. Again only a delta function representation of the PDF was produced.

This technique may also be rephrased as a least squares fit of a more general functional form. It is first important to understand that the measured quantity is a histogram of the temperature rise. This corresponds to a normalized integral over a small interval of the PDF of temperature rise. If $\mathcal{P}_k(\xi_\phi)$ denotes the value of this histogram at the k^{th} temperature interval, it may be expressed explicitly as,

$$\mathcal{P}_k(\xi_\phi) \quad = \quad \int_{\Delta T_k}^{\Delta T_{k+1}} P_T(\Delta T; \xi_\phi)\, d(\Delta T) \tag{C.6}$$

This must next be related to the PDF of composition. Starting with the relation between the PDF of temperature rise and composition, Equation $B.3$, the integral over an arbitrary interval can be taken,

$$\int_{\Delta T_1}^{\Delta T_2} P_T(\Delta T;\xi_\phi)\, d(\Delta T) = \xi_\phi \int_{\Delta T_1}^{\Delta T_2} P\left(\xi_\phi \frac{\Delta T}{\Delta T_f}\right) d\left(\frac{\Delta T}{\Delta T_f}\right) + (1-\xi_\phi) \int_{\Delta T_1}^{\Delta T_2} P\left(1-(1-\xi_\phi)\frac{\Delta T}{\Delta T_f}\right) d\left(\frac{\Delta T}{\Delta T_f}\right) \quad (C.7)$$

Denoting the measured histogram for the k^{th} temperature interval as

$$\mathcal{P}_{ijk} = \mathcal{P}_k(\xi_{\phi_i}, y_j) \quad (C.8)$$

and using Equations $C.7$ and $C.2$ to express the calculated histogram as a function of the constants α_n, a new scalar function may be defined as

$$\Phi(\alpha_n) = \sum_{ijk} \left(\mathcal{P}_k(\xi_{\phi_i}, y_j; \alpha_n) - \mathcal{P}_{ijk}\right)^2 \quad (C.9)$$

The values of the constants α_n which minimize this scalar are sought.

Using Equation C.7, the fit approximation to $\mathcal{P}_k$ may be expressed as,

$$\int_{\Delta T_1}^{\Delta T_2} P_T(\Delta T;\xi_\phi)\, d(\Delta T) = \int_{\xi_\phi \frac{\Delta T_1}{\Delta T_f}}^{\xi_\phi \frac{\Delta T_2}{\Delta T_f}} \mathrm{P}(\xi;\alpha_n)\, d\xi + \int_{1-(1-\xi_\phi)\frac{\Delta T_2}{\Delta T_f}}^{1-(1-\xi_\phi)\frac{\Delta T_1}{\Delta T_f}} \mathrm{P}(\xi;\alpha_n)\, d\xi \quad (C.10)$$

This points out an important feature for the efficient implementation of this scheme. Since the flexibility of the fit function is directly related to the spatial variation which it is capable of displaying, numerical integration requires a number of functional evaluations directly in proportion to the flexibility. If a functional form for $\mathrm{P}(\xi, y; \alpha_n)$ is chosen such that its indefinite integral is analytic and can be expressed in terms of simple functions or rational approximations, then evaluation

of $\mathcal{P}_k$ is reduced to calculating these functions at the endpoints of each integral. For a fixed computational load, the analytic evaluation of these integrals allows the choice of more flexible functions. This has been taken advantage of in the present work. The PDFs which appear in the text are composed of the sum of several simple components;

i. Components representing the probablility of pure fluid from either stream.

These are delta functions at $\xi = 0, 1$ whose integrals with respect to ξ were specified as exponentiated polynomials of y. Because these distributions are assymetric in y, the highest order term of the polynomial is odd.

$$e^{P_0(y;\alpha_n)}\ \delta(\xi) \quad \text{and} \quad e^{P_1(y;\alpha_n)}\ \delta(\xi - 1)$$

ii. Components representing one side of mixing with each free-stream.

Decaying exponentials at $\xi = 0, 1$ are used whose heights and widths are exponentiated polynomials of y. Symmetry considerations suggest that the height of the exponential should be even and the width should be odd with repect to y.

$$e^{P_0(y;\alpha_n)}\ e^{-\xi/\sigma_0} \quad \text{and} \quad e^{P_1(y;\alpha_n)}\ e^{\xi-1/\sigma_1}$$

where

$$\sigma_0 = e^{P_0(y;\alpha_m)} \quad \text{and} \quad \sigma_1 = e^{P_1(y;\alpha_m)}$$

ii. A component representing the remainder of the mixed fluid. This component was composed of two parts, each of which was a Gaussian in ξ possessing independent width, height and mean. At a splicing point in ξ, which was variable with y, continuity of the function and its first derivative were enforced

analytically. This left five independent parameters for the fit in ξ which were functions of the position y.

The specific technique used for minimization is called steepest descent. This name results from the visualization of the scalar as a height of a surface in an $(n+1)$-dimensional space above the plane formed using the constants, α_n, as coordinates. The topology of this surface is determined by both the experimental data which are being fit, and the functional form chosen for $\mathrm{P}(\xi, y; \alpha_n)$. At a given set of values α_n, the gradient of the height of this surface is calculated and a minimum is searched for along the path

$$d\alpha_n \quad \| \quad -\frac{\partial \Phi}{\partial \alpha_n} \tag{C.11}$$

When this minimum is found, another gradient is calculated and the search repeated. While convergence is slow, the technique does not appear to be as fussy about the quality of the initial estimate for the parameters. Steepest descent has been found to be more robust than either familiar techniques based on the "normal equations" or the more elaborate hybrid schemes.

As with any non-linear least squares fit technique, the process will not necessarily converge to a global minimum. The topology of the surface may be extremely complex and only exhaustive search can guarantee global minimization. The accuracy of the resulting fit is also limited by the flexibility of the form chosen. Although the results demonstrate that the form settled upon in the present work has great flexibility, some limitations are inherent in any functional form chosen for $P(\xi, y)$. If the physical quantity is oscillatory, yet a fit is attempted with an exponential form, the resulting fit will poorly represent the physics. Much effort was expended to ensure that features in the fit were not the result of being trapped in a local minimum or the result of unintentional constraints. Several other

functional forms were investigated, combined with starting the minimization from many different initial guesses. The merit of the resulting fit is measured by the residual remaining at the minimum. The results plotted are in every case the best fit that was achieved according to this measure.

Appendix D. Laminar Strained Diffusion Flame

Flow visualization in turbulent mixing flows indicate that in the initial region of large structure formation, distinct interfaces separating regions of unmixed fluid from the freestreams can be identified. These can be seen to persist for large distances in the shear layer and for many diameters in the jet, particularly in high Schmidt number flows. Persistence of these interfaces suggests that they might present a natural building block for modeling the mixing process. Even in very high Reynolds number flows, where the existence of these ideal structures are less certain, their utility as a modeling tool may remain.

A laminar strain flame approximation may be valid where the thickness of the diffusion interface is much smaller than its radius of curvature. The large structures in the global flow determine the local strain rate imposed on a locally irrotational flow. While considerable literature exists in which this type of analysis has been pursued, much can still be learned from it, and it is in the spirit of an instructive exercise that it will be conducted. Familiarity with these results will aid in understanding the experimental system appearing in Chapter 5.

In this section a close look will be taken at the interaction of three separate physical phenomena, convective and diffusive transport of species along with chemical reaction between species. While this analysis is usually phrased in terms of the mass or mole fraction of species, the present work will use the more convenient variables of number density. If the number density of the i^{th} species is labeled n_i, the integral transport equation takes the form (Culick 1962),

$$\frac{\partial}{\partial t}\int_V n_i \, dV \;+\; \int_S n_i \vec{u}\cdot d\vec{S} \;+\; \int_S \vec{J}_i \cdot d\vec{S} \;=\; \int_V \sum_j \mathcal{R}_{ij} \, dV. \qquad (D.1)$$

In this expression, the first integral is the change in the total number of the i^{th} species, the second is the convective flux of species through the boundary at the properly defined velocity and the third is the diffusive flux of this species through the boundary. The right hand side of this equation is the source or sink terms due to, in this instance, the chemical reactions which may take place. Specifically, $\mathcal{R}_{ij}$ denotes the rate of production of the i^{th} species due to the j^{th} reaction.

The first area of discussion/approximation that will be tackled is the diffusive flux terms. Perhaps the most straightforward yet general representation for diffusion in low pressure gas mixtures is presented in Reid, Prausnitz and Sherwood. This takes the form of a side system of linear equations for the diffusive fluxes, $\vec{J}_i$, which involve the binary diffusion coefficients for the i^{th} - k^{th} species, $\mathcal{D}_{ik}$, the number density fields and their gradients, ∇n_i. If the convention

$$n = \sum_k n_k \qquad (D.2)$$

is used, these equations take the form,

$$\vec{J}_i \sum_k \frac{n_k}{\mathcal{D}_{ik}} - n_i \sum_k \frac{\vec{J}_k}{\mathcal{D}_{ik}} = n_i \nabla n - n \nabla n_i. \qquad (D.3)$$

For general tertiary or larger systems, this side system of equations must be solved simultaneously with the transport equations. This represents considerable effort if the system of interest consists of a dozen species (*i.e.*, $H_2/NO/F_2$) and especially if several dozen species are involved (*i.e.*, hydrocarbon/air combustion). In addition, there is a lack of data on the binary diffusion coefficients. Although most common species have been studied in one or two inert diluents and there exist several empirical correlations which could be applied, data for the interdiffusion of radical and intermediate species does not exist in most cases. For reasons of both

expedience and necessity this analysis will be confined to the simplified system of very dilute reactants in a single inert diluent.

In this limit the equations for the diffusive fluxes again reduce to the familiar form

$$\vec{J}_i = -\mathcal{D}_i \nabla n_i \qquad (D.4)$$

where the binary diffusion coefficient, $\mathcal{D}_i$, now refers to the diffusion of the i^{th} species into the inert diluent and will be assumed constant.

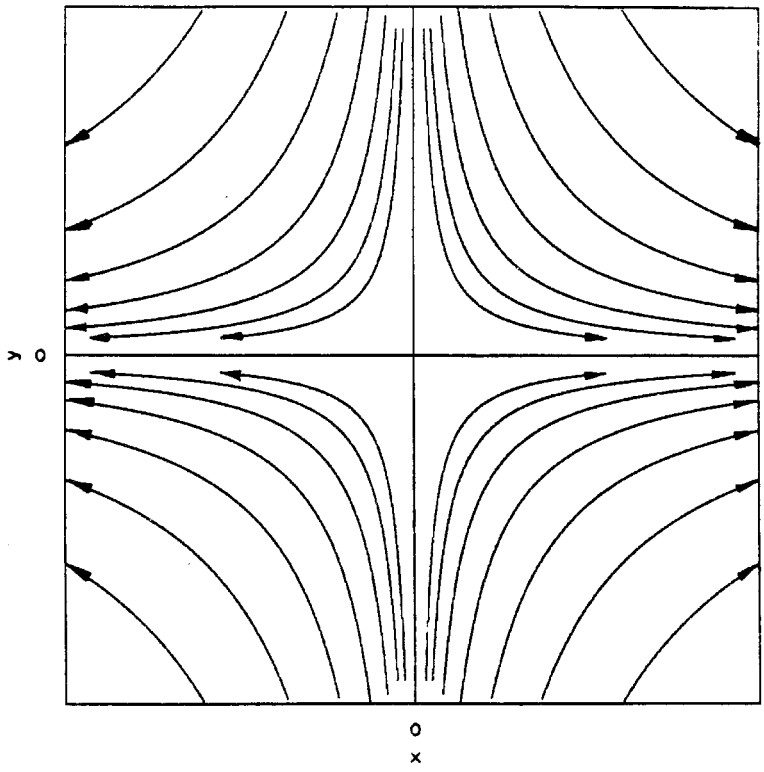

Figure D.1 Streamlines for 2D irrotational strain.

The next term to tackle is the convective fluxes. The velocity field will be taken to be that of simple $2D$ irrotational strain in order to simplify the notation. Specifically, the velocity field will be chosen as

$$\vec{u}(\vec{x},t) \;=\; \varepsilon(t)\cdot(x,-y) \qquad (D.5)$$

where ε is the time dependent strain rate. A sketch of this flow is shown in Figure D.1. Note that results of this section can be related through a simple geometric scaling to the case of uniaxial $3D$ irrotational strain. The velocity field chosen above can be used to reduce the problem to one space dimension and time. Using the differential form

$$\frac{\partial n_i}{\partial t} \;+\; \nabla\cdot(n_i\vec{u}) \;=\; \nabla\cdot(\mathcal{D}_i\nabla n_i) \;+\; \sum_j \mathcal{R}_{ij} \qquad (D.6)$$

along with the assumption that initial conditions do not depend on x, the equations may be simplified to

$$\frac{\partial n_i}{\partial t} \;-\; \varepsilon\, y\, \frac{\partial n_i}{\partial y} \;=\; \mathcal{D}_i\frac{\partial^2 n_i}{\partial y^2} \;+\; \sum_j \mathcal{R}_{ij}. \qquad (D.7)$$

In fact, it is easy to show using Equation $D.6$ that even if the initial conditions for the species are a function of x, but smoothly approach boundary conditions which are independent of x, then the non-uniformity vanishes at least exponentially in time. Since the asymptotic behavior is of considerable interest, this analysis will be limited to the case where profiles of concentration are independent of x.

While this velocity field is a conventional analysis model, its use obscures several subtle phenomena for gas phase flows which deserve mention. Large-scale flow structures provide the boundary conditions for the small scale flow we are attempting to model. These are in the form of pressure gradients which are imposed in the far field of this local analysis. If one were to experimentally

construct or numerically stipulate these boundary conditions and simultaneously solve the momentum and species conservation equations, the result can be approximated by Equation D.5 for constant density flows. However, for gas phase reacting flows the density does not remain constant and the velocity will differ from this simple flow. Preferential acceleration of dilated fluid toward low pressure boundary conditions will occur through (or accompanied by) baroclinic production of vorticity. While unimportant in most liquid reacting flows, for gas-phase flows (especially hydrocarbon combustion) these effects will be significant. This phenomena has been noted and included in flame calculations and analysis (*e.g.,* Cetegan & Kubota 1981, Marble 1981 and Fleming 1982). These effects on the velocity field have been neglected in the present work due to the complications they introduce.

The remaining effects of dilatation may be approximately corrected for by assuming a quadratic temperature dependence of the diffusion coefficient. If in conjunction, a Howarth transformation of space is applied, the governing equations remain in the form of Equation D.3. Details of this may be found in Fleming (1982). Results of the analysis in this section will therefore be applicable to liquid reacting flows and also a reasonable approximation for gas flows with small heat release.

Another simplification which only slightly reduces the generality of the problem is the similarity transformation of Marble (1981). Using the time coordinate,

$$\hat{t} = \int_0^t e^{2\int_0^{t'} \varepsilon(t'')dt''}\, dt' \qquad (D.8)$$

and a space coordinate

$$\zeta = y\, e^{\int_0^t \varepsilon(t')dt'} \qquad (D.9)$$

the equations are reduced to the system

$$\frac{\partial n_i}{\partial \hat{t}} - \mathcal{D}_i \frac{\partial^2 n_i}{\partial \zeta^2} = \frac{y^2}{\zeta^2} \sum_j \mathcal{R}_{ij}. \qquad (D.10)$$

If next the reduced time is defined as

$$\tau = 4\, e^{-2\int_0^t \epsilon dt'} \int_0^t e^{2\int_0^{t'} \epsilon dt''} dt' \qquad (D.11)$$

with a dimensionless similarity space coordinate

$$\eta = \frac{\zeta}{2\sqrt{\mathcal{D}\hat{t}}} \qquad (D.12)$$

the governing equations are reduced to the system of coupled non-linear ODE's

$$D_i \frac{d^2 n_i}{d\eta^2} + 2\eta \frac{dn_i}{d\eta} = -\tau \sum_j \mathcal{R}_{ij} \qquad (D.13)$$

which depend on τ only as a parameter. With the additional stipulation that the initial conditions may be represented in these similarity coordinates, this transformation collapses the entire spectrum of unsteady strained flame and transient interface problems onto a single one parameter family of similarity profiles. As was discussed for the spatial dependence, any solution whose initial conditions are not part of this family of solutions will approach these asymptotic solutions exponentially in time. Note that since a single diffusivity must be chosen to define the similarity space coordinate, D_i is now the ratio of the diffusivity of the i^{th} species to this chosen diffusivity.

The next area to receive attention will be the source and sink terms $\mathcal{R}_{ij}$. In their most general form, these are

$$\mathcal{R}_{ij} = \mathcal{R}_{ij}(T, n_1, n_2, \ldots) \qquad (D.14)$$

where T represents the absolute temperature. For most gas phase homogeneous reactions this has the form

$$\mathcal{R}_{ij} \;=\; -\beta_{ij}\,\kappa(T)\,\prod_k n_k^{\beta_{kj}}. \qquad (D.15)$$

Here κ_j is the temperature dependent rate constant of the j^{th} reaction and β_{ij} is the stoichiometric coefficient for the i^{th} species in the j^{th} reaction.

While this level of generality will be needed later, let us first look at a much simpler problem. Suppose that two bodies of fluid are initially separated by an impermeable membrane lying along the x-axis at $y = 0$. Each body of fluid contains a reactant which is uniformly distributed, with reactant A occupying $y > 0$ and B occupying $y < 0$. At time $t = 0$ the membrane is removed, the two bodies of fluid begin to interdiffuse and reaction begins to form a product C. If the simple one-step second order homogeneous reaction

$$A + B \xrightarrow{\kappa} C \qquad\qquad \kappa = k\,e^{-\theta_i/T} \qquad (D.16)$$

is considered, and the definitions

$$\begin{aligned} n_1 &= [A] \\ n_2 &= [B] \\ n_3 &= [C] \end{aligned} \qquad (D.17)$$

are used, the governing equations take the form

$$\frac{d^2 n_1}{d\eta^2} + 2\eta\frac{dn_1}{d\eta} = \tau\, n_1\, n_2\, e^{-\theta_i/T}$$

$$\frac{d^2 n_2}{d\eta^2} + 2\eta\frac{dn_2}{d\eta} = \tau\, n_1\, n_2\, e^{-\theta_i/T}$$

$$\frac{d^2 n_3}{d\eta^2} + 2\eta \frac{dn_3}{d\eta} = -\tau\, n_1\, n_2\, e^{-\theta_i/T}$$

$$\gamma \left[\frac{d^2 T}{d\eta^2} + 2\eta \frac{dT}{d\eta} \right] = -\tau\, n_1\, n_2\, e^{-\theta_i/T} \qquad (D.18)$$

It has been assumed that all species and heat diffuse at the same rate. It is also assumed that the ratio of specific heat of the fluid to the enthalpy released due to reaction, denoted γ remains constant. It is left as an exercise for the reader to demonstrate that the energy equation can be reduced to this form.

These four partially coupled, non-linear, homogeneous equations can be solved directly. However, most of the work can be saved if some insight is used into the nature of the solutions. Note that the non-linear terms all have the same form. This allows several linear combinations of the dependent variables to be formed whose governing equations do not contain the non-linear term. The resulting equations can be solved analytically and these solutions used to considerably simplify the problem. If the initial condition for the product is chosen to be $n_3 = 0$ everywhere and the temperature is initially specified to be a constant value, the set of four equations can be reduced to the single non-linear ODE,

$$\frac{d^2 c}{d\eta^2} + 2\eta \frac{dc}{d\eta} = Da\; e^{-\frac{\tau_i}{\tau_\infty + c}} \left(erf(\eta) - c \right) \left(\phi (1 - erf(\eta)) - c \right) . \qquad (D.19)$$

Here the following definitions have been used;

$$n_{1\infty} = \lim_{\eta \to \infty} n_1(\eta)$$

$$c = \frac{n_3}{n_{1\infty}}$$

$$Da = \tau\, k\, n_{1\infty}$$

$$\phi = \lim_{\eta \to -\infty} \frac{n_2(\eta)}{n_{1\infty}}$$

$$erf(\eta) \;=\; \frac{1}{\sqrt{\pi}} \int_{-\infty}^{\eta} e^{-z^2}\, dz \;. \qquad (D.20)$$

The reaction rate has been expressed in terms of $\mathcal{T}_\infty$, the non-dimensional ambient temperature and $\mathcal{T}_i$, the non-dimensional activation energy or ignition temperature. The Damköhler number, Da, which is the ratio of the fluid mechanical time to the chemical time is formed from the reduced time combined with a relevant reaction rate and concentration. Note that $Da \rightarrow \infty$ represents the fast-chemistry limit. Results will appear more intuitive if the reader considers the Damköhler number a dimensionless time for the classic transient interface problem, or alternatively, a dimensionless inverse strain-rate for the laminar strained flame. It should be remembered, however, that the similarity transform indicated above includes each of these limiting cases along with the arbitrary time dependent case. The Damköhler number may be formed for the more general problem, Equation D.13, however for more complex chemical systems a unique choice of reaction rate and concentration do not exist. The resulting number will be an adequate parameterization for solution of the numerical problem, or for presentation of experimental data. However, results will not be applicable to other chemical systems unless carefully crafted definitions are used uniformly in the context of specific engineering questions. Differences as basic as freestream concentrations in the same chemical system can lead to these difficulties. This provides additional motivation for the simplification in Equation D.18, which provides simpler choices for the reaction rate and concentration.

Results for Hypergolic Reactions

For the case of finite kinetic rate, no analytic result of a general nature exists although some progress in that direction is the intent of this work. A casual look at the gross non-linearity will convince the reader that an analytic solution to this

problem would be unlikely, and if found would probably be of as little use as the solution found for the homogeneous reactor in Appendix E. Numerical solution of this problem poses no insurmountable difficulty, therefore an attempt has been made to find a rational approximation. It is hoped that this approximation will find use in computational modeling of reacting flow, while perhaps accurate over a restricted range of the variables and parameters.

Solution of Equation D.19 was accomplished using a finite difference technique combined with Newton's method. Using yet another spatial transform, this time related to the solution of the linear part of the equation, a scheme which is 4^{th} order accurate can be derived which retains the tridiagonal nature of the conventional difference scheme (see *e.g.*, Keller 1976). Once a solution was converged upon, parametric studies were performed using Euler-Newton continuation. While results will be plotted with the Damköhler number as the independent variable, the solution was computed using a variation of arc-length parameterization and Da was actually found as an eigenvalue for the resulting problem (Keller (1976)). Although this twist is not necessary for reactions which are hypergolic, if the system has a large ignition temperature the solutions are not a single-valued function of Da and parameterization is essential. Although computed solutions consisted of complete spatial distributions, results plotted here will be restricted to integrals of the number density of product and will be normalized by the fast-chemistry limit

$$\begin{aligned} I(\infty,\phi) &= \lim_{Da\to\infty} I(Da,\phi) = \lim_{Da\to\infty} \int_{-\infty}^{\infty} c(\eta;Da,\phi)\, d\eta \\ &= \frac{1}{\sqrt{\pi}} \frac{\phi}{1+\phi}\, e^{-\left(erf^{-1}\left(\frac{\phi}{1+\phi}\right)\right)^2} \end{aligned} \qquad (D.21)$$

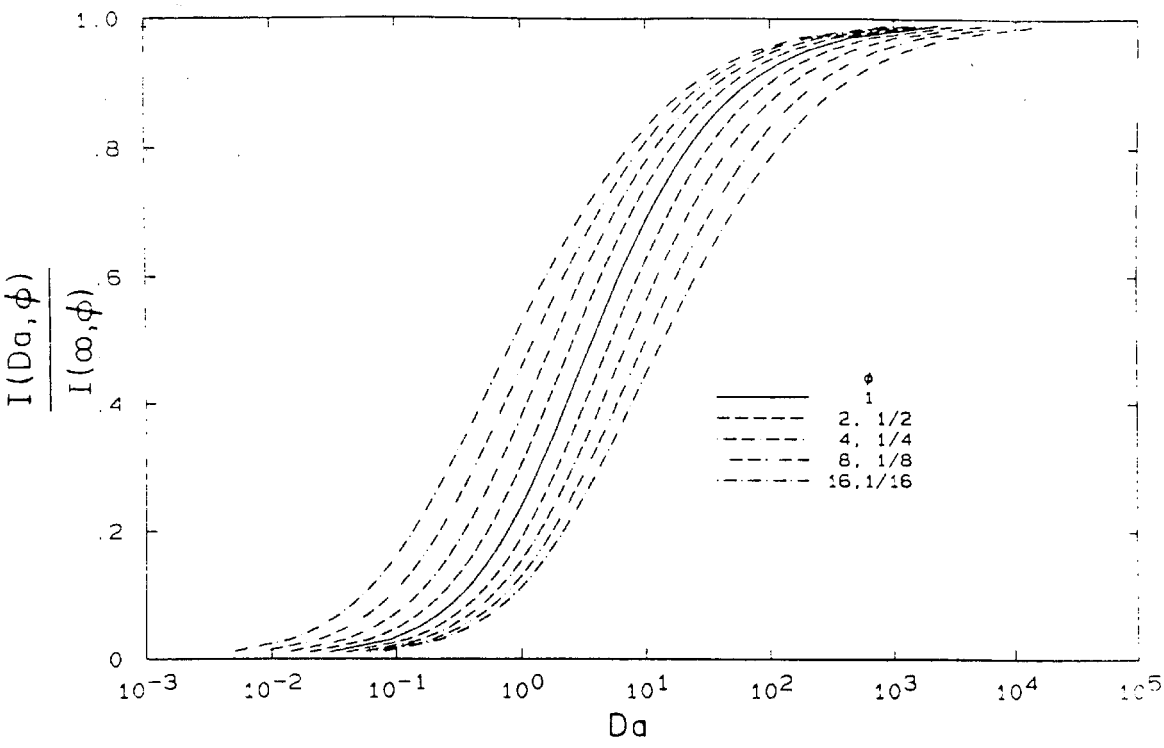

Figure D.2 Product in LSDF with finite kinetics.

For the case of $\mathcal{T}_i = 0$, the amount of product in the laminar strained flame is shown in Figure D.2. Note the increase in Da necessary to reach a fixed amount of product as ϕ decreases. This is an artifact of the choice of concentration in the definition of Da. If instead of the concentration of species A, the stoichiometric concentration is chosen, so that the Damköhler number is now given by

$$Da = \frac{\phi}{1+\phi} \tau k n_{1\infty} \qquad (D.22)$$

the plot takes the form shown in Figure D.3. Although much better, substantial dependence upon the equivalence ratio remains and it would be useful to be able to collapse these curves further.

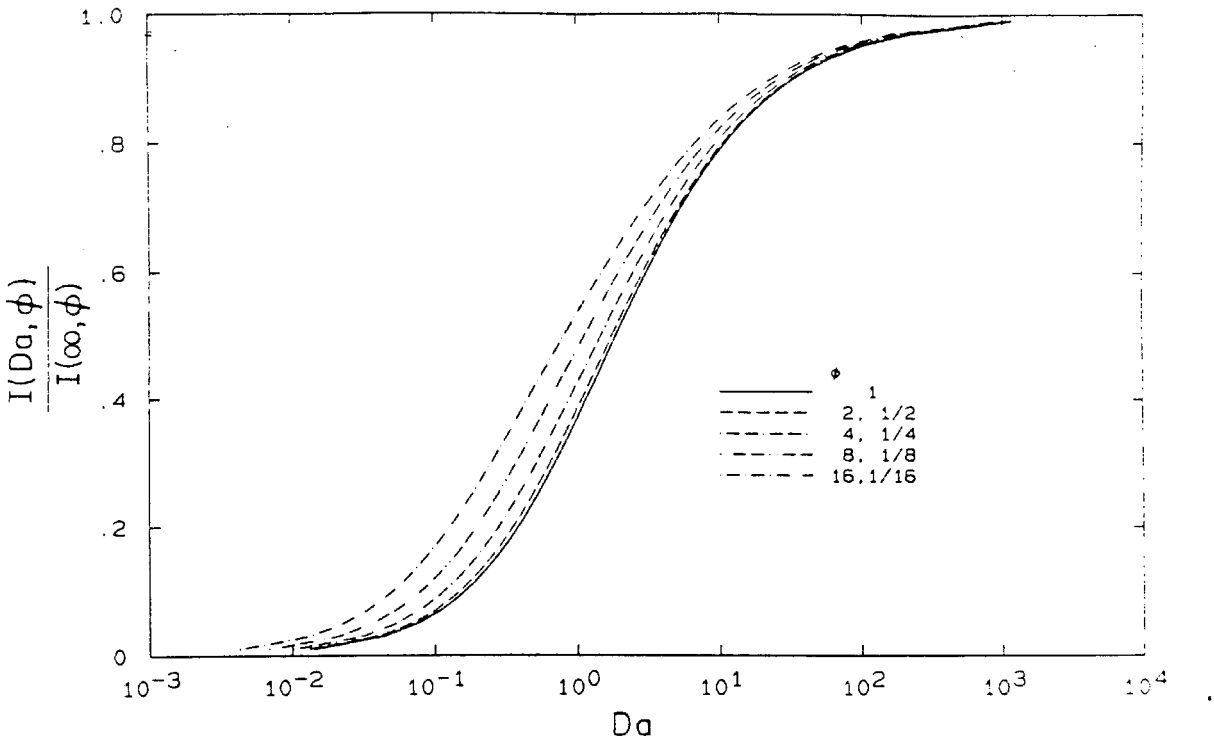

Figure D.3 Product in LSDF with Damköhler number based on stoichiometric conditions.

From the governing equation it can be shown that in the limit of slow chemistry, the total amount of product varies directly with the Damköhler number. This dependence is demonstrated by Figure D.4.

For the limit $Da \rightarrow \infty$, (*i.e.*, the amount of product approaching the fast-chemistry limit), an asymptotic solution can be derived from the Greene's function solution to the linear part of this problem.

$$c(\eta) = \int_{\infty}^{-\infty} \mathcal{S}(\xi)\, \mathcal{G}(\xi;\eta)\, d\xi \qquad (D.23)$$

Substituting the non-linear reaction term from Equation $D.19$ as the source, $\mathcal{S}(\xi)$, yields an expression from which one can derive that the amount of product must

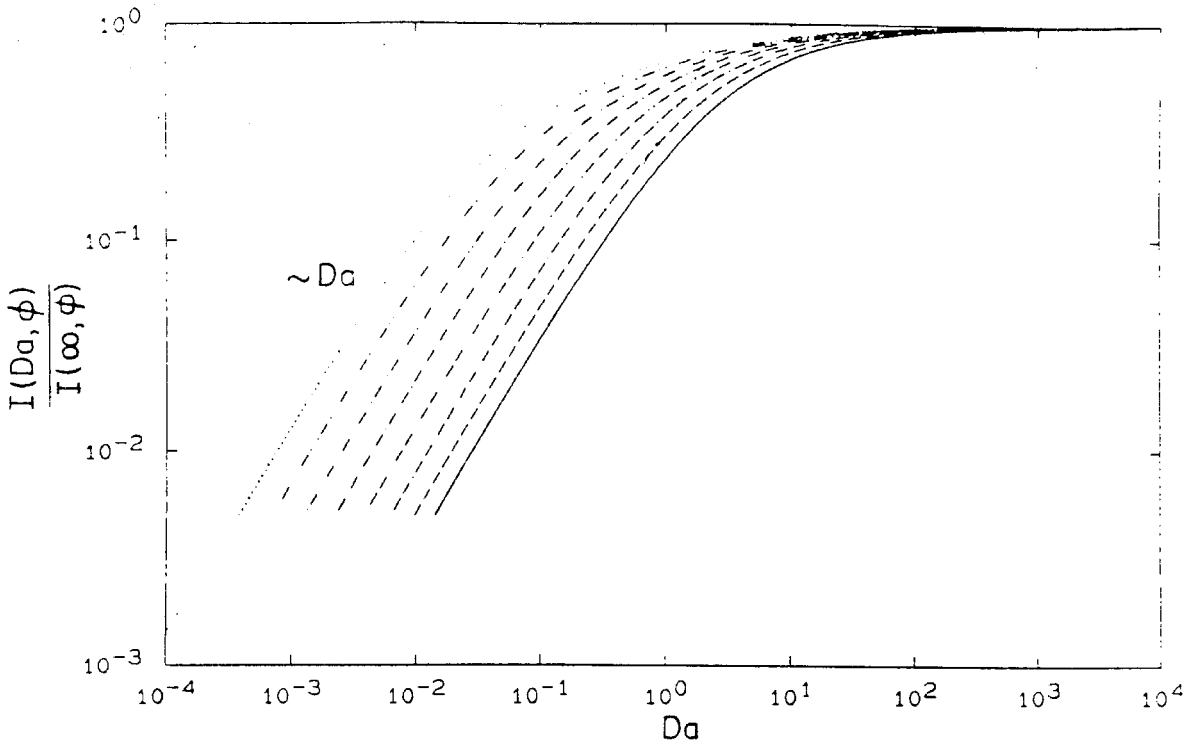

Figure D.4 Slow chemistry dependence of product in LSDF.

approach the fast-chemistry limit as $Da^{-\frac{2}{3}}$. Again, this is easy to confirm numerically, and the results are shown in Figure D.5.

Using these two limits to construct a patched asymptotic solution, the integral product can be approximated by the expression

$$\begin{aligned} \frac{I(Da,\phi)}{I(\infty,\phi)} &\approx f(Da,\phi;\alpha,\beta_1,\beta_2,\nu) \\ &= \left(1+\beta_1 Da^{-1}+\beta_2\left(\phi^{\alpha}+\phi^{-\alpha}\right)^{\nu} Da^{-2/3}\right)^{-1}. \end{aligned} \qquad (D.24)$$

The additional functional dependence upon ϕ for the fast-chemistry limit stems from the fact that the shape of the reaction zone is fundamentally different in this

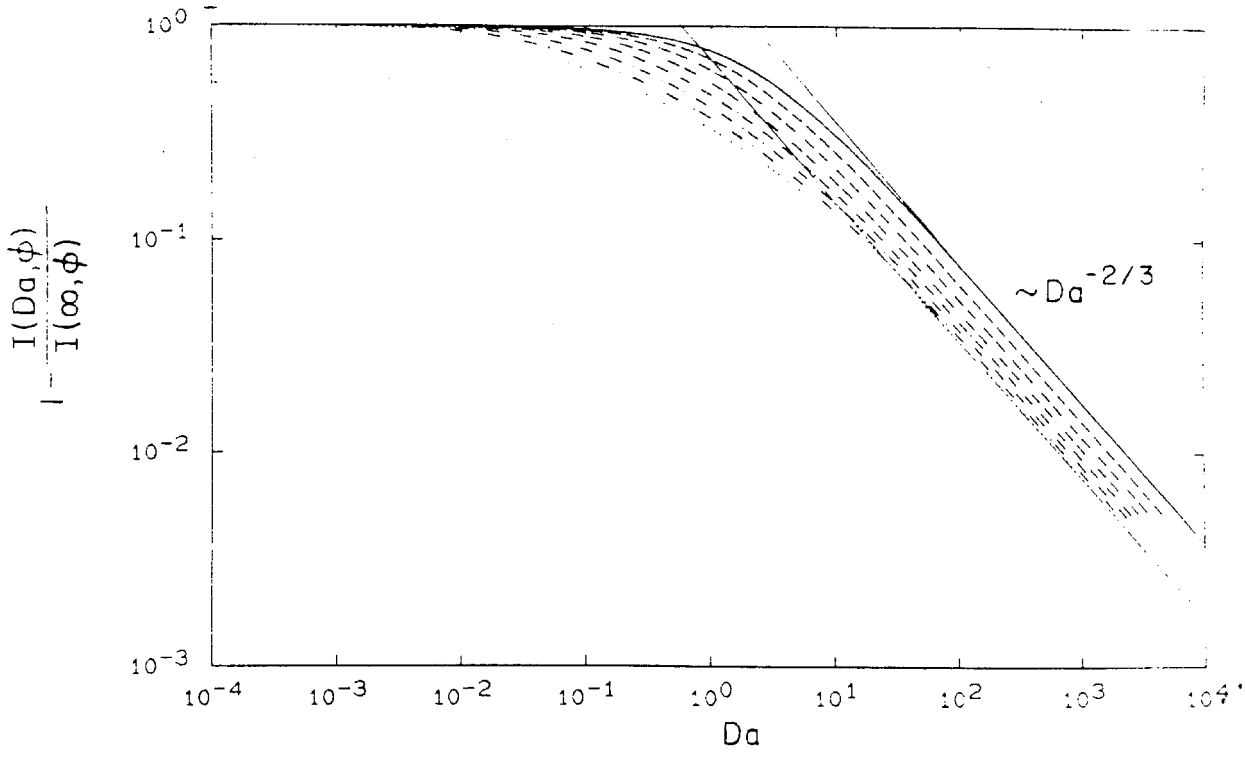

Figure D.5 Fast chemistry dependence of product in LSDF.

limit, and has a different dependence upon ϕ. This additional dependence was least-squares fit exclusively to the fast-chemistry limit, yielding the values

$$\alpha = 3/8 \qquad \nu = 2 \tag{D.25}$$

to three significant digits. While this convergence to rational numbers suggests that some physical basis must exist, none could be found. For this reason, all four adjustable constants were simultaneously fit to the data, and the resulting values were found to be

$$\beta_1 = .900 \qquad \beta_2 = .316$$

$$\alpha = .355 \qquad \nu = 1.356 \tag{D.26}$$

The performance of this correlation is demonstrated by Figure D.6. Here the normalized amount of product is shown versus this fit function of the Damköhler number. The accuracy can be seen to be very good over the range $1/16 < \phi < 16$ with errors less than 5% .

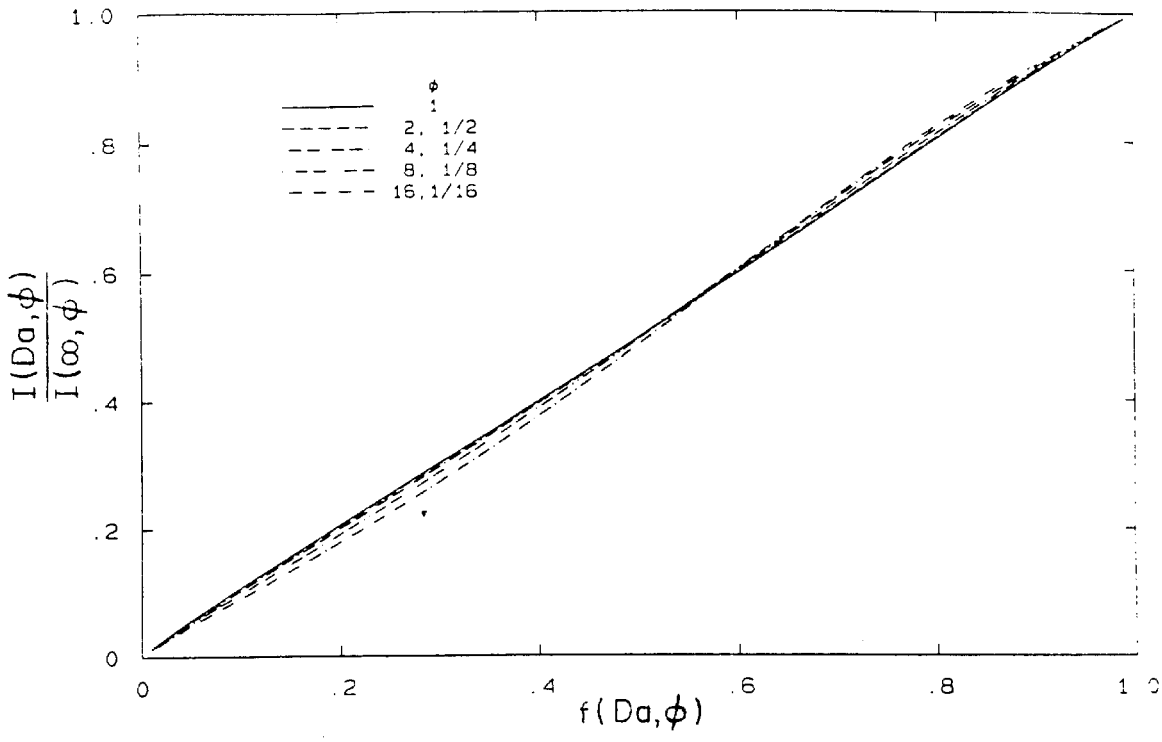

Figure D.6 Demonstration of patched asymptotic approximation.

Discussion and Results for Finite Activation Energy

This could be slightly extended to cover reacting systems with finite activation energies. Figure D.7 shows the solutions for the case $\phi = 1$, $\mathcal{T}_\infty = .5$ and (from left to right) $\mathcal{T}_i = \frac{1}{4}, \frac{1}{2}, 1, 2, 4, 8$. Note the change from a single valued function of the Damköhler number, to a multivalued one. For the simple chemical system

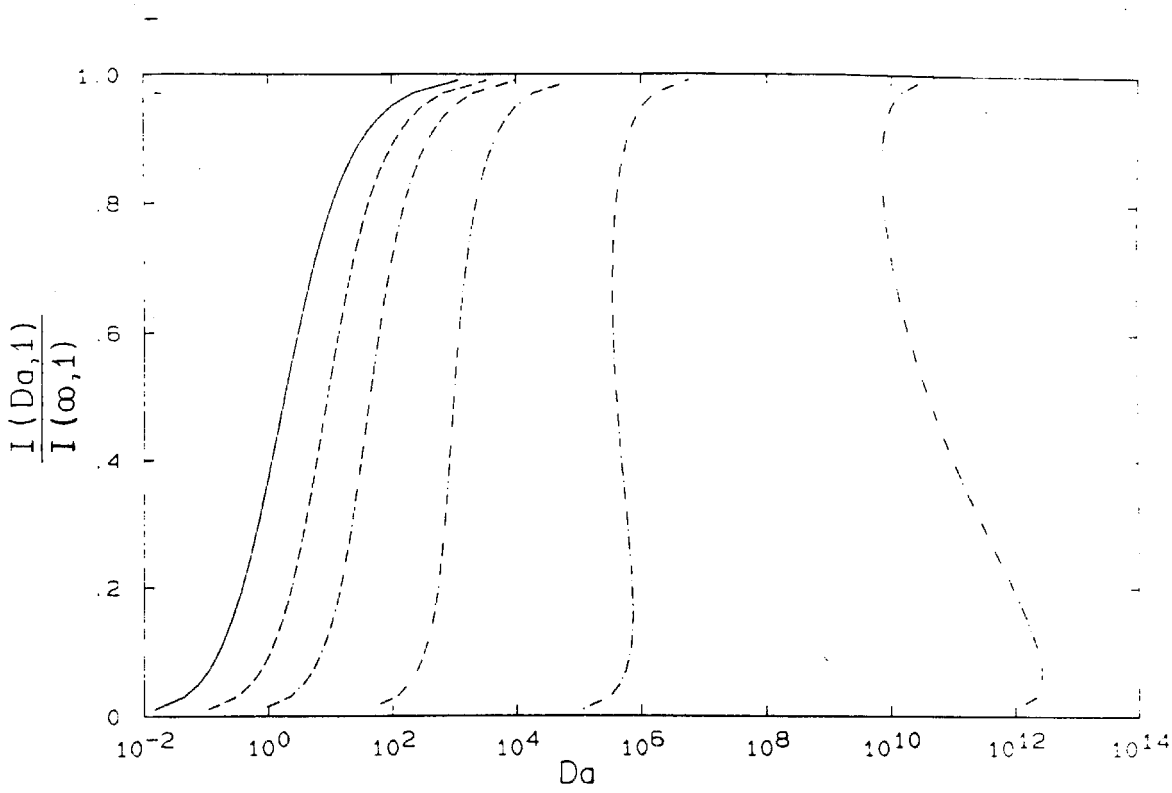

Figure D.7 Product in finite kinetic rate LSDF for several ignition temperatures.

here, the behavior can be described as having two limits. Figure D.8 shows the result of defining Da based on the reaction rate for the cold conditions, *i.e.*,

$$Da = \frac{\phi}{1+\phi} \tau k n_{1\infty} e^{-\mathcal{T}_i/\mathcal{T}_0}. \qquad (D.27)$$

Figure D.9 shows the result of defining Da based on the reaction rate for the hot conditions.

These plots demonstrate that the solution converges in two cases, when $\Delta T \cong 0$ everywhere and the reaction proceeds at a uniform temperature, or when the reaction zone is very thin $(Da \to \infty)$ and again the reaction proceeds at a single (therefore uniform) temperature. This suggests that the correlation

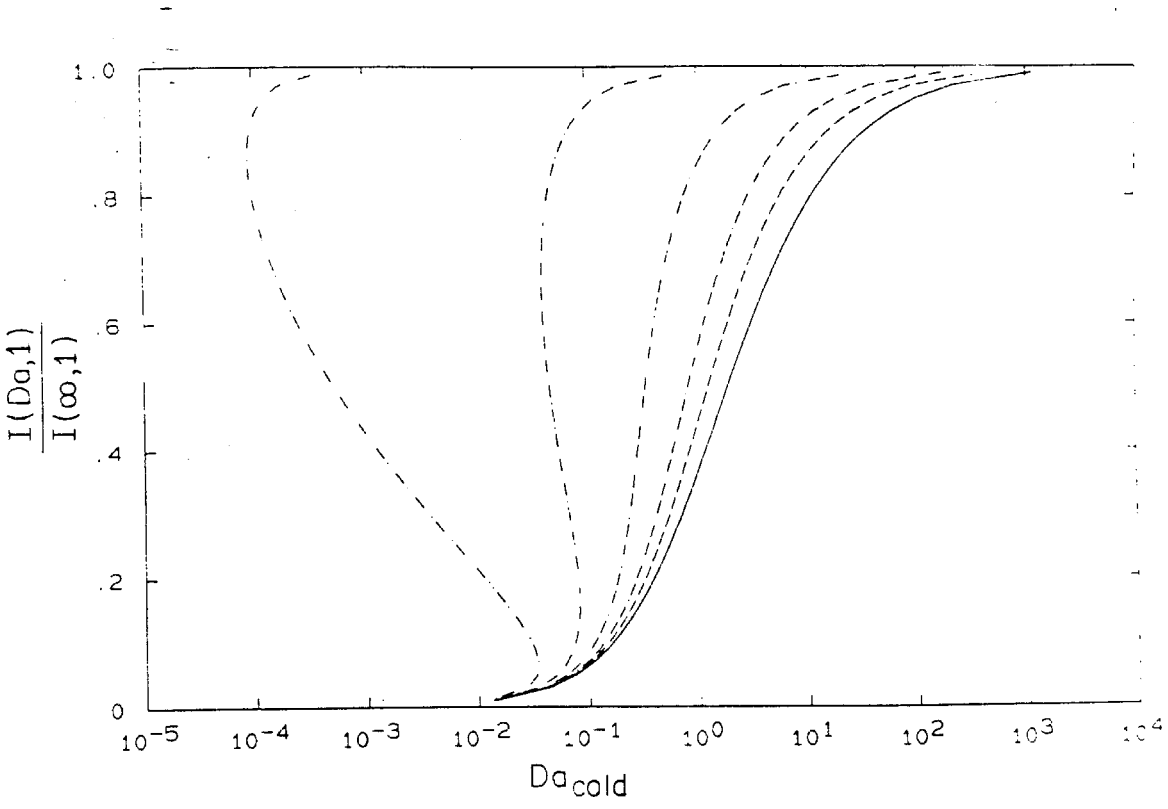

Figure D.8 Collapse for Damköhler number based on cold conditions.

used above might be extended if the terms within Equation $D.24$ representing the low and high Damköhler number limits were based on the cold and hot conditions respectively. While this deserves further exploration, note that for high ignition temperatures there is no possibility of such a correlation because the amount of product is not a single valued function of the Damköhler number. Another tack might be taken. Performing calculations on a wide range of ϕ, $\mathcal{T}_\infty$ and $\mathcal{T}_i$, it might be possible to find a correlation in the form of an implicit function, ie.,

$$Da \approx f\left(\frac{I(Da,\phi)}{I(\infty,\phi)}, \phi, \mathcal{T}_i, \mathcal{T}_\infty\right) \qquad (D.28)$$

This is similar to the approach taken in the numerical solution. However the mass of calculations, the derivation of a functional form motivated by the physics of

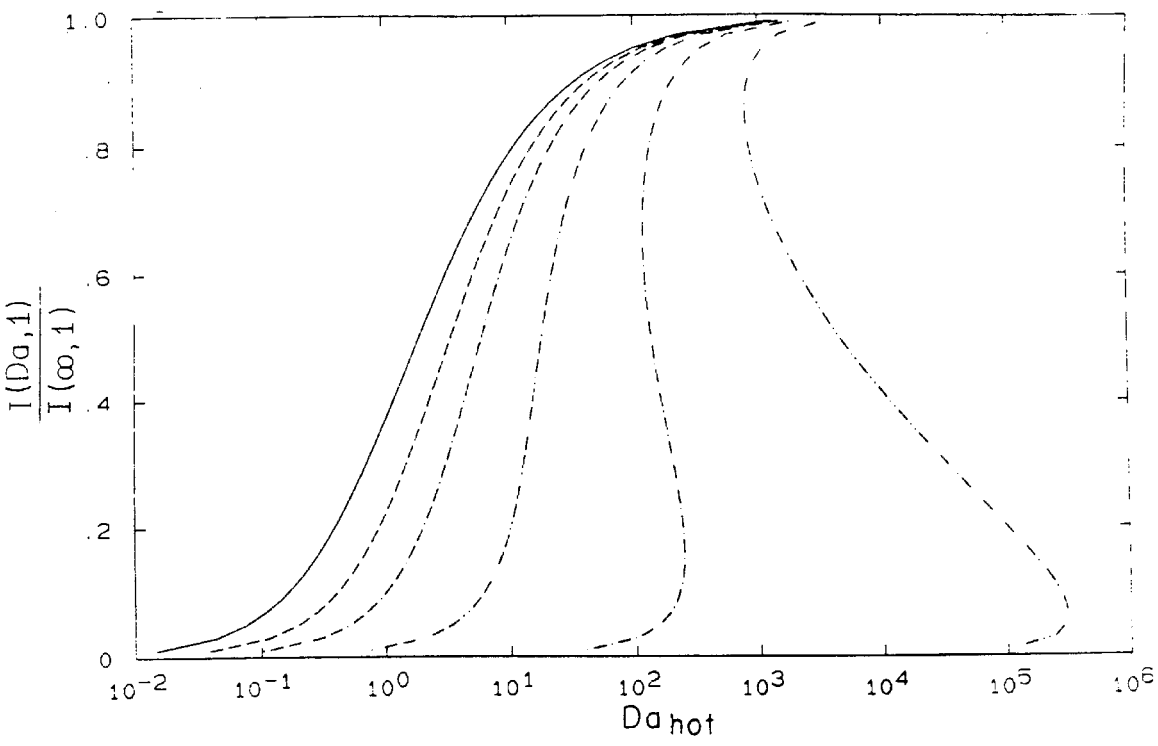

Figure D.9 Collapse for Damköhler number based on adiabatic flame conditions.

the problem, and fitting of the appropriate constants would be a reasonable size research endeavor in its own right. Time constraints and enthusiasm limits have determined that this be left for the future.

Another reason that this last topic was not pursued, is the actual physical character of the solutions when the activation energy is large. The solutions in the middle section of these "S"-shaped curves are linearly unstable. This means that a system initially on the curve in this region will, if infinitesimally disturbed, move toward the part of the solution curve above or below it depending on the sign of the perturbation. Physically, these unstable solutions are never realized. If a flame is on the lower section of the curve, and the Damköhler number were slowly

raised, it would proceed along the curve until it reached the turning point. At this point it would depart from the curve and jump up to the "hot" solution at that Damköhler number. The reverse happens if the flame is started on the hot part of the solution curve and the Damköhler number is decreased. This hysteresis and non-equilibrium transition are the "light-up" and "blow-out" familiar from hydrocarbon combustion. Whether these features can ever be properly modeled is unclear. For this reason, modeling reacting flows using the laminar strained flame must be approached cautiously when the chemical system has very high activation energies, such as hydrocarbon combustion.

Appendix E. Homogeneously Mixed Reactor

In this section, the analysis of chemical reactions taking place in a specific and very simplified mixing environment will be described. The formulation of this problem is not new, and has been published in the appropriate chemical engineering journals. In addition, it has recently been used in connection with reacting gas-phase flow by Dimotakis and Hall (1987). It is included here for two reasons, first because several phenomena dealt with elsewhere in this tome are better understood in light of these results, and because several of the analytic results are interesting in there own right.

This section will begin by considering the following scenario. Starting with an isolated, insulated container of a certain volume (V) which contains some initial concentrations of reacting species. When the evolution is started and these species are allowed to react, additional reactants and diluents are simultaneously injected at specific concentrations and rates. These injected fluids are mixed throughout this container at a rate much greater than any other relevant time-scale, including kinetic rates, for this calculation it can be assumed that the container holds a perfectly homogeneous mixture. Further, only the constant pressure case will be considered where in the absence of heat release, the volume is directly proportional to the amount of injected fluid.

The integral transport equations for number density of the i^{th} species were given in Appendix D,

$$\frac{\partial}{\partial t}\int_V n_i \, dV \;+\; \int_S n_i \vec{u}\cdot d\vec{S} \;+\; \int_S \vec{J}_i \cdot d\vec{S} \;=\; \int_V \sum_j \mathcal{R}_{ij} \, dV. \qquad (D.1)$$

The volume integrations can be eliminated using the assumed homogeneity, *i.e.*,

$$\int_V n_i \, dV \longrightarrow n_i V$$

$$\int_V \sum_j \mathcal{R}_{ij} \, dV \longrightarrow V \sum_j \mathcal{R}_{ij} \qquad (E.1)$$

The diffusive flux integrals will be ignored. The remaining surface integrals may be related to the rate of injection of this species as

$$\int_S n_i \, \vec{u} \cdot d\vec{S} \longrightarrow \sum_k e_k \, n_{ik} \qquad (E.2)$$

where e_k is the volume injection rate from the k^{th} source and n_{ik} is the number density of the i^{th} species in the k^{th} source. This reduces the equations to the form

$$\frac{d}{dt}(n_i V) + \sum_k e_k \, n_{ik} = V \sum_j \mathcal{R}_{ij} \qquad (E.3)$$

along with the continuity equation

$$\frac{dV}{dt} = \sum_k e_k. \qquad (E.4)$$

Restricting attention to the simple second order homogeneous reaction discussed in Appendix D,

$$A + B \xrightarrow{\kappa} C \qquad \kappa = k e^{-\theta_i/T} \qquad (D.16)$$

and again identifying the three number densities as,

$$\begin{aligned} n_1 &= [A] \\ n_2 &= [B] \\ n_3 &= [C] \end{aligned} \qquad (D.17)$$

the governing equations can be written as a system of three partially coupled, non-linear, non-homogeneous first order ODEs.

$$\begin{aligned}
V\frac{dn_1}{dt} + n_1\frac{dV}{dt} - e_1\, n_{1\infty} &= -k\, n_1\, n_2\, V \\
V\frac{dn_2}{dt} + n_2\frac{dV}{dt} - e_2\, n_{2\infty} &= -k\, n_1\, n_2\, V \\
V\frac{dn_3}{dt} + n_3\frac{dV}{dt} &= k\, n_1\, n_2\, V \\
\frac{dV}{dt} &= e_1 + e_2 \qquad (E.5)
\end{aligned}$$

Here the injection has been restricted to two sources, one containing reactant A at a number density $n_{1\infty}$ in diluent and the other containing reactant B at $n_{2\infty}$ in diluent. Species C is produced only by reaction in the volume and the reaction rate has been assumed a constant independent of temperature.

The last of these equations may be integrated to yield

$$V = (e_1 + e_2)t + V_o \qquad (E.6)$$

where V_o corresponds to the initial volume. Performing a change of dependent variables from time to volume, and using a judicious selection of parameters for non-dimensionalization the problem may be drastically simplified. The appropriate selection of parameters for non-dimensionalization is given by,

$$\begin{aligned}
\hat{n}_1 &= \frac{n_1\,(e_1+e_2)}{e_1\, n_{1\infty}} \qquad & \hat{t} &= \frac{k\, e_1\, n_{1\infty} V}{(e_1+e_2)^2} \\
\hat{n}_2 &= \frac{n_2\,(e_1+e_2)}{e_2\, n_{2\infty}} \qquad & \mathcal{E} &= \frac{e_2\, n_{2\infty}}{e_1\, n_{1\infty}} \\
\hat{n}_3 &= \frac{n_3\,(e_1+e_2)}{e_2\, n_{2\infty}} \qquad & & \qquad (E.7)
\end{aligned}$$

If the accent for dimensionless quantities is dropped, and the definitions $E.7$ are left implicit, the governing equations become

$$\begin{aligned} \dot{n}_1 \; + \; \frac{n_1 - 1}{t} \; &= \; -\mathcal{E}\, n_1\, n_2 \\ \dot{n}_2 \; + \; \frac{n_2 - 1}{t} \; &= \; -n_1\, n_2 \\ \dot{n}_3 \; + \; \frac{n_3}{t} \; &= \; n_1\, n_2 \end{aligned} \qquad (E.8)$$

Thus normalized, it will be seen that the solutions for non-reacting cases will asymptote to 1 for large times. In the reacting cases, if A is the rich reactant, n_1 will asymptote to $1 - \mathcal{E}$ and the product will asymptote to 1. Also if B is the rich reactant, n_2 will asymptote to $1 - 1/\mathcal{E}$ and the product will asymptote to $1/\mathcal{E}$. The equation for product density may be solved in terms of the reactant densities,

$$n_3 \; = \; \frac{1}{t}\left(\int_0^t n_1(t')\, n_2(t')\, t'\, dt' \; + \; n_{3o} \right) \qquad (E.9)$$

where n_{3o} is a constant of integration and corresponds to the initial concentration of product in V_o. Since these equations are only partially coupled, if a solution for the first two equations may be obtained, the corresponding solution may be obtained by quadrature from this relation.

Since the non-linear term in each of the equations is similar, any linear combination of the dependent variables which eliminates this term can also be solved. Specifically, if n is defined as,

$$n \; = \; n_1 - \mathcal{E}\, n_2 \qquad (E.10)$$

then Equations $E.8$ can be combined to eliminate the non-linear term. The resulting equations take the form

$$\dot{n} \; + \; \frac{n}{t} \; = \; \frac{1 - \mathcal{E}}{t} \qquad (E.11)$$

which has the solution

$$n \;=\; 1-\mathcal{E} \;+\; \frac{\alpha}{t}. \qquad (E.12)$$

Hence, this linear combination has the solution

$$n_1 - \mathcal{E} n_2 \;=\; \left(1-(n_{1o}-1)\frac{t_o}{t}\right) \;-\; \mathcal{E}\left(1-(n_{2o}-1)\frac{t_o}{t}\right). \qquad (E.13)$$

This expression displays an asymptotic approach ($\sim 1/t$) to the constant $1-\mathcal{E}$.

Now, on to solving the entire problem. If the following substitutions are now made

$$n_1 \;=\; \frac{g_1}{\dot{g}_1\, t} \qquad\qquad n_2 \;=\; \frac{g_2}{\dot{g}_2\, t} \qquad (E.14)$$

Equations $E.8$ become

$$\begin{aligned} \frac{\ddot{g}_1}{\dot{g}_1} \;&=\; \frac{\mathcal{E}\, g_2}{\dot{g}_2\, t} \\ \frac{\ddot{g}_2}{\dot{g}_2} \;&=\; \frac{g_1}{\dot{g}_1\, t} \end{aligned} \qquad (E.15)$$

which may be combined with the first integral Equation $E.13$ to give the two independent, linear second order homogeneous ODEs

$$\begin{aligned} t\,\ddot{g}_1 \;+\; ((1-\mathcal{E})\,t-\gamma t_o)\;\dot{g}_1 \;-\; g_1 \;&=\; 0 \\ t\,\ddot{g}_2 \;+\; ((1-\mathcal{E})\,t-\gamma t_o)\;\dot{g}_2 \;-\; \mathcal{E}\,g_2 \;&=\; 0. \end{aligned} \qquad (E.16)$$

Here the constant γ, defined as

$$\gamma \;=\; (n_{1o}-1) \;-\; \mathcal{E}(n_{2o}-1) \qquad (E.17)$$

has been introduced to simplify notation.

These have the analytic solution

$$g_1 \;=\; \alpha_{\pm}\, t^{-\gamma/2}\, e^{-(1-\mathcal{E})t/2}\; \mathbf{W}\left(\pm\left(\frac{1}{1-\mathcal{E}}-\frac{\gamma}{2}\right), \frac{\gamma-1}{2}, \pm(1-\mathcal{E})t\right)$$

$$g_2 \;=\; \beta_{\pm}\, t^{\gamma/2}\, e^{(1-\mathcal{E})t/2}\; \mathbf{W}\left(\pm\left(\frac{\mathcal{E}}{1-\mathcal{E}}+\frac{\gamma}{2}\right), \frac{\gamma+1}{2}, \pm(1-\mathcal{E})t\right) \qquad (E.18)$$

where $\mathbf{W}$ are Whittaker functions and the notation follows the Bateman Manuscript Project. The constant $\alpha_{\pm}$ is intended to indicate that the solution is composed of two terms, a constant (α_+) times the Whittaker function evaluated with the + choice of the arguments, plus another term which is a constant (α_-) times the Whittaker function evaluated with the − choice of the arguments. In principle, if one were able to evaluate the constants $\alpha_{\pm}$ and $\beta_{\pm}$ (only two of which are independent) in terms of the initial conditions, then substitution of these expressions into Equations $E.14$ would provide general solutions for reactant concentrations n_1 and n_2. In turn, these results could be used in Equation $E.9$ to give the exact solution for the product concentration. However, until a Whittaker function key appears on calculators, these results must remain simply a starting point for analysis of special cases and asymptotics.

Several interesting cases do exist.

I. $\mathcal{E} = 1$

The solutions $E.18$ become

$$g_1 \;=\; \alpha_{\pm}\, t^{\frac{1-\gamma}{2}}\, \mathbf{C}_{\gamma-1}(2i\sqrt{t})$$

$$g_2 \;=\; \beta_{\pm}\, t^{\frac{1+\gamma}{2}}\, \mathbf{C}_{\gamma+1}(2i\sqrt{t}) \qquad (E.19)$$

where $\mathbf{C}_{\nu}$ is the Bessel function of order ν. Next if we specify

$$n_{1o} \;=\; n_{2o} \qquad \text{or} \qquad t \gg t_o \qquad (E.20)$$

the solutions for the reactants become

$$n_i(t) \;=\; \alpha_i\sqrt{t}\,\frac{\mathbf{I}_1(2\sqrt{t}) \;+\; \beta_i\,\mathbf{K}_1(2\sqrt{t})}{\mathbf{I}_0(2\sqrt{t}) \;-\; \beta_i\,\mathbf{K}_(2\sqrt{t})} \qquad (E.21)$$

$\mathbf{I}_\nu$ and $\mathbf{K}_\nu$ are the modified Bessel functions of order ν with α_i and β_i are chosen to satisfy the initial conditions. Either from this expression, or directly from the Ricatti equation that $E.18$ simplifies to under these assumptions,

$$\dot{n_i} + \frac{n_i - 1}{t} = n_i^2 \qquad (E.22)$$

it is easy to derive the leading order behavior, *i.e.*,

$$n_i \sim t^{-1/2} \qquad (E.23)$$

Using this dependence for the reactant concentrations in Equation $E.9$, the product concentration is to leading order,

$$n_3 \sim 1 - \frac{\alpha}{t} \qquad (E.24)$$

In physical terms, if

i. the ratio of the stoichiometric mixture ratio to the entrainment ratio is unity,

ii. the initial conditions for the reactants are identical, or the initial volume has been greatly diluted, than the concentrations of both reactants are equal and approach zero as $Da^{-\frac{1}{2}}$. Here Da is the Damköhler number and represents the ratio of fluid mechanic to chemical times. This asymptotic behavior can be used to solve for the behavior of the product concentration and results in a rise to the fast chemistry limit as $1-Da^{-1}$. It is important to note that this rise to the fast chemistry limit is faster then the rise of the laminar strained diffusion flame analysed in Appendix D.

II. $n_1 \gg \mathcal{E} n_2$ for $t \geq t_o$

The equation for n_1 becomes

$$\dot{n_1} + \frac{n_1}{t} = \frac{1}{t} \tag{E.25}$$

which has the solution

$$n_1 = 1 + \frac{\alpha}{t} \tag{E.26}$$

This may be inserted in the governing equation for n_2 to obtain

$$\dot{n_2} + \frac{n_2 - 1}{t} = -n_2 \left(1 + \frac{\alpha}{t}\right) \tag{E.27}$$

which has the solution

$$n_2 = t^{-(1+\alpha)}\, e^{-t} \left[\int_{t_o}^{t} t^{\alpha}\, e^{t}\, dt + \beta\right] \tag{E.28}$$

While this could again be used to solve for the product concentration, the presence of a transcendental integral is an inconvenience. If it is further assumed that n_1 starts at its asymptotic value (*i.e.*, $n_1 = 1$ for $t \geq t_o$), then Equation $E.27$ becomes

$$\dot{n_2} + \frac{n_2 - 1}{t} = -n_2 \tag{E.29}$$

which has the solution,

$$n_2 = \frac{1 - (1 - t_o\, n_{2o})\, e^{t_o - t}}{t} \tag{E.30}$$

From this the solution for the product may be obtained as,

$$\begin{aligned} n_3 &= \frac{1}{t}\left[\int n_1\, n_2\, t\, dt + \alpha\right] \\ &= \frac{1}{t}\left[\int (1 - (1 - t_o\, n_{2o}))\; e^{t_o - t}\, dt + \alpha\right] \\ &= 1 - \frac{t_o}{t} - \frac{(1 - t_o\, n_{2o})(1 - e^{t_o - t})}{t} \end{aligned} \tag{E.31}$$

Physically, this limiting case corresponds to

i. the ratio of the stoichiometric mixture ratio to entrainment ratio is vanishingly small (or arbitrarily large, if the roles of n_1 and n_2 are interchanged)

ii. the initial concentration of the rich reactant is its asymptotic value or the initial volume has been greatly diluted then the concentration of the rich reactant remains constant, and the concentration of the lean reactant decreases as Da^{-1}. The product concentration in this case rises to its asymptote as $1 - Da^{-1}$. This solution is the same as the Broadwell and Mungal (1986) solution and displays the same asymptotic behavior of the product concentration.

CHEMKIN Solutions

As illuminating as the previous analysis was, several major assumptions were made which limit the direct comparison of the results to a real reacting system, for instance the reacting shear layer. Among these are the assumption that reaction only takes place in a spatially uniform environment, that the process can be represented in a Lagrangian frame of reference with a single convective velocity, and also that the chemistry can be reduced to the simple model reaction described above. Although the first two limitations are difficult to avoid, the later has been for the most part removed by more extensive modeling of the reaction system. Using the CHEMKIN package, put out by Sandia, described by Mungal and Frieler (1988), and using the model above (Programming courtesy of Mr. Jeff Hall) solutions for the $H_2/NO/F_2$ system were computed. All the reactions included in Table 5.1 for which rate expressions appear have been included. These

calculations correspond to the solution of Equation $E.3$ along with the proper continuity and energy equations. For the subsonic, constant pressure conditions of interest here, the continuity equation for perfect gases takes the form,

$$\frac{d(V/T)}{dt} = \sum_k e_k/T_k \qquad (E.32)$$

and the energy equation becomes

$$\frac{d(HV)}{dt} = \sum_k e_k\, H_k + V \sum_j \Delta H_j \qquad (E.33)$$

In these, T_k represents the temperature in the k^{th} stream, E_k represents the enthalpy of the k^{th} stream and ΔE_j represents the rate of enthalpy release by the j^{th} reaction. An example of the results of these calculations appear in Figure E.1.

The vertical axis in this figure is the temperature rise normalized by the final temperature rise (denoted as ΔT_h for "homogeneous" temperature), plotted here versus time in seconds. Shown are time temperature traces for the $\phi = 8$ case used in the experiments reported in Mungal and Frieler. The concentrations of the reactants for each calculation are shown in the right hand column of the figure with the remainder of each stream being N_2 . This particular set had 8% H_2 in one stream (here labeled HSS for High-Speed Stream), and 1% F_2 in the other. Various amounts of nitric oxide (NO) were included in the hydrogen bearing stream, roughly corresponding to the range of values used in the experiments. The entrainment ratio was assumed to be 1.3, and the initial volume and concentrations were chosen to approximate the experiments, as detailed in Dimotakis and Hall (1987). The strong dependence of the overall reaction rate upon the concentration of NO is clearly demonstrated here. For very low concentrations of NO , the system behaves as a simple second order reaction, with the rate being proportional to the concentration of NO . This particular result can be demonstrated from the

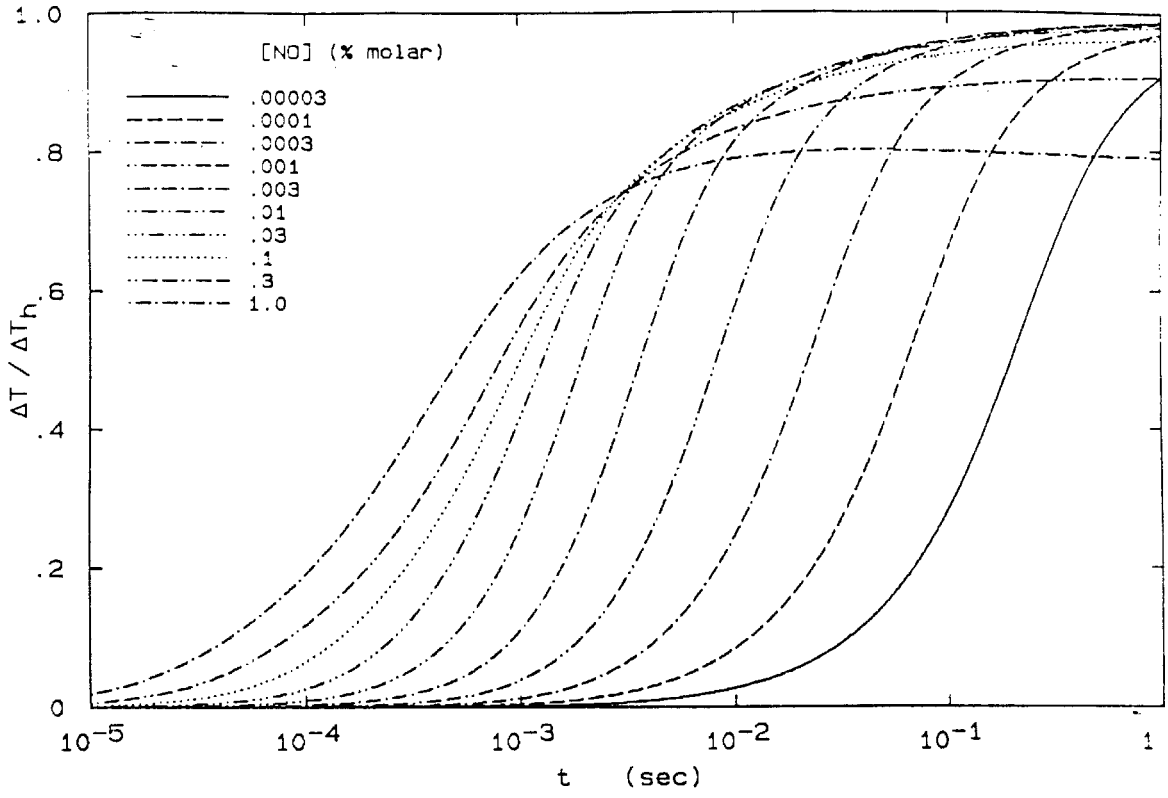

Figure E.1 Temperature rise in homogeneous reactor for H_2 / NO / F_2 .

$(\phi = 1/8, \Delta T_h \cong 82K)$

governing equations However, at this stoichiometry, the behavior differs markedly from second order when the concentration of NO is large. Note the relatively rapid rise to roughly two thirds, and the comparitively slow rise thereafter to the flame temperature.

Figure E.2 shows the same calculations for the $\phi = 1$ case. It is nearly indistinguishable from Figure E.1. This demonstrates that for cases where H_2 is the rich reactant, the reaction rate (in fact, the entire temperature time-series) depends only on the concentrations of NO and F_2 .

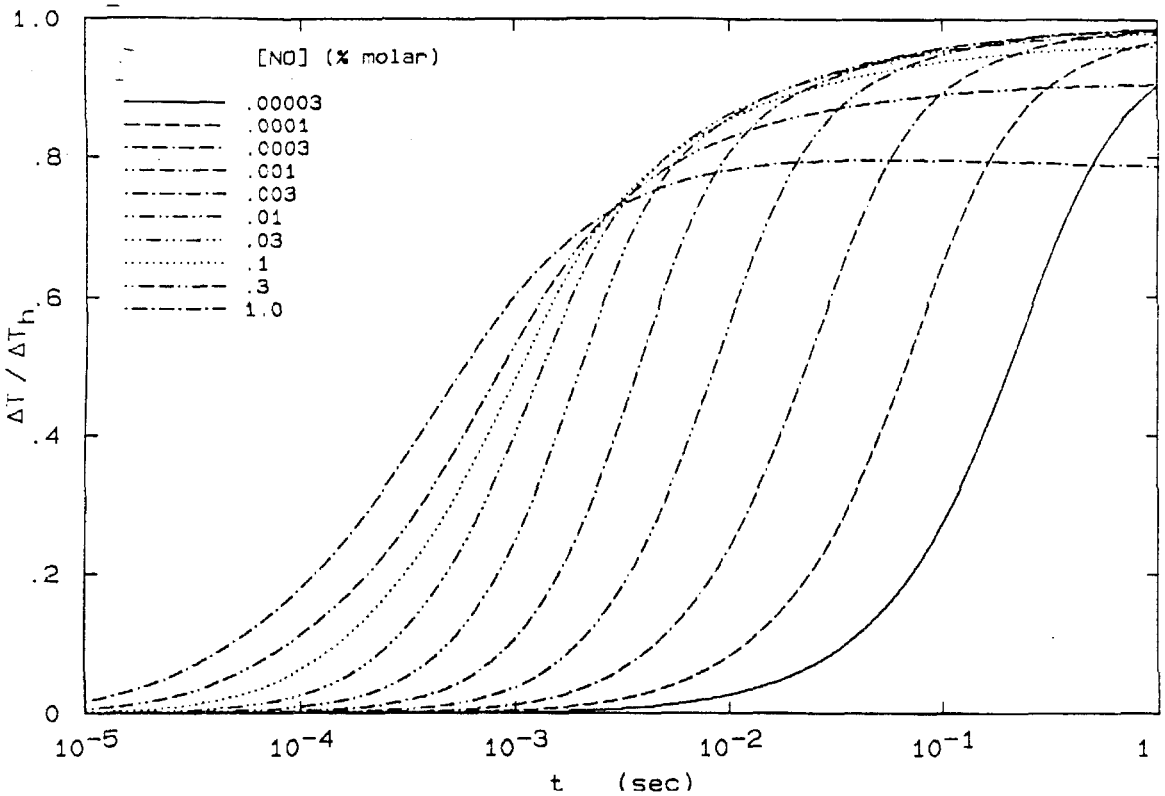

Figure E.2 Temperature rise in homogeneous reactor for H_2 / NO / F_2 .

$(\phi = 1, \Delta T_h \cong 82K)$

Shown in Figure E.3 is the equivalent set of calculations performed for the $\phi = 7$ case. The differences are dramatic. The overall reaction again appears to behave as a second order system, with the rate dependent on the concentration of NO . Note that this overall rate is significantly greater than either of the cases above, being nearly a factor of 10 faster over the entire range of NO concentrations.

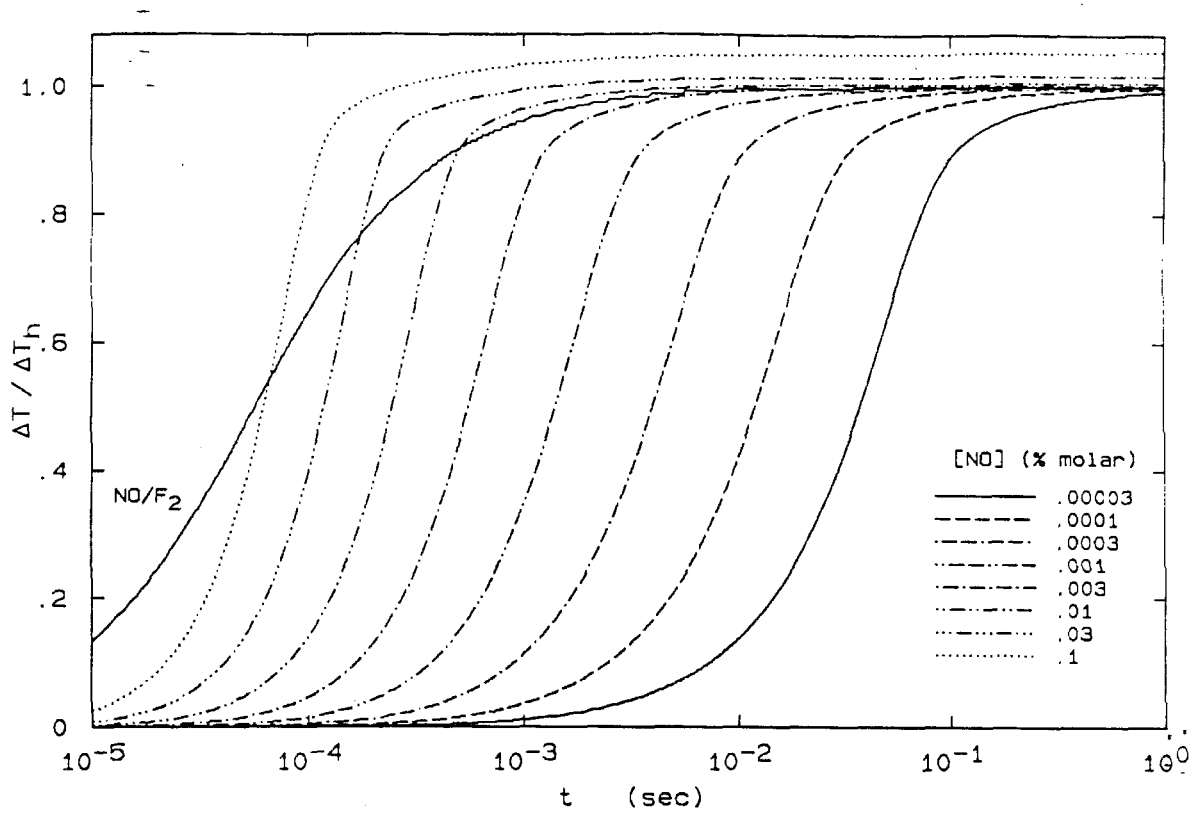

Figure E.3 Temperature rise in homogeneous reactor for $H_2 \,/\, NO \,/\, F_2$.

$(\phi = 7, \Delta T_h \cong 56K)$

REFERENCES

BALLANTYNE, A., BOON, D. J. and MOSS J. B. [1976] "Measurements of Fluctuating Temperature in Open Diffusion Flames Employing Fine Wire Thermocouples." U. of Southampton, . AASU Memo 763.

BATT, R. G. [1975] "Some Measurements on the Effect of Tripping the Two-Dimensional Shear Layer", AIAA J. 13, 245-247.

BATT, R. G. [1977] "Turbulent Mixing of Passive and Chemically Reacting Species in a Low-Speed Shear Layer", J. Fluid Mech. 82, 53-95.

BAULCH, D. L., DUXBURY, J., GRANT, S. J. and MONTAGUE, D. C. [1981] "Evaluated Kinetic Data for High Temperature Reactions", J. Phys. Chem. Ref. Data, 10, Suppl. 1.

BECKER, H. A. and YAMAZAKI, S. [1978] "Entrainment, Momentum Flux and Temperature in Vertical Free Diffusion Flames", Combustion and Flame 33, 123-149.

BEGUIER, C., FULACHIER, L. and KEFFER, J. F. [1978] "The Turbulent Mixing Layer with an Asymmetrical Distribution of Temperature", J. Fluid Mech. 89(3), 561-587.

BERNAL, L. P. [1981] The Coherent Structure of Turbulent Mixing Layers:
I. Similarity of the Primary Vortex Structure.
II. Secondary Streamwise Vortex Structure.
California Institute of Technology, Ph. D. thesis.

BERNAL, L. P., BREIDENTHAL, R. E., BROWN, G. L., KONRAD, J. H. and ROSHKO, A. [1979] "On the Development of Three-Dimensional Small Scales in Turbulent Mixing Layers." Turbulent Shear Flows 2, Second International Symp. on Turbulent Shear Flows, July 1979, Springer Verlag, 305-313.

BETCHOV, R. [1948] "L'influence de la Conduction Thermique sur les Anémomètres à Fils Chauds", Proc. Ned. Akad. Wetenshappen 51, 721.

BILGER, R. W. [1980] "Turbulent Flows with Nonpremixed Reactants", Turbulent
Reacting Flows Springer-Verlag, Topics in Applied Physics 44 1980, Ed. P. A. Libby, F. A. Williams, 65-113.

BIRCH, S. F. and EGGERS, J. M. [1972] "A Critical Review of the Experimental Data for Developed Free Turbulent Shear Layers", Free Turbulent Shear Flows Volume I Conference Proceedings NASA SP-321, 11-40.

BLUMEN, W., DRAZIN, P. G. and BILLINGS D. F. [1975] "Shear Layer Instability of an Inviscid Compressible Fluid", J. Fluid Mech. 71, 305-316.

BOGDANOFF, D. W. [1984] "Interferometric Measurement of Heterogencous Shear-Layer Spreading Rates", AIAA J. 22(11), 1550-1555.

BOND, D. L., GUENTHER, M. E., STIMPSON, L. D., TOTH, L. R. and YOUNG, D. L. [1979] "Experience with Fluorine and Its Safe Use as a Propellant." JPL Publication 79-64.

BRADSHAW, P. [1966] "The Effect of Initial Conditions on the Development of a Free Shear Layer", J. Fluid Mech. 26(2), 225-236.

BRAY, K. N. C. and LIBBY, P. A. [1981] "Countergradient Diffusion in Premixed Turbulent Flames", AIAA J. 19, 205-213.

BREIDENTHAL, R. E. [1978] A Chemically Reacting, Turbulent Shear Layer, California Institute of Technology, Ph. D. thesis.

BREIDENTHAL, R. E. [1981] "Structure in Turbulent Mixing Layers and Wakes Using a Chemical Reaction", J. Fluid Mech. 109, 1-24.

BROADWELL, J. E. [1987] "A Model for Reactions in Turbulent Jets: Effects of Reynolds, Schmidt, and Damköhler Number", Presented at the United States-France Joint Workshop on Turbulent Reactive Flows, 6-10 July, 1987.

BROADWELL, J. E. and BREIDENTHAL, R. E. [1982] "A Simple Model of Mixing and Chemical Reaction in a Turbulent Shear Layer", J. Fluid Mech. 125, 397-410. also GALCIT Report FM81-10.

BROADWELL, J. E. and DIMOTAKIS, P. E. [1986] "Implications of Recent Experimental Results for Modeling Reactions in Turbulent Flows", AIAA J. 24(6), 885-889.

BROADWELL, J. E., DAHM, W. J. A. and MUNGAL, M. G. [1984] "Blowout of Turbulent Diffusion Flames", Twentieth Symposium (International) on Combustion, The Combustion Institute, 303-310.

BROADWELL, J. E. and MUNGAL, M. G. [1986] "The Effects of Damköhler Number in a Turbulent Shear Layer–Analysis", GALCIT Report FM85-01.

BROWAND, F. K. and LATIGO, B. O. [1979] "Growth of the Two-Dimensional Mixing Layer from a Turbulent and Non-Turbulent Boundary Layer", Phys. Fluids 22(6), 1011-1019.

BROWN, G. L. [1974] "The Entrainment and Large Structure in Turbulent Mixing Layers", Presented at the Fifth Australasian Conference on Hydraulics and Fluid Mechanics, University of Canterbury, Christchurch, New Zealand, December 9-13, 1974.

BROWN, G. L. and REBOLLO, M. R. [1972] "A Small, Fast Response Probe to Measure Composition of a Binary Gas Mixture", AIAA J. 10(5), 649-652.

BROWN. G. L. and ROSHKO, A. [1971] "The Effect of Density Difference on the Turbulent Mixing Layer", Turbulent Shear Flows, AGARD-CP-93, 23.1-12.

BROWN, G. L. and ROSHKO, A. [1974] "On Density Effects and Large Structure in Turbulent Mixing Layers", J. Fluid Mech. 64, 775-816.

BROWN, J. L. [1978] Heterogeneous Turbulent Mixing layer Investigations Utilizing a $2D$ 2-Color Laser Doppler Anemometer and Using a Concentration Probe. U. Missouri-Columbia, Ph.D. thesis.

BURKE, S. P. and SCHUMANN, T. E. W. [1928] "Diffusion Flames", Ind. Eng. Chem. 20, 998-1006.

CALDWELL, F. R. [1962] "Thermocouple Materials", National Bureau of Standards Monograph40, United States Department of Commerce, National Bureau of Standards, 7-8.

CANTWELL, B. J. [1978] "Similarity Transformations for the Two-Dimensional, Unsteady, Stream-Function Equation", Fluid Mech. 85(2), 257-271.

CARRIER, G. F., FENDELL, F. E. and MARBLE, F. E. [1975] "The Effect of Strain Rate on Diffusion Flames." SIAM J. Appl. Math. 28(2), 463-500.

CETEGEN, B. M. and KUBOTA, T. [1981] "Integral Solution of a Bouyant Diffusion Flame", Report, Daniel and Florence Guggenheim Jet Propulsion Center, California Institute of Technology.

CHANDRSUDA, C. MEHTA, R. D. WEIR, R. D. and BRADSHAW, P. [1978] "Effect of Free-Stream Turbulence on Large Structure in Turbulent Mixing Layers", J. Fluid Mech. 85(4), 693-704.

CHMIELEWSKI, G. E. [1974] "Boundary Layer Considerations in the Design of Aerodynamic Contractions", J. Aircraft. 11, 435-438.

COHEN, N. [1982] "A Review of Rate Coefficients for Reactions in the H_2 - F_2 Laser System." The Aerospace Corporation, Report TR-0073(3430)-9.

COHEN, N. and BOTT, J. F. [1982] "Review of the Rate Data for Reactions of Interest in HF and DF Lasers", The Aerospace Corporation, Report SD-TR-82-86.

COHEN, N. and WESTBERG, K. R. [1983] "Chemical Kinetic Data Sheets for High-Temperature Chemical Reactions", J. Chem. Phys. Ref. Data 12(3), 531-544.

COLES, D. [1981] "Prospects for Useful Research on Coherent Structure in Turbulent Shear Flow", Proc. Indian Acad. Sci. 4(2), 111-127.

CULICK, F. E. C. [1962] "The Equations of Conservation for Multicomponent Reacting Gas Flows", Technical Report 48, Massachusetts Institute of Technology Aerophysics Laboratory.

DAVEY, R. F. and ROSHKO, A. [1972] "The Effect of a Density Difference on Shear-Layer Instability", J. Fluid Mech. 53(3), 523-543.

DAVIS, L. R. [1968] "Experimental and Theoretical Determination of Flow Properties in a Reacting Near Wake", AIAA J. 6(5), 843-847.

DEISSLER, R. G. [1982] "Turbulent Solution of the Navier-Stokes Equations for an Inhomogeneous Developing Shear Layer", NASA-TM-82969.

DELCOURT, B. A. G. and BROWN, G. L. [1979] "The Evolution and Emerging Structure of a Vortex Sheet in an Inviscid and Viscous Fluid Modelled by a Point Vortex", Second International Symposium on Turbulent Shear Flows, July 1979, Proceedings, 14.35-14.40.

DIMOTAKIS, P. E. [1986] "Two-Dimensional Shear Layer Entrainment", AIAA J. 24(11), 1791-1796.

DIMOTAKIS, P. E. [1989] "Turbulent Free Shear Layer Mixing and Combustion", AIAA-89-0262, 27th Aerospace Sciences Meeting (Reno, Nevada), 9-12 January 1989.

DIMOTAKIS, P. E. and BROWN G. L. [1976] "The Mixing Layer at High Reynolds Number: Large Structure Dynamics and Entrainment", J. Fluid Mech. 78(3), 535-560 +2 plates.

DIMOTAKIS, P. E. and HALL, J. L. [1987] "A Simple Model for Finite Chemical Kinetics Analysis of Supersonic Turbulent Shear Layer Combustion", AIAA/SAE/ASME /ASEE Joint Propulsion Conference Colloquium on Supersonic Combustion, AIAA-87-1879
29 June - 2 July 1987 (San Diego, California).

DOWLING, D. R. [1988] Mixing in Gas-Phase Turbulent Jets, California Institute of Technology, Ph. D. thesis.

DOWLING, D. R. and DIMOTAKIS, P. E. [1988] "On Mixing and Structure of the Concentration Field of Turbulent Jets", Submitted to the First National Fluid Dynamics Congress, July 1988.

DZIOMBA, B. and FIEDLER, H. E. [1985] "Effect of Initial Conditions on Two-Dimensional Free Shear Layers", J. Fluid Mech. 152, 419-442.

FAUVRE, A. [1965] "The Equations of Compressible Turbulent Gases, Parts I & II" Extrait du J. de Mechanique, 4(3,4).

FIEDLER, H. F. [1974] "Transport of Heat Accross a Plane Turbulent Mixing Layer", Advances in Geophysics 18A, Academic Press, 93-109.

FIEDLER, H. F. [1975] "On Turbulent Structure and Mixing Mechanisms in Free Shear Flows", Turbulent Mixing in Nonreactive and Reactive Flows. A Project SQUID Workshop. Plenum Press, 381-410.

FIEDLER, H. F., KORSCHELT, D. and MENSING, P. "On Transport Mechanism and Structure of Scalar Field in a Heated Plane Shear Layer", in Structure and Mechanisms of Turbulence II, Proceedings, Berlin 1977, 58-72.

FIEDLER, H. F. and THIES, [1977] "Some Observations in a Large Two Dimensional Shear Layer", Structure and Mechanics of Turbulence I, Lecture Notes in Physics, 75, Springer Verlag, 108-117.

FLEMING, G. C. [1982] Structure and Stability of Buoyant Diffusion Flames, California Institute of Technology, Ph. D. thesis.

FRIELER, C. E. and DIMOTAKIS, P. E. [1988] "Mixing and Reaction at Low Heat Release in the Non-Homogeneous Shear Layer", AIAA-88-3626.

GANJI, A. T. and SAWYER, R. F. [1980] "Experimental Study of the Flowfield of a Two-Dimensional Premixed Turbulent Flame", AIAA J. 18(7), 817-824.

GHONIEM, A. F., HEIDARINEJAD, G and KRISHNAN, A. [1988] "On Mixing, Baroclinicity and the Effect of Strain in a Chemically Reacting Shear Layer", AIAA-88-0729, 26th Aerospace Sciences Meeting, January 1988.

GIBSON, C. H. and LIBBY, P. A. [1972]
"On Turbulent Flows with Fast Chemical Reactions.
Part II.
The Distribution of Reactants and Products Near a Reacting Surface"
Combustion Science and Technology 6, 29-35.

GIVI, P., JOU, W. H. and METCALFE, R. W. [1986] "Flame Extinction in a Temporally Developing Mixing Layer", Twenty-first Symposium (International) on Combustion / The Combustion Institute, 1251-1261.

Gmelin Handbuch der Anorganischen Chemie [1980] "Fluorine", Supplement Vol. 2, System-Nummer 5, Springer-Verlag, 108.

GROPENGIESSER, H. [1970] "Study of the Stability of the Boundary Layer in Compressible Fluids", NASA TT-F-12, 786.

HERMANSON, J.C. [1985]
Heat Release Effects in a Turbulent Reacting Shear Layer,
California Institute of Technology, Ph. D. thesis.

HERMANSON, J. C. and DIMOTAKIS, P. E. [1989] "Effects of Heat Release in a Turbulent Reacting Shear Layer", J. Fluid Mech. 199, 333-375.

HERMANSON, J. C. , MUNGAL, M. G. and DIMOTAKIS, P. E. [1985] "Heat Release Effects on Shear Layer Growth and Entrainment", AIAA J. 25(4) and AIAA-85-0142, 578-583.

HILL Jr., W. G. and PAGE, R. H. [1969] "Initial Development of Turbulent, Compressible Free Shear Layers", J. Basic Engineering, 67-73.

HO, C. M. and HUANG, L. S. [1982] "Subharmonics and Vortex Merging in Mixing Layers", J. Fluid Mech. 119, 443-473.

HO, C. M. and HUANG, L. S. [1983] "Development of Free Shear Layer",
Turbulence and Chaotic
Phenomena in Fluids, Proceedings of the International Symposium, Kyoto, Japan, September 5-10, 1983 (A85-24951) Amsterdam, N. Holland, 1984, 327-332.

HO, C. M. and HUERRE, P. [1984] "Perturbed Free Shear Layers",
Annual Review of Fluid Mechanics 16, 365-424.

HOWARTH, L. [1948] "Concerning the Effect of Compressibility on Laminar Boundary Layers and Their Seraration",
Proceedings of the Royal Society of London A 194, 16-42.

HUERRE, P. and MONKEWITZ, P. A. [1985] "Absolute and Convective Instabilities in Free Shear Layers", J. Fluid Mech. 159, 151-168.

JANAF Thermochemical Tables, [1985] J. Phys. Chem. Ref. Data 14(1) Part II.

KEE, R. J., MILLER, J. A., and JEFFERSON, T. H. [1980]
"CHEMKIN: A General Purpose, Problem Independent, Transportable, Fortran Chemical Kinetics Code Package."
SANDIA Report SAND80-8003.

KELLER, H. B. [1976] "Numerical Solution of Two Point Boundary Value Problems", J. W. Arrowsmith Ltd., Bristol 3, England.

KELLER, J. O. and DAILY, J. W. [1985] "The Effects of Highly Exothermic Chemical Reaction on a Two-Dimensional Mixing Layer", AIAA J. 23(12), 1937-1945.

KERSTEIN, A. R. [1989] "Linear-Eddy Modeling of Turbulent Transport II: Application to Shear Layer Mixing", Combustion and Flame 75(3,4), 397-413.

KOLLMAN, W. and JANICKA, J. [1982] "The Probability Density Function of a Passive Scalar in Turbulent Shear Flows", Phys. Fluids 25(10), 1755-1769.

KONRAD, J. H. [1976] "An Experimental Investigation of Mixing in Two-Dimensional Turbulent Shear Flows with Applications to Diffusion-Limited Chemical Reactions", Ph.D. Thesis, California Institute of Technology, also Project SQUID Technical Report CIT-8-PU.

KOOCHESFAHANI, M. M. [1984] Experiments on Turbulent Mixing and Chemical Reactions in a Liquid Mixing Layer,
California Institute of Technology, Ph. D. thesis.

KOOCHESFAHANI, M. M., CATHERASOO, C. J., DIMOTAKIS, P. E., GHARIB, M. and LANG, D. B. [1979] "
Two-Point LDV Measurements in a Plane Mixing Layer", AIAA J. 17(12), 1347-1351.

KOOCHESFAHANI, M. M. and DIMOTAKIS, P. E. [1985] "Laser-Induced Fluorescence Measurements of Mixed Fluid Concentration in a Liquid Plane Shear Layer", AIAA J. 23(11), 1700-1707.

KOOCHESFAHANI, M. M. and DIMOTAKIS, P. E. [1986] "Mixing and Chemical Reactions in a Turbulent Liquid Mixing Layer", J. Fluid Mech. 170, 83-112.

KOOCHESFAHANI, M. M., DIMOTAKIS, P. E. and BROADWELL, J. E. [1985] "A 'Flip' Experiment in a Chemically Reacting Turbulent Mixing Layer", AIAA J. 23, 1191-1194.

KOOCHESFAHANI, M. M. and FRIELER, C. E. [1987] "Inviscid Instability Characteristics of Free Shear Layers with Non-Uniform Density", AIAA-87-0047.

KOOP, C. G. and BROWAND, F. K. [1979] "Instability and Turbulence in a Stratified Fluid with Shear", J. Fluid Mech. 93(1), 135-159.

LAUFER, J. [1969] "Turbulent Shear Flows of Variable Density", AIAA J. 7(4), 706-713.

LIBBY, P. A. and WILLIAMS, F. A. [1980] "Turbulent Reacting Flows", Topics in Applied Physics 44, Springer Verlag, 76.

LIBBY, P. A. and WILLIAMS, F. A. [1981] "Some Implications of Recent Theoretical Studies in Turbulent Combustion" AIAA J. 19(3), and AIAA-80-0012R, 261-274.

LIEPMANN, H. W. and LAUFER, J. [1947] "Investigations of Free Turbulent Mixing." NACA TN 1257.

LIN, P. and PRATT, D. T. [1987] "Numerical Simulation of a Plane Turbulent Mixing Layer, with Applications to Isothermal, Rapid

Reactions", AIAA-87-0224, 25th Aerospace Sciences Meeting, January 1987.

LIÑAN, A. [1980] "Lewis Number Effects on the Structure and Extinction of Diffusion Flames Due to Strain." The Role of Coherent Structures in Modelling Turbulence and Mixing, Proc. Int. Conf., J. Jimenez. Ed., Springer Verlag, Berlin, 333-339.

LOCK, R. C. [1935] "The Velocity Distribution in the Laminar Boundary Layer Between Parallel Streams", Quart. J. Mech. Appl. Math. 4, 42-63.

LUNDGREN, T. S. [1984] "The Product Spectrum in a Turbulent Reactor with Fast Bimolecular Reactions", Chem. Eng. Science.

MAGRE, P. and DIBBLE, R. [1987] "Finite Chemical Kinetics Effects in a Subsonic Turbulent Hydrogen Flame", AIAA-87-0378.

MARBLE, F. E. [1981] "Growth of a Diffusion Flame in the Field of a Vortex", Recent Advances in the Aerospace Sciences, Edited by Corrado Casci, 395-413.

MARBLE, F. E. and BROADWELL, J. E. [1977] "The Coherent Flame Model for Turbulent Chemical Reactions." Project SQUID Tech. Rep. TRW-9-PU.

MASLOWE, S. A. and KELLY, R. E. [1971] "Inviscid Instability of an Unbounded Heterogeneous Shear Layer", J. Fluid Mech. 48(2), 405-415.

MASLOWE, S. A. and THOMPSON, J. M. [1971] "Stability of a Stratified Free Shear Layer", Phys. Fluids 14(3), 453-458.

MASON, E. A. and SAXENA, S. C. [1958] "An Approximate Formula for the Thermal Conductivity of Gas Mixtures.", Phys. Fluids 1(5), 361-369.

MASUTANI, S. M. [1985] "An Experimental Investigation of Mixing and Chemical Reaction in a Plane Mixing Layer", High Temperature Gasdynamics Laboratory Topical Report Number T-246, Mechanical Engineering Department, Stanford University.

MASUTANI, S. M. and BOWMAN. C. T. [1986] "The Structure of a Chemically Reacting Plane Mixing Layer", J. Fluid Mech. 172, 93-126.

MATHESON Gas Data Book [1980] 6th edition, Matheson Gas Co., 330.

MATTINGLY, G. E. and CRIMINALE, W. O. [1972] "The Stability of an Incompressible Two-Dimensional Wake", J. Fluid Mech. 51(2), 233-272.

McMURTRY, P. A., JOU, W. H., RILEY, J. J. and METCALFE, R. W. [1985] "Direct Numerical Simulations of a Reacting Mixing Layer with Chemical Heat Release." AIAA-85-0143, 23rd Aerospace Sciences Meeting, January 1985.

MEHTA, R. D. and WESTPHAL, R. V. [1985] "An Experimental Study of Plane Mixing Layer Development", NASA TM-86698.

MERZKIRCH, [1974] Flow Visualization, Academic Press, New York, 86-100.

MIAU, J-J. and KARLSSON, S. K. F. [1986] "Evolution of Flow in the Developing Region of the Mixing-Layer with a Skew Laminar Wake as Initial Condition", Phys. Fluids 29(11), 3598-3607.

MICHALKE, A. [1965] "On Spatially Growing Disturbances in an Inviscid Shear Layer", J. Fluid Mech. 23(3), 521-544.

MIKSAD, R. W. [1972] "Experiments on the Nonlinear Stages of Free-Shear Layer Transition", J. Fluid Mech. 56(4), 695-719.

MONKEWITZ, P. A. and HUERRE, P. [1982] "Influence of the Velocity Ratio on the Spatial Instability of Mixing Layers", Phys. Fluids 25(7), 1137-1143.

MUNGAL, M. G. [1983] Experiments on Mixing and Combustion with Low Heat Release in a Turbulent Shear Flow, California Institute of Technology, Ph. D. thesis.

MUNGAL, M. G. and DIMOTAKIS, P. E. [1984] "Mixing and Combustion with Low Heat Release in a Turbulent Mixing Layer", J. Fluid Mech. 148, 349-382.

MUNGAL, M. G., DIMOTAKIS, P. E. and BROADWELL, J. E. [1983] "Turbulent Mixing and Combustion in a Reacting Shear Layer", AIAA-83-0473, Reno, Nevada. AIAA J. 22(6), 797-800.

MUNGAL, M. G. and FRIELER, C. E. [1988] "The Effects of Damköhler Number in a Turbulent Shear Layer", Combustion and Flame 71, 23-34, GALCIT Report FM85-01.

MUNGAL, M. G., HERMANSON, J. C. and DIMOTAKIS, P. E. [1985] "Reynolds Number Effects on Mixing and Combustion in a Reacting Shear Layer", AIAA J. 23(9), 1418-1423.

OH, Y. H. and BUSHNELL, D. M. [1976] "Influence of External Disturbances and Compressibility on Free Turbulent Mixing", Aerodynamics Analysis Requiring Advanced Computers NASA-SP-347 Part 1, N76-10018, 341-376.

OSTER, D. and WYGNANSKI, I. [1982] "The Forced Mixing Layer Between Parallel Streams", J. Fluid Mech. 123, 91-130.

OSTER, D., WYGNANSKI, I. and FIEDLER, H. F. [1976] "Some Preliminary Observations on the Effect of Initial Conditions on the Structure of the Two-Dimensional Turbulent Mixing Layer", Turbulence in Internal Flows, Project SQUID workshop S.N.B. Murthy ed., Hemisphere, Washington, 67-87.

OU, J-J. and RANZ W. E. [1983] "Mixing and Chemical Reactions Chemical Selectivities", Chem. Eng. Science 38(7), 1015-10194.

PARANTHOEN, P., PETIT, C. and LECORDIER, J. C. [1982] "The Effect of the Thermal Prong - Wire Interaction on the Response of a Cold Wire in Gaseous Flows (Air, Argon and Helium)", J. Fluid Mech. 124, 457-473.

PETERS, N. and WILLIAMS, F. A. [1980]
"Coherent Structures in Turbulent Combustion."
The Role of Coherent Structures in Modelling Turbulence and Mixing, Proc. Int. Conf., J. Jimenez, Ed.,
Springer Verlag, Berlin 1981, 364-393.

PITZ, R. W. and DAILY, J. W. [1980] "Experimental Studies of Combustion in a Two-Dimensional Free Shear Layer", AIAA-A80-49251, 18th Aerospace Sciences Meeting, January 1980.

PITZ, R. W. and DAILY, J. W. [1983] "Combustion in a Turbulent Mixing Layer Formed at a Rearward-Facing Step", AIAA J. 21(11), 1565-1570.

PRANDTL, L. [1925] "Bericht uber Untersuchungen zur augesbildeten Turbulenz", Ztschr. angew. Math. Mech. 5(2), 136-139.

RAJAGOPALAN, S. and ANTONIA, R. A. [1980] "Properties of the Large Structure in a Slightly Heated Turbulent Mixing Layer of a Plane Jet.", J. Fluid Mech. 105, 261-281.

RAPP, D. and JOHNSTON, H. S. [1960] "Nitric Oxide-Fluorine Dilute Diffusion Flame", J. Chem. Phys. 33(3), 695-699.

REBOLLO, M. R. [1973] Analytical and Experimental Investigation of a Turbulent Mixing Layer of Different Gases in a Pressure Gradient.
California Institute of Technology, Ph. D. thesis.

RILEY, J. J. and METCALFE, R. W. [1985] "Direct Numerical Simulations of Chemically Reacting Turbulent Mixing Layers", AIAA-85-0321, 23rd Aerospace Sciences Meeting, January 1985.

ROBERTS, F. A. [1985] Effects of a Periodic Disturbance on Structure and Mixing in Turbulent Shear Layers and Wakes.
California Institute of Technology, Ph. D. thesis.

SABNIS, J. S., CHOI, S-K., BUGGELN, R. C. and GIBELING, H. J. [1988] "Computation of Two-Phase Shear-Layer Flow Using an Eulerian-Lagrangian Analysis", AIAA-88-3202, 26th Aerospace Sciences Meeting, January 1988.

SAIY, M. and PEERLESS, S. J. [1987] "Measurement of Turbulence Quantities in a Two-Stream Mixing Layer", J. Fluid Mech. 89(4), 709-722.

SANDBORN, V. A. [1972] Resistance Temperature Tranducers, Metrology Press, 428-431.

SCADRON, M. D. and WARSHAWSKY, I. [1952] "Experimental Determination of Time Constants and Nusselt Numbers for Bare-Wire Thermocouples in High-Velocity Air Streams and Analytic Approximation of Conduction and Radiation Errors.", NACA TN 2599.

SCHMIDT, H. W. [1967] " Fluorine and Fluorine-Oxygen Mixtures in Rocket Systems." NASA SP 3037.

SHEPHERD, I. G. and DAILY, J. W. [1984] "Rayliegh Scattering Measurements in a Two-Stream Free Mixing Layer", University of California, Berkeley, WSS/CI Paper 84-45.

SPAULDING D. B. [1984] "The Two-Fluid Model of Turbulence Applied to Combustion Phenomena.", AIAA-84-0476, 22nd Aerospace Sciences Meeting, January 1984.

SPENCER, B. W. and JONES, B. G. [19] "Statistical Investigation of Pressure and Velocity Fields in the Turbulent Two-Stream Mixing Layer", AIAA-71-613, AIAA 4th Fluid and Plasma Dynamics Conference, June, 1971.

STERLING, J. D. and ZUKOWSKI. E. E., [1987] "Longitudinal Mode Combustion Instabilities in a Dump Combustor", AIAA-87-0220, 25th Aerospace Sciences Meeting, January 1987.

VANDROMME, D. and KOLLMANN, W. [1981] "Second Order Closure for Variable density Free Shear Layer", Turbulent Shear Flows 3, International Symposium, 3rd, Davis,CA September 9-11,1981 (A83-33651 15-34). Berlin, Springer Verlag, 1982, 275-290.

VARMA, A. K., BEDDINI, R. A. and FISHBURNE, E. S. [1976] "Second-Order Closure Analysis of Turbulent Reacting Flows", Heat Transfer and Fluid Mechanics Institute, Meeting 25th, Davis, CA, June 21-23, 1976, Proceedings (A76-35401 17-34) Stanford, CA, Stanford University Press, 1976, 229-240.

WALLACE, A. K. [1981] Experimental Investigation of the Effects of Chemical Heat Release in the Reacting Turbulent Plane Shear Layer, University of Adelaide, Australia, Ph.D. thesis, AFOSR-TR-84-0650.

WEISBROT, I., EINAV, S. and WYGNANSKI, I. [1982] "The Nonunique Rate of Spread of the Two-Dimensional Mixing Layer", Phys. Fluids 25, 1691.

WINANT, C. D. and BROWAND, F. K. [1974] "Vortex Pairing: The Mechanism of Turbulent Mixing-Layer Growth at Moderate Reynolds Number", J. Fluid Mech. 63(2), 237-255.

WITTE, A. B., BROADWELL, J. E., SHACKLEFORD, W. L., CUMMINGS, J. C., TROST, J. E., WHITMAN, A. S., MARBLE, F. E., CRAWFORD, D. R. and JACOBS, T. A. [1974] "Aerodynamic Reactive Flow Studies of

the H_2 - F_2 Laser-II", Air Force Weapons Lab, Kirtland Air Force Base, New Mexico, AFWL-TE-74-78, 33.

WYGANANSKI, I. and PETERSEN, R. A., [1985] "Coherent Motion in Free Shear Flows", AIAA-85-0539, 23rd Aerospace Sciences Meeting, January 1985.

WYGANANSKI, I. and FIEDLER, H. E., [1970] "The Two-dimensional Mixing Region", J. Fluid Mech. 40, 327-361.

ZHANG, Y-Q., HO, C-H. and MONKEWITZ, P. [1984] "The Mixing Layer Forced By Fundamental and Subharmonic, Laminar-Turbulent Transition", Proc. IUTAM Symp., Novosibirsk, USSR, July 9-13, Springer-Verlag, 385-395.